

Alma Mater Studiorum - Università di Bologna

DOTTORATO DI RICERCA IN
SCIENZE E TECNOLOGIE DELLA SALUTE

Ciclo 35

Settore Concorsuale: 05/E2 – BIOLOGIA MOLECOLARE

Settore Scientifico Disciplinare: BIO/11 - BIOLOGIA MOLECOLARE

CONTENT-AWARE APPROACH FOR IMPROVING BIOMEDICAL IMAGE
ANALYSIS: AN INTERDISCIPLINARY STUDY SERIES

Presentata da: Ilaria De Santis

Coordinatore Dottorato

Marco Viceconti

Supervisore

Alessandro Bevilacqua

Co-supervisore

Laura Calzà

Esame finale anno 2023

Keywords

Automated quantitative imaging

Image processing and analysis

Biomedical imaging

Interdisciplinarity

Cancer imaging

Microscopy

External reviewers

Prof. Thimios A. Mitsiadis,

University of Zürich, Switzerland

e-mail: thimios.mitsiadis@zzm.uzh.ch

Dr. Enrico Lucarelli,

Rizzoli Orthopaedic Institute, Italy

e-mail: enrico.lucarelli@ior.it

Abstract

Biomedicine represents the most important and significant multidisciplinary field of the medical science, as it defines the fundamental theoretical framework for most of the present health science and technology research. In the last decade, the introduction of new imaging technologies in microscopy, as well as the improvement of the existing ones, has allowed obtaining images of increasing resolution and sharpness, thus considerably advancing the possibility to investigate biological phenomena. Accordingly, quantitative image analysis is now a routine activity for most of biomedical researchers, that rely on many available commercial and freeware software to autonomously analyse their own images, even customizing – to a certain extent – processing pipelines and methods. However, the effectiveness of this approach is bounded by the limited knowledge that a biologist, by professional training, has of the computer tools at the disposal. On the other hand, if computer vision scientists could be the most effective ones for efficiently handling biomedical images, they do not own, by professional training, the necessary knowledge of the biological world that should drive a meaningful image processing. The possible solution to make up for both these lacks lies in training biologists to make them interdisciplinary researchers able to develop dedicated image processing and analysis tools by exploiting a content-aware approach.

The aim of this Thesis is to show the effectiveness of a content-aware approach to automated quantitative imaging, by its application to different biomedical studies, with the secondary desirable purpose of motivating researchers to invest in interdisciplinarity. In the first study, I apply a content-aware approach to the phenomization of tumour cell response to stress by confocal fluorescent imaging, by developing on-purpose methods for the subcellular segmentation and quantification of RNA:DNA hybrids in different tumour cell lines. In the second study, I face a muscle-to-bone crosstalk problem, aiming at elucidating the effect of the muscular protein sclerostin on bone structures. Here, starting from micro-

CT scans, I innovatively apply the Gabor filtering method to the texture analysis of trabecular bone microarchitecture. Third study addresses the characterization of new 3-D multicellular spheroids of human dental pulp stem cells where, merging molecular and imaging analysis, I also contribute to the improvement of the experimental planning of the study. In the fourth study, I investigate the role of the Nogo-A protein in tooth innervation by developing a dedicated pipeline for the 3-D segmentation and morphological description of the tooth neuronal network. Finally, I also apply the content-aware approach to developing two novel methods for local image analysis and colocalization quantification.

In conclusion, the content-aware approach has proved its benefit through building new approaches that has improved the quality of image analysis, strengthening the statistical significance to allow unveiling biological phenomena. Hopefully, this Thesis will contribute to inspire researchers to striving hard for pursuing interdisciplinarity.

Contents

Abstract	vii
Contents	ix
1 Introduction and Thesis overview	1
2 Biomedical models	11
2.1 <i>In vitro</i> 2-D models.....	13
2.1.1 2-D cell cultures.....	13
2.1.2 <i>In vitro</i> 2-D models limitations.....	18
2.2 <i>In vitro</i> 3-D models.....	19
2.2.1 Spheroids.....	22
2.2.2 <i>In vitro</i> 3-D models limitations.....	25
2.3 <i>In vivo</i> and <i>ex vivo</i> models.....	25
2.3.1 Mouse model.....	27
2.3.2 <i>In vivo</i> models limitations.....	30
2.4 Concluding remarks.....	32
3 Imaging modalities and analysis: principles and techniques	33
3.1 Digital images.....	35
3.2 Microscopy.....	37
3.2.1 Bright Field microscopy.....	39
3.2.2 Differential Interference Contrast microscopy.....	41
3.2.3 Fluorescence microscopy.....	43
3.2.4 Optical microscopy artifacts.....	49
3.3 Computed Tomography.....	52
3.3.1 Micro Computer Tomography.....	53
3.3.2 Micro Computer Tomography artifacts.....	56
3.4 Concluding remarks.....	57
4 Density Distribution Maps: a novel tool for subcellular distribution analysis and quantitative biomedical imaging	59
4.1 Study context.....	60
4.2 Theoretical background.....	61
4.2.1 Principles of local analysis.....	61

4.2.2	Image segmentation and thresholding.....	63
4.3	State of the art.....	64
4.4	Material and methods.....	67
4.5	Results and discussion.....	75
4.6	Conclusions.....	90
4.7	Content-aware contribution and future developments.....	91
5	Co-Density Distribution Maps for advanced molecule colocalization and co-distribution analysis.....	93
5.1	Study context.....	93
5.2	Theoretical background.....	95
5.2.1	Image arithmetic and morphology.....	95
5.2.2	Coefficients for colocalization quantification.....	97
5.3	State of the art.....	103
5.4	Material and methods.....	105
5.5	Results and discussion.....	111
5.6	Conclusions.....	127
5.7	Content-aware contribution and future developments.....	128
6	Content-aware approach in oncology: RNA:DNA hybrids role in tumour stress response by automated quantitative imaging.....	131
6.1	Study context.....	132
6.2	Theoretical background.....	133
6.2.1	RNA:DNA hybrids.....	133
6.2.2	Geodesic reconstruction.....	134
6.3	State of the art.....	136
6.4	Material and methods.....	138
6.5	Results and discussion.....	142
6.6	Conclusions.....	156
6.7	Content-aware contribution and future developments.....	158
7	Content-aware approach in neuromotor science: morphometric analysis and trabecular classification of murine tibial bone in micro-CT scans.....	161
7.1	Study context.....	162
7.2	Theoretical background.....	163
7.2.1	Bone architecture and remodelling.....	163
7.2.2	Texture analysis and Gabor filtering.....	166
7.3	State of the art.....	169

7.3.1	Muscle-bone crosstalk.....	169
7.3.2	Bone quantitative imaging.....	170
7.4	Material and methods.....	171
7.5	Results and discussion.....	178
7.6	Conclusions.....	184
7.7	Content-aware contribution and future developments.....	185
8	Content-aware approach in developmental and regenerative dental biology: characterization of hDPSCs spheroids and molar innervation by automated quantitative imaging.....	187
8.1	Study context.....	188
8.2	Theoretical background.....	189
8.2.1	Tooth anatomy and DPSCs.....	189
8.2.2	Odontogenesis and tooth innervation.....	192
8.3	State of the art.....	195
8.3.1	MSCs niche modelling.....	195
8.3.2	Nogo-A role in the central nervous system.....	196
8.4	Material and methods.....	199
8.4.1	hDPSC spheroids characterization.....	199
8.4.2	Nogo-A role in tooth innervation.....	204
8.5	Results and discussion.....	209
8.5.1	hDPSC spheroids characterization.....	209
8.5.2	Nogo-A role in tooth innervation.....	214
8.6	Conclusions.....	218
8.7	Content-aware contribution and future developments.....	219
9	Conclusions.....	223
	List of abbreviations.....	227
	List of figures.....	235
	List of tables.....	239
	Bibliography.....	241
	Acknowledgements.....	277

Chapter 1

Introduction and Thesis overview

The rise and affirmation of biomedicine represents one of the most important and significant developments of the last century, as it defines the fundamental theoretical framework for most of present health science and health technology research. Among the set of biomedical sciences promoting the advancement of biomedicine, some stands out for their capability to dissect modern problems complexity. First, biology permits to reduce biomedical problems to their basic components, exploring the fundamental principles of mechanisms and diseases down to the molecular level. Accordingly, biology is one of the key disciplines that guide the understanding of pathophysiological processes in preclinical investigation and drug discovery. Secondly, since the advent of the digitalization era, a capital driver of health science advancement has been computational biomedicine, that brings together mathematics, statistics, and importantly, computer science and computer technology, to allow the production, handling and analysis of increasingly amount of digital biomedical data. Last but not least, a relevant and sometimes underestimated player in the modern health science research is biomedical digital imaging, that is pillar to a vast range of studies, from subcellular molecular investigations to diagnostic whole-body imaging.

Regardless of its application, digital imaging can provide unique advantages to the experimental design. Foremost, the possibility to visualize the samples in a non-invasive and non-disruptive way, eventually also over time, enables the observation of phenomena that cannot be detected by molecular assays. One representative example is the increasingly recognized capability of imaging to better capture sample spatio-temporal heterogeneity, an issue that is considered a major barrier to drug development and disease treatment. If we recognize images not only as pictorial figures, but also – and firstly – as representation of physical

quantities, we can extract from them numerical information about tissue composition, morphology and function, as well as a quantitative description of many fundamental biological processes. Furthermore, the automation of image collection and processing can make the analysis less labour-intensive and higher in throughput, increasing the quantity of collectable data, their reproducibility and reliability, besides their statistical validity and robustness. As a result, quantitative image analysis has become a routine activity for most of biomedical researchers that, thanks to many available commercial as well as open-source software, can autonomously analyse their own images, even customizing – to a certain extent – processing pipelines and methods.

However, as health science advances and biomedical problems increase in complexity, researchers are often confronted with the challenge of handling, processing and interpreting images of increasing complexity and richness, which not only demands advanced computational infrastructure, but also users with theoretical and practical expertise of computer vision, to fruitfully navigate the potential of such data. Although employing computer vision scientists could be the optimal choice for efficient handling of biomedical digital images, they do not possess, by formation, the necessary knowledge and therefore sensibility towards the biological significance of the data. In this scenario, to overcome this deadlock, and more generally ensure continuing progress in biomedicine, there is no doubt that multidisciplinary is the cornerstone of modern research. However, to benefit multidisciplinary work at most, the knowledge transfer between researchers of the single disciplines is mandatory. This is yet more true in the biological field, since a proper image processing and analysis requires that the experiments are designed since beginning also considering the needs of automated image analysis to extract reliable quantitative information.

The Doctorate path has represented a technical knowledge transfer that has enabled me, a molecular biologist, to develop and apply a *content-aware* approach to biomedical image processing and analysis. With this approach, the experiments are carried out by weighing both the biological aims and the data analysis needs, from the first experimental design stage throughout the whole image analysis pipeline, thus providing methodological solutions that increase the statistical significance of the data, meanwhile enforcing the biological outcomes and, even

more, paving the way for new findings. Being at first “just” a molecular biologist, the application of such interdisciplinary approach first required me a big mindset change, to start thinking also “as an engineer”. This has meant moving from thinking of images as corollary confirmative pictures for my molecular experiments, to consider them as a precious source of numerical information with their own dignity. Working with images, I needed to stop being satisfied by just what I could check by eye, and to develop a new sensibility towards numerical data, their fluctuation especially, and consequently reproducibility. In doing so, I have realized how, though effective in my experiments, I was enormously undervaluing, and underexploiting, my images, neglecting a great part of their informative content, accepting what I have realized being levels of inaccuracy, misled by the intrinsic uncertainty of the biological processes, and basically wasting energy, resources and data by simply not analysing them in the best possible way. Step by step, I started realizing that, as much as more time consuming, and harder, an interdisciplinary approach was really repaying in terms of quantity and quality of data that could be extracted through a more accurate image analysis. Of course, to achieve interdisciplinarity, I also had to learn, train and experience in image processing methods and techniques. This allowed me first to better understand what the available software tools I was using were actually doing to my images, to setup, *consciously*, a proper software pipeline using commercial tools and, above all, to customize the program execution selecting the correct parameter values, aware of their meaning, because aware of the underlying algorithm employed. I could also detect some limitations and applicability issues to my biological problem, that pushed me to devise and design some possible solutions. In fact, a training in the MATLAB® programming language completed my formation, allowing me to develop, when necessary, my own methods for image analysis, to replace some parts of an existing processing pipeline or to be used stand-alone, to reach the biological effectiveness that sometimes a general-purpose tool prevents. All considered, the benefits of such new content-aware approach are manifold, and mutual between the fields of biology and engineering (Figure 1.1).

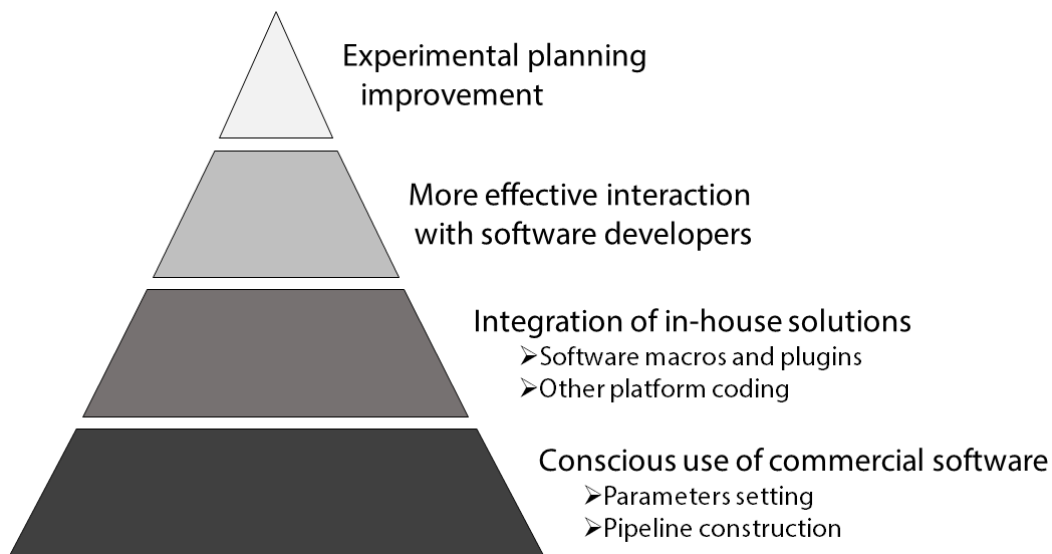


Figure 1.1. Pyramid of the benefits from a content-aware approach. First of all, by a content-aware approach we make a more conscious use of commercial software, because we know why and how tuning the software parameters, and how to build more effective pipelines. Secondly, we can better evaluate if our (free or commercial) software is too general for the purpose, or if an image processing task should be more effectively carried out with a different method. In these cases, we can intervene by developing our own, more specific and effective method, both as a solution to be integrated with the commercial software, if possible, or as a stand-alone product. Third, having knowledge of both the biomedical problem and the technical instruments available for its solution, we can more effectively interact with software developers. For example, when we know what to do but not how to do it, and the problem requires high-level computing skills, we can more proficiently communicate our needs to the programmer, and collaborate to implement the more effective solution. Finally, and most importantly, the content-aware approach helps optimizing the planning of those experiments that involve imaging, because knowing all the steps from sample collection to image acquisition and analysis, we can improve each step, aware of the entire process.

The aim of this Thesis is then to demonstrate the effectiveness of a content-aware approach to automated quantitative imaging, by its application to different studies of biomedical character, to desirably motivate researchers to invest in interdisciplinarity.

Collecting all what has been done in these three years in a single coherent work was not easy. First, because the reported studies differ from each other in terms of research aims, employed biomedical technologies, and therefore applied image processing techniques. Secondly, because this diversity brings the necessity for a broad biological and methodological background, that need to be recalled at least in its basic part for the comprehension of the motivations that has driven our

analyses. The first Chapters therefore serve the theoretical introduction of two main topics that will recur throughout the work, namely preclinical models (Chapter 2) and imaging modalities (Chapter 3). Then, the activities that have characterized this PhD are presented in chronological order by dedicated Chapters. Since my learning and experiencing in image processing have always progressed parallelly, such order follows the increasing complexity of the methodological solutions I could provide to the studies, which then often recalls methods and approaches presented in previous Chapters. For this same reason, the next two Chapters present two image analysis methods we developed out of the main goals of presented studies, from which however they arise, namely the Density Distribution Map (DDM) method (Chapter 4) and the co-Density Distribution Map (cDDM) method (Chapter 5). Right after, Chapter 6 presents a study for the phenomization of cell response to stress by confocal fluorescent imaging, while Chapter 7 presents a morphometric analysis of distal bone microarchitecture from micro-Computed Tomography (μ CT) scans, for which a new dedicated method for trabecular analysis has been developed. Chapter 8 presents the two main activities carried out during my PhD research period abroad, respectively involving the characterization of new 3-D organotypic stem cell spheroids by optical imaging, and the investigation of tooth innervation architecture in different *in vitro* and *in vivo* models, by Differential Interference Contrast (DIC) microscopy and confocal fluorescence microscopy, respectively. The only common thread from Chapters 4 to 8 is then the application of the content-aware approach to problems of preclinical health science. Therefore, besides discussing the specific research, each of these Chapters includes: 1) an overview of the theoretical background necessary to understand the reasons of the analysis, if not discussed in previous Chapters, and 2) a discussion over the specific content-aware advantages to the study. The more general advantages will be recalled in the concluding Chapter 9, helping the shaping of take-home messages and hints for future works.

Besides the present introductory Chapter, the Thesis content is organised as follows (also described by the flowchart in Figure 1.2):

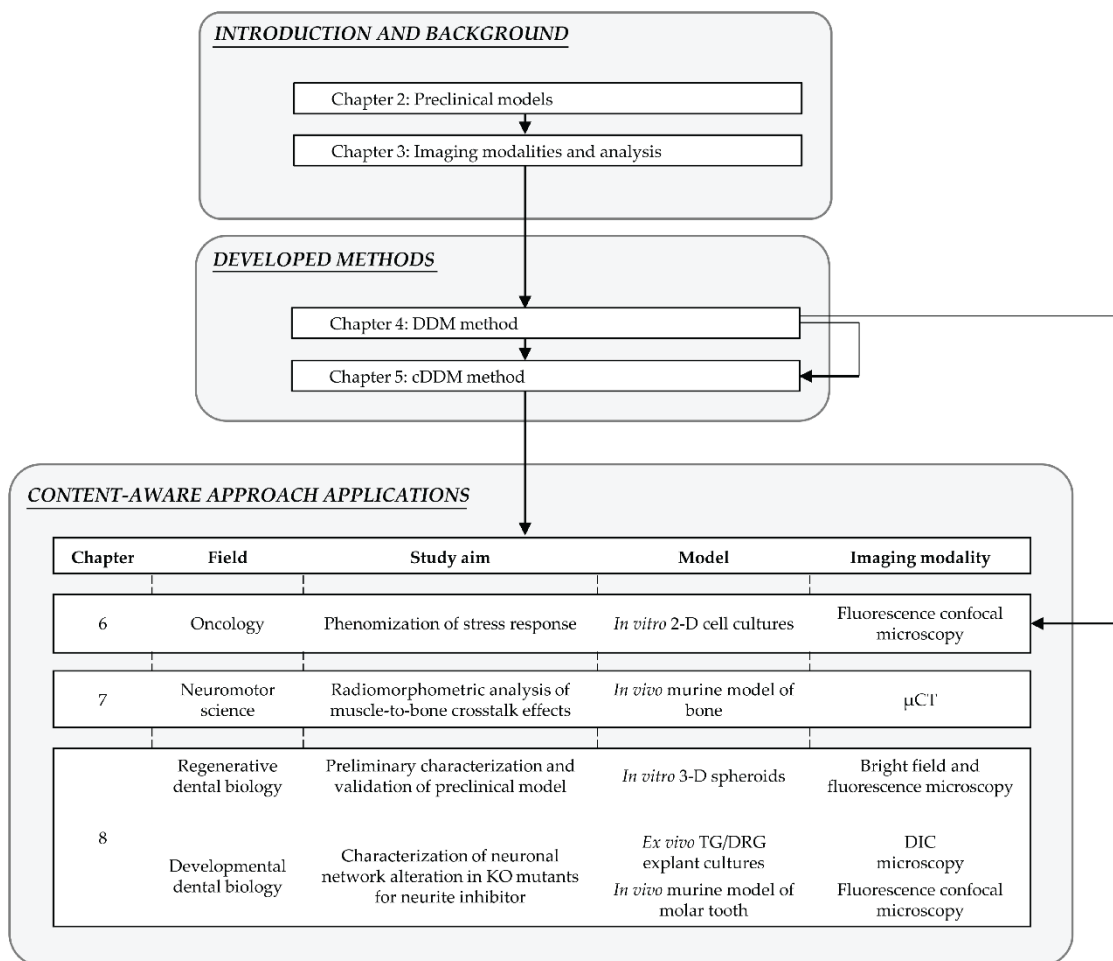


Figure 1.2. Thesis content flowchart. The Thesis is divided into three Chapter blocks. The *Introduction and background* block introduces the basic topics of preclinical models and imaging modalities, also discussing the principles of image formations useful for the successive Chapters comprehension. The *Developed methods* block discusses the two innovative methods for automated image analysis that have been developed during this PhD. The *Content-aware approach applications* block addresses the content-aware image analysis performed in different collaboration studies, applying both state-of-art and self-developed methods (also from the previous block) for image analysis.

- Chapter 2 offers an overview of the most used models in biomedical research, that are *in vitro* two-dimensional (2-D) and three-dimensional (3-D), *in vivo* and *ex vivo* models, focusing on the specific models applied in the studies of this Thesis
- Chapter 3 describes the imaging modalities employed in the PhD activities, discussing instruments design and functioning, respective principles of image

formation and related image artifacts and issues relevant for the analysis performed in the subsequent Chapters

- Chapter 4 presents the Density Distribution Map (DDM) method for the analysis of spatial distribution of signals in 2-D images, conceived as resolution- and instrumentation-independent, for any-level laboratory equipment. Besides discussing the method principles and properties and demonstrating its effectiveness, the Chapter survey the principle of image local analysis, segmentation and thresholding, that constitute the theoretical background for methods comprehension. After exemplifying the benefit of the DDM method to different cases of spatial distribution investigation, my content-aware contribution to the method is provided, together with its possible future developments
- Chapter 5 presents the co-Density Distribution Map (cDDM) method for the analysis of spatial *co*-distribution of signals *pairs* in 2-D images, and for the quantification of their colocalization. The method extends the previous Chapter 4's methodology, appending to the theoretical background the concepts of image arithmetic and morphology, and an outline of most used coefficients for colocalization quantification. Again, the method principle, effectiveness and applicability are presented, followed by a scrutiny of the benefit of a content-aware approach to its conceiving and development, together with the methods future perspectives
- Chapter 6 discusses the results obtained for a project study on the phenomization of tumour cells response to extrinsic stress at the subcellular level. The study aimed at mapping the subcellular distributions of signalling molecules in confocal fluorescent micrographs, in order to obtain insights on their functioning and interactions after cellular stressing. Specifically, beside describing the development and application of image analysis methods for the characterization of RNA:DNA hybrids molecules, the Chapter also surveys the project's molecular results that have been compared to the image analysis results we obtained. My content-aware contribution to the project and its future perspective conclude the Chapter

- Chapter 7 presents an investigation of the radiomorphometric properties of metaphyseal bone in response to bone morphogen administration. The analysis was part of a study aimed at elucidating the role of the sclerostin protein in the muscle-to-bone crosstalk in an *in vivo* murine model. Together with the relevant molecular and image processing results, the Chapter presents the Gabor-based Trabecular Map (TbM) method, that we developed for the classification of bone metaphyseal trabeculae after texture analysis. My content-aware contribution to the project and its future perspective conclude the Chapter
- Chapter 8 presents two studies from the dental biology field. The first study concerned the characterization of a novel 3-D spheroid model of Dental Pulp Stem Cells (DPSCs), performed through Bright Field imaging at the morphological level and by metabolic and viability assays. The second study involved the characterization of the neuronal network morphology of two related models, that are an *in vivo* murine molar and *ex vivo* Trigeminal Ganglia (TG) and Dorsal Root Ganglia (DRG) explants, cultured *in vitro*. The study was aimed at gaining insights on the role of the neurite inhibitor protein Nogo-A during tooth development. After presenting methods and results for the performed assays and image analyses, my content-aware contribution to the project and its future perspective conclude the Chapter
- Chapter 9 provides concluding remarks and hints for future works.

Research presented in this Thesis have been carried out within the:

- Computer Vision Group (CVG), Dept. of Computer Science and Engineering (DISI) and Advanced Research Center on Electronic System (ARCES), University of Bologna, Italy.
Head: Prof. Alessandro Bevilacqua and in collaboration with the following institutions:
- Drug Discovery and Radiobiology Unit, IRCCS Istituto Romagnolo per lo Studio dei Tumori (IRST) "Dino Amadori", Meldola, Italy.
Head: Dr. Anna Tesei

- Department of Biomedical, Metabolic and Neural Sciences, Section of Human Morphology, University of Modena and Reggio Emilia, Modena, Italy.
Chair: Prof. Carla Palumbo
- Regenerative Therapies in Oncology, IRCCS Istituto Ortopedico Rizzoli, Bologna, Italy.
Head: Dr. Enrico Lucarelli
- Iret Foundation, Ozzano dell'Emilia, Bologna, Italy.
Founder and Scientific Director: Prof. Laura Calzà
- Orofacial Development and Regeneration Unit, Centre of Dental Medicine, Institute of Oral Biology, University of Zürich, Switzerland.
Head: Prof. Thimios A. Mitsiadis.

Chapter 2

Biomedical models

Studying human health involves two general experimental approaches: examining human or primate cells, tissues, and organs that constitute relatively direct models of human disease, and using a variety of non-human biomedical models that offer special features and advantages that can be translated on the human model by virtue of their degree of homology [1]. In simpler terms, a biomedical model is a surrogate for a human biologic system that can be used to understand normal and abnormal function, from gene to phenotype, and to provide a basis for preventive or therapeutic intervention in human diseases. The use of biomedical models is enabled by the biochemical and genetic unity of life and the principles and mechanisms of evolution, all of which provide an irrefutable rationale for wide-ranging comparative studies to understand the human condition. In accordance, as a result of evolution from a common origin, organisms share many genetic sequences and common functions, consistently with the time of their phylogenetic divergence. In general, species that have diverged most recently have the closest resemblances in DNA, RNA and proteins sequences and functions. So, dependently on the phenomenon under investigation, more or less phylogenetically distant organisms can be used to model human processes [1,2].

The choice of the model is intuitively critical to the representation accuracy of the desired biological phenomenon, and consequently to its descriptive and predictive capability. It is usually a trade-off between conceptual advantages and practical limitations, driven by what is generally referred to as *convenience*. At a minimum, a good model must be tractable and offer access to the phenomenon to be investigated; however, many more are the factors that are suggested to be considered, together with the details of any specific case [3]. When properly chosen, a good biomedical model of study is what provides an effective foundation

to support basic science research that has strong potential for translation into human medicine. Numerous *in vivo*, *ex vivo*, *in vitro* and *in silico* models have been developed in the last two centuries to infer conclusions about how a molecule, cell, organ, and/or organism works, and how all this can be altered by pathological conditions or treatments.

In vivo models, whether animal or human, provide direct analysis of living organism responses to stimuli. Similarly, *ex vivo* models allow the investigation of living cells and tissues, but after their explant from the animal and transfer to an external stable environment, with minimal alteration of natural conditions. Logically, it is relatively straightforward to translate results obtained from *in vivo* and *ex vivo* models into humans. However, these models' complexity, high cost of maintenance and related ethical concerns strongly hamper their application in routine research, where is rather encouraged their reduction and replacement [4]. The development of *in vitro* techniques was a response to such drawbacks, but also to the necessity for a more stringent control on experimental conditions. *In vitro* models consist of microorganisms, isolated cells, biological molecules, cell culture systems, tissue slice preparations, or isolated organs, grown in optimum conditions outside their normal biological context. So, while biological events are investigated in their wholeness in the *in vivo* system, *in vitro* models allow for phenomena dissection and examination of the cellular structures involved. Finally, in more recent *in silico* models pharmacological or physiological processes are mathematically modelled combining the advantages of both *in vivo* and *in vitro* experimentation, without subjecting itself to the ethical considerations and lack of control associated with *in vivo* experiments. A main advantage of *in silico* models is that they can be used as a first in virtue screening tool to predict the effect of a drug or stimulus on cells and tissues. If on one side this enormously helps the experimental planning of preclinical and clinical trials, on the other side *in silico* results remain theoretical until validation by *in vivo* studies [5, 6].

This Chapter surveys the main characteristics of 2-D *in vitro* models (Section 2.1), 3-D *in vitro* models (Section 2.2), and animal models (Section 2.3) applied in biomedical research, discussing their applicability in terms of strengths and weaknesses, before providing some concluding remarks (Section 2.4). Throughout

the Chapter, we will outline the biomedical models applied in the studies presented in this Thesis. These are:

- *In vitro* two-dimensional (2-D) cell cultures of different tumour cell lines, applied in the PHENOMICS Project (Chapter 6)
- *In vitro* three-dimensional (3-D) spheroids of human dental pulp stem cells (hDPSCs), characterized at the University of Zürich (UZH, Chapter 8)
- *In vivo* mice tibial bone, involved for the investigation of the effect of muscle sclerostin on bone morphometry in collaboration with the University of Modena and Reggio Emilia (Chapter 7)
- *In vivo* mice molars, involved also for the investigation of Nogo-A contribution in tooth innovation at the University of Zürich (Chapter 8)
- *Ex-vivo* mice trigeminal (TG) dorsal root ganglia (DRG) *in vitro* cultures, applied for the investigation of Nogo-A contribution in tooth innovation at the University of Zürich (UZH, Chapter 8).

2.1 *In vitro* 2-D models

2.1.1 2-D cell cultures

In vitro 2-D models are all those cellular models characterized by a monolayer growing adherent to a surface. The surface is usually the inert plastic or glass surface of a Petri dish, but cells can be grown on transwell or other materials as well. In most *in vitro* cultures, cells are not directly exposed to air, but covered by culture medium, that provides nutrients and mediates catabolites elimination. 2-D *in vitro* cultures have relatively basic environmental requirements for optimal grow: controlled temperature, a substrate for cell attachment, and appropriate growth medium and incubator that maintains correct pH and osmolality [7]. In many cases, establishment of appropriate culture condition is sufficient to maintain cells viability and natural behaviour, constituting an easy-to-handle yet effective platform for investigating phenomena at the pure molecular and cellular level [8], and extending to the basic investigation of cell-cell interaction in case of

2-D *in vitro* co-cultures (Figure 2.1) [9]. In their simplicity, 2-D *in vitro* cell culture models make it possible to understand cell biology, tissue morphology, mechanisms of diseases, drug action and protein production, besides providing the setting for the development of tissue engineering solutions [10].

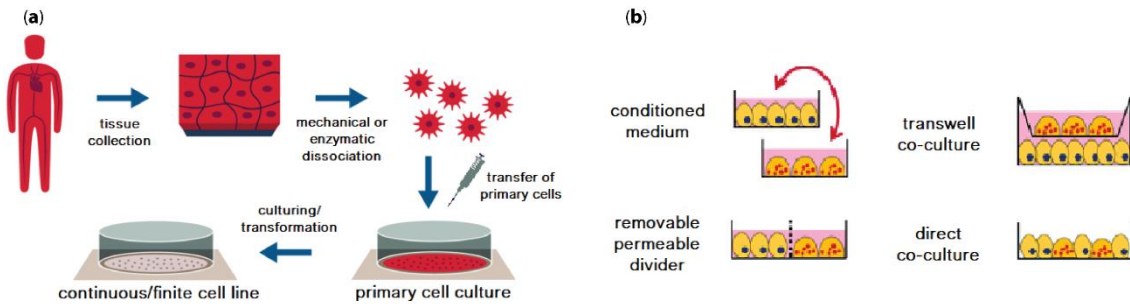


Figure 2.1. 2-D *in vitro* cell models. In 2-D models, cells grow adherent to a flat surface while submerged by culture medium or in suspension. 2-D *in vitro* models can be generally divided in mono- (a) and co-cultures (b). (a) Monocultures (*i.e.*, one cell type) include primary cell cultures, with short lifespan but high resemblance to the original tissue, and cell lines, with longer lifespan and stability. Human/animal tissues are collected and disaggregated by mechanical, chemical, or enzymatic methods to yield viable cells, to be cultures with tailored media. Primary cultures are sub-cultured as secondary before confluence. Secondary cultures may be immortalized (*continuous cell lines*) by spontaneous (*e.g.*, cancer cell lines) or induced (*e.g.*, chemicals, viruses). Non-transformed cells can be passaged for a limited number of population doublings (*finite cell lines*). (b) Co-cultures (*i.e.*, more than one cell type) can be divided in indirect co-cultures (*i.e.*, monocultures are conditioned by another cell culture medium), transwell and membrane cultures (allow cell-cell communication but not interaction), and direct co-cultures (allow cell-to-cell interactions). Image adapted from [11] and [12] under the CC-BY Creative Commons Attribution 4.0 International licence.

The first 2-D *in vitro* cell culture was carried out by Harrison in 1907, during research into the origin of nerve fibres [13]. Since then, the method has been improved and integrated with new technologies, making 2-D *in vitro* cultures an important and necessary process in drug discovery and cancer research, as well as stem cell study. Nowadays, experiments can be conducted using primary cells isolated directly from the donors' material or using established cultures deposited in cell banks [14]. In primary cultures, the cells are directly isolated from living organisms or patients, and thus usually contain populations of different cell types present in the source tissue. Primary culture cells are quite significant in terms of being the closest forms of the state of the cells that they represent in normal tissues. Therefore, their most significant use is in cancer and disease research, where

functional experiments are performed after tissue biopsy to gain insights about the nature and physiology of collected cells. However, because of their limited life span, these cells need to be reproduced with serial passages, that postpone - but ultimately not prevent – primary cell senescence. Furthermore, when the cells are taken out of the living tissue and transferred into the culture environment, this inevitably leads to a certain amount cellular stress, and loss of characteristics and morphologies in most cases [15]. On the contrary, established cell lines from primary human or animal cells can be propagated repeatedly outside their natural environment, thus providing an indefinite source of biological material for experimental purposes, besides enabling more prolonged investigation than primary cultures. Under the right conditions and with appropriate controls, authenticated cell lines retain most of the genetic properties of the tissue of origin. Accordingly, established cell lines are widely applied to cancer studies, where stabilized and immortalized tumour cell lines are routinely used to unravel new feature of cancer disease and to test the efficacy of anticancer drugs [16].

In this PhD's activities, we used 2-D *in vitro* culture models of both primary cells and established cell lines. Primary (patient-derived) 2-D cell cultures of hDPSCs were used to create 3-D spheroids, to be cultured *in vitro* and characterized in terms of stemness, morphology and viability, as to start the evaluation of their reliability as preclinical models [17]. DPSCs characteristics are discussed in Chapter 8, where the spheroid characterization study is presented. Instead, several cell line cultures were used in the PHENOMICS Project, to model RNA:DNA hybrids subcellular re-distribution after cell irradiations or oxidative stress (Chapter 6) [18, 19]. In particular, we focused on three established tumour cell lines, bearing (A549) or not (H1299, HeLa) a functional isoform of the oncosuppressor p53, to investigate its relation to RNA:DNA hybrids response. As a further control, two cell lines have been genetically engineered to repress (A549/shp53) or ectopically express (H1299 p53+) the p53 protein. The main characteristics of the employed cell lines are presented as follows.

A549

A549 is a continuous human lung adenocarcinoma cell line initiated in 1972 by D. J. Giard through explant culture of lung carcinomatous tissue from a 58-year-

old Caucasian male and isolation of alveolar basal epithelial cells [20]. These cells are squamous in nature and are responsible for the diffusion of substances such as water and electrolytes across the alveoli of lungs. This cell line is categorized as a non-small-cell lung carcinoma (NSCLC), which tends to be less aggressive and spread less quickly than small cell lung carcinoma (SCLC) but proves to be more common, accounting for 85-88% of all cases of lung cancer [21]. The A549 cell line is widely used as a model of lung adenocarcinoma, as well as an *in vitro* model for type II pulmonary epithelial cells. The A549 cell line is hypotriploid with a modal chromosome number of 66, which occurs in 24% of cells. Modal numbers of 64 and 67 is relatively common with higher ploidies occurring at an infrequent rate (0.4%). The cells are able to synthesize lecithin and contain a high percentage of unsaturated fatty acids, which are utilized by the cytidine-diphosphocholine pathway and important for the maintenance of membrane phospholipids in cells. A549 cells are positive for keratin by immunoperoxidase staining [22]. The cells can be grown *in vitro*, in suspension or adherently as a monolayer on plastic surface with a doubling time of 24-40 h, and serve as suitable transfection hosts. A549 adenocarcinoma cells are grown in Dulbecco's Modified Eagle Medium (DMEM) modified with 10% FBS, pH 7.0 to 7.6, at 37°C and 5% CO₂ air atmosphere. A549 cells can be cryopreserved in complete growth medium supplemented with 5% dimethyl sulfoxide (DMSO) and stored in liquid nitrogen vapor phase. Their biosafety level is 1 and therefore pose a minimal potential threat to laboratory workers and the environment [20, 23, 24].

H1299

H1299, also known as NCI-H1299 or CRL-5803 [25], is a human non-small cell lung carcinoma cell line derived from the lymph node metastatic site isolated from the lung of a 43-year-old Caucasian male patient with carcinoma. This immortalized epithelial-like cell line was deposited by A. F. Gazdar, H. K. Oie and J. D. Minna, and can be used in cancer and immuno-oncology research [25, 26]. These cells have a homozygous partial deletion of the TP53 gene and as a result, do not express the tumour suppressor p53 protein which in part accounts for their proliferative propensity [27]. These cells have also been reported to secrete the peptide hormone neuromedin B, but not gastrin releasing peptide [28]. H1299 cells

can be grown *in vitro* in suspension or adherently as a monolayer on plastic surface with a doubling time of 20-25 h [29], and serve as suitable transfection hosts. H1299 cells are grown in RPMI 1640 medium supplemented with 10% FBS and glutamine 2 Mm, pH 7.0 to 7.6, at 37°C and 5% CO₂ air atmosphere. H1299 cells can be cryopreserved in complete growth medium supplemented with 5% DMSO and stored in liquid nitrogen vapor phase. Their biosafety level is 1 and therefore pose a minimal potential threat to laboratory workers and the environment [25].

HeLa

HeLa is a continuous human cervix epithelioid adenocarcinoma cell line initiated in 1951 by G. O. Gey through explant culture of cervical cancer cells taken from the patient Henrietta Lacks, a 31-year-old African-American woman after which the cell line has been named [30]. HeLa is the oldest and one of the most commonly used human cell line. The cells are characterized to contain human papillomavirus 18 (HPV-18)—one of the two HPV types responsible for most HPV-caused cancers. The virus cancer-causing ability is linked to two proteins it produces, HPV E6 and HPV E7, that can target and destroy two major human proteins that protect against cancer, p53 and retinoblastoma (Rb) respectively. As p53 and Rb are crucially involved in cell division regulation, their inactivation by HPV proteins lead to the almost indefinite division of HeLa cells. Since their creation, HeLa cells have continually been used for research into cancer, AIDS, the effects of radiation and toxic substances, gene mapping, and countless other scientific pursuits [31]. HeLa cells are rapidly dividing cancer cells, and the number of chromosomes varied during cancer formation and cell culture. The current estimate is a hypertriploid chromosome number (3n+), which means 76 to 80 total chromosomes (rather than the normal diploid number of 46) with 22–25 clonally abnormal chromosomes, known as "HeLa signature chromosomes" [32]. HeLa cells can be grown *in vitro* in suspension or adherently as a monolayer on plastic surface with a doubling time of about 15-30 h, depending on the culture medium and the growth mode [33-35]. HeLa can also serve as suitable transfection hosts. HeLa cells are grown in Eagle's Minimum Essential Medium (EMEM) supplemented with 10% FBS, pH 7.0 to 7.6, at 37°C and 5% CO₂ air atmosphere. HeLa cells can be cryopreserved in complete growth medium supplemented with

5% DMSO and stored in liquid nitrogen vapor phase. Because HeLa cells contain HPV integrated in the genome, HeLa biosafety level is 2, and is therefore highly recommend wearing appropriate personal protective equipment when handling these cells [25].

2.1.2 *In vitro* 2-D model limitations

Cell monolayer cultures are commonly used by researchers for large-scale drug testing, as they are easy to handle and cost effective [36]. Unfortunately, adherent cultures fail to address various physiological conditions and the complex interactions among different cell types of tissues and organs. First, after isolation from the tissue and transfer to the 2-D conditions, the morphology of the cells is altered. This inevitably leads to the loss of diverse phenotypes [37, 38] and alteration of cell internal organization, function [8, 39, 40] and response to various phenomena [41, 42]. As a result, 2-D cultured cells do not mimic cellular organization and tumour proliferation kinetics observed in the natural 3-D structures of tissues or tumours [43]. Moreover, 2-D *in vitro* models lack the ability to correctly mimic stromal heterogeneity and extra cellular matrix (ECM) composition of original tissues and tumour. Cell-cell and cell-extracellular environment interactions are not represented as they would be in the original tissue, therefore altering cell differentiation, proliferation, vitality, expression and splicing of genes, proteins synthesis, responsiveness to stimuli, drug metabolism and other cellular functions that depends on cellular interactions [43–47]. Furthermore, while cells in the monolayer have unlimited access to the ingredients of the medium, such as oxygen, nutrients, metabolites and signal molecules, the architecture of 3-D *in vivo* tissues creates a barrier to the free circulation of these molecules, leading to the establishment of biochemical centripetal gradients in tissues and tumour non-vascularized microregions. Therefore, 2-D models also fail in recapitulating the biochemical gradients that characterize physiological tissues, and especially tumour masses [48].

Because of their multifaceted inability to accurately model *in vivo* conditions, 2-D *in vitro* cultures have been addressed as a major cause of trial drops in the clinical phase, where the mechanisms of action of new compounds results not

adequately predicted, drug doses are often ineffective when scaled to patients, and diffusion kinetics found in *in vitro* and *in vivo* experiments varies dramatically. [36, 49, 50]. Owing to the many disadvantages of 2-D systems, 3-D culture systems have arisen as alternative models, capable to better mimic natural tissues complexity.

2.2 *In vitro* 3-D models

A 3-D cell culture is an artificially created environment in which cells are permitted to grow or interact with their surroundings in all three dimensions, imitating the architecture of the parental tissue more accurately than is possible in 2-D models. Accordingly, 3-D cultured cells have been shown to grow more similarly to *in vivo* ones, in terms of cellular morphology and heterogeneity [8], gene expression [51], signalling and metabolism [52, 53] and differentiation [54]. Moreover, 3-D culturing enables realistic cell-cell and cell-environment interactions [55], therefore improving the physiological responsiveness of cells [56]. Finally, their amenability to high-throughput analysis makes 3-D cell cultures the most used *in vitro* biomedical model in preclinical investigation [57].

The idea of 3-D cell/tissue culture was conceived in 1912 by A. Carrel and his pioneering explant and *in vitro* maintenance of a chick embryo cells [58]. J. A. Leighton further developed the system proposed by Carrel, by culturing the tissues on a substrate sponge matrix [59]. Other approaches were gradually developed involving cell embedding in collagenous gels and culturing on mesh supports [60, 61]. Today, many methods, technologies and materials are available for *in vitro* cell culturing in three dimensions. Progress in 3-D cell culture technology created the possibility of tissue engineering development and enhanced progress in the regenerative medicine [62].

3-D models can be divided between scaffold-based, scaffold-free and hybrid models. (Figure 2.2).

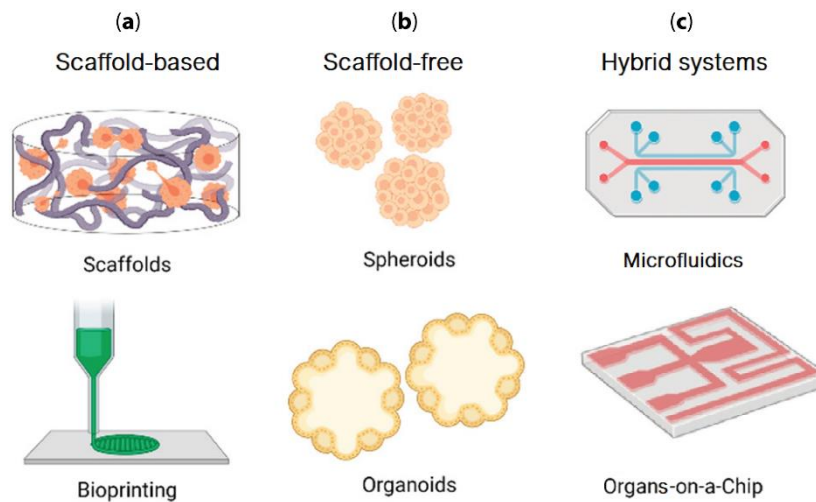


Figure 2.2. Scheme of diverse 3-D cell culture strategies. In 3-D cell culture, cells self-assemble or grow in structures that resemble the extracellular matrix. The 3-D cell culture can be divided into three groups: scaffold-based (a), scaffold-free (b), and hybrids models (c). (a) Scaffold-based systems use structures that mimic the extracellular matrix. 3-D printing techniques can be used to create scaffold with precise morphology, even directly encapsulating the cells (*bioprinting*). (b) In scaffold-free systems, cells aggregate as occurs in natural processes of organogenesis, without the physical support of a scaffold. (c) Hybrids systems use a matrix or a scaffold to support scaffold-free systems. Image adapted from [63] and from [64] under the CC-BY Creative Commons Attribution 4.0 International licence.

In scaffold-based cultures, a physical scaffold is provided to mechanically support the cells while mimicking their ECM composition, to simulate their native microenvironment. Several biomaterials and methods can be used to generate structures that support cell growth and provide physical and biochemical stimuli for optimal cell organization and differentiation. They can be adapted to the mechanical and physical characteristics required to study tissue physiology and pathophysiology [63]. The scaffold nature ranges from simple concentrated medium or gel-like substances to solid and often porous structures that mimic the inorganic microenvironment peculiar to the used cells. 3-D matrices of polymers such as collagen, alginate, Matrigel™ and polyesters are used as a base for growing multiple layers of cells over long periods, allowing for their differentiation [57]. The 3-D bioprinting technology is one of most intriguing innovation concerning scaffold-based models [57]. While at the beginning the technology was only serving the creation of inorganic 3-D scaffolds for biological materials, it is now already employed to simultaneously print living cells layer-by-layer into special

3-D scaffolds [65-67]. Scaffold-based 3-D models have been used to study intercellular interactions, cellular migration and invasion, and tumour cell biology. Although these systems are advantageous in maintaining the 3-D architecture of a tissue, they are not able to mimic the conditions of the mass transport gradient of a tumour environment [68]. Moreover, the non-toxic constituents of the scaffold can have sometimes an effect on cell growth [69-71], including the limiting of cells movement and interaction. This does not happen in scaffold-free models, where cells are cultured in suspension or on non-adherent plates and left free to aggregate (more or less) spontaneously. The most important scaffold-free *in vitro* 3-D models includes spheroids and organoids. 3-D multicellular spheroids are self-assembled, sphere-shaped 3-D cell aggregates which produce their own ECM. When incorporating more than one cell type and acquiring tissue-like organization and functioning, these spherical aggregated take the name of organoids. An organoid is a miniaturized and simplified 3-D version of an organ produced *in vitro* that shows realistic micro-anatomy, such that it can be used to study aspects of that organ in the tissue culture dish. They are derived from one or a few cells from a tissue, embryonic stem cells or induced pluripotent stem cells, which can self-organize in 3-D culture, owing to their self-renewal and differentiation capacities. With respect to “simple” 3-D co-cultures, the processes that form these tissues *in vitro* are thought to better resemble the natural development and tissue maintenance [72, 73]. Accordingly, organoid technology applies in multiple infectious diseases, monogenic hereditary diseases, and personal and regenerative medicine [63].

A third new type of 3-D models can be considered as a hybrid and advanced version of the previous ones (Figure 2.3). These hybrid systems include scaffold-based characteristics like synthetic matrix and external physical supports, that are used to define a culturing environment for scaffold-free models. A clear example of these models is the Organ-On-a-Chip (OOC) system, that integrates bioengineering and microfluidics to better mimic the *in vivo* microenvironment [63]. In OOC systems, also known as Lab-On-Chips, cells are seeded and perfused in a chip-like array to model the minimal functional units of an organ or a tissue. By specifically designing the chip topology to reproduce an *in vivo* situation, OOCs can model miniaturized organs, recapitulating the multicellular architectures,

tissue-tissue interfaces, physicochemical microenvironments and vascular perfusion of the body, and producing such levels of tissue and organ functionality as it is not possible with conventional 2-D or 3-D culture systems [74].

In this PhD's activities, we modelled *in vitro* the 3-D growth of human dental pulp stem cells by spheroids derived from primary cultures [17]. hDPSCs are staminal cells, whose proliferation, differentiation and functioning are importantly affected and directed by their microenvironment. With respect to traditional 2-D cultures, 3-D multicellular spheroids have been demonstrated to more accurately model the mesenchymal stem cells (MSCs) cellular microenvironment, and to consequently better preserve stemness through culture [75-76]. Therefore, hDPSCs culturing in 3-D, rather than in 2-D, is expected to strongly influence their stemness, morphology and viability, that we characterised and compared to monolayer culture in the study presented in Chapter 8. The main features of 3-D multicellular spheroids are presented in the next Subsect. 2.2.1.

2.2.1 Spheroids

3-D multicellular spheroids are self-assembled, sphere-shaped 3-D cell aggregates which produce their own ECM. In their simplicity, spheroids recapitulate the complex *in vivo* multicellular architecture, the barriers to mass transport, the proliferative heterogeneity of cells found *in vivo*, and the ECM deposition. Accordingly, in 3-D tumour spheroids it is possible to replicate the conditions of hypoxia, necrosis, angiogenesis, invasion, metastasis, cell adhesion and tumour-immune cell interactions [57]. Spheroids have therefore become an election model for better prediction of drug effects and delivery, and the most used 3-D *in vitro* culture for modelling tumours, especially in their initial non-vascularized phase [77-78].

The first cell aggregation studies date back to 1944, when J. Holtfreter described a method for the production of stable and spherical aggregates of amphibian embryonic cells [79]. Then, in 1970 R. Sutherland applied the methodology developed by Moscona [80] and Holtfreter to form the first tumour spheroids by rotating the cells in spinner flasks and used them as a model system for radiobiological studies [81]. Initially, spheroid cultures were mainly applied in

experimental radiotherapy and chemotherapy settings; it was only in the 2010s, that advanced 3-D spheroid models received greater interest in the research field as high-throughput manipulation and analysis methods has become available [82]. Spheroids can be conventionally produced starting from different cell types by a variety of methods that share the common feature of promoting cell–cell coupling by resisting cell–surface interactions. Methods for spheroids creation can be broadly divided between scaffold-based and scaffold-free methods (Figure 2.3).

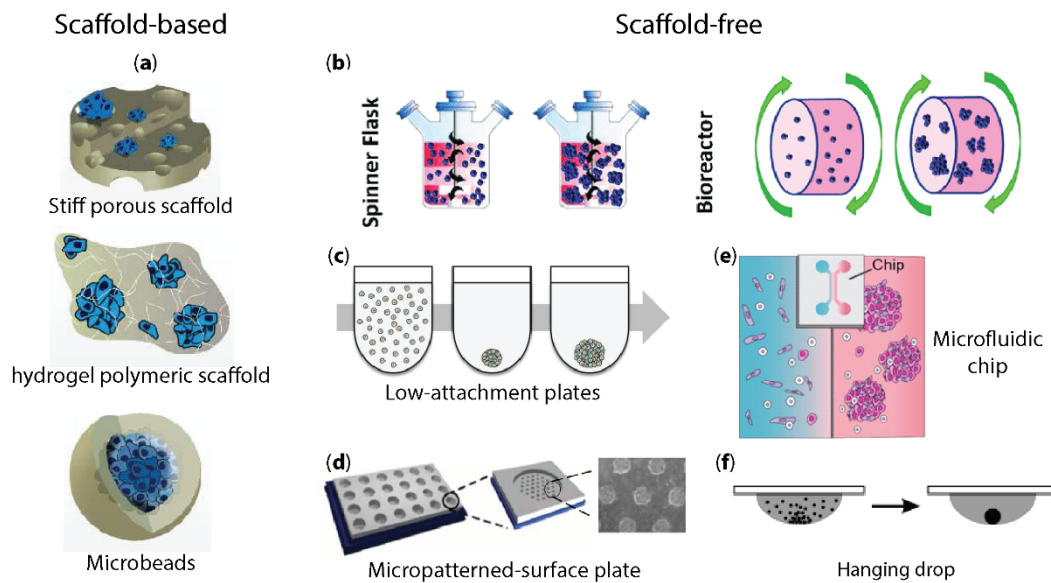


Figure 2.3. Methods for spheroids creation. (a) Scaffold-based methods provide a physical support for cell aggregation, either by solid matrices, hydrogels or microcarrier beads. Among the most used scaffold-free methods for spheroids creation there are: (b) spinning flasks, bioreactors and other rotating culture systems, (c) low and ultra-low attachment plates, (d) culture plates with micropatterned wells, (e) microfluidic culture chips, (f) hanging drop method.

Scaffold-based methods promote cell aggregation into spheres by mean of specifically designed porous solid or semisolid matrices. Alternatively, microcarrier beads can be used as a non-flat surface on which promote cellular aggregation [83]. Scaffold-free methods employ physical or chemical properties to promote cell aggregation in a scaffold-free environment. Among the most employed scaffold-free methods there are low-adherence plates, micropatterned surfaces, rotating culture systems, hanging drop applications and microfluidics chips [83-86] (Figure 2.3). In particular, the hanging drop method has been used to

produce the hDPSCs spheroids whose characterization is presented in Chapter 8. Briefly, in the hanging drop method the cells are seeded into drops of culture medium and left hanging from plate lids [87] or other structures [88]. While drops do not fall thanks to water surface tension, gravity promotes the self-assembly of 3-D spheres at the bottom of the drop. This method has been demonstrated to lead to the production of spheroids with well-controlled size in a rapid manner [57].

Depending also on the method employed for their creation, spheroids size can range from 20 μm to over 1 mm in diameter [68]. As a main feature, spheroids develop centripetal gradients of nutrients, oxygen and wastes based on the diffusion potential of molecules (Figure 2.4).

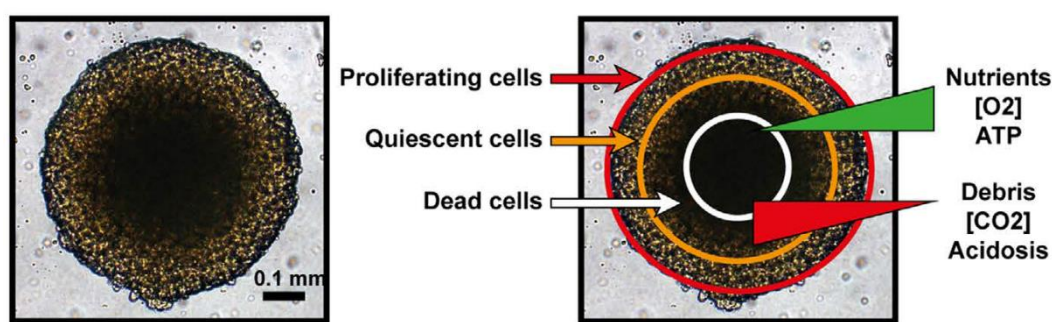


Figure 2.4. Spheroid pathophysiological gradients and viability differentiation. ATP, Adenosine triphosphate. Image reproduced from [89] under the CC-BY Creative Commons Attribution 4.0 International licence.

As a consequence of these gradients, spheroids with a diameter of at least 500 μm [89] have been reported to internally differentiate in three different functional layers: an external proliferating zone, an intermediate quiescent zone, and an inner necrotic core. This layered structure importantly resembles the cellular heterogeneity of solid *in vivo* non-vascularized tumours [90]; however, it may also contribute to reduce the reproducibility of data collected with this model. Indeed, it has been shown that a number of morphological parameters affect the response of large spheroids to treatment, and that spheroids heterogeneous in volume and shape constitute a potentially dangerous source of variability [89]. Therefore, it is of primary importance to standardize spheroids culturing and selection for treatment, also by mean of quantitative imaging, as we have done in this Thesis.

2.2.2 *In vitro* 3-D models limitations

Despite their numerous and undoubtable advantages over monolayer cultures, current 3-D *in vitro* models are not a truly reliable and accurate representation of human physiopathology yet. If on one side this may be ascribed to their simplified biological properties, on the other side technological burdens prevent the full exploitation of their potential.

From a technological point of view, even after decades of research, the lack of standardized culturing, testing and analysis procedures have been more than once reported to negatively affect 3-D models reproducibility [89, 91, 92]. To this respect, the applications of emerging technologies like microfluidics, computational modelling and high-throughput analysis systems can reduce the variability of cultures and, consequently, the consistency and reproducibility of their results. Finally, the integration of cutting-edge technologies for culture imaging can introduce unprecedented advantages in both research and industry settings. Real-time imaging of cultures can provide profiling of drug response directly on target, besides the monitoring of cellular phenotypes within complex samples, with consequent quantification of sample heterogeneity. Finally, live-imaging opens to the investigation of peculiar cell processes, such as cell attachment, migration, vesicle formation, angiogenesis and stem cell differentiation [62]. Clearly, interdisciplinarity is a key player for the functional integration of these technologies, with the potential to provide significative advancement to biomedical research.

2.3 *In vivo* and *ex vivo* models

In vivo and *ex vivo* models are biomedical models that involve direct (*in vivo*) or indirect (*ex vivo*) experimentation in animals or human subjects. Animal models are essential in human studies because, differently from 2-D and 3-D *in vitro* cultures, they provide systemic information regarding the interaction between several organs. Accordingly, animal models represent a unique source of *in vivo* data for various fields of biomedical research. In preclinical trials, animal models are used to assess drug pharmacokinetics, efficiency and safety, representing the

last decisive pre-clinical validation before translation into clinical trials [93]. Animal models are also widely applied to the development of vaccines and antibiotics, and in general to the investigation of all those physiological and pathological phenomena whose complexity cannot be fully captured by *in vitro* models. As complete organisms, animal models are essential for investigating systemic living functions, as immune response and reproduction, and to provide proof-of-principle validation to results obtained by *in vitro* models [94].

With respect to 2-D and 3-D *in vitro* cultures, *in vivo* animal models possess unquestionable biological advantages, first of all the higher level of accuracy in the representation of human physiopathology. However, ethical concerns, high costs and model complexity limit their use in routine biomedical research. An interesting intermediate option is represented by *ex vivo* models, which merge advantages of *in vitro* and *in vivo* models. As the name suggests, *ex vivo* systems involve the explant of tissues or organ parts from an *in vivo* model and their culturing *in vitro*, under controlled and reproducible conditions. Therefore, the convenience of *ex vivo* models lies in the fact that they retain a very high level of resemblance with the original tissue environment, while raising less ethical concerns and being as practical as *in vitro* models, gaining in robustness and compatibility with high-throughput processes [95-97]. Another primary advantage of using *ex vivo* tissues is the ability to perform tests or measurements that would not be possible, or ethical, in living subjects [98]. However, *ex vivo* models have repeatedly reported to suffer from limited viability [99, 100], availability and reproducibility [57].

Through the years, different vertebrate and invertebrate animal models have shown to be suitable for diverse purposes. *C. elegans* is used to study a large variety of biological processes including apoptosis, cell signalling, cell cycle, cell polarity, gene regulation, metabolism, ageing and sex determination [101]. *Drosophila* is an historical model for genetic investigation and engineering [102]. Thanks to its transparency, Zebrafish (*Danio rerio*) is an established model of vertebral development and physiology [103], while rodents and primates are preferred for neurodegenerative diseases modelling and investigation of brain physiology [104]. Finally, genetic manipulation and engineering of small animals can be used to induce gene ectopic expression, deletion and silencing of endogenous genes, and

to produce chimeric and transgenic animals, to increase the model relevance to the topic of study [105, 106]. In the next Subsection, we will survey the general feature of the mouse model, as it is the one applied to the *in vivo* and *ex vivo* studies of this Thesis.

2.3.1 Mouse model

Today, almost 60 million animal subjects are used in biomedical research [107], dominated by mouse and rat models [108]. The house mouse of North America and Europe, *Mus musculus*, is a small mammal belonging to the order Rodentia, whose physiology has been extensively characterized [109]. Reducing reliance on higher-order species, *M. musculus* has become the animal model of choice for biomedical researchers, firstly because of its high similarity to humans in terms of organ shape, structure, and physiology. Further reasons include small size (facilitating housing and maintenance), short reproductive cycle and lifespan, wealth of information regarding mouse anatomy, genetics, biology, and physiology, and the availability of a plethora of methods for their breeding, mutation, genetic manipulation and testing [110]. Mice primary application in biomedical research concerns the investigation of a multitude of human diseases, such as hypertension, diabetes, heart disease, Parkinson's, Alzheimer's and other neurodegenerative diseases, spinal cord injuries (SCIs), muscular dystrophy, cystic fibrosis, AIDS and various cancers. Mice are also used in behavioural, sensory, aging, nutrition, and genetic studies. This list is in no way complete as geneticists, biologists, and other scientists are rapidly finding new research application for the domestic mouse [109].

However, the mouse model does not come without challenges, first of all the high intrinsic variability that characterize all high-order species. To this regard, an important element to consider is the link between the study outcome reproducibility and the animal welfare. Researchers working with animal models have an obligation to safeguard their welfare and minimise the discomfort [111]. While this is largely driven by ethical concerns, this approach has been proved more than once to be also beneficial for the experimental outcome, as it significantly reduces animal stress and ultimately the variability of response to

treatments [112-116]. Speaking of mice, it is therefore of primary importance to provide appropriate resources of food, shelter, and environment enrichment, to optimize and standardize mice handling procedures, and, in general, to continuously weight the effect of animal distress on data reproducibility [116].

In this PhD's activities, both *in vivo* and *ex vivo* mice models were used. In the first year, the PHENOMICS Project used an immunodeficient (athymic) nu/nu CD-1 mice (Crl:NU-Foxn^{1nu}, Charles River Laboratories) for demonstrating the dependence of abscopal effect on the oncosuppressor p53, excluding the sole effect mediation by T cells [18]. This model, on which I have not performed any image analysis, is described elsewhere [117]. In the first year, collaborating with the University of Modena and Reggio Emilia, I investigated the microarchitecture of mouse tibial bone in μ CT scans, and how it is affected by a muscle production of the sclerostin protein [118]. Finally, in the third year, we investigated the role of the Nogo-A protein in tooth innervation using both *in vivo* and *ex vivo* mice models, imaging and analysing the neuronal network of the first mice molars and of *in vitro* cultures of explanted trigeminal and dorsal root ganglia [119]. The main characteristics of the *in vivo* and *ex vivo* mice models investigated by image analysis in this PhD are presented as follows.

***In vivo* mouse model of muscle-to-bone crosstalk**

The morphological effect of the muscle protein sclerostin on adjacent bone microarchitecture was investigated in C57BL/6NCrl mice (Charles Rivers Laboratories). The C57BL/6 inbred strain was developed starting in 1921 by Clarence Little at the Jackson Labs. At that time, a "black subline" (C57BL) and a "brown subline" (C57BR) were established and bred independently. The C57BL subline was further separated into two sublines designated "subline 6" and "subline 10." These sublines would eventually give rise to the C57BL/6 and C57BL/10 inbred stains we know today. Substrains are distinguished by the series of letters following the C57BL/6 designation, identifying the laboratory of origin (*lab codes*).

C57BL/6 Inbred strains are defined as colonies produced by a minimum of 20 generations of brother-sister mating, traceable to a single founding pair. Due to relatively robust breeding performance and confidence in the strain origin, the

C57BL/6 is the most used inbred strain in research. C57BL/6 mouse colonies are genetically identical and exhibit a high degree of uniformity in their inherited characteristics, or phenotypes, which include appearance, behaviour, and response to experimental treatments. In 2002, the mouse genome was firstly sequenced from the C57BL/6 strain (substrain J) [120]. The C57BL/6 strain is a general multipurpose model, applicable to studies of diet-induced obesity, transgenic/knockout model development, safety and efficacy testing and immunology studies. As it shows an increased preference for narcotics and alcohol, the C57BL/6 strain is also very suitable for genetic studies of substance abuse.

***In vivo* molar model of tooth innervation**

The effect of the neurite growth inhibitor protein Nogo-A on the innervation morphology in developing tooth was investigated in the first molar of transgenic C57BL/6 mice, engineered for the homozygous deletion of the exons 2 and 3 of the RTN4 gene, encoding for the Nogo-A protein (Figure 2.5). The procedures for the generation and genotyping of the of knockout (KO) mice are described in [121].

The first molar of C57BL/6 Nogo-A KO mice was extracted at different postnatal (PN) stages (*i.e.*, 4, 7, 9, 20, 25 or 27 days after birth) for the immunostaining and imaging of the developing tooth neuronal network.

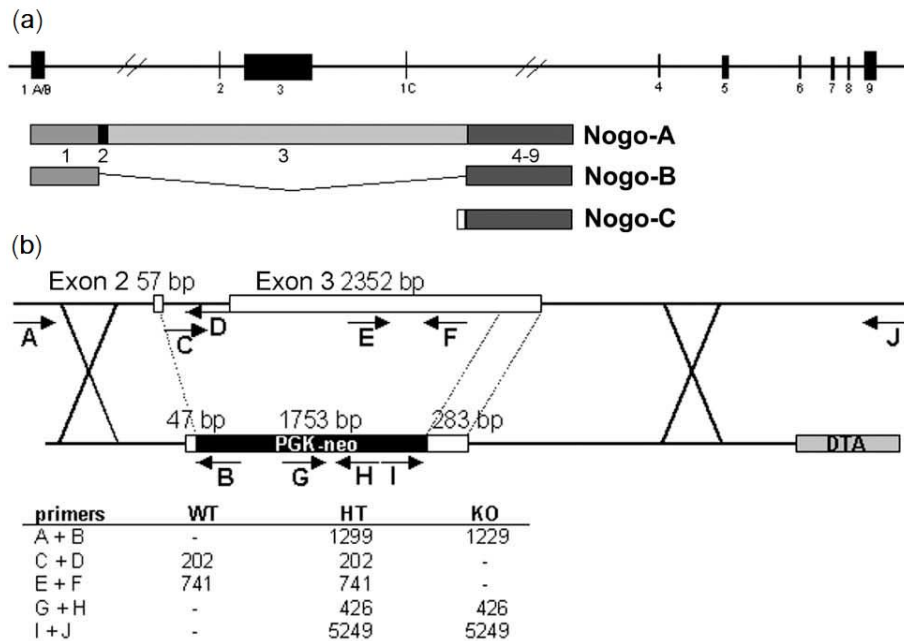


Figure 2.5. Deletion scheme for the RTN4 gene exons 2 and 3, from Simonen et al. [121]. (a) Schematic representation of the RTN4 gene and its major protein products Nogo-A, -B, and -C. (b) Genomic region covering exons 2 and 3 of the RTN4 gene and the Nogo-A knockout (KO) construct. The PCR screening strategies for the transfected embryonic stem cells and for the mice are shown, as well as the expected PCR products from Nogo-A wild-type (WT), heterozygous (HT), and KO mice. Primers A, B, I, and J were used to screen the transfected embryonic stem cells. For genotyping the mice, all five PCR reactions were performed. Figure and caption reproduced from Simonen et al. [121] under the CC-BY Creative Commons Attribution 4.0 International licence.

Ex vivo TG and DRG cultures

The Nogo-A effect on the morphology of developing neuronal network was further investigated in two *ex vivo* mice models, namely *in vitro* cultures of trigeminal ganglia (TG) and dorsal root ganglia (DRG) explanted from C57BL/6 Nogo-A KO mice at the embryonic stage E14 (*i.e.*, 14 day after birth). The C57BL/6 Nogo-A KO strain was generated as before [121]. In these cultures, the ganglia are plated on glass coverslip coated for their attachment, and the neuronal network grows bi-dimensionally, spreading radially from the ganglia. In these cultures, TG and DRG grow comparably in terms of network morphology. While TG network investigation is relevant for understanding Nogo-A effects in the early phases of tooth development, DRG have been here firstly considered for more technical reasons, *i.e.*, setup of culturing and imaging protocols.

2.3.2 *In vivo* models limitations

Animal models limitations can be traced to three main areas of concern, including study design and data analysis, translation of preclinical animal trials to human clinical trials, and ethical concerns [122]. Most of the data coming from trials that use animal models have been criticized for their inconsistency, lack of randomization, blinding, and inadequate or absent use of formal statistical analysis [123]. Data derived from animal models easily suffer of poor reproducibility [124]. If one side this is related to the intrinsic complexity of a living model, on the other side much more can be done to contain the variability introduced by genetic and phenotypic heterogeneity of the selected samples. All these factors inevitably contribute to lower the translatability of results from preclinical animal models to clinics. Nonetheless, preclinical investigation still cannot help from using animal models for testing safety and efficacy of new devices, procedures, and drugs.

In 1959, Russel and Burch introduced the Three R's of animal research: Replacement, Reduction, and Refinement [4]. First, using experimental animals should be avoided when possible; secondly, the number of animals used per experiment should be reduced, and finally, methods to minimize animal suffering should be implemented. These three principles were designed to serve as a foundation for the development of future alternatives to the use of animals in research. It was not until the 1980s, however, that legislative bodies across Europe and the United States began to develop committees and laws to govern the use of animals in research, many of which are largely based upon the three Rs [122]. As the use of animals in research moves forward, it is important to prioritize the commitment to the three R's, to reduce animal suffering to a minimum.

Finally, animal models present practical challenges relatively to their high cost for maintenance, the requirement of dedicated space and specialists to carry out complicated and laborious techniques, and the impossibility to model some specific phenomena, as for example human virus pathophysiology, that is linked to human cell tropism [63].

2.4 Concluding remarks

This Chapter has surveyed the main features of available models for biomedical research, presenting and comparing their strengths and weaknesses, and outlining the specific models applied throughout this Thesis. While no perfect model exists, that can flawlessly apply to any study, it is up to the researchers' responsibility to carefully weigh benefits and drawbacks of each, in the context of the purposes and methods of his own study, in order to make the most of the crucial step of model selection.

Nevertheless, some general considerations can still be drawn. *In vitro* 2-D models are still remarkably present in biomedical and preclinical research, despite the increasing evidence for their limited capability to represent the *in vivo* systems. However, the use of *in vivo* models is limited by ethical, economic, and statistical concerns. The replacement of 2-D cultures with 3-D *in vitro* models, underway now for more than a decade, is returning highly promising results. Cutting-edge technologies and techniques, such as co-culturing, microfluidic devices, high-throughput screening and high-content imaging, are showing their potential to increase 3-D models representativeness and reproducibility, making promises for a substantial reduction and replacement of animal models in biomedical research. In the near future, the challenge will be to integrate 3-D culture systems with advanced informatics and technology tools, to maximize their potential and establish them to the routine biomedical research.

Chapter 3

Imaging modalities and analysis: principles and techniques

Vision is the most advanced of our senses and the human perception relies more on for the investigation of the world that surround us. It is no surprise that, from ancient times, man has devoted resources and energy to the creation of instruments and machines to explore what is beyond his eye, on unreachable macroscopic and microscopic scales. Thanks to its outstanding applicability, the use of imaging technologies in research, and in particular in the biomedical field, has grown steadily over time, boosted by the progressive digitization of equipments. However, unlike humans, who are limited to the visual band of the electromagnetic (EM) spectrum, imaging machines cover almost the entire EM spectrum, ranging from gamma to radio waves, also operating on images generated by sources that humans are not accustomed to associate with images. From nanotechnologies, astronomy, medicine, vision psychology, remote sensing, security screening, to the digital communication technologies, images have helped mankind to see objects in various environments and scales, to sense and communicate distinct spatial or temporal patterns of the physical world, as well as to make optimal decisions and take right actions.

Imaging sciences consist of three distinct as well as interconnected components: image acquisition, image processing, and image interpretation. This Chapter focuses on the first subject, though the three are intimately related and interdependent. If from one side it is relatively straightforward to snap pictures on modern imaging instruments, generating quantitative image data, however, requires thoughtful planning and careful execution at all stages of the experiment. Quantitative imaging involves rigorous specimen preparation, careful selection of

an appropriate instrument for a given application, stringent instrument set up and operation in a way that enables equal and fair assessment of control and experimental conditions. Care must be taken to avoid bias and ensure that the measured differences are statistically meaningful. And though all image processing and analysis steps must be performed consciously, cautiously and with integrity too, image acquisition remain the main stumbling block for a meaningful quantitative imaging analysis, requiring to be planned and performed also in the perspective of the subsequent steps.

This Chapter surveys the main principles and techniques of the imaging modalities applied during this PhD, namely optical microscopy and computed tomography. After introducing digital images (Section 3.1), the basic principles of microscopy are given (Section 3.2), together with a more specific survey of the modalities we encountered, that are Bright Field microscopy (Subsection 3.2.1), differential interference microscopy (Subsection 3.2.2) and fluorescence microscopy (Subsection 3.2.3), the latter focusing on the applied widefield and confocal microscopy modalities. The main artifacts related to these imaging modalities and techniques, namely the vignetting effect and photobleaching, are also discussed (Subsection 3.2.4). Then, the basic principles of computed tomography (CT) are introduced in Section 3.3, with a deepening on the applied micro-CT (μ CT) technique (Subsection 3.3.1) and on the most common image artifacts associated to CT (Subsection 3.3.2). Concluding remarks are provided in Section 3.4, opening a small window on image post-processing and its relationship with image acquisition. The imaging modalities and techniques applied in the studies presented in this Thesis, and outlined throughout the Chapter, are:

- *Bright Field microscopy*, applied to the morphological characterization of human dental pulp stem cells (hDPSCs) spheroids, at the University of Zürich (UZH, Chapter 8)
- *Differential Interference Contrast microscopy*, applied to the investigation of the neuronal network in dorsal root ganglia (DRG) *in vitro* cultures, at the University of Zürich (Chapter 8)
- *Widefield Fluorescence microscopy*, applied to the quantification of hDPSC spheroids viability, at the University of Zürich (UZH, Chapter 8)

- *Confocal Fluorescence microscopy*, applied to the investigation of subcellular molecules distribution in the PHENOMICS Project (Chapter 6) and to the characterization of the neuronal network morphology in developing mice molars, at the University of Zürich (UZH, Chapter 8)
- *Micro Computer Tomography*, applied to the investigation of the effects of muscle sclerostin on bone morphometry, in collaboration with the University of Modena and Reggio Emilia (Chapter 7).

3.1 Digital images

An optical image is a continuous distribution of light intensity across a two-dimensional surface. In other words, an image is a (usually) two-dimensional (2-D) function $f(x, y)$, where x and y are *spatial coordinates*, and the amplitude of f at any pair of coordinates (x, y) represents the *intensity* or *grey level* of the image at that point. When x , y , and f are all finite, discrete quantities, produced by the process of digitalization, we call the image a digital image [125]. A digital image is therefore a grid of discrete elementary units, the *pixels*, each defined by a unique triple of x , y and $f(x, y)$. The range of variation for x and y displacements defines the image width (X) and height (Y) respectively, while the range of variation for the values of f is defined by the response function of the image sensor, and its tonal range. In practice, during image acquisition they are delimited by the image bit-depth (*i.e.*, the number of bits used to discretize the dynamic range of the scene, commonly, 8, 12 or 16). Properly done, image digitization yields a numerical representation of the specimen that is true to the original spatial distribution of light that emanates from the specimen (Figure 3.1 (a)).

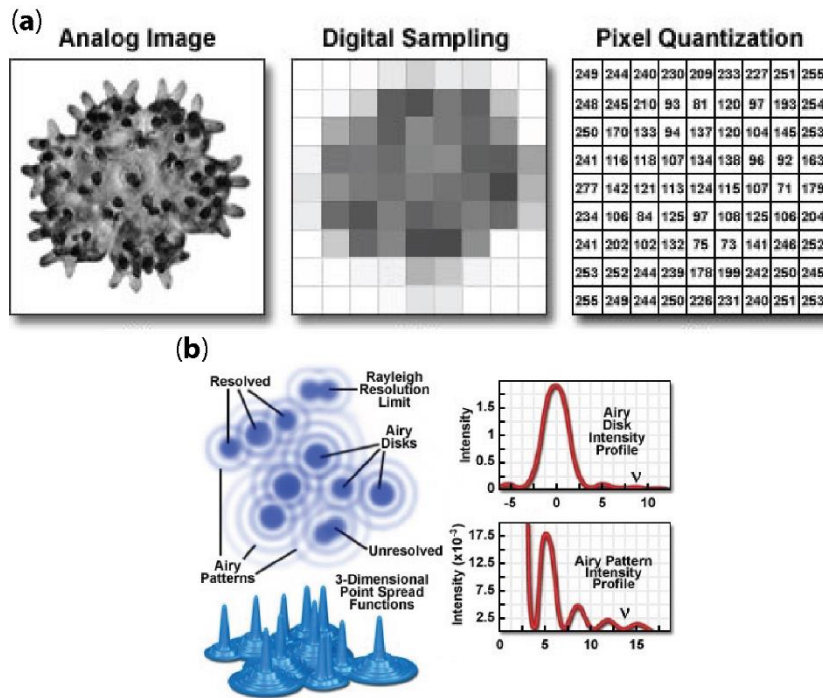


Figure 3.1. Digital images quantization and point spread function. (a) The process of image digitalization consists of sequential *sampling* and *quantization*. The sampling process discretizes the space and measures the intensity at successive locations in the image and forms a 2-D array of small rectangular blocks (*i.e.*, pixels), each containing information about brightness at given location. of intensity information. The quantization process discretize the dynamic range of the scene and each pixel location is assigned a specific quantized brightness value (*i.e.*, *grey level*), ranging from black to white (in case of one colour-channel only). (b) Airy disk and diffraction pattern intensity profile. The point spread function (PSF) describes the response of a focused optical imaging system to a point source or point object. The intensity distribution of the PSF in the focal plane is described by the Airy pattern, whose shape is determined by the cylindrical symmetry of the lenses. Images reproduced from [126].

Image resolution

The resolution of a digital image can be defined in many ways. To the scope of this Thesis, *pixel resolution* refers to the image dimension (*i.e.*, the number of Y pixel rows and X pixel columns [127], while *spatial resolution*, or simply resolution, refers to the pixel density of an image (*i.e.*, the number of pixels necessary to cover a field of view), that in microscopy is commonly expressed as pixel/ μm (or pixel/nm). The spatial resolution is a primary characteristic of every imaging system, as it corresponds to the minimum distance at which two points can be detected as separated at a given focal length, thus indicating the sharpness and the level of

detail of an image. All optical microscopes are limited in the resolution they can achieve by a series of physical factors related to light diffraction and described for a perfect optical system by Abbe's equation [128]:

$$d = \frac{\lambda}{2n \sin\theta} = \frac{\lambda}{2 \text{ NA}} \quad (3.1)$$

where, d is the minimum resolvable distance, λ is the light wavelength, n is the refractive index of the medium and θ is the half angular aperture of the lens, whose \sin is also known as the lens numerical aperture (NA). Because of the light diffraction limit, in optical microscopy the distribution of pixel intensity is described by a *point spread function* (PSF), that in 2-D images appear as a disk with concentric rings of decreasing intensity (*Airy disk*, Figure 3.1 (b)), whose width is determined by Abbe's equation [129]. Actual specimens are not point sources, but can be regarded as a superposition of an infinite number of objects having dimensions below the resolution of the system. Therefore, in real systems the PSF always negatively affects the certainty of signal mapping and object location, as it is reasonable to assume that the values of adjacent pixels are correlated to each other. Different technologies and methodologies have been (and are being) developed to increase the resolution, and the certainty of signal location, accordingly. Among these, our DDM method (Chapter 4) is an example of post-processing method, that explores pixel connectivity to increase the certainty of signal position [130].

3.2 Microscopy

The first microscope building is attributed to Hans and Zaccharias Janssen, two Dutch spectacle makers that in 1590 laid the foundation of compound microscopes by placing multiple glass lenses at the opposite end of a tube. However, it was not until 1666 that the microscope becomes a scientific instrument, thanks to Antonj van Leeuwenhoek that, inspired by Robert Hooke's studies, perfected the lenses geometry until he was able to observe the microscopic world of cells and bacteria and described them for the first time [131]. Since the time of these pioneers, the basic technology of the microscope has developed in many ways.

Over the past three centuries, microscopy has evolved from being largely descriptive and qualitative to become a powerful tool capable of uncovering new phenomena and exploring molecular mechanisms in a way that is also accurately quantitative [132]. Today, thanks to many different imaging modalities, not necessarily limited to the use of optical lenses, the microscope has become an invaluable tool in diverse research fields, including biomedical and biological research.

Microscopes are classified based on their working principle and application. A first separation is between simple and compound microscopes. Simple microscopes, as the one invented by Van Leeuwenhoek, places a single lens between the viewer and the specimen. Compound microscopes, mostly used nowadays, combine two magnifying lens to reach higher magnification powers: the objective lens (typically 4x, 10x, 40x or 100x), close to the specimen, and the eyepiece lens (typically 10x), close to the viewer. By varying in their optical configurations, cost, and intended purposes, compound microscopes serve a variety of imaging modalities (Figure 3.2). Compound microscopes are further classified in light (optical) and electronic microscopes. Light microscopes use visible light and magnifying lenses to generate magnified images of small objects. Electron microscopes uses a beam of accelerated electrons as a source of illumination, thus increasing their resolving power of more than 1000 times with respect to optical microscopes [133]. Both light and electron microscopy undergo further classification, as schematized in Figure 3.2.

Among the numerous microscopy modalities and techniques available today, we hereafter focus on those that we have encountered in the studies discussed in this Thesis, that are Bright Field microscopy, Differential Interference Contrast microscopy, widefield fluorescence microscopy and confocal fluorescence microscopy.

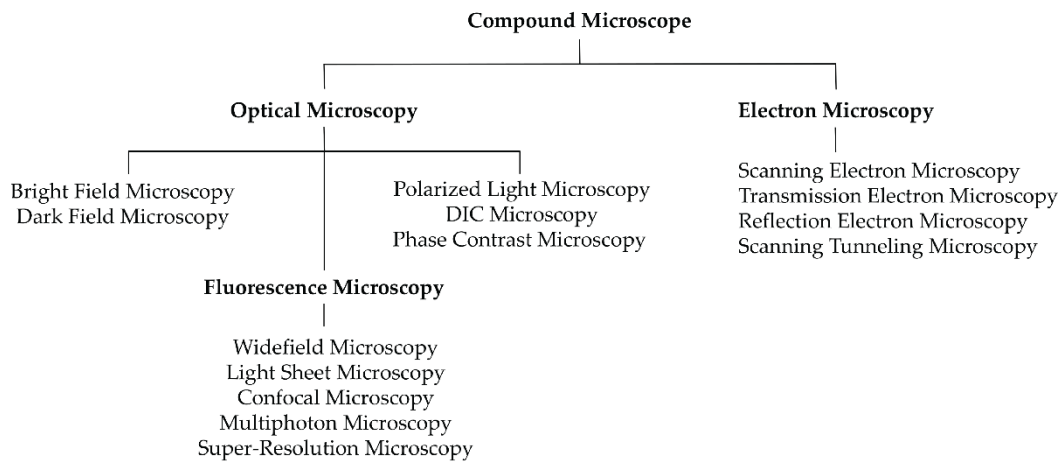


Figure 3.2. Microscopy classification. Compound microscopes are multi-lenses systems that serves a variety of imaging modalities. Optical microscopes deliver photons or light energy to the sample using simple lenses; electron microscopes direct an electron beam on the specimen using electrostatic or electromagnetic lenses. In Bright Field microscopy a dark sample on a bright background is illuminated with visible light; in Dark Field Microscopy a special aperture focuses incident light on the specimen, that appears bright on a dark background. Polarized microscopes investigate specimen's optical properties by mean of polarized light. In Differential Interference Contrast Microscopy (DIC), image contrast in transparent samples is produced by interference of polarized light. Similarly, in Phase Contrast Microscopy phase-shifted incident light is used to generate image contrast. In Fluorescence Microscopy, the sample illumination is extended out of the range of visible light to collect the light emitted by specific fluorescent molecules. Light Sheet and Confocal Microscopy increase the penetrating and resolution power of optical microscopy, by respectively illuminating one thin optical plane at the time (light sheet) or using a pinhole to focus a smaller beam of light at one narrow depth level at a time (confocal). The Multiphoton microscope also restricts the excitation of fluorophores at the focal plane. Super-Resolution Microscopy refers to a collection of hardware and software methods used to increase the resolution of light microscopy. In Electron Microscopy, the focused beam of electrons scans the specimen surface or is transmitted through the specimen to collect transmitted (Transmission Electron Microscopy), secondary (Scanning Electron Microscopy) or scattered (Reflection Electron Microscopy). A scanning tunnelling microscope can image surfaces at the atomic level.

3.2.1 Bright Field microscopy

Bright Field microscopy (BFM) is the simplest among the optical microscopy illumination techniques. In BFM, illumination light is transmitted through the sample and the contrast is generated by the absorption of light in dense areas of the specimen, resulting in an image with a bright field or background (Figure 3.3).

After being transmitted through the sample, the incident visible light (390-700 nm), usually emitted from a halogen lamp or LED source, is focused by an objective lens to produce a real image. At its simplest, the objective is a cylinder containing one or more lenses, consisting of very high-powered magnifying glass, with very short focal length. The objective is characterized by its magnification and numerical aperture (NA), that is a measure of its ability to gather light and resolve fine specimen detail at a fixed object distance [134].

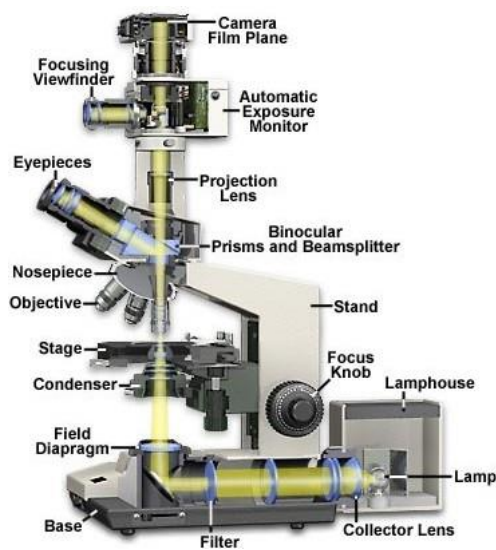


Figure 3.3. Modern bright-field compound microscope configuration. The emitted light (*lamp*) passes through a *collector lens* and a series of *filters* before it is reflected by a mirror and passed through the *field diaphragm* and into the substage *condenser*. The condenser forms a cone of illumination that bathes the specimen, located on the microscope *stage*, and subsequently enters the *objective*. Light leaving the objective is diverted by a *beam splitter/prism* combination either into the eyepieces to form a virtual image, or straight through to the projection lens mounted in the trinocular extension tube, where it can then form a latent image on film housed in the camera system. Research-level microscopes also contain one of several light-conditioning devices that are often positioned between the illuminator and condenser (*filters*), and a complementary detector or filtering device that is inserted between the objective and the eyepiece or camera. The conditioning device(s) and detector work together to modify image contrast as a function of spatial frequency, phase, polarization, absorption, fluorescence, off-axis illumination, and/or other properties of the specimen and illumination technique. Image reproduced from [126].

Bright Field microscopes are cost-effective, easy to setup and compatible with live cell imaging [135]. Their limitations include low resolution, due to the blurry appearance of out-of-focus material, and low contrast for weakly absorbing samples [136]. Staining is often required to face this latter problem, which comes

with the disadvantage that live imaging is difficult due to staining killing the cells. Other imaging modalities, based for example on light polarizing filters [137] or darkfield condensers [138], can be used in place of staining to increase the contrast. On the other side, BF illumination is useful for samples that have an intrinsic colour, as chloroplasts in plant cells [139] or cell aggregates, as the spheroids imaged in this Thesis (Chapter 8). As other optical microscopes, BF microscopes are limited in resolution by Abbe's diffraction limit, which is about $0.25\ \mu\text{m}$ [128]. By definition, this limit can be improved (and the resolution, accordingly, increased) by decreasing the incident light wavelength (*e.g.*, UV and X-ray microscopes, whose high energy however damage biological samples) or increasing the refractive index of the lens working medium. (*e.g.*, oil immersion objectives). Contrarily, longer wavelengths improve tissue penetration at the expense of point separation [140].

3.2.2 Differential Interference Contrast microscopy

Differential interference contrast (DIC) was introduced to microscopy by George Nomarski in 1952 [141], and since the late 1960s it has become increasingly popular for its capability to enhance the image contrast of transparent specimens or with low surface reflectivity [142]. Like polarized light microscopy (PLM), DIC makes use of prisms to precisely modify the polarization of the light waves, to see otherwise invisible features. In PLM a first polarizer, placed beneath the stage inside or below the condenser, sets the incident light wave oscillation to a unique plane (*i.e.*, polarization). Image contrast then arises from the interaction of the polarized light with a birefringent (or doubly-refracting) specimen, to produce two individual wave components polarized in mutually perpendicular planes. The velocities of these components are different and vary with the propagation direction through the specimen. After exiting the specimen, the light components become out of phase with each other, but are recombined with constructive and destructive interference when they pass through a second polarizer, called the analyser, placed downstream the objective (Figure 3.4 (a, c)). In DIC, two birefringent compound prisms known as Wollaston or Nomarski prisms, are added to the standard configuration of a polarized microscope (Figure 3.4 (b)). The

first prism (beam splitter) separates the incident light into two perpendicular beams, which take slightly different paths through a sample depending on its optical density. When the beams pass through the second prisms (beam combiner), their interference reveals interfaces between regions of different thickness and/or refractive index, giving the illusion of a three-dimensional image (Figure 3.4 (d)).

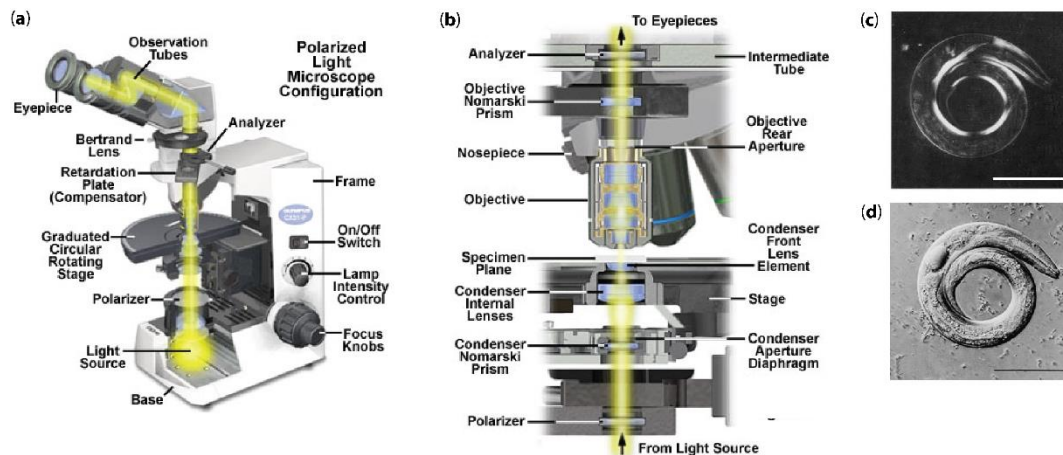


Figure 3.4. Polarized light and DIC microscope configuration. (a) At a minimum, a polarized light microscope is equipped with two linear polarizing elements (*polarizer* and *analyzer*). Many PLMs are equipped with a *graduated circular rotating stage* for quickly changing the specimen orientation with respect to the polariser transmission axes, to vary the degree of image brightness. Advanced microscopes include a *Bertrand lens* for conoscopic observation of interference patterns. Finally, polarized light microscopes should have an accessory slot in the nosepiece or intermediate tube into which a retardation plate or compensator can be inserted for quantitative analysis of birefringent specimens. Image reproduced from [126]. (b) In its standard configuration, a DIC microscope contains the basic polarizing elements of a PLM and, in addition, two Nomarski prisms. The first is located between the first PLM's polarizer and the condenser and serves to align and shear incident polarized wavefronts into two orthogonal components. These perpendicular sheared wavefronts are focused by the condenser into parallel bundles that traverse the specimen plane and respond to refractive index and thickness gradients by deformation according to optical path length parameters of the specimen. Light waves gathered by the objective converge at the rear focal plane where a second Nomarski prism is located, to recombine sheared and deformed wavefronts into linear and elliptically polarized light, before passing through the PLM's analyser, oriented perpendicularly to the substage polarizer. The linear polarized light components that emerge from the analyser recombine through constructive and destructive interference at the image plane. Image reproduced from [126]. (c, d) Exemplificative *C. elegans* micrographs imaged by PL (c) and DIC (d) microscopy, adapted from [143] according to journal policy. Scale bars: 100 μm .

DIC allows for high resolution imaging of unstained and living cells and organisms, and for 'optical sectioning' of thick samples [144]. DIC retains several

advantages with respect to phase contrast microscopy, its “antagonist” modality for image contrast enhancement. First, an ‘halo’ artefact is present in phase contrast but not DIC images [145]. Second, without phase plates or condenser annuli to severely restrict the size of condenser and objective apertures, DIC microscopy can produce excellent high-resolution images at large aperture sizes. Finally, the correlation between image contrast and specimen orientation in DIC microscopy, absent in phase contrast microscopy, can often be used to advantage in the investigation of extended linear specimens, as highly ordered mineral structures [126]. In biomedicine studies, DIC is mostly used in multimodal imaging systems, as together with fluorescence microscopy, to define objects boundaries and find the areas of interest, because using transmitted light and without requiring sample staining, DIC will reduce photodamage and toxicity to the sample [146]. Also, unlike phase contrast in which dark phase ring unfortunately blocks precious fluorescence photons, DIC objectives have no effect on fluorescence intensity [146]. As what concern limitations, DIC imaging is quite expensive (because of the prisms) and not suitable to some birefringent specimens (*e.g.*, many kinds of crystals) and specimen carriers (*e.g.*, Petri dishes), because of their effect upon polarized light. For such specimens, Hoffman modulation contrast may be a better choice. Apochromatic objectives may not be suitable because such objectives themselves may significantly affect polarized light. DIC microscopy is not decisive in imaging regions having very shallow optical path slopes, such as those observed in extended flat specimens, as they produce insignificant contrast and often appear in the image at the same intensity level as the background. For such specimens, polarized light microscopy may be a better choice.

3.2.3 Fluorescence microscopy

In contrast to other modes of optical microscopy that are based on macroscopic specimen features, such as phase gradients, light absorption, and birefringence, fluorescence microscopy is capable of imaging the distribution of a single molecular species based solely on the properties of fluorescence emission. In a biological system, fluorescence is the emission of light by an endogenous or exogenous substance that has absorbed light or other electromagnetic radiation.

Endogenous molecules, as the green fluorescent protein (GFP) and its variants, are intrinsically fluorescent (*i.e.*, autofluorescent) proteins that are mostly used as genetic tags for protein components of living systems. Exogenous molecules, better known as fluorophores or fluorochromes, are synthesized fluorescent chemical compounds that can highlight specific molecules in fixed samples [147]. Fluorescence is a three steps mechanism: 1) a fluorophore in its ground (relaxed) state (*i.e.*, singlet state, S_0) is hit by an external source of energy, such as a photons or electrons; 2) the fluorophore absorbs the energy by moving an electron into a more energetic orbital, thus transitioning to an excited state (usually a singlet S_n , with $n>0$); 3) the fluorophores rapidly relaxes back to the ground state by emitting light radiation (*i.e.*, photons of lower energy and longer wavelength than the absorbed photon) and by non-radiative processes, including internal conversion followed by vibrational relaxation [148]. The difference between the exciting and emitted wavelengths, known as the Stokes shift, is the critical property that define the signal-to-noise ratio of the fluorophore signal and its usability in combination with other fluorophores [148, 149]. By completely filtering out the exciting light without blocking the emitted fluorescence, it is possible to see only the objects that are fluorescent, setting to a black background any other component of the specimen. Because of its intrinsic selectivity, fluorescence imaging has become one of the most used imaging modalities in molecular biology and living specimens for the selective visualization of molecules of interest. When carried out methodically, fluorescence microscopy becomes a valuable tool for quantitative imaging, opening for spatial precise location and monitoring of intracellular components, as well as their associated diffusion coefficients, transport characteristics, and interactions with other biomolecules. As a main example, colocalization studies are usually carried out by mean of fluorophores (see also Chapter 5) that, however, only confirm the closeness of the two fluorescent tags to each other, located within the resolution limit of the microscope. True interaction between marked species cannot be verified by fluorescence emission but by fluorescent transfer, trough dedicated techniques for quantitative measurements of dynamics and interactions [150-152]. Furthermore, fluorescence microscopy has found application outside the field of signal mapping, either visual or quantitative, as in photo-uncaging [153], photoactivation [154] and optical-sensing [155]

applications, where the dramatic response in fluorescence to localized environmental variables enables the investigation of pH, viscosity, refractive index, ionic concentrations, membrane potential, and solvent polarity in living cells and tissues [126].

Nonetheless, fluorescence microscopy presents several technical challenges, after the chemical nature of the used fluorophores. Many commercially available dyes suffer from small Stokes shifts, resulting in poor signal-to-noise ratio and self-quenching on current microscope configurations. The magnitude of the Stokes shift itself varies considerably from one fluorophore to another. In general, the more conjugated bonds in the molecule, the broader the Stokes shift, the lower the excitement energy requirement, and the lower the possibility for specimen photodamaging and fluorophore photobleaching [148]. Finally, the simultaneous use of more than one fluorophore in the same acquisition setting is a common practice in biomedicine, to observe molecules co-distribution. However, not all fluorophores can be combined with each other, as their overlapping Stokes shift may lead to severe crosstalk between the channels and signal bleed-through [148]. Consequently, next generation applications, like single-molecule analysis, demand fluorescent dyes with large and tuneable Stokes shifts to achieve precise imaging and accurate sensing [149].

Another major concern in fluorescence microscopy is resolution, that is limited by the Abbe diffraction limit to approximately one-half of the excitation wavelength [128]. To overcome this limitation, in the last four decades a growing number of microscopy techniques has been developed, capable to increase contrast and spatial resolution in fluorescence images. Light sheet fluorescence microscopy (LSFM) [156], confocal microscopy [129], multi-photon microscopy [157] and super-resolution techniques [158] are currently among the most powerful approach to seeing microscopic structures in three dimensions, even deep within tissues, with increased resolution and contrast. Hereafter, the main characteristics of widefield and confocal fluorescence microscopy are summarised.

Widefield fluorescence microscopy

Reflected light fluorescence microscopy is overwhelmingly the current method of choice for widefield investigations with non-coherent light sources, as well as

those conducted with laser scanning confocal and multiphoton instruments. This popular mode of fluorescence microscopy is also known as incident light fluorescence, episcopic fluorescence, or simply epifluorescence. In widefield microscopy (WFM), the incident and emitted light travel through the same objective lens in a non-linear light path by mean of dichromatic mirrors. Beside curving the light path, these mirrors crucially serve as pass-band filters, that keep the excitation and emission wavelengths separated, thus reducing the signal-to-noise ratio (Figure 3.5).

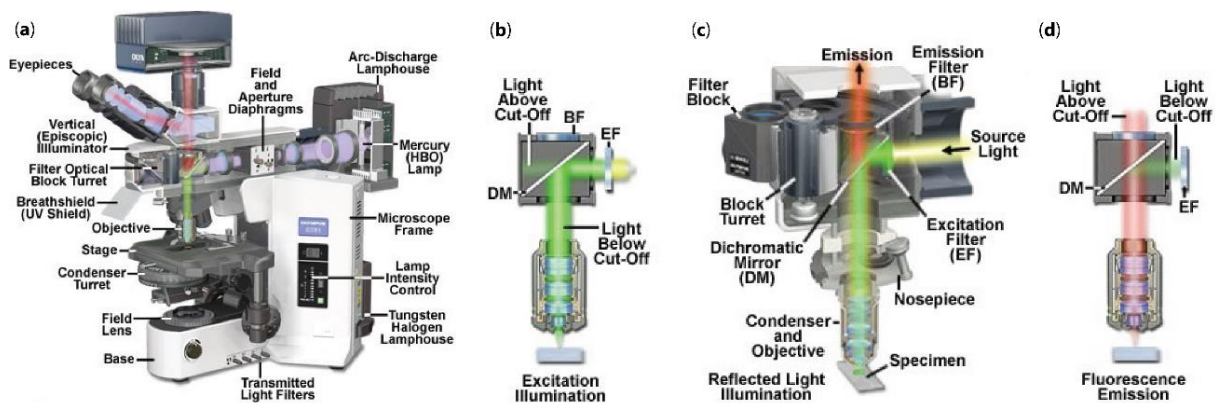


Figure 3.5. Widefield epifluorescence microscope. (a) Microscope configuration. (b, c, d) Details of the designed light path. (b, c) A mercury-vapor (or xenon arc-discharge) lamp outputs a wide spectrum of excitation wavelengths at high flux density (usually covering most of the ultraviolet and the entire visible spectrum). The light first passes through an emission filter (EF), that selects the proper wavelength band for excitation, and then reaches a dichromatic mirror (DM), designed to selectively reflect the EF-filtered light (b, *Light below cut-off*) onto the specimen (90° angle) through the objective rear aperture, while transmitting (*i.e.*, discarding) both shorter and longer wavelengths (b, *Light above cut-off*). (c, d) The fluorescence emitted by the specimen, whose intensity is three to six orders of magnitude lower than the source light [126], is gathered by the same objective and transmitted through the DM and a barrier filter (BF), designed to allow only light of emission wavelengths (d, *Light above cut-off*) to reach the microscope eyepieces and/or detector, while reflecting out the unwanted excitation wavelengths (d, *Light below cut-off*). Images reproduced from [159].

The main advantage of an epifluorescence imaging system is that, while it is relatively simple and inexpensive to use, it is highly light efficient [146]. Accordingly, WFM is widely used in cell biology, as the illumination beam easily penetrates the full depth of a cell monolayer, allowing easy imaging of intense signals [146]. However, sample illumination with relatively high intensity light brings different disadvantages. First, it means that all the fluorophore molecules

in the specimen are excited, including those out of the current field of view or the current focal plane, therefore possibly leading to photobleaching (Subsection 3.2.4) and serious phototoxicity phenomena, such as free radicals formation [160]. Second, fluorophores excitation out of the field of view means collection of undesired out-of-focus fluorescence, that lowers the signal-to-noise ratio and reduces contrast [161]. Finally, the lack of optical sectioning also prohibits the in-depth investigation of the specimen and the discrimination of signal (accidentally or not) aligned on the axial (depth) direction, thus limiting the precise localization of fluorescence molecules and the interpretation of 3-D spatial data [162, 163]. Collectively, these problems can be resolved by the introduction of optical sectioning that, working one optical plane at the time, allows exciting only the fluorophores of interest (containing photobleaching, phototoxicity and out-of-focus contributions) to investigate the three-dimensionality of the specimen and to perform accurate measurements of signal localization and colocalization, all this while reducing noise and increasing contrast.

Confocal fluorescence microscopy

Confocal laser scanning microscopy (CLSM), or simply confocal microscopy, is an optical imaging technique that increases optical resolution and contrast of a micrograph by using a spatial pinhole that axially and longitudinally restricts the field of view, such that sharp images from the focal plane alone (“slices”) can be acquired and z-stacked to form a composite 3-D image. When applied to fluorescence microscopy, a confocal technique additionally provides a mean to reduce photobleaching and photodamaging.

In CLSM, a laser beam is focused into a specimen, where it excites fluorescent molecules throughout the entire cone of illumination. The emitted fluorescence is then collected by the objective lens and focused by a second lens through a carefully aligned pinhole (Figure 3.6 (a)), that blocks fluorescence emission from above or below the focal plane, making sure that only fluorescence that originates at the focal point is captured by the detector. Scanning mirrors are used to sweep the laser beam across the specimen, generating an image pixel by pixel [126].

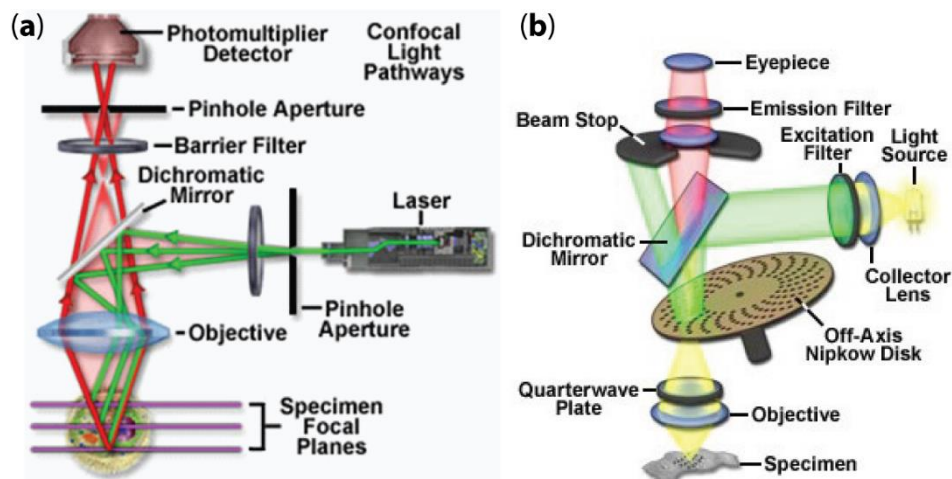


Figure 3.6. Laser scanning and spinning-disk confocal microscopy. (a) Confocal principle in epi-fluorescence laser scanning microscopy. Coherent light emitted by the laser system (*excitation source*) passes through a *first pinhole* aperture, situated in a conjugate plane (confocal) with a scanning point on the specimen. As the laser is reflected by a *dichromatic mirror* and scanned across the specimen in a defined focal plane, secondary fluorescence emitted from points on the specimen (in the same focal plane) passes back through the dichromatic mirror and is focused as a confocal point at a *second pinhole* aperture, placed in front of the detector. The significant amount of fluorescence emission occurring above and below the objective focal plane (*Out-of-Focus Light Rays*) is not confocal with the pinhole: it forms an extended *Airy disk* in the aperture plane, mostly blocked out by the pinhole and thus not detected by the photomultiplier. However, a small fraction of the out-of-focus fluorescence is delivered through the pinhole, contributing to image blurring. Figure reproduced from [126]. (b) Optical system of a spinning-disk confocal microscope. A confocal disk is set on the intermediate imaging plane and rotates on its centre axis while excitation light is irradiated on its peripheral portion, where pinholes are spaced so as not interfere with each other.

A CLSM provides superior resolution, depth penetration and contrast compared to a widefield microscope, but is generally less sensitive and slower. This makes confocal microscopy less well-suited to live-cell imaging, but a state-of-art choice for 3-D quantitative investigation of molecules spatial distributions [146]. Unfortunately, even the latest confocal microscopes may suffer from instrumentation problems that can dramatically affect their ability to generate quantifiable data. As for all optical microscopes, illumination intensity may vary substantially from the centre of the image to the periphery, favouring an artifact known as *image vignetting* (discussed in Subsection 3.2.4). Particularly troubling are laser power fluctuations that can substantially alter the intensity over a single imaging session. Other unexpected pitfalls could include variability in fluorophore emission depending on the sample mounting media and changes in image analysis

processes with software updates [146]. However, a major concern in confocal fluorescence microscopy remains the spatial resolution, limited by Abbe's diffraction limit and by other biological factors such as cell viability and sensitivity to thermal damage and photobleaching, that place limits on the light intensity and duration of exposure. Over the years, several techniques have been introduced to increase the resolution of optical sectioning systems. One such alternative is a spinning-disk confocal microscopy (SDCM, Figure 3.6 (b)), which illuminates the sample using an array of pinholes arranged in a special pattern on a disk, creating hundreds of focused beams. Parallelizing multiple confocal light paths, SDCM brings advantages of imaging speed and decreased excitation energy, phototoxicity and photobleaching, often making SDCM the preferred system for imaging live cells or organisms [164]. For thick specimens, such as whole zebrafish embryos or cleared tissues and organs, light sheet microscopes offer advantages in both speed and low phototoxicity, though typically at the cost of resolution [146]. A multiphoton microscope uses a pulsed infrared laser to achieve greater depth penetration and control over the excitation volume definition, enabling localized photoactivation [165]. Among such technological improvements, super-resolution techniques, such as TIRF, SIM, STORM and PALM just to cite a few of them, allow optical systems to bypass the diffraction limit and greatly improve spatial resolution. Although such enhancement typically comes at the expense of speed, sample viability and depth penetration, super-resolution techniques are expected to dominate the quantitative microscopy scenario for the next decades [166].

3.2.4 Optical microscopy artifacts

Visual artifacts in digital images are anomalies that occur during acquisition, handling or processing of the image, that disrupt its integrity and informativeness. Besides noise, signal distortion and compression artifacts, two types of artifacts are crucial to hinder quantitative imaging in optical microscopy: the vignetting effect, associated to all optical microscopy modalities, and the photobleaching effect, specific to fluorescence microscopy.

Vignetting

Images acquired with optical microscopes are typically characterized by an attenuation of brightness intensity that radially expand from the projection of the principal point (*i.e.*, image centre) towards the image edges, called the vignetting effect [167]. It is intrinsic to a lens system, and when it shows a perfect radial symmetry it can be treated quite effectively. However, in practice often this is not the case. This may be attributed to multiple factors, such as imperfect illumination of the specimen, optical aberrations in the objectives, and different sources of camera noise [168]. While uneven distribution of the intensity over the field of view is often tolerable, high illumination variations can prevent the effective application of many image processing techniques, such as threshold-based segmentation [169], object tracking [170], or mosaicing [167, 171]. The vignetting problem is emphasized in quantitative imaging applications, where it also prevents reliable intensity measurements [172]. In these cases, a rigorous experimental approaches require the estimation of the vignetting function and its correction in post-processing, both with [173, 174] or without [167] *a priori* assumption on its values distribution over the image domain. Flat-field correction (FFC) is one of the most used techniques to cancel the effects of vignetting and other shading effects [175]. The goal is to estimate the shading field from a reference image, so that the original image can be recovered by subtraction [167]. However, alternative methods of FCC where the correction functions are directly estimated from the images of interest have been developed [176]. Collectively, several linear and nonlinear vignetting correction approaches have been proposed in literature for grey-level images, and the problem has been extensively discussed [171, 177].

Photobleaching

Although in principle a fluorophore can cycle between ground and excited states for an unlimited number of times, its efficiency has been shown to gradually decrease through the cycles [148, 178]. Among all those processes that cause the fluorescent signal to fade permanently, photobleaching is perhaps the most serious one in fluorescence microscopy. In consequence of fluorophore overexposure to

light, either in terms of time or laser intensity, different processes can be triggered at the molecular level that alter the fluorophore structure and hence behaviour. Mostly, bleaching is thought as to be associated with triplet state and its reaction with molecular oxygen, that can covalently alter the fluorophore to inactivate its ability to fluoresce. In addition, the singlet oxygen can interact with other organic molecules causing phototoxicity for living cells [179].

Not only photobleaching degrades the visual quality of the results, but it also represents a major concern for quantitative imaging and image processing in fluorescence microscopy. While its contribution can never be avoided, photobleaching can be minimized by proper experimental procedures (staining, samples storage and of course image acquisition setting), and even corrected in post-processing, after the characterization of the signal degradation function [180]. First, photobleaching can be reduced by some practical preventive measures, such as storage of fluorescence samples in the dark, sample fixation with antifade agents and specifically designed mounting medium, and by use of fluorophores with increased photostability [148]. In all imaging applications, the use of high-quality optical filters and cameras with high quantum efficiency allow to reduce the exposure time without losing in illumination [148]. However, to perform reliable measurements of absolute fluorescence intensity and quantitatively compare fluorescent samples with precision, photobleaching further needs to be corrected, either in real time or in post-processing. The most straightforward method consists in estimating the photobleaching function (*i.e.*, the time rate of fluorescence decay) in a reference image, possibly at each pixel intensity level, and to use it to compensate for the loss of intensity in the real dataset for a post-acquisition correction on the image radiance. Several different algorithms for such radiance normalization have been developed and are used by various researchers [180-182].

Finally, not all photobleaching comes to harm, as its occurrence is exploited in different microscopic investigation techniques. For instance, diffusion and motion of biological macromolecules can be investigated by observing the rates and pattern of fluorescence recovery in photobleached area (Fluorescence Recovery After Photobleaching, FRAP) or in their proximity (Fluorescence Loss In Photobleaching, FLIP). Different is the case of Fluorescence Resonance Energy

Transfer (FRET), that is based on *reversible* fluorescence fading (*i.e.*, quenching) [183].

3.3 Computed Tomography

Computed tomography (CT) is a non-disruptive imaging technique that uses the penetrating power of X-rays to investigate the internal structure of materials [184]. Since its introduction in the early seventies [185], CT has revolutionized the fields of archaeology [186], material science and manufacturing industry [187], but it is the field of radiology that it has found its most application [188]. A CT scan can be used to non-invasively create accurate cross-sectional and three-dimensional images of internal organs, bones, soft tissues and blood vessels. Accordingly, CT is routinely used to detect, monitor and diagnose cancer, diseases and internal injuries, as well as to plan and guide medical, surgical or radiation treatment [189]. In clinical CT scanning, a wide beam of X-rays crosses the patient and hit an opposite integral array of detectors. Emitter and detectors are integral and mounted in a ring that quickly rotates around the body axis, producing signals that are reconstructed to generate high resolution and high frequency tomographic slice sequences of the body (*tomographic images*). These slices can be digitally “stacked” together and processed to achieve a 3-D image of the body that allows for easier identification of the anatomic structures as well as possible tumours or abnormalities.

Tomography devices can be first divided based on the achievable spatial resolution. Conventional (medical or heavy industrial) CT generally refers to submillimetre resolutions (voxel sizes $\geq 100 \mu\text{m}$), microtomography (μCT) to micrometre resolutions (voxel sizes $\geq 0.1 \mu\text{m}$) and nanotomography (nCT) to nanometre resolutions (down to voxel sizes $\sim 10 \text{ nm}$) [184]. Given the reduced size of most animal models with respect to human, μCT and nCT are preferred in biomedical research. As the underlying physics and the working principle are the same, they will be surveyed in the next Subsection dedicated to μCT , that we applied to the investigation of the effect of muscle sclerostin on bone morphometry (Chapter 7).

3.3.1 Micro Computed Tomography

μ CT scanning was introduced in the 1980s by J. Elliott [190] for imaging materials and small animals with a micrometre resolution unachievable by medical CT, with which it shares the operating principle, that applies on a much smaller scale. The basic components of a μ CT scanner are the X-ray source, the rotating sample stage, the X-ray detector system and the images reconstruction system (Figure 3.7).

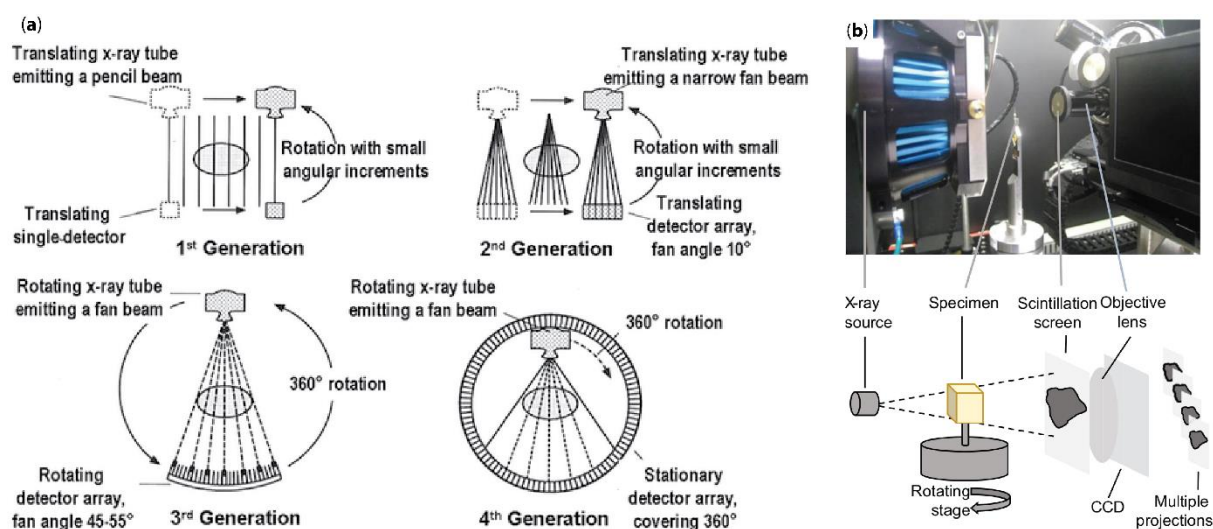


Figure 3.7. CT and μ CT. CT and μ CT devices differ in size and resolving power, though that the physical working principle is the same. In CT imaging of living beings the X-ray source revolve around the steady patient/animal to reduce motion artefacts (a), whereas in object CT imaging the resolution is improved by pointing a steady X-ray source on a rotating object (b). (a) Design and acquisition schemes of four generations of X-ray CT scanners. The first and second generation scan in parallel, the third (most used) and fourth generation use rotary fan-shaped scanning, with rotating (third) or stationary (fourth) detector. (b) Schematic of the main components of a μ CT system: X-ray source, rotating specimen stage, objective lenses, scintillation screens and a charge-coupled device (CCD) camera detector, replaced by more efficient complementary metal oxide semiconductor (CMOS) in the latest years. Images reproduced from [191] under the CC-BY Creative Commons Attribution 4.0 International licence.

X-rays with a broad energy spectrum are generated by accelerating electrons across a high voltage to collide with an anode composed of a high atomic number and high melting point material (commonly tungsten). The X-ray energy depends on the applied voltage and can be modified by metal filters. Since X-ray energy dictates their absorption by a given material, X-ray filtration can be used to both

reduce radiation dose and improve image quality, depending on the imaging task [192]. With respect to medical CT's, μ CT X-ray tubes usually have a much smaller focal spot (*i.e.*, area where the electron beam interacts with the anode), so as to greatly improve the maximum image resolution, however at remarkable speed costs [193, 194]. The generated X-ray cone beam travels from the tube focal spot to the detector across the specimen, which locally attenuates the ray transmission depending on its composition, by Compton scattering and photoelectric effect [194]. The total value of X-ray attenuation tracks linearly with the specimen density, that can be measured by calculation of the attenuation coefficient (μ) according to Lambert Beer's Law:

$$\mu = \frac{\ln\left(\frac{I_t}{I_0}\right)}{x} = \frac{\ln\left(\frac{I_t}{N_{(S,t)} \cdot h\nu}\right)}{x} \quad (3.2)$$

where x is the specimen thickness, I_t is the detected intensity of transmitted (attenuated) X-rays, and I_0 is the intensity of the incident X-rays (*i.e.*, the energy sum of N photons of wavelength ν passing through a unit area S in unit time t , h =Planck's constant). The attenuation is related to the photoelectric effect and the incoherent Compton scattering, negatively relating to the presence of hydrogen atoms in the tissue [195]. In general, the denser the specimen, the higher the attenuation, the lower the detected intensity I_t , and therefore the brighter the structure in the final image. The image formation process begins with the detector, composed of photosensor units that transform an optical signal into an electric one. Most of μ CT systems to date employ digital 2-D detectors, firstly composed of image intensifiers read by charge-coupled devices (CCDs), then coupled with scintillator screens via fiber-optic bundles, and more recently outperformed by complementary metal oxide semiconductor (CMOS) in terms of frame rate [193]. A collimator is commonly used to delimit the transmitted beam field and focus it on the detector, that record a 2-D projection image of the specimen. The sample stage is then rotated by a fraction of a degree, and another X-ray projection image is taken. This step is repeated through a 180- or 360- degree angle, and the projections are used to reconstruct the data, by different algorithms [193], into 2-D cross-sectional slices, that can be further processed into 3-D models and even

printed as 3-D physical objects for analysis. After reconstruction, each CT voxel values is normalized to an integer value (CT number, measured in Hounsfield Units, HUs) for easier interpretation, handling and displaying. The HU scale is a semiquantitative linear transformation of the original attenuation coefficient measurement into one in which the radiodensity of distilled water at standard pressure and temperature (STP) is defined as 0 HU, while the radiodensity of air at STP is defined as -1000 HU. In a voxel with average linear attenuation coefficient μ , the corresponding HU value is therefore given by:

$$HU = 1000 \cdot \frac{\mu - \mu_{H_2O}}{\mu_{H_2O}} \quad (3.3)$$

This normalization results in CT numbers ranging from -1000 (*e.g.*, air) to +3000 (*e.g.*, dense bone, or areas filled with contrast agents). The resulting tomography image is therefore a 3-D map of local x-ray density of the object.

Modern μ CT offers a mean for non-invasive high resolution 3-D imaging, with short scan time and cost-effectiveness, and high sensitivity to many organs and tissues such as bone, lung and the cardiovascular system [196, 197]. These unique μ CT features allow scientists to investigate specimen properties such as porosity, architecture, thickness, volume fraction, density, and fibres orientation. According to its great morphological investigation power, researchers use μ CT to study bone, teeth, but also soft tissue and organs, detect both high density (*e.g.*, clotted blood, hyperemia) and low density (*e.g.*, edema, necrosis) lesions, and investigate composite materials, biomedical scaffolds and other devices [198]. On the dark side, μ CT is still time consuming for high-resolution datasets, sometimes employs staining and contrast agents that might alter the specimen characteristics, and produces large size datasets that require non-standard computing power [197].

3.3.2 Micro Computed Tomography artifacts

μ CT artifacts are image reconstruction errors that appear in the volume but do not belong to the scanned object, therefore posing a major issue to the reliability of μ CT qualitative and quantitative data. μ CT artifacts can arise from the X-ray source, from the detector or from the reconstruction step. Beam hardening and noise are the main source-related artifacts. Beam hardening is the phenomenon that occurs when a polychromatic X-ray beam passes through an object, resulting in selective attenuation of lower energy photons. Consequently, the beam becomes “harder” or more penetrating, after passing through the object. CT beam hardening artifact has two distinct manifestations, streaking (dark bands) and cupping artifacts, that results in underestimation of sample density. To reduce beam-hardening during acquisition, filtration with attenuating materials (often metals) is typically used to pre-harden the X-ray spectrum, in order to reduce artifacts, however decreasing image contrast and increasing noise. Noise firstly arises from scattered radiation, occurring both as a sparse/diffuse grain or random bright and dark streaks, degrading image quality and contrast. Noise can be reduced by higher tube voltage, that also reduces the beam hardening. However, noise is typically corrected in post-processing by many denoising and smoothing methods, starting from Gaussian and median filtering. Ring artifacts are the most common μ CT artifacts associated to the detector. Ring artifacts occurs due to the miscalibration or failure of one or more detector elements in the scanner. Less often, it can be caused by insufficient radiation dose or contrast material contamination of the detector cover. Recalibration of the scanner will usually rectify the artifact, while its correction can be performed during image reconstruction (pre-processing) or directly in the final image (post-processing). Aliasing artifacts are associated to the reconstruction step. Aliasing refers to a signal undersampling that reduces the accuracy of analog to digital converter (ADC) during image digitization. In the reconstructed volume, aliasing artifacts appear as fine wavy lines (Moiré patterns) toward the periphery of the image. Regardless of the nature of the artifact, good practice includes identification of flawed detector elements by flat-field correction prior to image acquisition, proper setting of scan degree, frame average, and rotation step, and use of specific

algorithms and methods for correcting beam-hardening, ring, and misaligning artifacts [199-201].

3.4 Concluding remarks

This Chapter surveyed the different imaging modalities and technologies applied throughout the PhD, focusing on their principles of image formation, strengths, and limits. As for most imaging modalities today, the digitalization of the acquisition systems permits to obtain digital images that can be stored and modified to describe the observed phenomenon qualitatively, and above all, quantitatively. We have seen how acquisition and digitization in real systems are inevitably associated with the creation of artifacts, that a proper and mindful acquisition cannot always avoid. In these cases, artifacts correction and compensation, mandatory for a truly quantitative use of the data collected, require modification of the acquired images. The *post-processing* phase, often underestimated, is in fact fundamental, not only for correcting noise and other errors, but also for the extraction of numerical data, which does not necessarily stop at image intensity reading, or at the perfunctory use of commercial software. Therefore, imaging should not be thought as concerning only image acquisition, but to encompass all the steps that go from sample preparation to the extraction and the analysis of the final data, giving equal dignity to all the steps of the way (Figure 3.8).

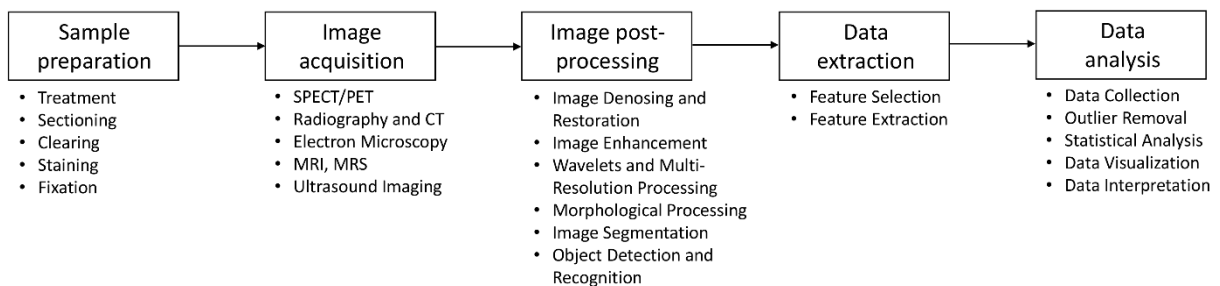


Figure 3.8. Biomedical quantitative imaging steps. SPECT, Single-Photon Emission Computed Tomography; PET, Positron Emission Tomography; CT, Computed Tomography, MRI, Magnetic Resonance Imaging; MRS, Magnetic Resonance Spectroscopy.

According to the variety of developed imaging modalities, in the past few decades numerous novel competing methods and tools for image processing have emerged, able to improve our capability to interpret biomedical image content. Image processing can range from simple and common tasks, such as creation of time series, image superposition or image dimensionality reduction (for example, by intensity projection), to more complex approaches and methods for image analysis, like pattern recognition, exploiting machine learning methods. In this PhD, the developed and applied image processing methods and techniques have ranged from image segmentation, to feature extraction and texture analysis. The following Chapters therefore deal with them in detail, within their application context.

Chapter 4

Density Distribution Maps: a novel tool for subcellular distribution analysis and quantitative biomedical imaging

There are many commercial and open-source software tools that assist biomedical researchers in performing independent image analysis. ImageJ [202], Imaris [203], CellProfiler [204], among the most famous ones, offer a wide range of functionalities that allow even the most inexperienced (in terms of software skills) user to inspect the content of his data. However, as soon as we move away from basic inquiry goals, or come to work on non-trivial data, such tools lack the necessary flexibility to adapt to the specificity of the problem, losing effectiveness on our data analysis.

The next two Chapters present two methods for image analysis that we developed to overcome this shortage and to specifically address our studies aim. For the sake of simplicity, hereafter we refer to the two methods as the *DDM method* and the *cDDM method*, respectively. The *DDM method*, discussed in this Chapter, was developed for the analysis of the spatial distribution of single signals in bidimensional images. The *cDDM method*, discussed in the following Chapter 5, expands the *DDM method* to the analysis of spatial co-distribution of signal couples, and therefore to the (semi-)quantification of their colocalization. Both methods have been already made public in the form of scientific research articles [130, 205]. To favour their accessibility to the scientific community, both methods

have also been made available as open-source software tools. The DDM method has also been already applied in actual preclinical studies, discussed in Chapters 6 and 7.

After introducing context and motivations for the DDM method conceiving and design (Sect. 4.1), its theoretical bases are discussed from both a biological and image processing point of view (Sect. 4.2). Then, after surveying the state of the art for signal mapping at subcellular level (Sect. 4.3), the method properties, innovation, and benefit to real biomedical problems are discussed and exemplified (Sects. 4.4 – 4.6). Finally, the contribution of the content-aware approach to the study is discussed, together with future perspectives (Sect. 4.7).

4.1 Study context

The DDM method arises from a necessity that we personally met working in the PHENOMICS Project, in the framework of a well-established collaboration with the Radiobiomics and Drug Discovery Unit of the IRCCS-IRST of Meldola (FC). The main goal of the PHENOMICS Project is the functional *in vitro* phenotypization of variously stressed tumour cells, through automatic microscopy image analysis. This phenotypization includes the characterization of the subcellular distribution of RNA:DNA hybrids (Chapter 6) through confocal fluorescent microscopy (Subsection 3.2.3) in A549 cells (Subsect. 2.1.1). A first issue arose when, comparing treated cells with untreated control cells, we realized that the treatment affected more the spatial distribution of imaged hybrids, rather than their intensity. Unfortunately, we also realised that hybrids could occur as smaller than the best resolution achievable by the microscope, this bringing the impossibility to estimate their subcellular position with a biologically relevant precision, and to detect and separate single from aggregated hybrids. Under these conditions, a local measurement necessarily becomes more informative than a single-point one. We therefore moved to estimating the local signal density (*i.e.*, number of signals per unit area), intending to also provide a visual support for its spatial distribution inside the sample. To this purpose we conceived the Density Distribution Maps (DDMs) and the method for their creation that, using local

image analysis, not only provides the unprecedented measure of local density, but parallelly increases the signal localization accuracy.

4.2 Theoretical background

4.2.1 Principles of local analysis

Given the principles of image formation by optical microscopy (Sect. 3.2), it is unreasonable to assume that the intensity value of pixels is independent of their position inside the image, and that the values of neighbouring pixels are uncorrelated to each other. In reality, and especially in the biomedical field, images contain a lot of structural information, that can be retrieved by an image analysis performed at the local level (*i.e.*, working on image patches), instead that at the global one (*i.e.*, the entire image). Local analysis is a core component of image processing and has indeed a great deal of applications, ranging from basic operations, as denoising and edge detection, to more complex tasks, as pattern recognition and video-based tracking.

An image patch can be defined as a small group of nearby pixels, generally of even dimensions, identified on a two-dimensional image by a rectangular $(2\Delta x+1)\times(2\Delta y+1)$ window (Figure 4.1 (a)).

The central pixel is defined as the *reference pixels*, while the other pixels in the patch that surround it are defined as *neighbouring pixels*, that together compose its *neighbourhood*. The *pixel connectivity* is the way in which the reference pixel relates to its closest neighbours, *i.e.*, those sharing at least a vertex with him. It is an important concept in digital image processing, as it is used for establishing boundaries of objects and components of regions in an image. In order to specify a set of connectivities, the dimensionality of the image N must be specified. In two-dimensional images ($N=2$), for a pixel p of coordinates (x, y) we can distinguish:

- four 4-connected (or *first*) neighbours at $(x+1, y)$, $(x-1, y)$, $(x, y+1)$ and $(x, y-1)$, sharing edges and vertices with the reference pixel

- four diagonal-connected (or *second*) neighbours at $(x+1, y+1)$, $(x+1, y-1)$, $(x-1, y+1)$ and $(x-1, y-1)$, sharing only the vertices which the reference pixel
- eight 8- (full-) connected neighbours, with which it shares its edges or vertices, that are the union of the 4-connected and the diagonal-connected neighbours.

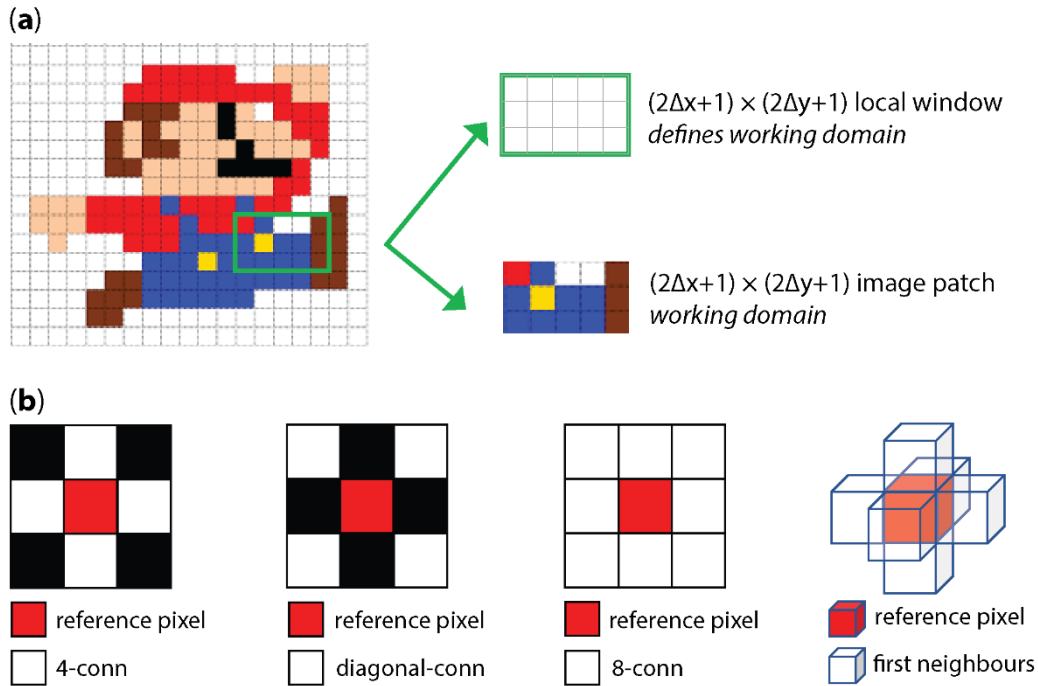


Figure 4.1. Local analysis and pixel connectivity. (a) Local analysis is performed on an image patch, defined by superposition of an $(2\Delta x+1)\times(2\Delta y+1)$ window on the input image. (b) The image dimensionality N define presence and position of the reference pixel's neighbours. In two-dimensional images ($N=2$), first neighbours can be related to the reference pixel by a 4-, diagonal- or 8- (full-) connectivity.

The definition of a neighbourhood and its connectivity permits to work locally, on selected patches of the image rather than on the whole. When applied locally, image operations (*neighbourhood operations*) recompute the value of the reference pixel basing on the values of its neighbours and a set connectivity, specified by a set of coordinate-dependent weights, called the kernel (see also Subsect. 7.2.2). When the neighbourhood-defining window is also a *moving* window, as in the case of the method we here developed, we can use it to investigate the spatial variability of image patterns, at a scale defined by the window size (WS).

4.2.2 Image segmentation and thresholding

Image segmentation is the process of partitioning a digital image into multiple *image regions* (or *objects*). An object is definable as a set of pixels typically contiguous (*i.e.*, connected) and semantically coherent. For examples, it may be the group of pixels with a similar intensity, or that together define a specific shape or texture. Segmentation is an important stage of image analysis because it serves to split the image into its meaningful components, usually called the Regions of interest (ROIs), some of which to be further processed and analysed, as for detection, recognition, or characterization purposes. In biomedicine, image segmentation is primarily needed to define the boundaries of target bodies, whether they are cellular or anatomical ones. A fundamental prerequisite to object segmentation is image binarization, that converts the image (grey) levels into binary ones. It consists of setting a usually single intensity-based threshold by which dividing the image pixels into two groups, either assigning them to the image *foreground* (*i.e.*, the sets of informative pixels, belonging to the object(s) of interest) or *background* (*i.e.*, the set of uninformative pixels, to exclude from further analysis).

While in principle the threshold can be selected manually by the user, this method is not advisable since it relies only on visual assessment that, besides being highly subjective and operator-dependent, it is not reproducible at all. In all cases where the output of segmentation has to be quantitatively assessed, it is mandatory to have an algorithm to set it automatically, so as to maximise objectivity, repeatability and reproducibility. Computer vision offers a huge number of methods for the calculation of the “best” threshold, based on the characteristics of the image being processed. A good trade-off between effectiveness and simplicity of use is represented by the direct or indirect histogram-based methods, that are the most common ones, and have been applied throughout this Thesis. These methods are based on the explicit creation of the image histogram, and the threshold setting is usually computed based on the position of its peaks and valleys. Instead, indirect methods rely on the calculation of properties of the histogram, that is seen as a probability density function. For instance, the entropy-

based methods extract the entropy, so that the threshold is set to yield, in this case, the maximum entropy, locally or over the entire image.

Usually, image binarization identifies a set of objects, rather than a single one, with different level of informativeness. Identification of single objects boundaries can be then performed by connected components labelling, *i.e.*, grouping pixels into objects (*components*) basing on pixel connectivity. Then, the assignment of a different numerical label to each identified connected component permits to address them separately.

Finally, a consideration on image segmentation assumptions. From an ideal point of view, the objects of interest are well-detected and fully connected, so as to be well separated from noise and clearly identifiable. However, in real-world applications this is far from being true, yet more in case of biomedicine. First, the dimension of the imaged object of interest depends on image resolution, so it may happen to deal with small objects, even of just few pixels. Second, objects can be detected as fragmented, because of suboptimal parameter settings in image acquisition, or processing that brings deteriorated signals, or even because the object actually *is* fragmented (*e.g.*, when investigating vesicular organelles, composed of many separate units). This discrepancy came to our attention working with RNA:DNA hybrids (Chapter 6), and led us to conceive the Density Distribution Maps (DDMs) hereafter described.

4.3 State of the art

Living cells are functionally defined by their anisotropy, as they rely on molecules distribution and compartmentalization to efficiently perform and control the biochemical reactions necessary to their life. Accordingly, abundance and especially location of molecules within the cell and the tissue are essential descriptors of their own behaviour and function [206]. In fact, subcellular mislocation of many proteins [207, 208] and RNAs classes [209, 210] is associated to a variety of diseases, including cancer. From a biological perspective, the investigation of molecules distribution requires not only the definition of their absolute position, but also of their absolute and relative abundance, as biochemical

reactions are threshold-dependent events, and the local concentration of compounds are major drivers of their triggering.

Although most of studies focus on proteins, any other kind of targetable molecule can be virtually addressed, such as specific drugs [211], organelles markers [212] or other bioactive species [213]. These studies commonly rely on optical fluorescence imaging techniques for selective molecules visualization [207, 208, 210-214], but too often their analysis is limited to visual annotation of targets location [215–218], which is mainly qualitative, subjective and prone to bias [219], and disregards the abundance information. Also, a key restriction of optical microscopy is its moderate resolution (Sec. 3.1) [128], which is limited to about half the wavelength of light (~200 nm) due to fundamental physical laws governing wave optics. Consequently, molecular processes taking place at the nanoscale scales (*i.e.*, 1 to 100 nm), cannot be studied by regular optical microscopy [220].

In recent years, a variety of super-resolution fluorescence microscopy techniques have been developed that circumvent the resolution limitation. Precise quantification of subcellular distribution of fluorescently marked molecules can now be achieved by single-molecule localization microscopy (SMLM) techniques [221, 224], which super-resolve via software the image beyond the physical limitation of optical resolution [223-227]. Despite its relevance, SMLM for routine and large-scale experiments is still restricted to large laboratories, due to technical and technological burdens. In fact, besides the high costs, the complexity of system calibration, image acquisition and computational reconstruction tasks [228, 229] preclude SMLM technologies to most users [230] and thwart their adoption [231].

On the other hand, image-based techniques with proper algorithms can often compensate for insufficient instrumentations. In fact, image processing has become an integral tool in the daily activity of most laboratories, where it mainly serves the automation of procedures that have been manual for many years, thus providing fast, quantitative and repeatable measurements of imaged structures descriptors, such as object's dimension and shape [232]. As a main example, preclinical *in vitro* studies, which typically assay drug efficacy and effectiveness by mean of commercial kits or user-validated protocols, have been profitably integrated with microscopy imaging as a further tool to complete the preclinical evaluation of antitumoral effects of the treatment investigated [233, 234].

Even when working at non-super instrument resolution, information conveyed by subcellular distribution can be preserved through image processing. As a main example, local image analysis permits to report pixel saliency as a function not only of the pixel itself, but also of its surroundings [235], thus permitting to reconstruct local geometric interactions, neither quantifiable, not even perceivable, in the native intensity images, which require a proper post-processing. To this purpose, investigating pixel connectivity is a simple yet powerful tool to go beyond intensity analyses and access local image structures [236].

Regarding spatial distributions, image analysis permits to capture phenomena hidden from visual inspection [237], to measure molecules dispersion and its variations [238], and to represent all of this as 2-D and 3-D pseudo-colour quantitative maps [239]. Intuitive and efficient visualization is indeed important at all steps of biomedical research: it is indispensable for quality control (for example, identification of dead cells, ‘misbehaving’ markers, or image acquisition artifacts), the sharing of generated resources among a network of collaborators, or the setup and validation of an automated analysis pipeline. Importantly, visualization tools have also to show relevant image-based data to biologists in an intuitive and interpretable manner, that enables them to identify meaningful characteristics and explore potential correlations and relationships between data. Several localization maps have been developed through years to facilitate the visualization of molecules distribution, especially when more than one molecule is investigated at once [216, 240, 241]. Since these maps are simply built on binarized signals, they all implicitly assume the perfect detectability of the object of interest, expected as compact, unfragmented (*i.e.*, made of connected pixels only) and dimensionally well distinguishable by noise. However, it may happen that after image pre-processing and thresholding the structural information of the ‘objects’ of interest can be partly lost, yet more in case of structures whose size is close to system resolution.

Starting from this latter concern, we developed a method that allows resolving subcellular structure location by reinforcing each pixel position with the information from the surroundings, introducing the novel concept of local density. This new concept also conveys three main innovations. The first is a novel

descriptor of the signal distribution, the local density index (LDI), representing pixel local density as the number of pixels, normalized by a unit area. The second consists in the intrinsic property of local analysis to preserve the informativeness of spatial distributions, even in images with a reduced resolution. Third, the application of the method enables the simple and fast creation of density distribution maps (DDMs). Besides quantitatively describing the objects absolute and self-relative location, DDMs offer a pictorial view of the density distribution of the whole imaged sample, representing an unprecedented support to detect possible subpopulations.

The effectiveness and robustness of DDMs is hereafter demonstrated and exemplified through their application to five image sets acquired with confocal fluorescence microscopy and micro computed tomography (μ CT), which demonstrates how local neighbour analysis can enhance information confidence even in the absence of high-resolution technologies, and how DDMs extend their applicability outside the mere spatial distribution analysis.

4.4 Materials and methods

Five datasets are considered in this study: COL7, MG-63, A549sh/p53, HeLa, μ CT. As the first step, we aim at showing the greater informative content conveyed by the DDM in structure identification and how it changes with their application to the same dataset sampled at a different resolution. To this purpose, the images of COL7 are downsampled, thus deriving a sixth dataset at a halved resolution (COL7-h). In this way, COL7 can be used as the benchmark for the analysis performed with COL7-h. Secondly, we apply DDMs at three different subcellular distribution studies in MG-63, A549sh/p53 and HeLa cells, imaged in homonymous datasets. Finally, we show the usefulness of DDMs in a mere technical context, to segment mice bone structures from μ CT images. Images of COL7 were downloaded free of charge from the public repository “The Image Cell Library” (CIL-CCDB) (<http://www.cellimagelibrary.org>) [242]. Images of A549sh/p53 and HeLa cells have been acquired for another study we are conducting to assess the effect of different stress conditions on RNA:DNA hybrids subcellular distribution (Chapter 6). The images of MG-63 have been kindly

provided by Dr. Enrico Lucarelli and the laboratory of Regenerative Therapies in Oncology (Unit of Osteoncology, Bone and Soft Tissue Sarcomas and Innovative Therapies) of the IRCCS Rizzoli Orthopaedic Institute. The images of μ CT have been kindly provided by the Prof. Carla Palumbo and her team of the Section of Human Morphology of the Department of Biomedical, Metabolic and Neural Sciences of the University of Modena and Reggio Emilia.

Image collection

(1) Images of monkey kidney fibroblast COL7 cells (The Cell Image Library [242], CIL:13701) were acquired with a confocal fluorescence laser scanning microscope LSM 510 or LSM 710 (Carl Zeiss, Inc., Oberkochen, Germany, equipped with a Plan-Apochromat 63 \times /NA 1.4 objective in multitrack mode. COL7 cells were indirectly immunolabeled against the wild-type and the W164S mutant of the vasopressin V2 receptor (V2R) with anti-myc antibody (Ab), and against endosomes with anti-transferrin Ab [243]. (2) Images of human osteosarcoma MG-63 cells, exposed or not to paclitaxel-loaded nanoparticles (PTX-Ce6@ker_{ag}), were acquired with a confocal fluorescence laser scanning microscope Ti-E A1R (Nikon, Amsterdam, The Netherlands) equipped with a 60 \times /NA 1.4 oil Plan-Fluo. MG-63 cells were indirectly immunostained against microtubules (MTs) with anti-tubulin Ab and incubated with Phalloidin-FITC for actin staining and with Hoechst for nuclei staining [244]. (3) Human lung adenocarcinoma A549 cells (ATCC, Manassas, VA, USA) were cultured in F12K (ATCC) supplemented with 10% FBS (Euroclone, Milan, Italy), 1% penicillin/streptomycin (GE Healthcare, Milan, Italy) and 2% amphotericin B (Euroclone, Milan, Italy), then plated at the density of 30,000 cells/well and infected with lentivirus LV-THMsh-p53 at MOI=10 TU/cell, as previously described [245]. Cells were seeded on a glass coverslip at the density of 30,000 cells/slide and underwent one-fraction 2-Gy gamma irradiation [246]. After 72 h cells were fixed and permeabilized with ice-cold methanol for 10 min and acetone for 1 min on ice, blocked with 2% BSA, stained with 1 μ g/mL 40,6-diamidino-2-phenylindole (DAPI) and immunostained for RNA:DNA hybrids (primary anti-S9.6 Ab (1:100 dilution, Kerfast, Boston, MA, USA), secondary goat anti-mouse Alexa Fluor 568 (1:250; Life Technologies, Carlsbad, CA, USA)). A549sh/p53 cells were imaged with inverted confocal laser scanning microscope

Eclipse Ti (Nikon Corporation, Tokyo, Japan) equipped with NIS-Elements Ar software. 12-bit images were acquired with a Plan Apo 60×/1.4 oil objective with lateral resolution of 0.1 $\mu\text{m}/\text{pixels}$ and axial resolution of 0.2 $\mu\text{m}/\text{pixels}$. (4) Human cervix adenocarcinoma HeLa cells (ATCC, Manassas, VA, USA) were cultured in EMEM (ATCC) supplemented with 10% FBS (Euroclone, Milan, Italy), 1% penicillin/streptomycin (GE Healthcare, Milan, Italy) and 2% amphotericin B (Euroclone, Milano, Italy). Hyperbaric Oxygen Therapy (HBOT) was applied at 1.9 absolute atmosphere (ATA) in a hyperbaric chamber for 1 h. After 72 h, cells were fixed and permeabilized with ice-cold methanol for 10 min and acetone for 1 min on ice, blocked with 2% BSA, stained with 1 $\mu\text{g}/\text{mL}$ 40,6-diamidino-2-phenylindole (DAPI) and immunostained for RNA:DNA hybrids (primary anti-S9.6 Ab (1:100 dilution, Kerastat, Boston, MA, USA), secondary goat anti-mouse Alexa Fluor 568 (1:250; Life Technologies, Carlsbad, CA, USA)). HeLa cells were imaged with inverted confocal laser scanning microscope Eclipse Ti2-e (Nikon Corporation, Tokyo, Japan) equipped with NIS-Elements Ar software. 12-bit images were acquired with a Plan Apo 60×/1.4 oil objective with lateral and axial resolution of 0.1 $\mu\text{m}/\text{pixels}$. (5) Images of harvested mice tibiae were scanned with a μCT using a microfocus X-ray tube KEVEX PXS10-65W (Thermo Scientific Co., Waltham, MA, USA; 70 kV, 0.035 mA) and captured with a VHR1:1 CCD camera (Photonic Science Ltd., East Sussex, UK; 4008×2672 pixels, 9 μm pixel size). Final voxel size (2× magnification) was isometric 4.5 μm^3 .

Image segmentation

All image processing procedures are implemented in MATLAB® (R2019a v.9.6.0, The MathWorks, Natick, MA, USA). (1) Marked V2R structures in COL7 and COL7-h cells are first segmented by grey level top hat filtering [125] with disk-shaped structuring elements (SE) of fixed size (in μm), then thresholded at the 95th percentile. (2) MTs in MG-63 cells are segmented by ISODATA thresholding [247] of single optical sections. (3) RNA:DNA hybrids in A549sh/p53 cells are segmented as follows: (i) maximum intensity projection (MIP) building and denoising by 8-bit quantization, (ii) nuclear region delineation by maximum entropy thresholding [248] of DAPI signal, (iii) grey level top-hat enhancement with disk-shaped SE of fixed size (in μm) in cytoplasm, (iv) ISODATA thresholding in cell nucleus and

cytoplasm, separately. (4) RNA:DNA hybrids in HeLa cells were segmented by ISODATA thresholding of MIPs' positive values. (5) Tibial metaphyseal trabeculae in μ CT images are segmented by (i) first performing an image denoising through 8-bit conversion, (ii) followed by an image contrast adjustment by adaptive histogram equalization [249], (iii) then thresholding the local intensity peaks by top-hat, and (iv) finally by applying our method to retain only densely distributed peaks, corresponding to metaphyseal trabeculae.

Local density analysis, LDI and DDMs

DDMs creation is a two-step procedure (Figure 4.2).

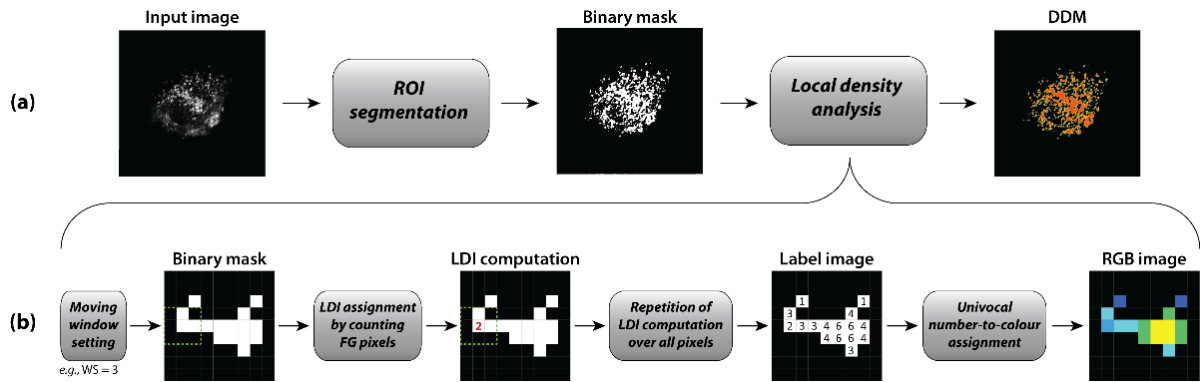


Figure 4.2. Flowchart of a DDM creation pipeline. (a) The acquired image is segmented in a binary mask. Then, the mask connectivity is explored by local density analysis to create the DDM in pseudo-colours. (b) Details of local density analysis: after setting the search (moving) window size, each foreground pixel of the binary mask is assigned a number representing the amount of foreground pixels in its locality (*i.e.*, LDI), this constituting the input to build the pseudo-colour DDM. Image reproduced from [130] under the CC-BY Creative Commons Attribution 4.0 International licence.

First, a 2-D-image (input) is segmented to achieve the foreground (binary) mask of the object(s) of interest (Figure 4.2 (a), left and centre). Second, local distribution analysis (Figure 4.2 (b)) is performed on the binary mask by assigning to each foreground pixel a value corresponding to the number of the foreground pixels in its neighbourhood, defined by a rectangular $(2\Delta x+1)\times(2\Delta y+1)$ search window, with Δx and Δy being the half-sides along X and Y directions, respectively. Therefore, our method refers to density as the “number of pixels for search window”. As an example, without losing generality, in case of a 3×3

window, possible values for the reference pixel range from 0 for isolated pixels, to 8 for full-connected ones. In practice, the value assigned to each pixel represents its LDI. The image containing the set of LDI is a DDM, which can also be visually represented in pseudo-colours. Therefore, each DDM's pixel is suggestive of the amount of information in its own neighbourhood. It is worth noting that the method can be applied to any distribution study, only requiring a binary input image, independently of the imaging technique and the acquisition system resolution.

The most important implication of DDM can be seen when created with a 5×5 (or larger) search window, as illustrated in Figure 4.3.

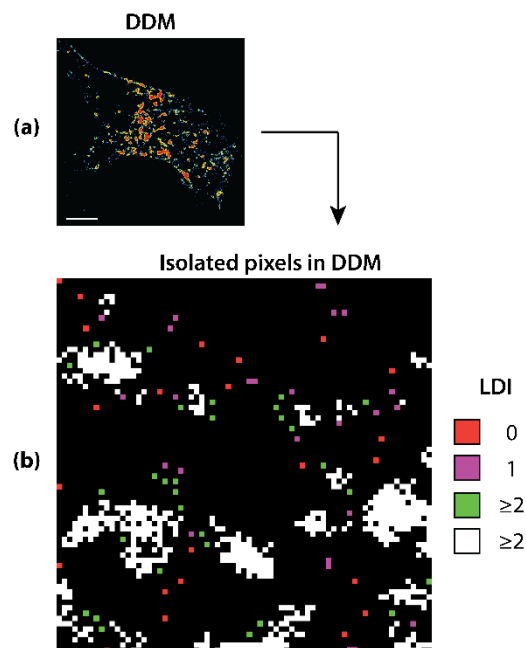


Figure 4.3. DDM mask creation. The acquired image is firstly segmented and the DDM (a) is then created with a 5×5 search window, that is the minimal window size that allows discriminating single pixels based on their locality. (b) Pixels semantics: (1) isolated red pixels, with LDI=0; (2) green pixels, isolated, but not alone in their 5×5 neighbourhood, with LDI ≥ 2 ; (3) either isolated or “end-point” purple pixels, with LDI=1; (4) connected white pixels, with LDI ≥ 2 . Scale bar: 5 μm . Image reproduced from [130] under the CC-BY Creative Commons Attribution 4.0 International licence.

Starting from a grey level input image and after an independent binarization procedure, the DDM is created (Figure 4.3 (a)). Figure 4.3 (b) shows how differently single and isolated pixels are semantically treated in this process. Here, red

isolated pixels are those having LDI=0, while green isolated pixels have LDI=2 or greater, as well as the white ones. Finally, purple pixels, with LDI=1 may be either isolated or “end-point” towards no-density space. Isolated red pixels have no connections with any object in their 5×5 neighbours and are the best candidate to be removed since they do not apparently retain any information. On the contrary, it can be seen that green pixels are isolated, but not alone, suggestive to belong to structured though fragmented objects that should hence be preserved. This is an example of semantic membership assignment of pixels based on their neighbour’s information. As LDI is function of single pixels, the objects can be composed of pixels with different LDI=1, as it happens for all the white pixels. However, with a 5×5 window, aggregates of two pixels can be subject to an uneven behaviour. In fact, depending on whether the aggregate is nearby a structured object or not, they can have one or both pixels with LDI=1, respectively. Nevertheless, if undesirable, this behaviour can be modified with ad-hoc assumptions.

DDM’s search windows for the analysed datasets

For COL7 dataset, a 5×5 search window is chosen for local distribution analysis in the imaged cells, this also permitting to have in COL7-h a halved-size search window (3×3) to perform the same analysis. For MG-63, A549sh/p53 and HeLa datasets, a 3×3 search window is employed for local distribution analysis, since the objects of interest are in the range of few pixels and the smallest window is suited for detection and discrimination of single particles from small aggregation events. For μ CT images, a search window of 29×159 pixels, approximating the real size of the imaged tibial metaphysis [250], is selected.

Assessment of results

Identifying objects for either object counting, or to know their position, represents one of the most grounding steps in biological quantitative imaging. Therefore, we choose object counting to evaluate the ability of our method to identify single structures and, consequently, the effectiveness in characterizing their spatial distribution. Counting is carried out in COL7 segmented images, after a preliminary step needed to remove foreground pixels expectedly due to “noise”

arising from sample preparation and/or acquisition process. Commonly, the denoising methods rely on area-based or connectivity-based thresholding. While the former aims at removing too small (or too big) aggregates, the latter also encodes neighbouring information aiming at preserving connected pixels. Differently, we use our DDMs for a density-based thresholding and compare our counting with those achieved by area-based and connectivity-based thresholding that is, respectively, after removing 1-pixel (*i.e.*, isolated) objects, or keeping pixels with 4-, diagonal- (D-) or 8-connectivity by sequential image opening and closing with same 3×3 SE. The outcome is assessed through statistical metrics, most of all derived from the contingency table. From here on, objects are defined as 8-connected. The number of objects in the original binarized image is used as true reference condition (*i.e.*, ground truth, GT), where condition positives are represented by the number of present objects, whereas condition negatives, in particular the true negatives (TNs), in most detection problems as ours cannot be univocally defined. The object countings performed after density-, area- and connectivity-based processing represent the predicted conditions, that in comparison procedure with the reference image allow distinguishing:

- True Positives (TPs), *i.e.*, the number of detected objects that are also in Im (*hits*)
- False Positives (FPs), *i.e.*, the number of detected objects that are not in Im (Type I errors)
- False Negatives (FNs), *i.e.*, the number of objects in Im that are not detected after processing (*miss*, Type II errors).

Besides TNs that cannot be estimated, also FPs are not detectable, given the subtractive nature of the processing methods being considered. Then, only TP and FN are reported, both in absolute (TP and FN) and percentage (TPR and FNR) form, computed as:

$$TPR \text{ (True Positive Rate)} = \frac{TP}{GT} \times 100 \quad (4.1)$$

$$FNR (False\ Negative\ Rate) = \frac{FN}{GT} \times 100 \quad (4.2)$$

To compare the number of surviving objects in the processed images with the original number in the input image, we check the overlap between the object's mask in denoised image and the original mask through the logical "AND" operator. The overlap by at least one pixel is enough to detect the object as a TP, otherwise it is considered missed (FN). Therefore, only a partial erosion ensures the overlap, and a greater overlap hints at a more conservative method, that preserves more object properties. Therefore, the overlap computed as:

$$Overlap = \frac{\text{number of preserved pixels after processing}}{\text{number of foreground pixels in the reference image}} \times 100 \quad (4.3)$$

becomes itself a quality index suggestive of the efficacy of the method. However, it may happen that the erosion keeps the object, but does not keep its integrity and fragments it. This leads the object to be counted as TP as many times as its number of fragments, yielding a consequent non-complementarity between TPR and FNR (*i.e.*, $TPR+FNR>100$). From the need to quantify such phenomenon we introduce the Stoichiometric Detection Rate (SDR) that, given a 1:*n* stoichiometric rate, is the percentage of *Im* detected objects (*i.e.*, the difference between GT and FN) that at least partly overlap with *n* objects in the processed image. In practice, *n* represents the number of fragments, with $n=1$ pointing out an object kept integer.

In addition, to assess the robustness of the DDM to varying image quality, we compare the informative-ness conveyed by DDMs applied to COL7 and to COL7-h, having a halved resolution, by performing a pattern matching using the normalized cross correlation (NCC).

The MG-63, A549sh/p53 and HeLa datasets are used to exemplify the different benefits of applying DDMs in subcellular distribution analysis, aiming at identifying a discriminant feature (descriptor) of different cell conditions. A visual inspection of DDMs in all datasets suggests us that the LDI percentage (*i.e.*, the ratio between the number of pixels with given LDI and the number of all analysed pixels) could be a suitable descriptor. Nevertheless, in the HeLa dataset, the

number of objects (or better, blobs) composing each density level (weighted by cell area) was also considered, in order to refine the assessment of the spatial gathering of pixels sharing a same LDI.

Finally, the μ CT dataset is used to exemplify the applicability of the method beyond the pure molecular distribution analysis, by using DDM to integrate the image segmentation procedure of tibial metaphyseal trabeculae.

Statistical analysis

Statistical analyses are performed in MATLAB®. Data deviation from normality is early verified by histogram inspection, followed by the Shapiro-Wilk test, based on which the discriminatory power of descriptors is assessed by either two-tail Student's t-test or Wilcoxon rank-sum test. p-values<0.05 were considered for statistical significance.

4.5 Results and discussion

DDMs are effective and robust to quantify spatial distributions

The DDM's capability to increase confidence in spatial distribution measurement is assessed by its application to object detection and counting in comparison with area- and connectivity-based thresholding (Figure 4.4 (a)).

Specifically, starting from a binarized COL7 image (Im): (1), DDM is created and binarized after that isolated pixels (LDI=0) are removed (DDMm); (2) area-based denoising is performed by removing isolated pixels (Im1); (3) 4- (Im2), diagonal- (Im3) and full- (Im4) connectivity-based denoising are carried out by morphological opening and closing (Figure 4.4 (a), the squares with the reference central red pixel). As reported in Table 4.1, DDMm is the image that better approximates the object counting in the original binarized image Im.

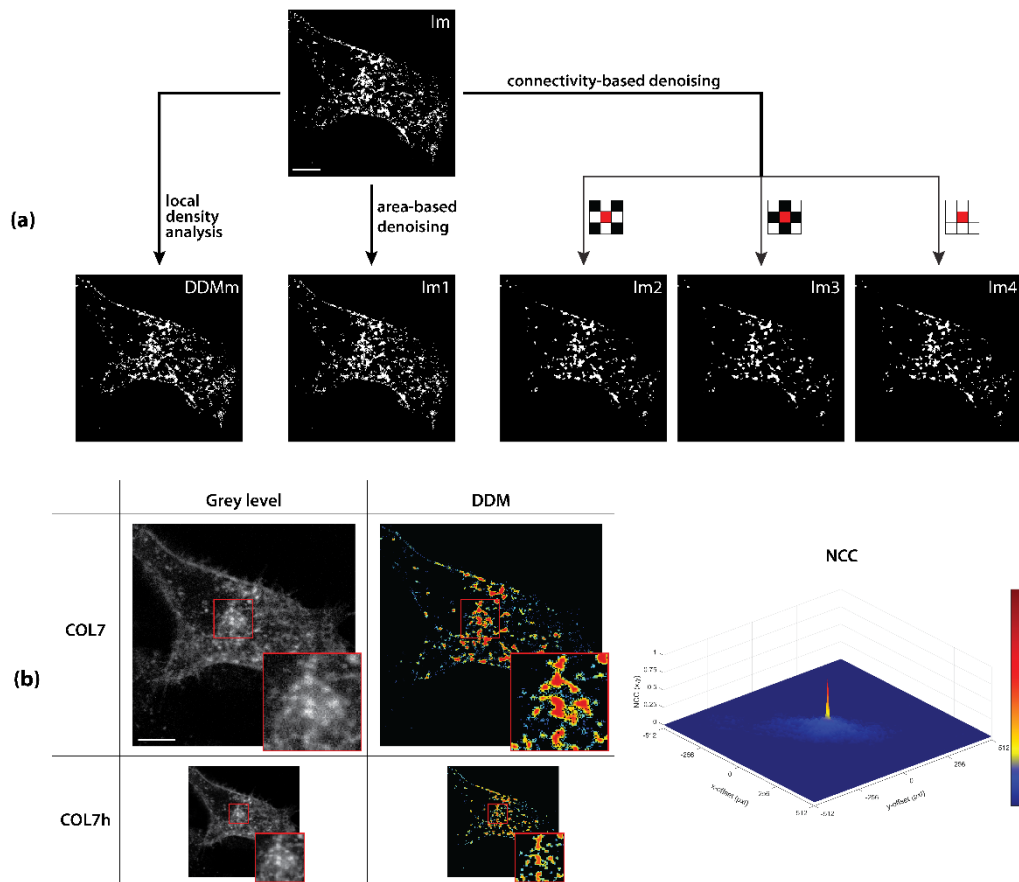


Figure 4.4. DDMs are effective and robust to quantify spatial distributions. (a) After signal binarization, area- (Im1, 1-pixel object removal) or connectivity-based denoising (Im2, Im3 and Im4, 4-, diagonal- and full- connectivity-based denoising, respectively) is performed. (b) The signal accuracy reduction caused by resolution halving of COL7 to COL7-h is better resisted by our method application, as quantified by a maximum NCC coefficient of 0.79 for COL7 and COL7-h DDMs. The colorbar indicates the normalized function values. Scale bars: 5 μm . Image reproduced from [130] under the CC-BY Creative Commons Attribution 4.0 International licence.

Table 4.1. Contingency table for object counting with density-, area- and connectivity-based approach.

Image ¹	TP	FN	TPR (%)	FNR (%)	SDR (%)		Overlap (%)
					1:1	$\geq 1:2$	
DDMm	1089	649	63	37	100	0	95
Im1	614	1124	35	65	100	0	92
Im2	170	1612	10	93	76	24	53
Im3	139	1625	8	93	82	18	51
Im4	94	1666	5	96	78	22	42

¹ Ground Truth (GT)=1738. TP, True Positive; FN, False Negative; TPR, True Positive Rate; FNR, False Negative Rate; SDR, Stoichiometric Rate.

Indeed, it shows by far the highest TPR=63%, and the lowest FNR=37%, accordingly. The non-complementarity of TP and FN in Im2, Im3 and Im4 hints at a fragmentation of Im objects induced by the connectivity-based denoising, as suggested by the 24%, 18% and 22% of objects that are detected with an in-correct (*i.e.*, $\geq 1:2$) SDR in these images, respectively (Table 4.2).

Table 4.2. Stoichiometric detection rate for object counting with density-, area- and connectivity-based approach.

Image ¹	Denoising principle	GT - FN	SDR (%)				
			1:1	1:2	1:3	1:4	1:5
DDMm	pixel density	1089	1089 (100)	-	-	-	-
Im1	object area	614	614 (100)	-	-	-	-
Im2	4-conn	126	96 (76)	19 (15)	8 (6)	3 (3)	-
Im3	D-conn	113	93 (82)	16 (14)	3 (3)	-	1 (1)
Im4	8-conn	72	57 (79)	10 (14)	3 (5)	2 (3)	-

¹ Ground Truth (GT)=1738. FN, False Negative; SDR, Stoichiometric Detection Rate.

On the contrary, neither the area-based nor our method fragment the objects. Finally, DDMm shows the highest overlap (*i.e.*, the best match) with Im (Table 4.1), this suggesting a better accuracy in estimating position and object extension. It is worth noting that the overlap difference between DDMm and Im1 is attributable to the 1-pixel objects that, being isolated but not alone, are discarded in the latter, but not in the former. In conclusion, the behaviour of the considered denoising methods can be summarized as following in Table 4.3:

Table 4.3. Comparison of density-, area- and connectivity-based approach effects on objects erosion during detection.

Denoising principle	Can cause objects:		
	partial erosion	complete erosion (removal)	fragmentation
Pixel density	Yes	Yes	No
Object area	No	Yes	No
Pixel connectivity	Yes	Yes	Yes

Finally, we use the NCC to perform a pattern matching between each analysed image and its half-resolved counterpart (Figure 4.4 (b) and Table 4.4). While the best result is in the presence of downsampling only (NCC=0.96, that is, 4% information loss), DDMm retains the highest correlation between results achieved at full and half resolution (NCC=0.79), meaning that it shows the highest robustness against resolution reduction.

Table 4.4. Comparison between COL7 and COL7-h.

Image ¹	NCC
Im	0.96
DDMm	0.79
Im1	0.75
Im2	0.73
Im3	0.75
Im4	0.71

¹ Abbreviation list: NCC, Normalized Cross Correlation.

For all these reasons, DDMm represents the best option for object detection, and consequently for distribution analysis, as it minimizes FN, maximizes TP and the object detection with correct stoichiometry. Therefore, our method can be preliminary considered also as an effective denoising procedure in itself that, besides retaining objects on the basis of their connectivity, can even keep the most informative ones on the grounds of their local density. More importantly, this reinforcement of each pixel position by exploiting information from surroundings makes our method to be the most robust to resolution variation. This means that, independently of the resolution of the acquisition device, our method can effectively improve the informativeness of the distribution analysis.

DDMs disclose hidden distribution properties

This example shows how to use local density information to strengthen ordinary analyses. Figure 4.5 addresses the MTs resolving in confocal images of

MG-63 cells exposed to Paclitaxel-loaded nanoparticles (PTX-Ce6@ker_{ag}) (Figure 4.5 (a)) [245].

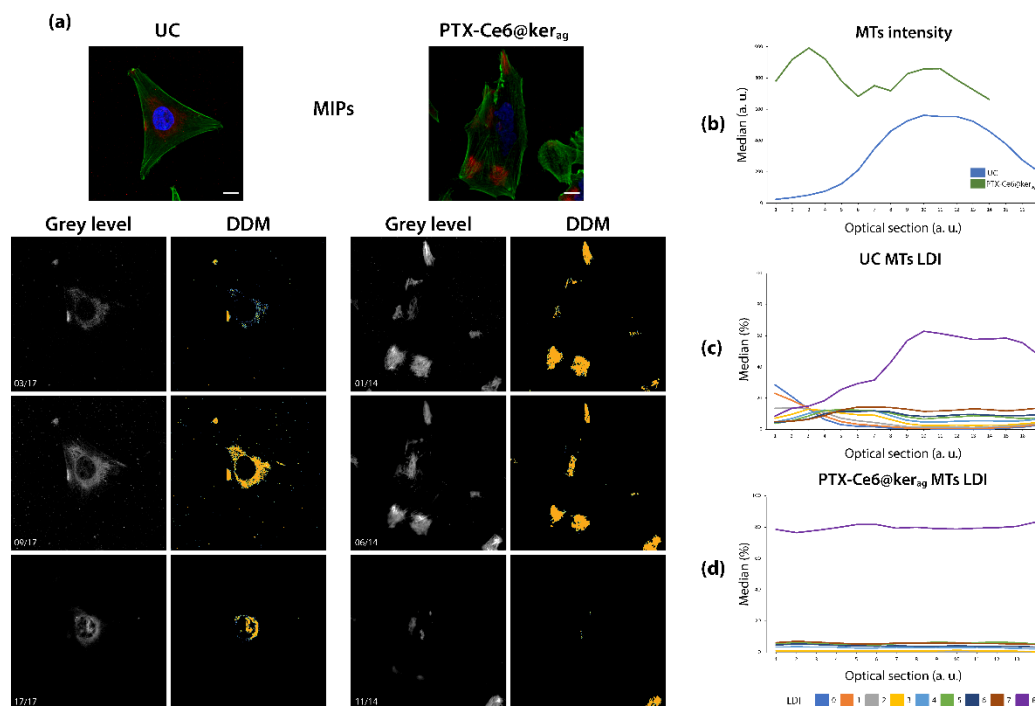


Figure 4.5. DDMs disclose hidden distribution properties. (a) Top: RGB MIPs of MG-63 untreated (left) or exposed to PTX-Ce6@ker_{ag} nanoparticles (right) cells, stained for DNA (blue) and actin (green), and immunolabeled against β -tubulin (red). Bottom: exemplificative optical sections (left) and DDMs (right) of β -tubulin signal distribution along Z-axis. Line plots of MTs median intensity (b) and percentage LDI distribution in UC (c) and PTX-treated cells (d) along the Z-axis. In PTX presence, MTs are brighter (+126% on average, $p < 10^{-5}$), denser (+69%, on average, $p < 10^{-5}$) and more present at a high density through the sections (average CV through sections for LDI=8: 0.02). Scale bars: 10 μ m. Image reproduced from [130] under the CC-BY Creative Commons Attribution 4.0 International licence.

As Paclitaxel (PTX) is expected to suppress MTs dynamic instability [251], the MTs signal is investigated through the optical sections. For visualization purposes, confocal sections are summarized in MIPs (Figure 4.5 (a), top colour images). By comparing untreated control (left) and PTX-treated (right) cells, a different subcellular location and intensity of MTs (red) can be noticed. This visual consideration still holds for single optical sections (grey level images, bottom left) and it is supported by MTs intensity quantification (Figure 4.5 (b): median intensity in treated cells greater than 126%, $p < 10^{-5}$, Table 4.5.

Table 4.5. Median MTs intensity in MG-63 cells.

Optical section	Median intensity \pm MAD	
	UC (n=17)	PTX-Ce6@-ker _{ag} (n=14)
1	24.0 \pm 5.00	782 \pm 197
2	36.0 \pm 8.00	918 \pm 233
3	53.0 \pm 11.0	991 \pm 250
4	76.0 \pm 17.0	920 \pm 236
5	123 \pm 27.0	781 \pm 193
6	210 \pm 46.0	683 \pm 163
7	347 \pm 76.0	752 \pm 195
8	460 \pm 105	717 \pm 180
9	525 \pm 128	828 \pm 216
10	563 \pm 143	857 \pm 236
11	555 \pm 148	862 \pm 237
12	553 \pm 147	789 \pm 214
13	524 \pm 141	726 \pm 198
14	460 \pm 124	663 \pm 181
15	377 \pm 103	-
16	277 \pm 72.0	-
17	199 \pm 50.0	-

Coefficient of variation (CV) through sections: 0.55 (UC), 0.44 (PTX)). However, local density analysis of MTs in single sections discloses a hidden aspect of the distribution. Indeed, the line plots of LDI percentage in UC (Figure 4.5 (c)) show a marked presence of the highest LDI=8 and a reduced presence of LDI between 0 and 7, which are also more stable through the optical sections (average CV=0.70). After PTX delivery (Figure 4.5 (d)), the presence of all LDI becomes constant through sections (average CV=0.15) and, most important, LDI=8 becomes nearly exclusive and the remaining LDIs almost disappear, since the former significantly increases (+69%, $p < 10^{-5}$), while the latter decrease (-68% on average, always $p < 10^{-3}$, Table 4.6). The predominant LDI=8 presence could be ascribed to the dense and crystallized MTs appearance induced by high PTX concentration [252]. Together with LDI=8 constant presence throughout optical sections, this finding suggests that Ce6@ker_{ag}-mediated PTX delivery is probably even more efficient

than what reported by the authors themselves, hence highlighting the prominence of such a delivery system for clinical application.

Table 4.6. Statistical analysis of MTs LDI percentage in MG-63 cells.

LDI	Median percentage (%) \pm MAD		p-value (≤ 0.05)
	UC (n=17)	PTX-Ce6@-ker _{ag} (n=14)	
0	1.40 \pm 0.96	0.05 \pm 0.01	$<10^{-5}$
1	2.15 \pm 1.26	0.10 \pm 0.02	$<10^{-5}$
2	3.01 \pm 1.53	0.31 \pm 0.03	$<10^{-5}$
3	4.54 \pm 1.87	0.96 \pm 0.06	$<10^{-5}$
4	5.94 \pm 1.05	3.13 \pm 0.16	$<10^{-5}$
5	8.15 \pm 1.08	5.88 \pm 0.38	$<10^{-3}$
6	9.27 \pm 0.79	4.07 \pm 0.16	$<10^{-5}$
7	12.4 \pm 0.79	5.84 \pm 0.33	$<10^{-3}$
8	47.1 \pm 14.2	79.5 \pm 0.84	$<10^{-5}$

DDMs can capture relevant spatial distributions blind to visual inspection

This example is probably the most effective showing how the hidden information disclosed and quantified by DDMs can provide added knowledge. Figure 4.6 reports A549sh/p53 UC cells or subject to γ irradiation (2 Gy), marked against RNA:DNA hybrids to assess how their subcellular distribution varies in response to treatment. An earlier image comparison between irradiated and non-irradiated cells (Figure 4.6 (a), left) suggests that hybrids differently redistribute in cytoplasm and nucleus after cell irradiation, displaying the emptying of nucleus and a pan-cytoplasmic dispersion of hybrids. However, DDMs computation (Figure 4.6 (a), centre) unveils that what appeared as an uninteresting cytoplasmic redistribution unexpectedly consists of an accumulation of hybrids in what looks like a cytoplasmic perinuclear ring, that after nuclear boundary segmentation results to lie inside the organelle (Figure 4.6 (a), magnification, right).

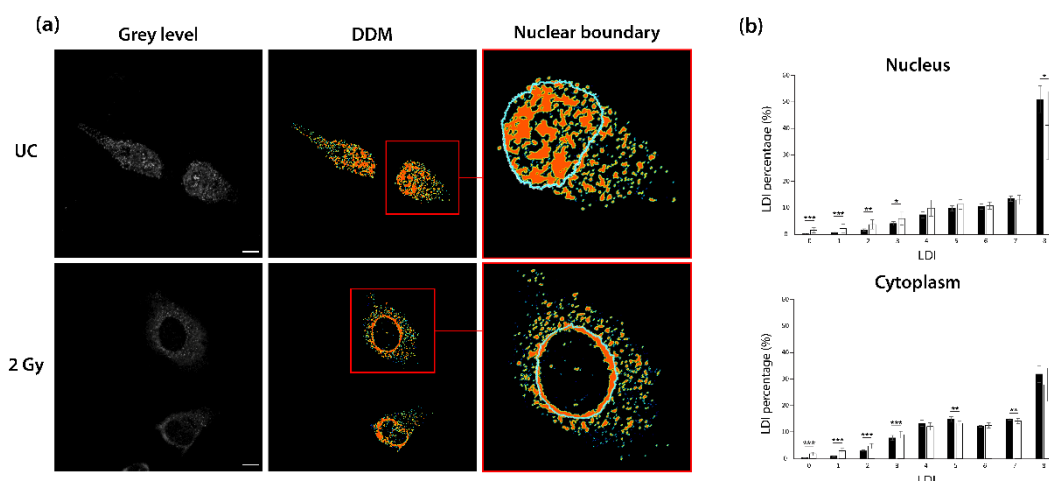


Figure 4.6. DDMs can capture relevant spatial distributions blind to visual inspection. (a) Grey level images of untreated and 2-Gy irradiated A549sh/p53 cells are used to compute DDMs for immunostained RNA:DNA hybrids. DDMs highlight a perinuclear hybrids crowding inside the nucleus of 2-Gy irradiated cells. (b) Bar graphs of LDI percentages in the main cell compartments. A549sh/p53 2-Gy irradiation induces hybrids de-condensation in both nucleus and cytoplasm, although with a slightly different magnitude. * $p < 0.05$; ** $p < 0.01$; *** $p < 0.001$. Scale bars: $10 \mu\text{m}$. Image reproduced from [130] under the CC-BY Creative Commons Attribution 4.0 International licence.

DDMs analysis allows quantifying a significant increase in both cell nucleus and cytoplasm of low LDI percentages (LDI=0-3 {0,1,2,3}, $p < 10^{-4}$), coupled with a symmetric decrease in high LDI percentages (LDI={5,7}, $p < 0.006$ in cytoplasm and LDI=8, $p = 0.012$ in nucleus, Figure 4.6 (b) and Table 4.7).

Table 4.7. Statistical analysis of hybrids LDI percentage in A549sh/p53 cells.

LDI	Nucleus			Cytoplasm		
	Median percentage (%) \pm MAD			Median percentage (%) \pm MAD		
	UC (n=14)	2 Gy (n=14)	p-value (<0.05)	UC (n=14)	2 Gy (n=14)	p-value (<0.05)
0	0.32 \pm 0.13	1.63 \pm 0.97	$<10^{-4}$	0.44 \pm 0.12	1.86 \pm 0.60	$<10^{-5}$
1	0.88 \pm 0.26	2.39 \pm 1.65	$<10^{-3}$	0.95 \pm 0.28	3.02 \pm 0.87	$<10^{-5}$
2	1.81 \pm 0.42	3.84 \pm 1.74	$<10^{-2}$	2.89 \pm 0.40	4.79 \pm 0.93	$<10^{-5}$
3	4.24 \pm 0.73	6.07 \pm 2.45	0.02	7.85 \pm 0.98	9.06 \pm 1.29	0.05
4	7.50 \pm 1.11	10.0 \pm 3.01	0.08	13.4 \pm 1.17	12.1 \pm 1.42	0.07
5	9.91 \pm 1.05	11.5 \pm 1.83	0.05	14.9 \pm 0.89	13.4 \pm 0.95	$<10^{-2}$
6	10.6 \pm 1.03	11.0 \pm 1.37	0.30	12.2 \pm 0.38	12.6 \pm 1.03	0.73
7	13.6 \pm 1.02	13.1 \pm 1.71	0.80	15.0 \pm 0.38	14.2 \pm 0.99	$<10^{-2}$
8	51.1 \pm 5.05	41.3 \pm 12.7	0.01	32.0 \pm 3.14	28.0 \pm 6.29	0.07

This means that 2-Gy irradiation leads to a hybrids de-condensation in both compartments, more heavily in cell nucleus, where the decrease involves higher density levels. Although this evidence would seem to disagree with the clear perinuclear hybrids crowding at 2 Gy, the de-condensation regards the whole cellular compartments, while the hybrid accumulation occurs at the sub-regional level. Notably, we can conclude that, despite the significant changes in LDI percentages, a 2 Gy irradiation can be said to peculiarly affects hybrids subcellular location, rather than aggregation state and density, accordingly. Such strong hybrids redistribution after treatment was not imaginable before applying DDMs. This finding highlights the need of local processing and the importance of DDMs to convey both quantitative and visual information, which have to be considered together to assist researchers in capturing the complexity of phenomena.

DDMs can detect and quantify sample heterogeneity

This example shows how DDMs can be used to disclose and discriminate subsamples by the local density distribution of marked structures.

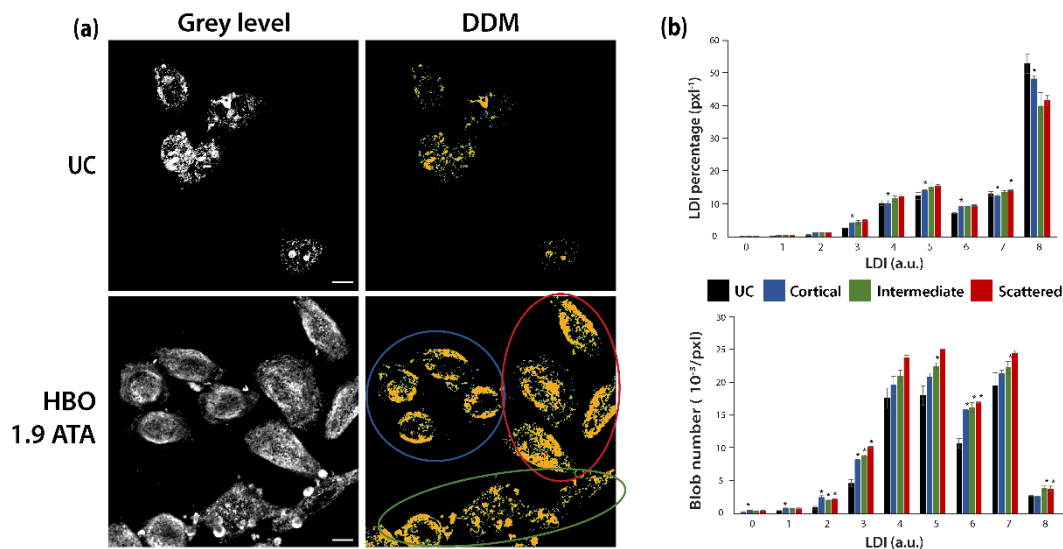


Figure 4.7. DDMs can detect and quantify sample heterogeneity. (a) Grey level images and DDMs of untreated (UC) and 1.9 ATA HBO-treated HeLa cells marked against RNA:DNA hybrids. DDMs separate three cell groups of cortical (blue), scattered (red) and intermediate (green) hybrids distributions among HBO-treated cells. (b) Bar graphs of LDI percentages and derived blob number in HeLa cells. * $p < 0.05$; ** $p < 0.01$; *** $p < 0.001$ for statistical comparison of the three groups with the untreated control. Scale bars: 10 μm . Image reproduced from [130] under the CC-BY Creative Commons Attribution 4.0 International licence.

Figure 4.7 reports HeLa cells exposed (HBO 1.9 ATA) or not (UC) to hyperbaric oxygen conditions and marked against RNA:DNA hybrids to assess their subcellular distribution variation in response to such stressing condition. Visual inspection of acquired images (Figure 4.7 (a)) suggests a difference in hybrids signal intensity and distribution between treated and untreated cells. This difference is confirmed and stressed by DDMs, which moreover disclose a heterogeneous hybrids subcellular distribution among HBO-treated cells, identifying three cell subgroups characterized by a cortical, scattered, and intermediate distribution, respectively (Figure 4.7 (a), coloured annotations). DDMs creation permits to differentiate the three distributions by both LDI percentage and number of blobs (Figure 4.7 (b) and Tables 4.8 and 4.9), where the latter varies more than the former, meaning that the groups are not so much characterized by different densities as they differ in the way the densities are spatially distributed.

Table 4.8. Median hybrids LDI percentage and blobs number in HeLa cells.

LDI	Median percentage (%) \pm MAD				(Median blob number (pixel ⁻¹) \pm MAD) $\cdot 10^{-3}$			
	UC (n=5)	Cortical (n=4)	Intermediate (n=3)	Scattered (n=3)	UC (n=5)	Cortical (n=4)	Intermediate (n=3)	Scattered (n=3)
0	0.06 \pm 0.03	0.20 \pm 0.03	0.15 \pm 0.01	0.16 \pm 0.04	0.11 \pm 0.05	0.44 \pm 0.07	0.32 \pm 0.01	0.36 \pm 0.08
1	0.30 \pm 0.04	0.51 \pm 0.03	0.49 \pm 0.02	0.48 \pm 0.01	0.38 \pm 0.01	0.76 \pm 0.04	0.67 \pm 0.05	0.67 \pm 0.14
2	0.58 \pm 0.10	1.27 \pm 0.11	1.18 \pm 0.05	1.25 \pm 0.05	0.85 \pm 0.20	2.43 \pm 0.24	1.99 \pm 0.13	2.15 \pm 0.05
3	2.62 \pm 0.14	4.21 \pm 0.17	4.50 \pm 0.56	5.01 \pm 0.29	4.57 \pm 0.55	8.12 \pm 0.07	8.75 \pm 0.20	10.10 \pm 0.12
4	10.30 \pm 0.78	10.30 \pm 0.75	11.70 \pm 0.78	12.40 \pm 0.57	17.6 \pm 1.54	19.60 \pm 1.34	21.00 \pm 0.88	23.80 \pm 0.38
5	12.50 \pm 1.02	14.10 \pm 0.32	15.30 \pm 1.12	15.64 \pm 0.44	18.00 \pm 1.46	20.90 \pm 0.51	22.50 \pm 0.52	25.00 \pm 0.08
6	7.26 \pm 0.16	9.12 \pm 0.25	9.24 \pm 0.07	9.51 \pm 0.26	10.70 \pm 0.77	15.80 \pm 0.09	16.20 \pm 0.76	16.90 \pm 0.13
7	13.20 \pm 0.58	12.60 \pm 0.32	13.50 \pm 0.56	14.28 \pm 0.14	19.50 \pm 1.99	21.40 \pm 0.49	22.30 \pm 0.96	24.50 \pm 0.41
8	53.00 \pm 2.99	48.3 \pm 1.05	40.00 \pm 4.11	41.68 \pm 1.70	2.63 \pm 0.10	2.54 \pm 0.08	3.79 \pm 0.36	3.71 \pm 0.44

Table 4.9. Statistical analysis of hybrids LDI percentage and blob number in HeLa cells.

LDI	p-value (<0.05)							
	LDI percentage (%)				Blob number (pixel ⁻¹)			
	UC- All	UC- Cortical	UC- Intermediate	UC- Scattered	UC- All	UC- Cortical	UC- Intermediate	UC- Scattered
0	<u>0.01</u>	<u>0.02</u>	0.14	0.14	0.26	0.19	0.99	0.32
1	<u><10⁻²</u>	<u>0.02</u>	0.14	0.07	0.24	0.22	0.50	0.68
2	<u><10⁻²</u>	<u>0.02</u>	<u>0.04</u>	<u>0.04</u>	0.38	0.76	0.79	0.25
3	<u><10⁻²</u>	<u>0.02</u>	<u>0.04</u>	<u>0.03</u>	0.37	<u>0.03</u>	0.57	0.39
4	0.31	0.73	0.25	0.07	<u>0.01</u>	<u>0.02</u>	0.07	0.25
5	<u>0.03</u>	0.41	0.07	<u>0.04</u>	<u>0.01</u>	<u>0.02</u>	0.07	0.25
6	<u><10⁻²</u>	<u>0.02</u>	<u>0.04</u>	<u>0.04</u>	<u>0.03</u>	<u>0.02</u>	0.07	0.79
7	0.31	0.90	0.57	<u>0.04</u>	<u><10⁻²</u>	<u>0.02</u>	<u>0.04</u>	0.07
8	<u><10⁻²</u>	0.06	<u>0.04</u>	<u>0.04</u>	<u>0.01</u>	<u>0.02</u>	0.07	0.29

When grouping all HBO-treated cells together, this heterogeneity results in a higher variance in spite of the increased number of samples (Table 4.10), with consequent weakening of statistical comparison between treated and control group [253].

Table 4.10. Variance of hybrids LDI percentage and blob number in HeLa cells.

LDI	Variance							
	LDI percentage (%)				Blob number (pixel ⁻¹) · 10 ⁻⁷			
	All (n=10)	Cortical (n=4)	Intermediate (n=3)	Scattered (n=3)	All (n=10)	Cortical (n=4)	Intermediate (n=3)	Scattered (n=3)
0	0.003	0.002	0.002	0.004	0.15	0.09	0.10	0.17
1	0.01	0.002	0.01	0.01	0.09	0.05	0.03	0.22
2	0.03	0.05	0.04	0.03	1.23	1.94	0.24	0.66
3	0.32	0.14	0.67	0.10	11.2	3.16	14.6	3.02
4	1.44	0.89	1.02	0.40	41.1	29.7	9.36	16.4
5	1.48	0.35	2.61	0.50	35.4	30.9	21.3	11.5
6	0.12	0.21	0.05	0.08	7.38	6.58	10.5	1.88
7	0.76	0.75	0.67	0.04	21.0	16.2	10.4	9.06
8	15.8	9.85	21.4	4.94	4.42	2.17	3.19	2.08

In conclusion, in this case DDMs provide some unprecedented information. First, they indicate that the sample may be not large enough to account for the heterogeneity of the entire population, and that a careful outliers detection and removal is needed before data analysis. Second, DDMs reveal that cells of a same subgroup are spatially gathered, thus raising doubts on the homogeneity of the created hyperoxic environment and suggesting new experiments, under strictly controlled conditions, also aiming at investigating the dependence of hybrids distribution on the oxygen concentration. At the end, independently of the sample heterogeneity, DDMs already reveal that hyperbaric conditions induce a redistribution of hybrids and a change in their condensation state.

DDMs can apply beyond distribution analysis

In the previous paragraphs, we showed how DDMs can reinforce, supplement or disclose distribution information. However, applicability of DDMs extends beyond distribution analysis in microscopy cell imaging, for instance, to improve image segmentation procedures. Figure 4.8 describes the main steps of the automated segmentation of metaphyseal trabeculae from a *Mus musculus* tibiae in μ CT images (Figure 4.8 (a) and Chapter 7), that involves local density analysis.

First, the image contrast is enhanced by 8-bit conversion (Figure 4.8 (b)) and adaptive histogram equalization (Figure 4.8 (c)). Then, a top hat filtering of the image (Figure 4.8 (d)) with proper SE (*i.e.*, with dimension comparable to that of trabeculae to be segmented) permits to retain local intensity peaks (corresponding to more mineralized structures), while disregarding irrelevant pixels with low values (corresponding to bone cavities). As this procedure well identifies metaphyseal trabeculae, it also includes unwanted information from other bone structures. To isolate metaphyseal trabeculae, local density analysis can be used with denoising purpose, when selecting an appropriate local window size (*i.e.*, with dimension comparable to that of metaphysis to be segmented). This way, the resulting DDM (Figure 4.8 (e)) permits to distinguish metaphysis trabeculae as the denser mineralized structures, and to exploit this information to segment them (Figure 4.8 (f)).

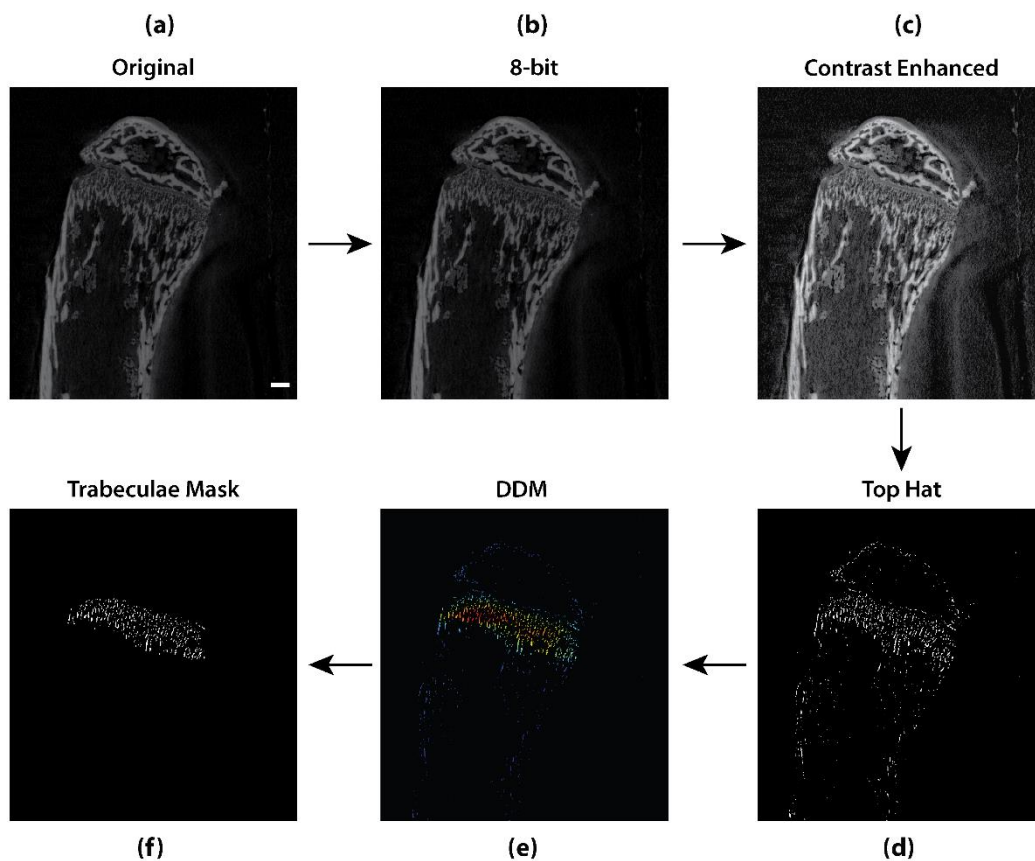


Figure 4.8. DDMs application to image segmentation. DDMs can be applied beyond distribution analysis in microscopy imaging: here, the segmentation of metaphyseal trabeculae in μ CT (coronal) images of *Mus musculus* tibiae. The acquired image (a) is 8-bit converted for denoising purposes (b), contrast-enhanced by local adaptive histogram equalization (c) and top hat-filtered for the segmentation of local intensity peaks (d). This procedure well detects metaphyseal trabeculae, but also includes less dense signal from other bone structures. DDMs (e) permit to discriminate metaphyseal trabeculae as the denser local peaks in the image, and accordingly to segment them based on their local density (f). Scale bar: 200 μ m. Image reproduced from [130] under the CC-BY Creative Commons Attribution 4.0 International licence.

GUI for DDMs creation

To allow users, even with basic skills, to build DDMs we supply *DDMaker* (Figure 4.9), a software program endowed with a user-friendly GUI, created with MATLAB® App Designer, which does not require any training or expertise before using.

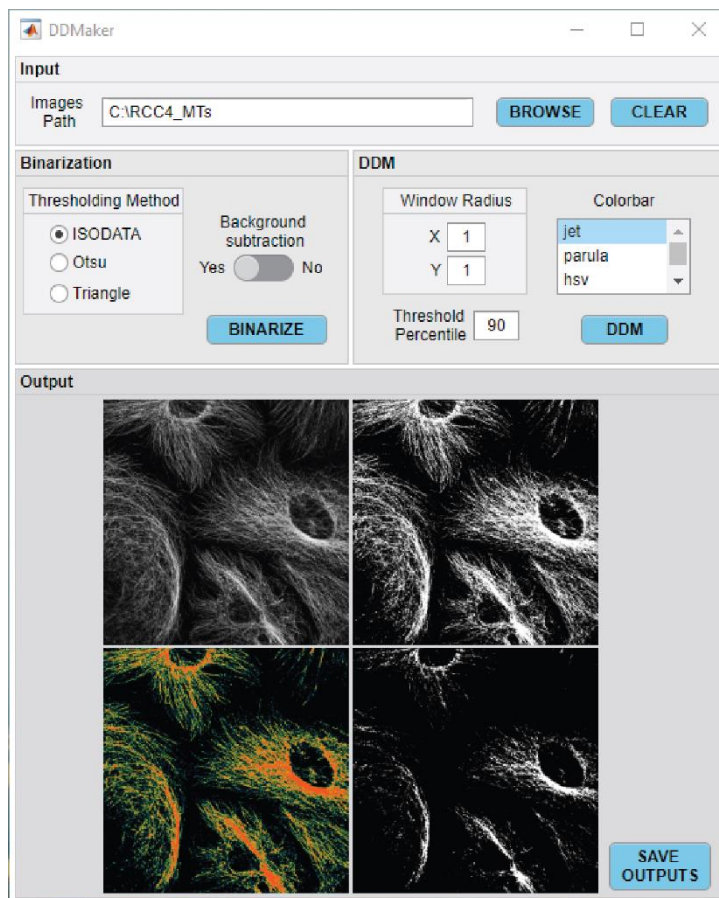


Figure 4.9. Main GUI and logo of DDMaker. The main window is divided into four sections: *Input*: to select the input images' folder; *Binarization*: to select the thresholding method, choosing whether considering zero-values subtraction before threshold calculation and performing image binarization; *DDM*: to select the half-sides of the search window for locality analysis and, to allow user creating and binarizing DDMs after setting, the colorbar for DDMs visualization in pseudo-colour and the percentile for DDMs thresholding; *Output*: to visualize and save intermediates and outputs. From left to right, top to bottom: grey level input image, binary mask, pseudo-colour DDM, binarized DDM. Image reproduced from [130] under the CC-BY Creative Commons Attribution 4.0 International licence.

In few steps, the software permits to customize the search window size and to create the DDMs either directly, starting from binary images, or indirectly, from RGB or grey level images, thanks to a dedicated module for image binarization. First, the user is required to select the folder where the input images to be processed are located. The folder can either contain RGB colour, grey level or binary images in the MATLAB-supported formats [254], including uncompressed ".tiff". In the first two cases, the user can binarize the images by choosing among

ISODATA, Otsu or Triangle thresholding methods, excluding or not background values (*i.e.*, zero-value pixels) from threshold calculation. The basic assumption regarding input images is that they are properly acquired, corrected for eventual vignetting distortion [177], and minimally affected by photobleaching degradation [180] (Subsect. 3.2.4). The resulting binary masks serve as the input for building DDMs. However, if users already have their own binary masks to be provided as the input, the segmentation step is skipped and DDMs are directly created starting from user's masks. The default search window defining the locality of the analysis is a 3 pixels-sided square, chosen assuming that the target structures of interest in the images are of few pixels, thus enabling the detection of small aggregation events and single particles as well. However, users can customize the search window size.

Moreover, DDMaker allows visualizing the derived DDMs with customizable colorbar, and to perform an original DDM's percentile thresholding, thus enabling the input image segmentation by mean of local density. For user's convenience, DDMaker also displays the last input image, the corresponding binary mask, and the derived DDM and DDM's mask. The user can finally save all the intermediate analysis as well as the outputs as uncompressed images and portable csv and excel files.

The software builds DDMs and save all data from few seconds to minutes on entry-level computers (*e.g.*, a dataset of one hundred grey level images is fully processed in a little more than one min on a PC endowed with Intel i3-4005U, 1.70 GHz processor, and 8 GB RAM). The simplicity in creating and interpreting DDMs, jointly with their effectiveness, make DDMaker a valuable tool for fast assessment of target distributions. All considered, DDMaker and DDMs could serve as a crucial checkpoint for long-lasting experiments, as well as for follow-up and large-scale studies, that can be monitored on-line and corrected in progress, or even stopped, based on the continuous feedback by DDMs. It is worth noting that this allows optimizing time and costs by adjusting or rapidly restarting experiments that would otherwise have been discarded, just after ending. DDMaker is available as a public open-source software written in MATLAB® and as a 64-bit stand-alone application [255].

4.6 Conclusions

In this Chapter, we have presented an innovative method for subcellular distribution analysis, able to semantically quantify the local density of pixels, summarize it as the Local Density Index, and finally exploit it to build a Density Distribution Map in pseudo-colours, to prompt visual survey of the distributions. The local density descriptor also provides foundation for a wise denoising, where importance and necessity for signal preservation is not restricted to connectivity only. Finally, being based on local analysis, DDMs use leads to a more accurate estimation of molecules position, and increased robustness to resolution variations, if compared with the standard approaches. This allows DDMs to characterize and quantify both evident and hidden subcellular distribution, thus opening to the formulation of new biological considerations. As such, DDMs appear as an innovative enabling tool to supplement intensity analysis even for visual assessment, besides quantification of signal distribution. In addition, our method can be used for density-driven segmentation, which allows a good identification of small and thin morphological structures, like in the μ CT images, that otherwise would have been merged. Finally, it is worth noting that as a resolution-independent technique enhancing the detection of native information DDMs can also benefit high-resolution technologies.

DDMs computation is within every user's reach with the DDMaker software we provide. The immediacy of DDMs creation, besides the exemplifying applications herein considered, allows DDMs to be employed in continuous monitoring routine and large-scale experiments, planning and progression of explorative investigations as for example in the study of cancer cell biology. In particular, DDMs analysis permits to detect heterogeneous responses to treatment in cell sub-populations, improving clinical drug development and with the potential to impact decisively on medicine in general and on oncology in particular.

As regards the limitations, the first is that DDMs can be applied to binary images only, although this is intrinsically due to the design of the method itself. The second limitation is that, for this reason, DDMs require that previous image

acquisition and segmentation steps have been properly carried on. For this reason, DDMaker is also endowed with a segmentation module.

4.7 Content-aware contribution and future developments

Many steps of this work benefitted of interdisciplinarity and a content-aware approach. Thanks to my double formation, I could first analyse both the biological and technical properties of my data, understanding what was keeping me to measure my objects (*i.e.*, RNA:DNA hybrids) distribution with a biologically significant accuracy. RNA:DNA hybrids can indeed range from few base pairs to more than 50 [256], and easily fall below the resolution limit of an optical microscope. Also, no prior knowledge about their aggregation state in the main cell compartments is available. On the contrary, under the hypothesis of their exportation from cells [257], their aggregation state should be deemed as informative and worthy of investigation. Therefore, even if detected as small, fragmented and disconnected, such objects should be retained, and their connectivity investigated.

Then, recognizing the inadequacy of pure signal location for the characterization of such object distribution, I could proficiently navigate the literature and understand that what is here needed was not available to the biologist. No measure of local density was being made whatsoever, and spatial distribution was investigated in the field at best with pseudo-colour localization maps, that facilitate the molecules position visualization, but add no real information about sparse distribution, as the one we were investigating.

Finally, and greatly, my double formation shaped the conceiving of the local density analysis method and the creation of the GUI for its aided execution. Thanks to an interdisciplinary approach, I was able to develop a method that is robust, effective, and yet provides a measure that is easily and straightforwardly interpretable from a biological point of view. Also, the method is supported by a software tool that can be installed on any laboratory computer without requiring any particular computational power or skills, that can be used in an intuitive way to easily obtain a biologically relevant result. In practice, being a biologist allowed

me to create the tool in the most biologist-friendly way I could, just as the tool I wish I had for myself before this PhD.

As what concern method future development, an issue that necessarily remain to be addressed is the photobleaching contribution to the subcellular distribution quantification. Most of subcellular species distribution studies indeed rely on fluorescence microscopy, where the use of fluorescent markers permits to selectively visualize the structures of interest. However, photobleaching is a degradative problem that always affect this microscopy modality (Sect. 3.2.4). While its contribution can never be completely avoided, it can be minimized by proper experimental procedures and even corrected in post-processing, after the characterization of the signal degradation function [177, 258]. Photobleaching is a function of time, meaning that it affects not only the reliability of signal intensity quantification, but also the execution of follow up experiments, including signal tracking.

Since photobleaching affects signal intensity but not signal structure, our method, being based on local density, is expected to be (almost) photobleaching insensitive. If we assume the absence of space artefacts in the image (*e.g.*, vignetting effect, Sect. 3.2.4), all image pixels intensities are comparably lowered by photobleaching, meaning that the image histogram will then be shifted, but not reshaped. Therefore, even if we apply histogram-based methods for binarizing the signal, the threshold would just be shifted down, and the definition of the foreground not significantly changed. Although compelling, this development has been so far left upstaged (but not forgot) because of the lack of a proper dataset for its demonstration.

Chapter 5

Co-Density Distribution Maps for advanced molecule colocalization and co-distribution analysis

In the previous Chapter we discussed the *DDM method*, developed for the analysis of the spatial distribution of single signals in bidimensional images. Here, we expand the DDM method to the analysis of the spatial distribution of signal *couples*. The resulting *cDDM method* permits to advance current colocalization analysis by introducing co-density distribution maps (cDDMs), which uniquely provide information about molecules absolute and relative position and local abundance. Also in this case, the method has been made available to the scientific community as an open-source software tool, *cDDMaker* [205].

Following the previous Chapter structure, context and motivations for the cDDM method conceiving and design is firstly introduced (Sect. 5.1), and its theoretical bases discussed from both a biological and image processing point of view (Sect. 5.2). Then, after surveying the method state of the art (Sect. 5.3), the method properties, innovation, and convenience to real biomedical problems are discussed and exemplified (Sects. 5.4 – 5.6). Finally, the contribution of the content-aware approach to the study is discussed, together with future perspectives (Sect. 5.7).

5.1 Study context

As the DDM method, the cDDM method arises in the framework PHENOMICS Project carried out in collaboration with the Radiobiomics and Drug Discovery

Unit of the IRCCS-IRST (Meldola, FC). The Phenomics project firstly involved the characterization of RNA:DNA hybrids (Chapter 6) through confocal fluorescent microscopy (Subsect. 3.2.3) in A549 cells (Subsect. 2.1.1), under the hypothesis of their involvement in the cell response to stress. However, given the small size of the imaged structures and the necessity to reliably locate their position, particularly affected by tested conditions, we developed the DDM method, mapping RNA:DNA hybrids by Density Distribution Maps. A second study hypothesis concerned the possibility for RNA:DNA hybrids to act as stress-induced second messengers, to be released by irradiated cells through CD63 positive extracellular vesicles (CD63+ EVs) to promote a senescent microenvironment. Therefore, we aimed at characterizing also the subcellular distribution of EVs, in A549 cells marked against RNA:DNA hybrids and the protein CD63 and imaged by confocal fluorescent microscopy, in order to compare the two species distributions and infer their colocalization as an indication of hybrids loading into EVs. However, as RNA:DNA hybrids, EVs can be smaller than the best resolution achievable by an optical microscope [259]. Therefore, their subcellular position, eventual aggregation, and colocalization with RNA:DNA hybrids especially, can hardly be estimated with a biologically meaningful certainty using this imaging modality. For this reason, CD63 signal also needed to be mapped with the help of DDMs, that working locally can improve the certainty of signal mapping. However, to compare RNA:DNA hybrids and CD63+ EVs distributions we would then need a method to compare two DDMs to each other, to gain information about the two structures local co-density. We therefore developed the cDDM method that, starting from two signals defined over the same bidimensional domain, first maps their single distributions through the DDM method, and then pixel-wise compare the resulting DDMs to create a co-Density Distribution Map (cDDM), which quantifies the local density, co-density and colocalization of the two signals.

5.2 Theoretical background

5.2.1 Image arithmetic and morphology

Image colocalization is by definition a matter of signals co-occurrence. This brings that, regardless of how we decide to quantify it, the first needed step will be image segmentation, to define the boundaries of our objects of interest (see Subsect. 4.2.2). Then, the second step will be a comparison between objects positions. The easiest (and faster) way to do it is by mean of image arithmetic. It applies one of the standard arithmetic operations or a logical operator to two or more images. The operators are applied locally, in a pixel-by-pixel fashion, which means that the value of a pixel in the output image depends only on the values of the corresponding pixels in the input images, that have therefore to be of the same size. Although applying image arithmetic is the simplest form of image processing, there is a wide range of applications. In our case, we make use of pixel-wise image subtraction for detecting differences between two signal's DDMs and producing a unique cDDM (Sect. 5.4). The pixel subtraction operator takes two images as the input and as the output produces a third image whose pixel values are simply those of the first image minus the corresponding pixel values from the second image, setting negative values to 0 in case of integer value images. The operation is performed independently for each dimension (*e.g.*, channel) of the image.

Derived from Boolean algebra, a logical operator is identified by a special symbol (or word) that connects two or more pieces of information, mostly to test whether a certain relationship between the two is true or false. The pixel values in a binary image, which are either 0 or 1, can be interpreted as truth values, corresponding to Boolean true (1) and false (0). Using this convention, we can perform logical operations on images simply by applying the truth-table combination rules to the pixel values from a pair of input images (or a single input image in the case of NOT), for example to isolate specific region of the imaged space. To our purpose, the logical ANDing of two signals' binary masks, identifying their own region of occurrence, permits to define their region of co-occurrence, fundamental to the quantification of the signals colocalization. As exemplified in Table 5.1, given two binary images I1 and I2 of same dimension,

their combination by image ANDing (\wedge) produce a third binary image I3 where the value of the pixel P3 of coordinates (x, y) is 1 only and if only both corresponding P1 and P2 value in I1 and I2 is 1. Conversely, image ORing (\vee) gives to the pixel P3 a value of 1 if at least one input pixel (P1 or P2) value is 1.

Table 5.1. Binary NOT, ANDing and ORing.

I1	I2	I3	I3	I3
P1 $_{(x,y)}$	P2 $_{(x,y)}$	\sim P1	P1 \wedge P2 $_{(x,y)}$	P1 \vee P2 $_{(x,y)}$
0	0	1	0	0
0	1	1	0	1
1	0	0	0	1
1	1	0	1	1

The use of logical operators can be also extended to more complex analyses. For example, when applied on local groups of pixels rather than on single ones, logical operators permit to investigate image objects morphology. *Morphological operators* often combine a binary image and a *structuring element* (SE) using a set Boolean operator, thus defining new region-based image processing operations, as erosion, dilation, opening and closing. A structuring element is nothing more than a little image (*i.e.*, matrix), whose dimension and distribution of values respectively identifies the neighbours of the central pixels (in the original image) to be considered when performing the morphological operation. Usually, the SE is set based on size and morphology of the objects to be investigated (Figure 5.1).

0	1	0
1	1	1
0	1	0

10	30	50	30	10
10	30	50	30	10
10	30	50	30	10
10	30	50	30	10
10	30	50	30	10

Figure 5.1. Structuring elements. In the simplest SE used with binary images for operations such as erosion (left), the elements only have two values, conveniently represented as 0 and 1. More complicated elements, such as those used with grey level morphological operations, may have other pixel values (right). The structuring element is sometimes called the *kernel*, however this term is often reserved for the similar objects used in convolutions (Subsect. 7.2.2).

When a morphological operation is carried out, the SE is shifted over the image and at each pixel of the image its elements are compared with the set of the underlying pixels. Discussing the cDDM method capability to selectively retain information at the objects edge, we will compare it to binary erosion (\ominus , Figure 5.2), which oppositely remove all edge pixels (or even non-edge, for object regions with remarkable border indentation).

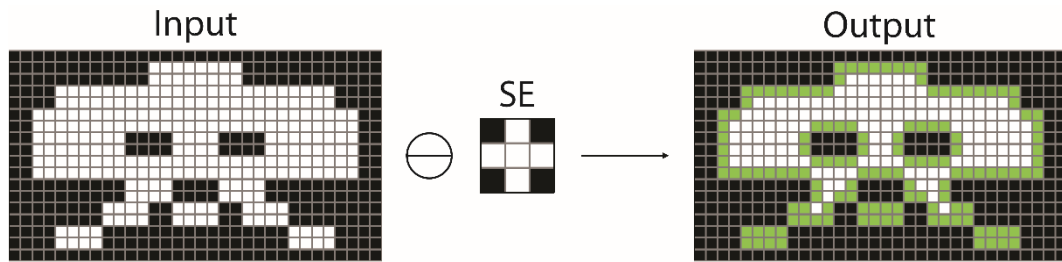


Figure 5.2. Binary erosion. If for every pixel in the SE (Structuring Element) the corresponding pixel in the image underneath (Input) is a foreground pixel, then the reference pixel (Subsect. 4.2.1) is left as it is (Output, white pixels). If any of the corresponding pixels in the image are background, the reference pixel is set to background (Output, green pixels). Erosion therefore results in objects size shrinking, especially where border indentation is higher (lower part of object), and holes enlarging.

5.2.2 Coefficients for colocalization quantification

In fluorescence microscopy, colocalization refers to the observation of spatial overlap between two or more different fluorescent markers, each having a separate emission wavelength. Colocalization analysis consists of at least two distinct sets of methods: *co-occurrence*, the simple spatial overlap of two probes, and *correlation*, in which the two signals, beside co-occurring, co-distribute in proportion to one another. Co-occurrence measurements are often best utilized to determine what proportion of a molecule is present within a particular area, compartment or organelle. However, it does not give insight into any concentration relationship between two molecules. Correlation, on the other side, is often used to assess a functional or stoichiometric relationship between two overlapping species. Nonetheless, caution should be used in talking about stoichiometry, since it assumes a linearity between marker intensity and marked molecules number that we cannot ensure, especially when immunostaining samples with more than one antibody that, besides increasing the probability for aspecific staining by cross-

reactivity, can give rise to signal amplification. Further, it is important to note that neither image correlation nor co-occurrence are direct measurements of molecular interaction. The resolving power of a microscope is conventionally limited to approximately half the wavelength of emitting light [128], while typical interaction distances between biomolecules are <10 nm. Even with the advent of super-resolution imaging techniques, intramolecular interactions cannot be unambiguously observed. Only nearfield biophysical techniques, such as Förster resonant energy transfer (FRET) or fluorescence recovery after photobleaching (FRAP), can be used to directly measure molecular interactions.

Nonetheless, biomolecules colocalization can still be inferred and semi-quantified from optical microscopes by co-occurrence and correlation descriptors, but with due caution and proper experimental settings before, during and after image acquisition. Of course, optimized sample preparation and convenient image acquisition settings are both essential for accurate analysis. In addition, post-acquisition image processing could be necessary, for example for correcting for inhomogeneous illumination or photobleaching (Subsect. 3.2.4), or for removing unwanted, non-biologically relevant signal. Finally, it is critical to isolate the pixels that contain signal from those containing predominantly noise, by image thresholding (Subsect. 4.2.2). Our co-density distribution maps fit exactly at this last step, providing a different meaning for image segmentation, introducing a density concept on which rely on, rather than relying on pixel intensity only.

Hereafter, we introduce the Pearson's, Spearman's and Mander's coefficient for co-occurrence and correlation quantification, that will be compared in Sect. 5.5 with cDDM for their capability to describe signal colocalization.

Pearson's Correlation Coefficient

In statistics, the Pearson's correlation coefficient (ρ , r , or PCC) is a measure of linear correlation between two sets of data. It is defined as the quotient of covariance (cov) and standard deviation (σ) between two variables x and y , over a population of n samples:

$$\rho = \frac{\text{cov}(x, y)}{\sigma_x \sigma_y} = \frac{\sum_i^n (x_i - \bar{x}) * \sum_i^n (y_i - \bar{y})}{\sqrt{\sum_i^n (x_i - \bar{x})^2 * \sum_i^n (y_i - \bar{y})^2}} \quad (5.2)$$

Therefore, ρ is essentially a normalized measurement of the covariance, and its result always has a value between -1 and $+1$. The correlation sign is determined by the regression slope: a positive slope (positive correlation) implies that the value of y increases with x , while a negative slope (anti-correlation) implies that the value of y decreases as x increases. The closer ρ value to the range extremes, the stronger the existing association between the variables, indicating a more linear relation. A value of 0 implies that there is no linear dependency between the variables (Figure 5.3).

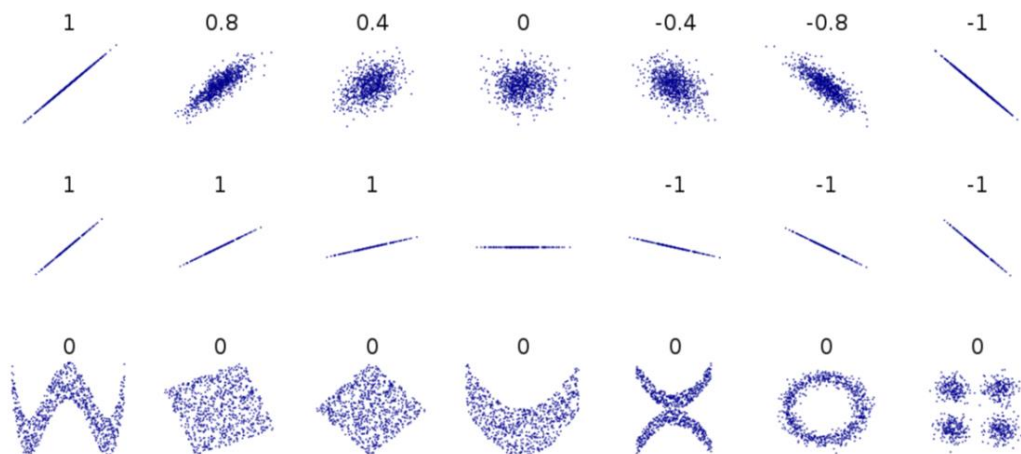


Figure 5.3. Pearson's coefficient quantifies linear correlation only. Several sets of (x, y) points, with the correlation coefficient of x and y for each set. Note that the correlation reflects the strength and direction of a linear relationship (top row), but not the slope of that relationship (middle), nor many aspects of nonlinear relationships (bottom). The figure in the centre has a slope of 0 but in that case the correlation coefficient is undefined because the variance of y goes to zero. Figure and caption reproduced from [260].

When the two variables x and y describe the pixel intensity of two markers imaged in the same domain (*i.e.*, the signals' co-occurrence region), Equation (5.1) can be used to quantify the extent of linear association between the signal intensities, as a measure of marked molecules colocalization [163, 261]. A key

mathematical property of the Pearson correlation coefficient is that it is invariant under separate changes in location and scale in the two variables. That is, we may transform x to $a+bx$ and y to $c+dy$ without changing the correlation coefficient, where a , b , c , and d are constants with $b, d > 0$. This means, that a linear correlation can be detected between two signals even if they don't take values in the same range, because of an offset or of a different magnitude. Many reviews further discuss the coefficient history [262], meaning [262, 263] and implications for image colocalization [162, 163, 264-266].

Spearman's Correlation Coefficient

When linearity between the two signal intensities cannot be assumed, correlation can be better assessed by the Spearman correlation coefficient (Q_s , r_s or SRCC), replacing in Equation 5.1 the variable values with their rank, *i.e.*, moving the variables from the interval to the ordinal scale, as exemplified in Table 5.2.

Table 5.2. Data ranking.

x	y	Rank of x	Rank of y	$Q(x, y)$	$Q_s(x, y)$
1	4	1	2		
8	17	3	5		
13	21	4	7.5	0.7541	0.8208
22	18	9	6		
30	21	10	7.5		

Data ranking is performed by pooling x and y values and sorting them in ascending order. Repeated values (*i.e.*, tied ranks) are assigned the mean of the ranks that would have been assigned to these ranks if they had not been tied. Q is computed on x and y values (columns 1 and 2), while Q_s is computed on x and y ranks (columns 3 and 4).

Q_s is a nonparametric measure of magnitude and direction of correlation, that assesses how well the relationship between two variables, whether linear or not, can be described using a monotonic function [267]. If there are no repeated values, a perfect Spearman correlation of +1 or -1 occurs when each of the variables is a perfect monotone function of the other, *i.e.*, where the values of y are either entirely nonincreasing or nondecreasing with x (Figure 5.4).

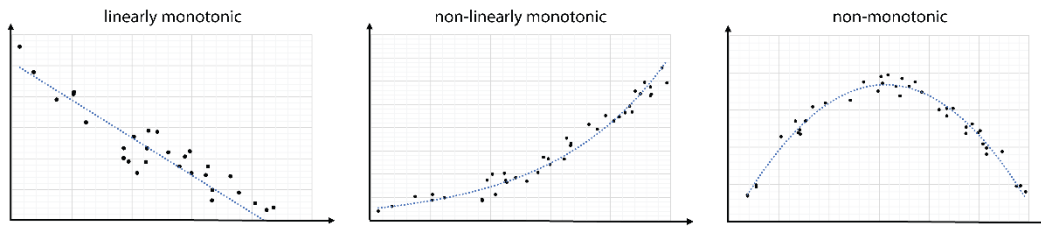


Figure 5.4. Monotonic functions. Whether linear or not, monotonic functions are functions between ordered sets that preserves or reverses the given order. Monotonicity is a less restrictive condition than linearity, as it can occur also when the order of relation between x and y is greater than 1.

Use of ρ_s instead of ρ can therefore be advisable in many biological investigations, where association between variables can be frequently non-linear, as it occurs for example studying gene, RNA and protein expression [268, 269], cell vesiculation [270, 271] or spatial distribution of imaged biomolecules [272, 273].

Mander's Coefficients

In 1993 Manders elaborated new coefficients for measuring objects colocalization in dual-colour images. He firstly introduced the overlap coefficient to supply the lack of interpretability for Pearson's coefficients negative values [163]:

$$MOC = \frac{\sum_i^n x_i * \sum_i^n y_i}{\sqrt{\sum_i^n (x_i)^2 * \sum_i^n (y_i)^2}} \quad (5.3)$$

By simply removing the average subtraction from the intensity values in Equation 5.1, the coefficient is claimed to become "insensitive to differences in signal intensities between the components of an imaged caused by different labelling with fluorochromes, photobleaching, or different settings of the amplifiers". The value of this coefficient ranges from 0 to 1, and accounts for the total amount of fluorophores that overlap with each other. To separate each fluorophore contribution and increase the coefficient interpretability, Manders further introduces the M_1 and M_2 coefficients, calculated after image thresholding:

$$M_1 = \frac{\sum_i^n x_{i,coloc}}{\sum_i^n x_i} \quad \begin{cases} x_{i,coloc} = x_i, \text{ if } y_i > 0 \\ x_{i,coloc} = 0, \text{ if } y_i = 0 \end{cases} \quad (5.4)$$

$$M_2 = \frac{\sum_i^n y_{i,coloc}}{\sum_i^n y_i} \quad \begin{cases} y_{i,coloc} = y_i, \text{ if } x_i > 0 \\ y_{i,coloc} = 0, \text{ if } x_i = 0 \end{cases} \quad (5.5)$$

Here, x_i and y_i refer to the i -th above-threshold pixel value for the first and second signal, respectively (m1 region and m2 region in Figure 5.5), with n total pixels in each image being analysed. The co-occurrence region is then defined by the logical ANDing (Subsect. 5.2.1) of the m1 and m2 regions (Figure 5.5).

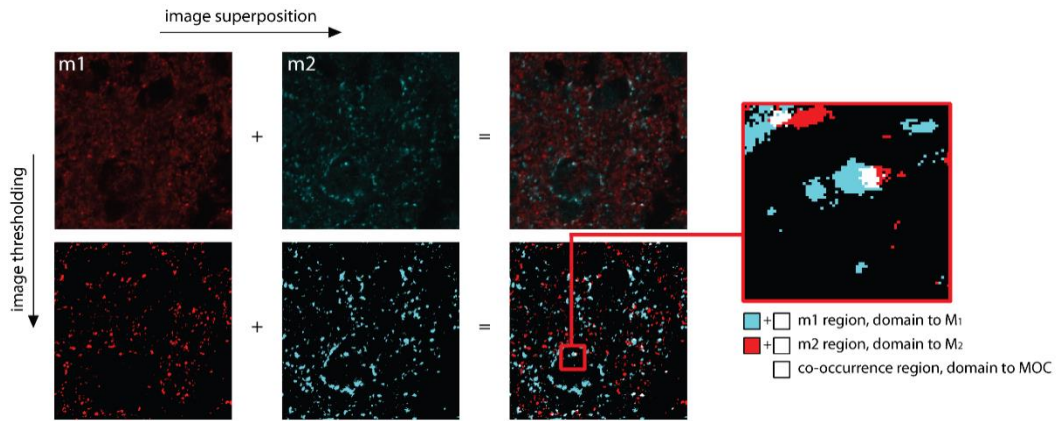


Figure 5.5. Definition of the image domains for Manders' coefficients computation. First, each imaged marker signal (m1 and m2) is thresholded to identify its own region of occurrence (m1 region and m2 region), that will define the domain of computation for the M_1 and M_2 coefficient. Then, the two signals are superimposed to identify their region of co-occurrence, within which will be defined a significant computation of the Mander's overlap coefficient (MOC), as outside this region the numerator of Equation 5.2 goes to 0.

M_1 and M_2 separate the fluorophores contribution to colocalization, by calculating for each fluorophore the fraction of the total intensity that co-occurs. Thus, M_1 can be defined as the co-occurrence fraction of the first signal with the second and, likewise, M_2 is the co-occurrence fraction of the second signal with the first. Manders' coefficients provide an important distinction over the simpler area overlap calculation, because they give greater importance to brighter pixels and lower weight to values near to the set intensity threshold. Since then, Manders' M_1 and M_2 coefficients have been widely used to quantify signals co-occurrence in

intensity images. However, doubts on the suitability of the MOC coefficient to the quantification of unbiased co-occurrence have been casted [266] and its use along with M_1 and M_2 coefficients is currently under heavy discussion [264,274–277].

5.3 State of the art

In a biological context, colocalization is defined as the presence of two or more different molecules residing at the same physical location in a specimen. Subcellular spatial colocalization analysis is fundamental for determining whether molecules are located in sites where they can interact with each other, especially when their reciprocal interaction and reaction cannot be assessed directly. The molecules location can be easily and efficiently addressed by confocal fluorescence microscopy [278]: while fluorescent probes allow the selective visualization of specifically marked molecules [279], the confocality of acquisition allows the investigation of their distribution in the whole cellular volume, while reducing the out-of-focus contributions to probes signal [264, 280] and avoiding image blurring accordingly, which can introduce false positives. A first common method to analyse colocalization of fluorescent signals is image superposition (*i.e.*, merging or, more technically, fusion) for visual inspection [274, 281]. However, such a method is subject to perceptive errors and biases [282], cannot discriminate between random and potentially functional colocalization [163] and is poorly quantitative [219]. Accordingly, several methods for quantifying colocalization have been developed through years. A first discrimination occurs between pixel-based and object-based methods [283, 284]. As for many other applications, the former is based solely on the intensity information in each pixel, while the latter is based on information from a set of semantically coherent pixels, called the object. Therefore, object-based methods are more appropriate for super-resolution microscopy, which is more suitable for accurately separating interacting molecules in adjacent pixels and discerning objects boundaries [265, 285], while the application of pixel-based methods is quite independent of microscopy resolution. Pixel-based methods conventionally regard colocalization as quantifiable by two components [283]: co-occurrence and correlation [263, 265]. This approach has given rise to a large number of different correlation coefficients [163, 261, 287-290],

first of all, Pearson's [292] and Manders' [274] coefficients, for their ease of implementation [292] and their capability to provide, respectively, a quantification of correlation and co-occurrence, when used in pair [266, 274, 282]. Many derived forms of these coefficients have been progressively introduced to overcome their main drawbacks, such as noise dependency [294], lack of linearity [286] and absence of spatial informativeness [263]. However, their adoption is still limited by their shared inadequacy to provide an intuitive and effective representation of colocalization that could really help researchers in the biological interpretation of results. In addition, none of them can provide information about the stoichiometry of colocalization [280], which is still approximated from the pixel intensities scatterplot as the slope of the fitting line assuming, a priori, a linear relation between the two signals intensities [162, 163, 295].

All methods exploiting pixel intensities neglect information regarding pixel interconnections that, if considered, could permit the enforcement of colocalization information. In fact, co-localized pixels, by definition, must appear with the same connecting pattern in both channels. Based on this assumption, we developed the concept of density distribution (DDM) [130] and co-density distribution (cDDM) map, a novel set of tools to automatically and quantitatively improve colocalization analysis in biomedical images. Working on densities, cDDMs introduce an additional constraint that makes the overall colocalization assessment more reliable, enabling the refinement of correlation coefficients computation, when these coefficients are chosen as quantifiers of colocalization. In addition, being representative of markers' local co-density, cDDMs offer a visual support preserving the spatial information and making the biological interpretation of results easier.

After presenting the cDDM method and discussing its main implications, we hereafter exemplify cDDM effectiveness through their application to two more real image datasets acquired by fluorescence microscopy, proving how cDDM can advance the actual colocalization analysis framework, provide information about markers' density and degree of colocalization and, thus, open to the formulation of new biological considerations. Finally, we updated our previously developed software program *DDMaker* [130] to *coDDMaker*, again endowed with a user-

friendly GUI, to support researchers in building DDMs and cDDMs and analysing signals colocalization for their own experiments.

5.4 Materials and methods

Three datasets are used to exemplify cDDM benefits to biomedical colocalization and co-distribution studies: (1) the SYP-VGLUT1 dataset is used to present cDDM utilization and main functional implications; (2) the Lamp-1-Ce6 dataset is used to present a case of limited colocalization between differently dense markers, where the analysis is complemented by novel information from the cDDM, including indication on the degree of colocalization; (3) the NF200-FM dataset is used to present a case of cDDM application at the tissue level, where local co-density numerical and spatial information also permits new biological considerations about sample's heterogeneity. The SYP-VGLUT1 and NF200-FM datasets have been kindly provided by Prof. Laura Calzà and her team at the IRET Foundation. The Lamp-1-Ce6 dataset has been kindly provided by Dr. Enrico Lucarelli and the laboratory of Regenerative Therapies in Oncology (Unit of Osteoncology, Bone and Soft Tissue Sarcomas and Innovative Therapies) of the IRCCS Rizzoli Orthopaedic Institute.

Image collection

(1) The 12-bit range images from rat brain immunostained for Synaptophysin (SYP, $\lambda_{EX}=488$ nm, $\lambda_{EM}=525$ nm) and vesicular glutamate transporter 1 (VGLUT1, $\lambda_{EX}=561$ nm, $\lambda_{EM}=595$ nm), as described in [296], were sequentially acquired with a Nikon Ti-E A1R laser confocal fluorescence microscope (Nikon, Tokyo, Japan), equipped with a Plan Apo 60x/1.4 objective at a resolution of $512 \times 512 \times 9$ pixels with a pixel size (XYZ) of $0.1 \times 0.1 \times 0.25$ μm^3 (Pinhole size= 39.59 μm). (2) The 12-bit range images of human osteosarcoma MG-63 cells exposed to Keratin-based nanoparticles (PTX-Ce6@ker_{ag} NPs, $\lambda_{EX}=649$ nm, $\lambda_{EM}=700$ nm) were sequentially acquired with a confocal fluorescence laser scanning microscope Ti-E A1R (Nikon, Amsterdam, Netherlands), equipped with a 60x/NA 1.4 oil Plan-Fluo at a resolution of $1024 \times 1024 \times 19$ pixels with a pixel size (XYZ) of $0.2 \times 0.2 \times 0.25$ μm^3 (Pinhole size= 24.27 μm). MG-63 cells were indirectly immunostained against the

Lysosomal-associated membrane protein 1 (Lamp-1, $\lambda_{EX}=563$ nm, $\lambda_{EM}=595$ nm) as described in [240]. (3) The 8-bit range images from rat spinal cord immunostained for neurofilaments (NFs, primary antibody: mouse anti-NF200, 1:800, Sigma Aldrich Saint Louis, MO; secondary antibody: Rhodamine RedTM-X, 1:100, Jackson Immuno Research, Cambridgeshire, UK, $\lambda_{EX}=570$ nm, $\lambda_{EM}=590$ nm) and stained for myelin with FITC-FluoromyelinTM (FM, Thermo Fisher, $\lambda_{EX}=479$ nm, $\lambda_{EM}=598$ nm) were acquired with a Nikon Eclipse E600 (Q Imaging, Surrey, BC, Canada), equipped with a Plan Apo 10x/0.4 objective and Q Imaging RETIGA-2000RV camera. For each sample, 10 images were acquired and stitched into a single mosaic (resolution: 3532×2384 pixels, pixel size: 0.74×0.74 μm^2) with Photoshop (Adobe Suite, release 22.4.2).

Image segmentation

All the following procedures are implemented in MATLAB[®] (R2019a v.9.7.0, The MathWorks, Natick, MA, USA). SYP and VGLUT1 signals are segmented by Isodata thresholding. Lamp-1 and Ce6 signals and NF200 and FM signals are segmented by Otsu method.

Local distribution and co-distribution analysis

Starting from pairs of input grey level images, the cDDM is computed from single DDMs (Figure 5.6 (a)).

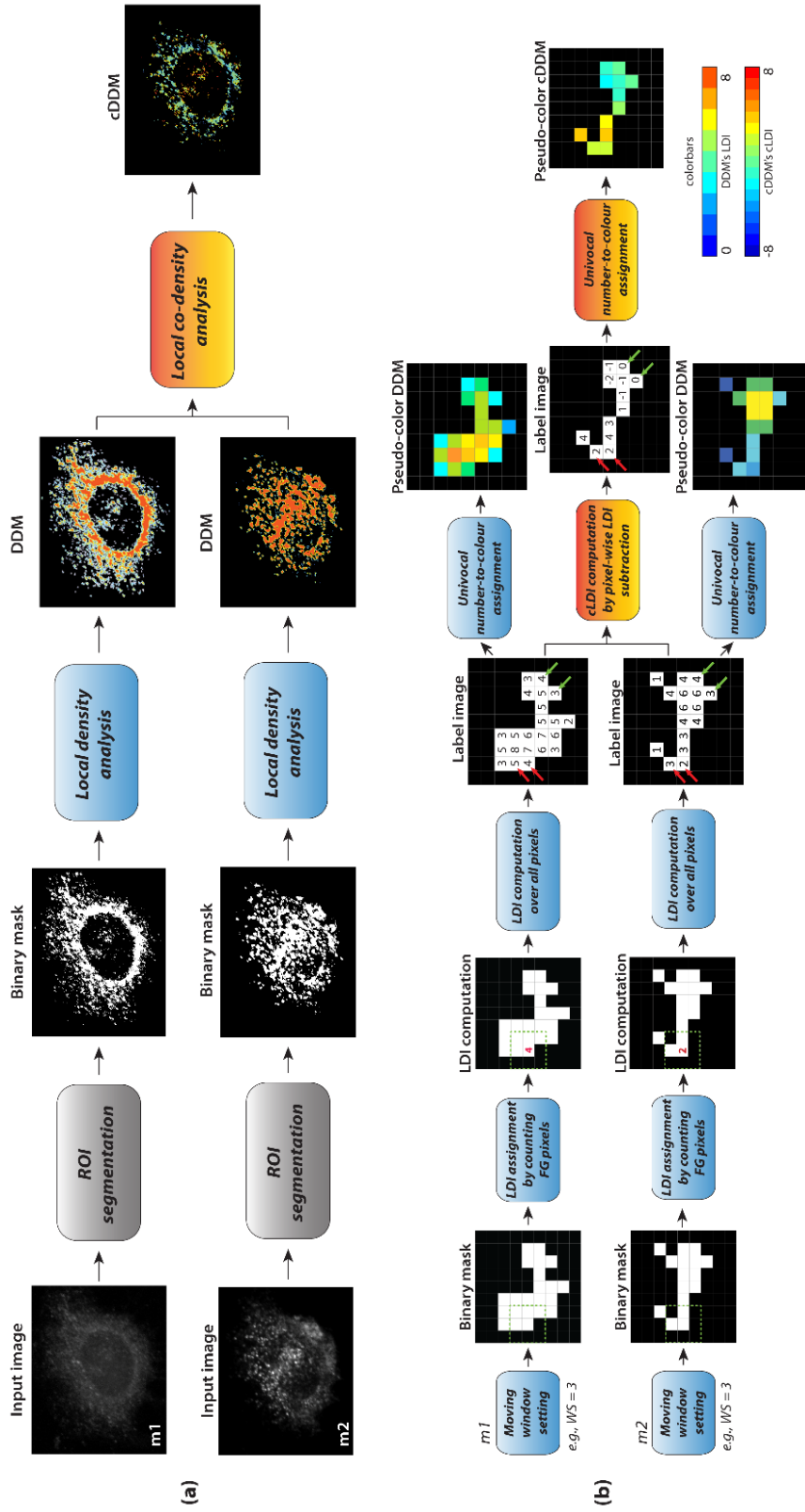


Figure 5.6. Flowchart of cDDM creation pipeline for a couple of markers (m1, m2). (a) The acquired (input) images are segmented in binary masks and their pixel connectivity separately explored by local density analysis for the two pseudo-colour DDMs building. Then, the cDDM is built through local co-density analysis, by subtracting the single markers DDMs pixel-wise. (b) Details of local density (blue boxes) and co-density (orange boxes) analyses: after setting the search (moving) windows size, each foreground pixel of each binary mask is assigned a number representing the amount of foreground pixels in its locality, this constituting the input to build the pseudo-colour DDM. Then, the local co-density analysis is performed by pixel-wise subtraction of the two DDMs. Image reproduced from [205] under the CC-BY Creative Commons Attribution 4.0 International licence.

As schematized in Figure 5.6 (b), distribution analysis is performed by firstly computing the local density indices (LDIs) and DDM of each imaged marker, as described in [130], after setting the search (moving) WS, which can differ for the two markers. Then, for each pair of markers, the co-distribution analysis is performed by computing the co-density distribution map (cDDM), by subtracting the two markers' DDMs pixel-wise. Consequently, the resulting cDDM values (*i.e.*, local co-density indices, cLDIs) can be only computed inside the markers co-occurrence region, resulting from ANDing the two marker masks, and can range from $-(WS^2-1)$ to $+(WS^2-1)$. Different LDI couples can result in the same cLDI (Figure 5.6 (b), red and green arrows). Negative cLDI values indicate pixels where the first marker signal is locally denser than the second one, the opposite holds for positive values. A cLDI equal to zero indicates pixels where the two markers are equally dense, hence defining the *equi-density region*, where the signals are in a 1:1 ratio (Figure 5.7).

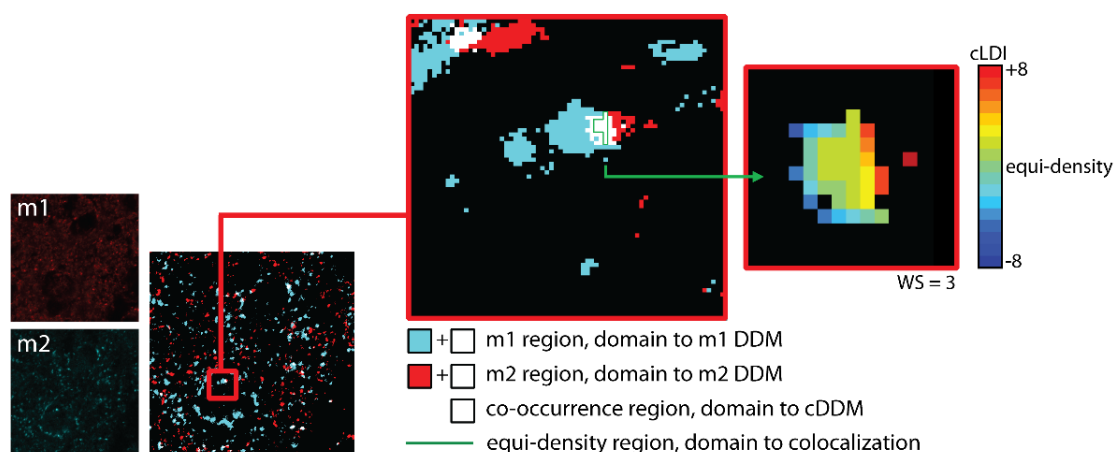


Figure 5.7. The equi-density region is strictly contained in the co-occurrence region. Recalling the m1 and m2 markers distribution of Figure 5.5, the m1 and m2 regions become the domain for the computation of m1 and m2 DDM, respectively, and the identified co-occurrence region becomes the domain of computation for the cDDM. Within the co-occurrence region, the cDDM identifies the equi-density region, composed of pixels of $cLDI=0$, where m1 and m2 signals are in a 1:1 ratio. As discussed in the following sections, m1 and m2 colocalization is more robustly assessed when quantified over the equi-density region, rather than on the co-occurrence. Image reproduced from [205] under the CC-BY Creative Commons Attribution 4.0 International licence.

However, non-zero cLDIs cannot be considered indicators of a specific ratio, but rather, of a specific difference in the markers' abundance that is, by definition,

a more correct indication of the degree of colocalization than of pixel intensities correlation. Finally, mapping cLDIs back to the image domain in pseudo-colours also allows us to gain information about the markers spatial co-distribution.

Pixel density as a measure of colocalization

An established requirement for signals colocalization is their co-occurrence. Co-occurring pixels can either be isolated (*i.e.*, they have no neighbouring pixels) or not. If we assume that isolated pixels as the result of spurious co-occurrences, colocalization is, hence, defined by the presence of at least two adjacent co-occurring pixels. This means that colocalization presents itself in patterns, in their turn defined by connections between pixels. As a consequence, there is the necessity to also quantify colocalization with a measure of pixel connectivity (*i.e.*, our local co-density), rather than using an intensity-based measure alone. Assuming that the objects of interest to be imaged are larger than single pixels, the 3×3 search window (*i.e.*, WS=3) is the smallest window to analyse pixel connectivities and, hence, local densities. Such an assumption is fundamental to determine whether the local co-density information carried by cDDMs also brings information about objects colocalization. Indeed, when imaging single-pixel objects, cLDI cannot be indicative of colocalization, being unable to discriminate between a real overlap and a close proximity, since non-overlapping single-pixel objects can fall within a single pixel. In such cases, more information about colocalization can be drawn from pixel-based correlation coefficients, under the assumption of proportionality between marker intensity and molecule number. Such an assumption is not exploited in our method, which relies on a more straightforward measure of the marked objects abundance based on local density.

Hence, co-density is a measure of colocalization when the search window has a size that is, at most, the same as that of the imaged objects. In such cases, a cLDI value of zero indicates the presence of co-occurring and co-dense objects, thus identifying those pixels where two signals colocalize not only because they co-occur (and perhaps correlate), but also because they do it by sharing the same pattern density.

Colocalization Analysis

We implemented a colocalization analysis framework according to the most common methods in the biomedical literature. Specifically, we quantify the signals overlap by Manders' coefficients MOC, M_1 and M_2 , and signals correlation by Pearson's (ρ) and Spearman's (ρ_s) [297] coefficients. Of note, MOC's informativeness as a co-occurrence estimator is actually an ongoing topic of discussion [264, 266, 275-277] and the MOC values reported hereafter should be carefully interpreted accordingly. In addition, we also evaluate:

- The markers overlap region through our co-occurrence maps (cOMs) built on top of segmented signals, highlighting in four different pseudo-colours the pixels where: (1) both markers are absent (background), (2) only the first marker is present, (3) only the second marker is present and (4) both markers are present (co-occurrence region)
- The local density and co-density of marked structures, by DDMs and cDDMs computation and analysis.

Assessment of results

We first verify the appropriateness of cLDI as a colocalization indicator by assessing the degree of an order relation between cLDI and correlation coefficient values. Hence, we apply a cLDI-based refinement of classical coefficients computation, which consists in restricting its domain from the co-occurrence region to the equi-density region.

For each image, each marker signal is binarized in a mask representing its own occurring region. Then, the two masks are ANDed to identify the signals' co-occurrence region. Finally, the cDDM analyses the co-occurrence region, restricting it to the co-density region. Correlation (by ρ and ρ_s) and overlap (by MOC, M_1 and M_2) are calculated for both the signal intensities (*i.e.*, between the pixel values in the two marker images) and the signals' local density (*i.e.*, between the pixel values in the two marker DDMs) to assess to what extent density and intensity are comparable descriptors of colocalization. The signal intensity correlation (and MOC) is calculated in three increasingly narrowed domains: the

entire image, the co-occurrence region, and the co-density region. As expected, the first narrowing, from the entire image to the co-occurrence region, always decreases the correlation coefficients value, excluding the random colocalization of the background. M_1 and M_2 coefficients are calculated for signal intensity with respect to both the co-occurrence and the co-density regions, according to Equations (5.3) and (5.4), where the “colocalizing” pixels at the numerators are the co-occurring and the co-dense pixels, respectively. The signal density correlation and co-occurrence are calculated only for the co-occurrence region. Indeed, density computation is theoretically impossible before the co-occurrence region definition, whilst inside the co-density region, the coefficients values would be biased by the density-based nature of the refinement itself (*i.e.*, all coefficient values would be set to 1).

In addition, we also compare our cDDM-based method to binary erosion (Subsect. 5.2.1) for the restriction of the co-occurrence region, using 4-connected and 8 (full) -connected SE. However, considering full connection for comparison is probably fairer, since cDDMs also explore full connectivity. The comparison regards the number of pixels and objects in the masks, as well as the correlation coefficient (ρ and ρ_s) values, before and after pixel removing by erosion and pixel selection by cDDMs.

More benefits and the effectiveness of cDDMs are then discussed in three examples.

5.5 Results and discussion

Functional implication of cDDMs

Colocalization can be defined as the functional and non-spurious co-presence of molecules, most commonly at the single-pixel level. While co-presence can be easily assessed, its functionality must be inferred by other measures, such as signal correlation. However, correlation between coexistent signals does not prove, but only suggests, the presence of colocalization. Such a suggestion can be then corroborated by local co-density analysis that, working locally, improves the information of co-location and, being in an order relation with correlation

coefficients, can serve to improve the specificity of colocalization analysis. The main functional implications of cDDM are schematized in Figure 5.8.

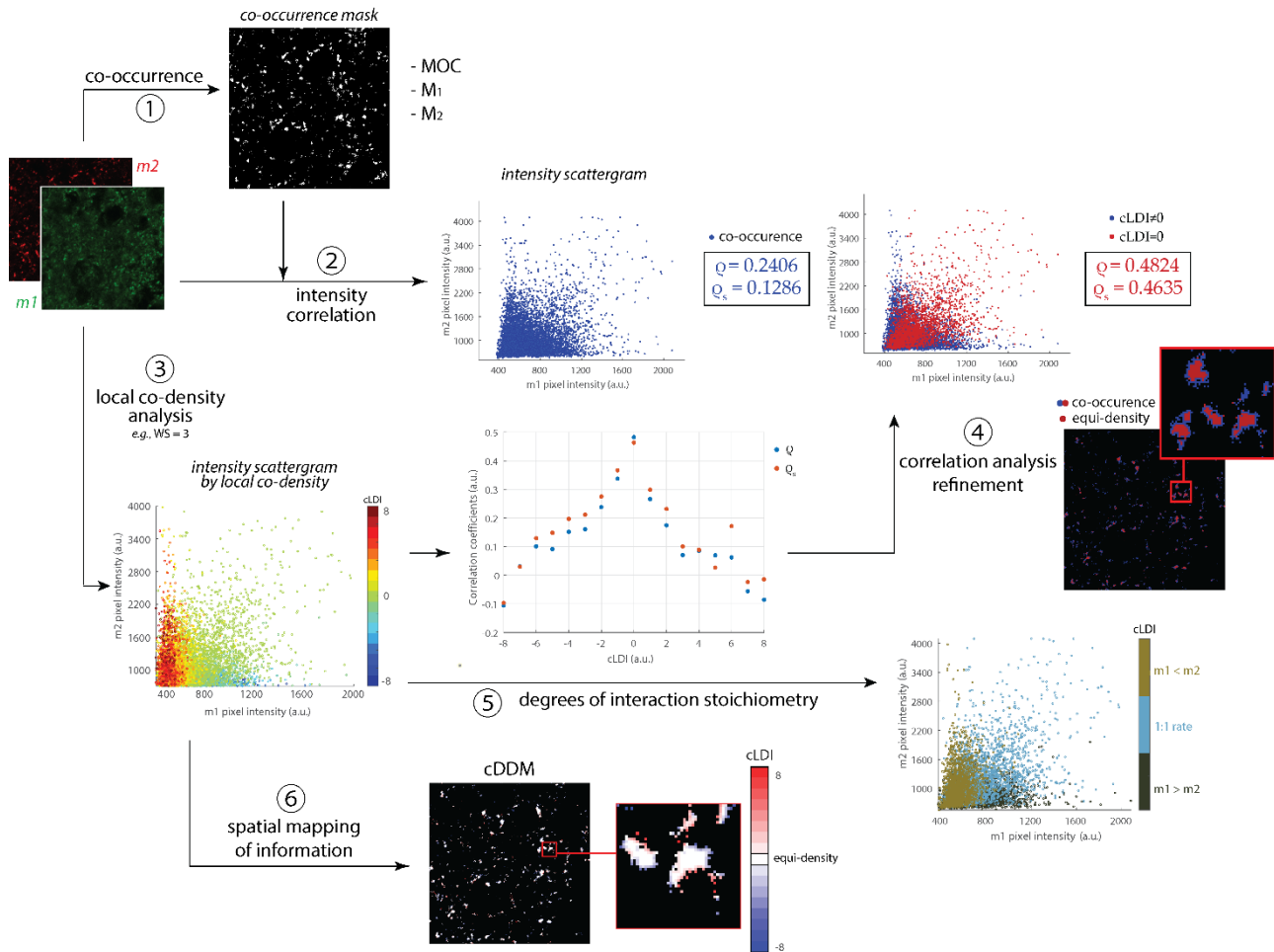


Figure 5.8. Functional implications of coDDM. Starting from a couple of imaged markers ($m1$ and $m2$), colocalization is usually quantified as a combination of markers overlap (by co-occurrence mask and Manders' MOC, M_1 and M_2 coefficients computation, ①) and intensity correlation (primarily by Q and Q_s correlation coefficients, ②). By cLDIs computation, co-occurring pixels can be further partitioned by their local co-density and resulting groups visualized in a pseudo-colour scattergram (③). When quantifying colocalization through markers intensity correlation, the analysis specificity can be increased by narrowing the computational domain from the co-occurrence to the equi-density region (*i.e.*, made of pixels with cLDI=0, ④). In addition, being based on density instead of intensity, cLDIs are more appropriate for estimating markers relative abundance(⑤). Finally, cDDM permits to preserve the spatiality of original images, additionally coding it with colours for the regional investigation of cLDI distribution (⑥). Colocalization quantification for the SYP-VGLUT1 dataset and details of presented scatterplot have been reported for completeness at the end of this subsection. Image reproduced from [205] under the CC-BY Creative Commons Attribution 4.0 International licence.

Colocalization is usually quantified by markers overlap and intensities in correlation coefficients within the co-occurrence region (Figure 5.8, ① and ②), defined by the intersection of the two marker (m_1 , m_2) masks. cLDIs computation allows the region to be split into subregions of homogeneous co-density, each one consisting of the set of pixels at which $LDI_{m_1} - LDI_{m_2} = c$, where c is a specific cLDI value (Figure 5.8, ③). If we now compute the correlation coefficients (ρ and ρ_s) within each cLDI-defined sub-region (Figure 5.8, central scattergram), we can see that correlation between signals intensity increases as cLDI moves from the highest (in absolute terms, *i.e.*, $|cLDI|=8$) to the equi-density condition (*i.e.*, $cLDI=0$). This proportionality confirms that cLDIs can serve as indicators of colocalization, just as ρ and ρ_s , at least when they hold. Then, cDDM can be applied for a density-based refinement of colocalization quantification by correlation coefficients, namely, by restricting their computation from the co-occurrence region to the equi-density one (Figure 5.8, ④). This means that cDDM can be considered also as a denoising tool. On one side, arising from a single step of image subtraction, it cannot add any noise to the colocalization quantification procedure, but just “conserve” the possible noise introduced during image acquisition and pre-processing. On the other side, noise is a bias that also affects the computation of correlation coefficients. Rather, decreasing the degrees of freedom of single pixels by requiring same densities co-occurrence, would probably make the cDDM computation more robust to noise. So, denoised by non co-dense signals, the new coefficients value will be valid only for the identified subpopulation of co-occurring, co-dense pixels. This results particularly helpful in case of heterogeneous images, in which colocalization does not concern all the signal and/or sample.

Apparently, the same restriction of the computational domain could be obtained by a simply binary erosion. However, even under the additional assumption of negligible colocalization at the edge of the co-occurrence region, a refinement by erosion would remove the outer pixels independently of their connection or the presence of colocalization. If this could produce a somewhat lightly divergent set of results when the co-occurrence region is dense (*i.e.*, the edge pixels are a clear minority), the erosion would yield an increasingly invalid

outcome as the border indentation of the co-occurrence region increases, or in the presence of small objects. Table 5.3 reports all the results, from the initial whole co-occurrence mask to the final masks, achieved by erosions and cDDM, used to assess colocalization. Accordingly, the numbers of edge pixels are complementary (*e.g.*, for NF200-FM the percentage of edge pixels is 34.65).

Table 5.3. Comparison between binary erosion and co-density analysis in refining the correlation computation domain.

MASKS		NF200-FM		SYP-VGLUT1		Lamp-1-Ce6	
Co-occurrence (before refinement)	Pixel nr (% ¹)	1465036	(100)	9343	(100)	737	(100)
	Object nr (%)	19068	(100)	968	(100)	199	(100)
	ρ (ρ_s)	0.5535	(0.3760)	0.2406	(0.1286)	0.1666	(0.1656)
Binary erosion refinement (4-conn) ²	Pixel nr (%)	957332	(65.35)	3011	(32.23)	88	(11.94)
	Object nr (%)	11244	(58.97)	244	(25.21)	24	(12.06)
	ρ (ρ_s)	0.6170	(0.4456)	0.3353	(0.2112)	0.1479	(0.1459)
Binary erosion refinement (8-conn) ²	Pixel nr (%)	810579	(55.33)	1865	(19.96)	31	(4.21)
	Object nr (%)	10162	(53.29)	158	(16.32)	9	(4.52)
	ρ (ρ_s)	0.6416	(0.4736)	0.3707	(0.2536)	0.3454	(0.3288)
cDDM refinement ³	Pixel nr (%)	851042	(58.09)	2394	(25.62)	99	(13.43)
	Object nr (%)	16300	(85.48)	378	(39.05)	46	(23.12)
	ρ (ρ_s)	0.6508	(0.5031)	0.4824	(0.4635)	0.5156	(0.4353)

¹ Percentages refer to the co-occurrence region (pixel or object number) before its refinement.

² 3×3 SE. ³ WS=3.

The co-occurrence region border indentation is quantifiable by the number of edge (border) pixels. Therefore, eroding with 4-connectivity makes the effects of indentation decrease from the NF200-FM dataset (35% of co-occurring pixels are on the region border) to SYP-VGLUT1 (68%) and Lamp-1-Ce6 (88%), which shows the smallest objects. As expected, this trend still holds when eroding by considering full connectivity of pixels, as cDDM does. We can also see that the masks achieved with 4-conn erosion are the widest ones (*i.e.*, having the highest number of pixels), while showing the worst correlations (hence, the worst colocalization performances) over all datasets. This definitely improves with 8-conn, although the mask achieved yields correlation values that still are poor for SYP-VGLUT1 and Lamp-1-Ce6. On the contrary, the masks achieved by cDDMs yield the best correlation coefficients, the only mask to bring fair correlations in the

two aforementioned datasets. Of course, the best result is achieved with Lamp-1-Ce6 because, having small objects, the effect of keeping (co-dense) edge pixels is emphasized. In practice, cDDMs preserve those edge pixels, removed by the erosion without distinction, deserving to be semantically retained instead, since contributing to the measured correlation, independently of their position within the co-occurrence region. Therefore, cDDMs end in preserving a greater number of meaningful pixels and objects than erosion, thus representing a tool for the more precise mapping of stronger colocalization regions.

Let's now deepen the analysis of the results using cDDM. We have seen that, exploiting pixels density, cDDM can also provide information about the degree of colocalization (Figure 5.8, ⑤). The markers' stoichiometric ratio of interaction is sometimes inferred from the slope of the fitting line in the intensity scattergram [292]. However, such an approach riskily depends on the assumption of linearity between the markers' intensities, that is not the rule when working with biological samples. Instead, cLDI reflects markers' density and is then, by definition, a more appropriate indicator of the markers' relative abundance, even when not relying on linearity assumptions.

Although in the previous case we used the co-density information at a global level, to compare it to current colocalization methods we can exploit the locality nature of cDDM to open for new investigation paths at the regional level (Figure 5.8, ⑥). Guided, for instance, by anatomical or functional motivations, co-densities distributions can be investigated in specific image sub-regions or, in the opposite way around, specific co-densities can be addressed one at a time and their distribution singularly investigated at each local level. As attested, especially by the last two datasets, cDDM can more generally open for the formulation of new biological considerations, as they include spatial quantitative information (neglected by most coefficients), which are also locally computed, to provide a more detailed and comprehensive overview of the investigated system.

Finally, cDDMs borrow all the advantages of DDM: first, the capability to provide a more accurate estimation of molecules position and an increased robustness to resolution variations based on DDM local density analysis [130]; second, cDDM is easy and fast to build and apply to any study, independently of the specific resolution involved.

Table 5.4. Comparison between SYP and VGLUT1 intensity and local density colocalization analysis, before and after refinement for local co-density.

SYP-VGLUT1			
	co-occurrence region ($n^1=9343$)		co-density region ($n^1=2394$)
	intensity	density	intensity
ρ	0.2406	0.0773	0.4824
ρ_s	0.1286	0.0953	0.4635
MOC	0.2420	0.2325	0.9317
M_1	0.1386	0.1354	0.0411
M_2	0.4574	0.4530	0.1479

¹ n : sample size, *i.e.*, number of considered pixels.

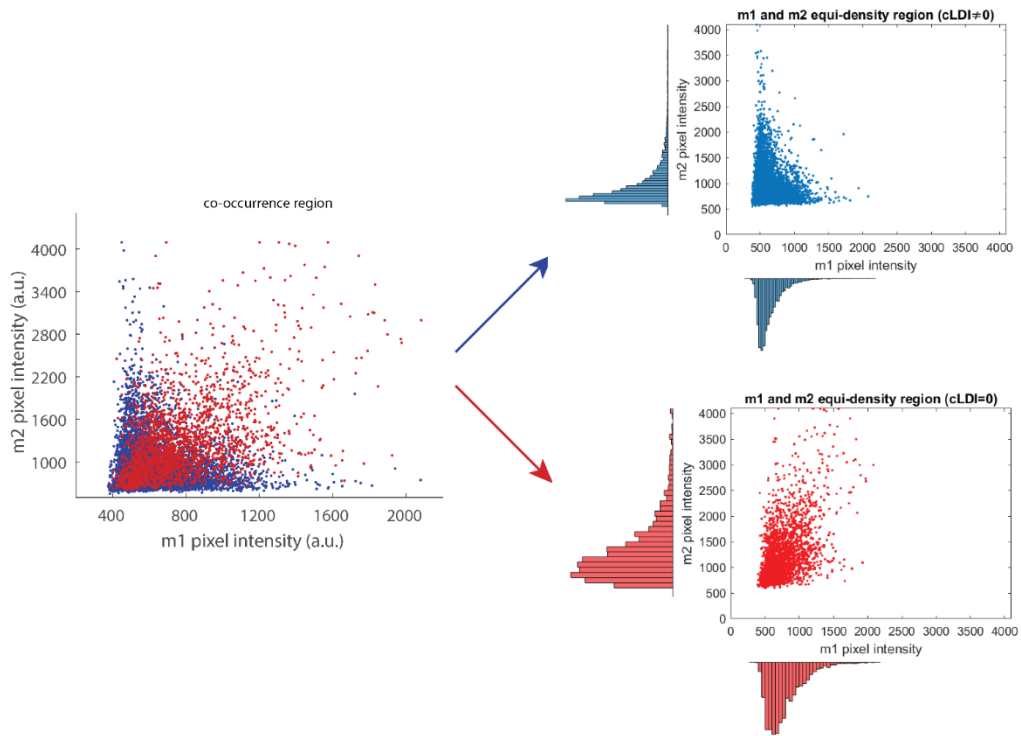


Figure 5.9. Scatterplot of m1 and m2 markers intensity for the SYP-VGLUT1 dataset of Figure 5.8, within (red) and outside (blue) the equi-density region identified by the cDDM. Image reproduced from [205] under the CC-BY Creative Commons Attribution 4.0 International licence.

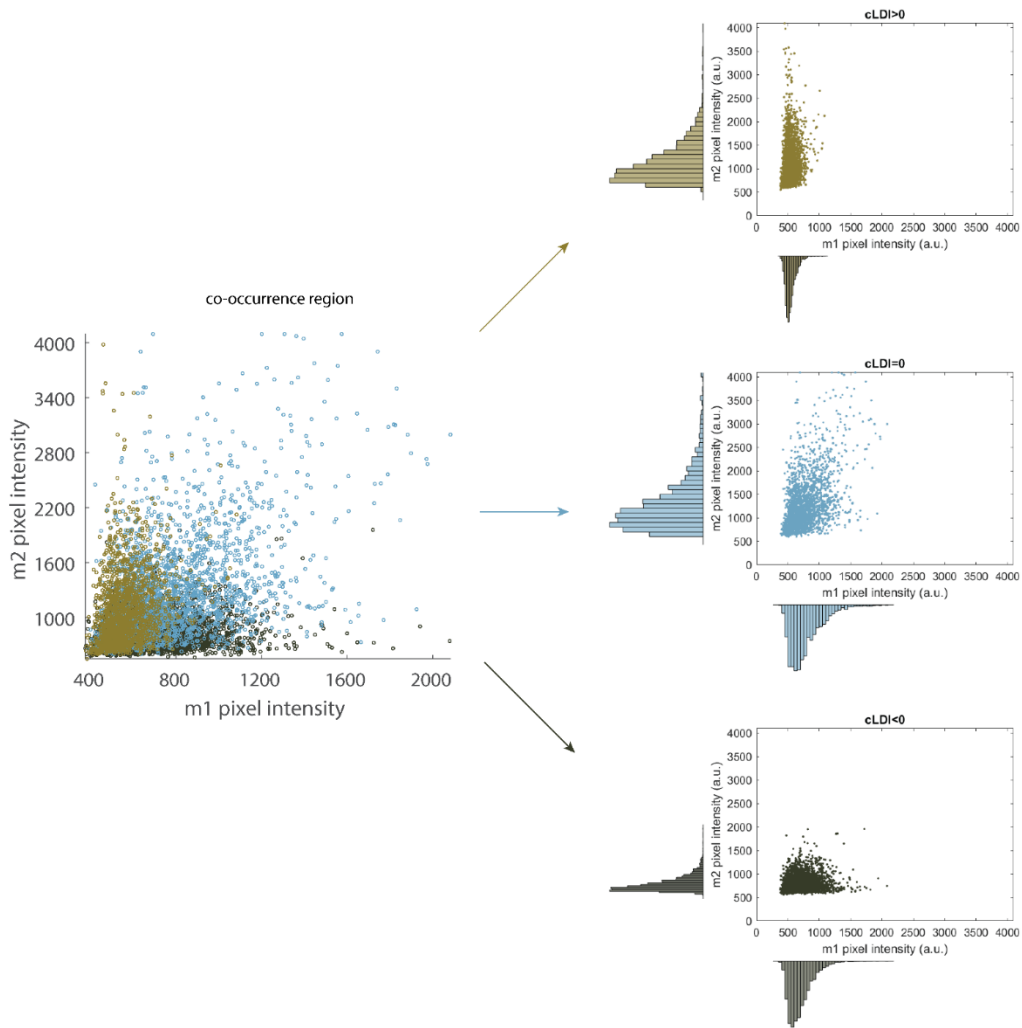


Figure 5.10. Scatterplot of m1 and m2 markers intensity for the SYP-VGLUT1 dataset of Figure 5.8, partitioned by cLDI sign. Image reproduced from [205] under the CC-BY Creative Commons Attribution 4.0 International licence.

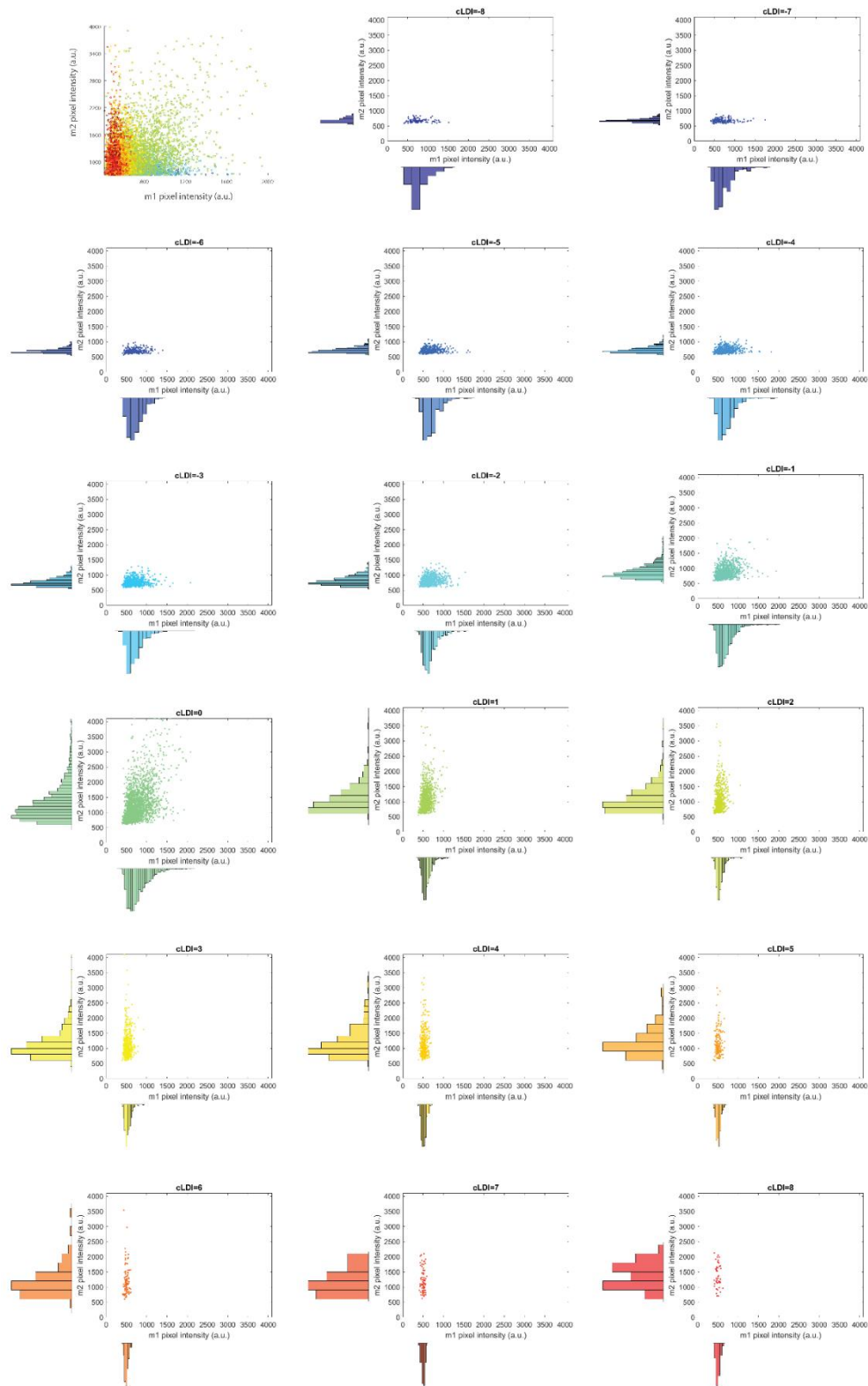


Figure 5.11. Scatterplot of m1 and m2 markers intensity for the SYP-VGLUT1 dataset of Figure 5.8, partitioned by cLDI value. Image reproduced from [205] under the CC-BY Creative Commons Attribution 4.0 International licence.

cDDMs Disclose Information about the Degree of Colocalization

The second analysed dataset refers to a study of *in vitro* characterization of a drug delivery system [244], in which the authors verify the compartmentalization of the developed nanoparticles (PTX-Ce6@ker_{ag} NPs) into late endosomes (marked by Lamp-1 staining) (Figure 5.12 (a), top).

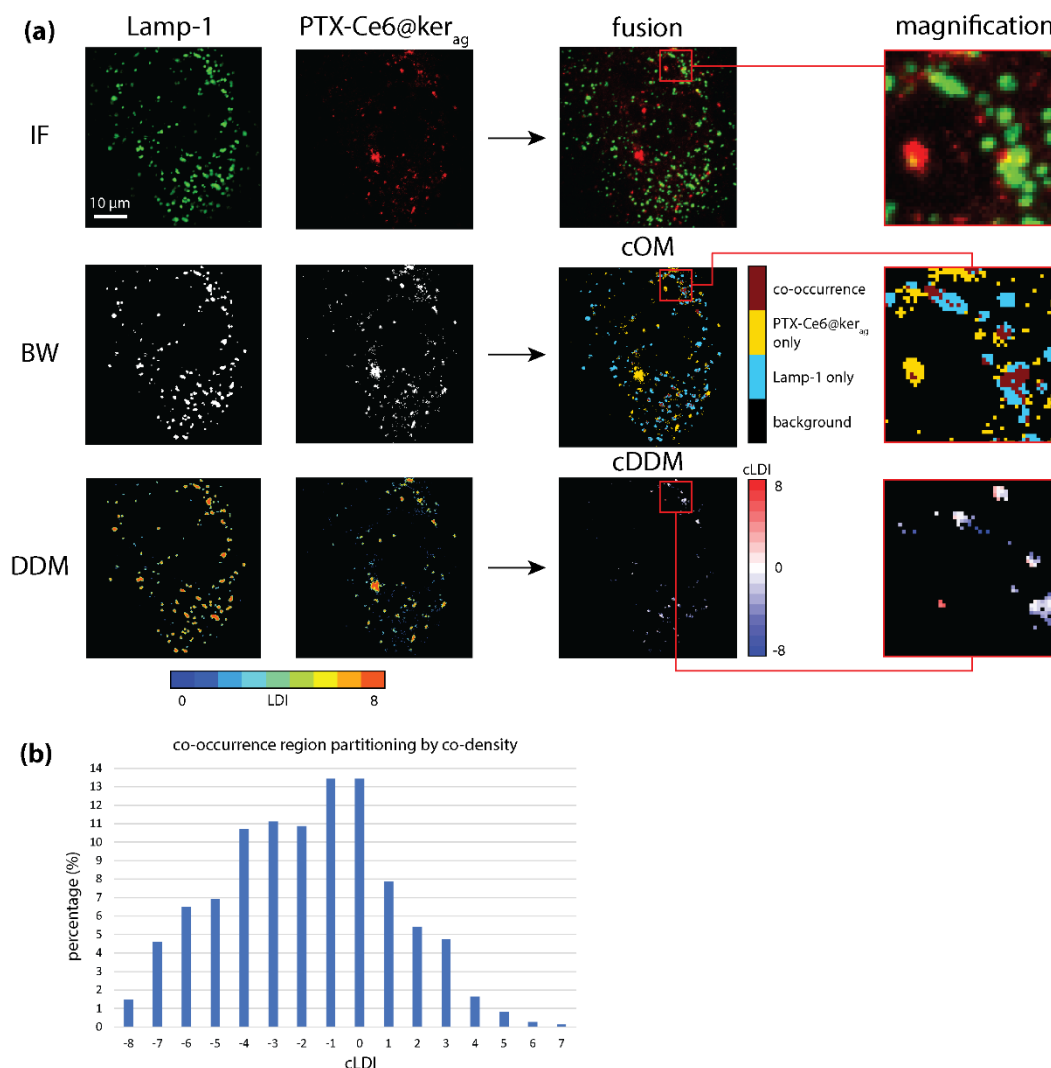


Figure 5.12. cDDM discloses information about the degree of colocalization. (a) Top: Exemplificative immunofluorescence (IF) images of MG-63 cells exposed to PTX-Ce6@ker_{ag} NPs, marked against late endosomes (Lamp-1), with Ce6 (NPs), or both (fusion). Middle: Lamp-1 and Ce6 signals' binary masks (BW), whose combination produce the co-occurrence map (cOM). Bottom: Lamp-1 and Ce6 DDMs and cDDM. (b) Bar graph of co-occurrence region partitioning by co-density, showing a prevalence of negative cLDI values that indicate NPs as generally denser than late endosomes. Image reproduced from [205] under the CC-BY Creative Commons Attribution 4.0 International licence.

We find that 19% of Ce6 signal overlaps with 17% of the Lamp-1 signal, with compatible MOC=0.16 and ρ =0.17. Such low MOC and ρ values are explainable by the small and sparse nature of the marked structures, which can also explain the low correlation values between marker local densities (Table 5.5, first and second columns).

Table 5.5. Comparison between Lamp-1 and PTX-Ce6@ker_{ag} intensity and local density colocalization analysis, before and after refinement for local co-density.

	Lamp-1-Ce6		
	co-occurrence region ($n^1=737$)		co-density region ($n^1=99$)
	Intensity	Density	Intensity
ρ	0.1666	0.1278	0.5156
ρ_s	0.1656	0.1270	0.4353
MOC	0.1564	0.1669	0.9059
M_1	0.1852	0.1662	0.0246
M_2	0.1712	0.1958	0.0275

¹ n : sample size, *i.e.*, number of considered pixels.

However, the fact that the co-density-based refinement increases the correlation coefficients values while decreasing the area of investigation (and consequently M_1 and M_2 value) hints at the capability of our method to selectively retain the colocalization between signals, more so than with false positives.

The cOM (Figure 5.12 (a)) indicates the presence of signals overlap spots (Figure 5.12 (a), red spots in cOM magnification) enclosed in single-marker spots (Figure 5.12 (a), blue and yellow regions in cOM magnification), suggestive of NPs internalization into late endosomes. The cDDM (Figure 5.12 (a)) further separates co-occurring pixels by cLDI, reporting co-densities dispersed across the cLDI range, with 11 out of 16 cLDIs capturing at least 5% of co-occurring pixels and only 13% of co-occurring pixels being also equally dense (*i.e.*, cLDI=0, Figure 5.12 (b)). The similarity of all coefficient values between the first and second columns of Table 5.5 indicates the local density as being an indicator of colocalization, at least as valid as pixel intensity. Restricting correlation analysis to pixels with cLDI=0 strongly increases ρ and ρ_s values (Table 5.5, third column), suggesting the existence of a real, although spatially limited, colocalization. Its detection by

correlation coefficients is initially weakened by the scarcity of marked structures within the co-occurrence region, but subsequently strengthened by cDDM-driven increase in analysis specificity. Moreover, co-density analysis reveals that Ce6 signal tends to be locally denser than Lamp-1, as attested by the prevalence of negative values in the cDDM (Figure 5.12 (b)). This last finding, in agreement with expectedly denser NPs due to their nanoformulation [244], also suggests that NPs' internalization into late endosomes could occur at a ratio higher than 1:1, with many NPs entering the same endosomes at once. On one hand, this is positive for the pharmacokinetic-improving function of the developed system, but on the other hand, it opens to the possibility that a different nanoformulation, producing less dense NPs, could result in better colocalization values and NPs internalization.

In summary, the local co-density analysis here improves colocalization quantification under different aspects. First, it advances the intensity correlation analysis, identifying the sub-regions where a stronger colocalization is likely to occur. Second, it provides indication about the degree of colocalization (here, the degree of internalization) that, in this case, is suggested to also occur at ratios different from 1:1. Finally, the cDDM also allows the formulation of new biological hypotheses, whose verification could lead to improvements in the developed drug delivery system.

cDDMs Open to The Formulation of New Biological Considerations

The third dataset analysed is part of a study aimed at investigating the myelination pattern in whole spinal cord coronal section, hence requiring lower resolution and greater image size with respect to previously discussed datasets. Specifically, the NF200-FM dataset concerns the assessment of co-distribution of axons, visualized by NF-200 immunostaining (red), and the surrounding myelin sheaths, visualized by Fluoromyelin (green) in rat spinal cord (Figure 5.13 (a), top).

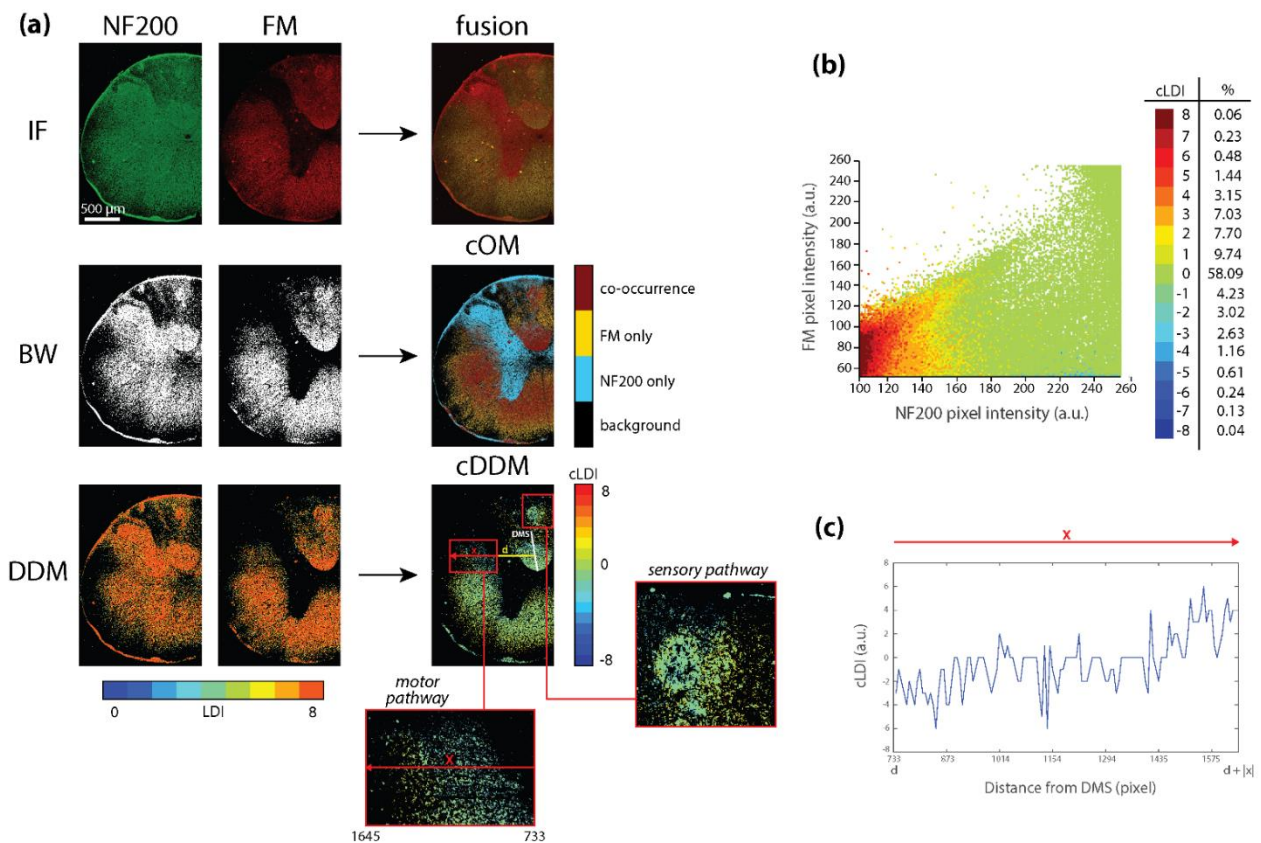


Figure 5.13. cDDM opens to the formulation of new biological considerations. (a) Top: Exemplificative immunofluorescence (IF) images of rat spinal cord, marked against the axonal (NF200), the myelin (FM) components of the cord, or both (fusion). Middle: NF200 and FM signal binary masks (BW), whose combination produce the co-occurrence map (cOM). Bottom: NF200 and FM DDMs and cDDM. (b) Scattergram of NF200 and FM signals intensity colour-coded by cLDI, showing a clear prevalence of equi-density pixels (grey, cLDI=0). (c) The line plot reports the cLDI values underlying the horizontal red arrow (x) inside the “motor pathway” magnification. The cLDI medio-lateral distribution is shown in function of the pixel distance (d , yellow line) from the dorsal median sulcus (DMS, white line), highlighting a progressive myelin thinning from spinal cord centre to periphery. Image reproduced from [205] under the CC-BY Creative Commons Attribution 4.0 International licence.

Both ascending and descending sensory and motor pathways run in the spinal cord and the quantitative evaluation of respective distribution in low-power micrographs would permit a rapid quantitative evaluation in physiological and pathological conditions, for example, after spinal cord injury. The cOM (Figure 5.13 (a)) well presents a dorso-ventral pattern, reasonably reflecting the distribution of sensory versus motor pathways. In fact, ascending sensory paths, localized in the dorsal funiculus and the external part of the lateral funiculus,

reveal a different signals' co-density compared to the other areas of the white matter, occupied by descending motor paths (Figure 5.13 (a), cOM, the two magnifications). Motor and sensory pathways are quite different under many aspects, such as axonal density, myelin sheaths thickness and percentage of unmyelinated fibres [297]. In particular, axonal density and myelin sheath thickness are lowered in sensory paths. The cDDM (Figure 5.13 (a)) further investigates the co-occurrence region, in which the intensity correlation is quite fair, but the overlap is suspiciously high ($\rho=0.55$, $MOC=0.57$, Table 5.6, first column).

Table 5.6. Comparison between NF200 and FM intensity and local density colocalization analysis, before and after refinement for local co-density.

	NF200-FM		
	Co-Occurrence Region ($n^1=1465036$)		Co-Density Region ($n^1=851042$)
	Intensity	Density	Intensity
ρ	0.5535	0.2064	0.6508
ρ_s	0.3760	0.2520	0.5031
MOC	0.5741	0.7221	0.9782
M₁	0.4909	0.5060	0.2983
M₂	0.6772	0.6601	0.4212

¹ n : sample size, *i.e.*, number of considered co-occurring pixels.

Such an MOC value could be read as an artifact of the offsets that seem to characterize the FM signal (shifted up, scatterplot Figure 5.13 (b)), that have been proved to positively affect the MOC, especially when a scarce correlation between the intensities is found [266]. In this sense, a less biased measure of co-occurrence can be derived from the cOM and the M_1 and M_2 coefficients. Most probably, these results (Table 5.6, first and second columns) can be interpreted as an artifact of image resolution, which is not able to fully capture the concentric nature of the myelin signal, surrounding the axon, without overlapping. In any case, these results confirm the outcome of cDDM already seen in Lamp1-Ce6, where a reduction of the signals co-occurrence is coupled with a marked increase in correlation values (ρ and especially ρ_s value, Table 5.6, third column). In fact, the resolution problem seems to be alleviated by our approach, indeed reducing the signals overlap, quantified by M_1 and M_2 of about 40%. The increase in correlation

coefficients also indicates that markers intensities should not be assumed a priori to linearly correlate, according to the functional heterogeneity of axons and myelin distribution in the tissue. Even though most of the co-occurring pixels are also equally dense (58%, $cLDI=0$, Figure 5.13 (b)), a remarkable prevalence of positive values in cDDM indicates axons tendency to be denser than myelin, agreeing with the reduced myelin sheaths thickness observable for some pathways. Indeed, a lower myelin thickness reasonably reflects a lower local density of FM, but not of NF200 signal, therefore bringing higher cLDI values and decorrelating the two markers density (Table 5.6, second column). Moreover, by locally analysing cDDM, we can see that the local density pattern depends on the nature of the anatomical pathway (Figure 5.13 (a), cDDM left magnification), specifically being enriched in low values (hence, in myelin) in the proximity of the dorsal median sulcus (DMS) and in high values (hence, in less myelinated axons) away from it (Figure 5.13 (c), line plot of the pixel values underlying the red line in cDDM motor pathway magnification). In conclusion, besides exemplifying its applicability at the tissue level, here the cDDM also provides new biological information, revealing and mapping the spatial heterogeneity of the myelination pattern, which could not be derived from the original image. This makes the local co-density an effective indicator of the local degree of myelination and the cDDM a possible discriminator of neuronal pathways.

GUI for cDDMs Creation

To allow any user to work with coDDM we developed *coDDMaker*, a software endowed with a user-friendly GUI, created with MATLAB® App Designer (Figure 5.14). The software is conceived as an upgrade of the DDMaker software [130] and permits the performance of a density-including colocalization analysis of two markers co-distribution.

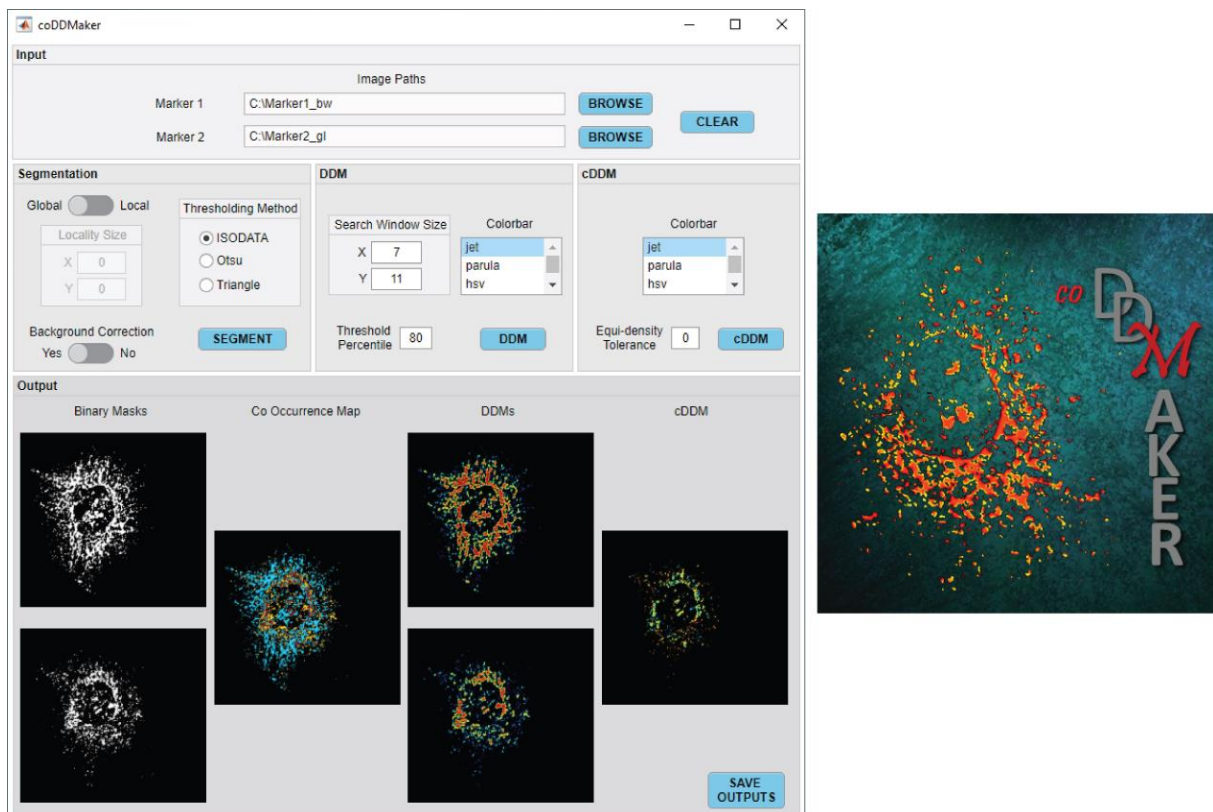


Figure 5.14. Main GUI and logo of *coDDMaker*. The main window is divided into five sections: *Input*: to select the input images folders; *Segmentation*: to select the thresholding method, its locality of application and to eventually perform background correction before threshold calculation and image binarization; *DDM*: to select the search window size for local density analysis and to allow user creating and binarizing DDMs after setting the colorbar for pseudo-colour DDMs visualization and the percentile for DDMs thresholding; *cDDM*: to allow user creating and binarizing cDDMs after setting, the colorbar for pseudo-colour cDDMs visualization and the tolerance for equi-density region segmentation; *Output*: to visualize and save intermediates and outputs. From left to right: markers binary masks, cOM, pseudo-colour DDMs, pseudo-colour cDDM. Image reproduced from [205] under the CC-BY Creative Commons Attribution 4.0 International licence.

coDDMaker was conceived for the guided analysis of the distributions and co-distribution of marker pairs. Starting from RGB, grey level or directly binary images and based on customized search WS, the software builds the markers DDMs, cDDM and cOM and tabulates their numerical content. With coDDMaker, we also introduce a module for the background correction of non-binary input images [298] and a module for their local segmentation to also be used as tools for image denoising and correction of distortions.

First, the user is required to select the two folders (*i.e.*, one for each marker to be analysed) where the input images to be processed are located. Images can either be RGB colour, grey level, or binary, in the MATLAB-supported formats [299]. The user can binarize RGB and grey level images by choosing among ISODATA or Otsu thresholding method. With coDDMaker, the user can now also decide to apply the thresholding algorithm locally, by specifying the locality dimension. The Triangle method is also supplied for global image thresholding, where it can serve outliers removal in heavy-tailed histograms. In addition, images can now be pre-processed for the correction of uneven illumination that may result from vignetting distortion, inaccurate image acquisition or noise [298]. Binary masks, resulting from thresholding or already provided by the user, serve as the input for building the DDMs, cDDM and cOM. Local density analysis is performed using a default $WS=3$, chosen assuming that the target structures of interest in the images are of few pixels, thus enabling the detection of small aggregation events and single particles as well. However, users can customize the search WS , besides the colorbar for maps visualization. The resulting DDMs can be binarized by percentile thresholding, while the equi-density region, identified in the cDDM by $cLDI=0$, can be binarized by setting a co-density tolerance (*e.g.*, a tolerance of 2 identifies as co-dense pixels with $cLDI$ ranging from 0-2 to 0+2). To help the user in finding the best parameter setting for its analysis, coDDMaker also displays the last binary mask for each marker and the derived DDMs, cDDM and cOM. When satisfied with the setting, the user can save all the intermediate and final outputs of the analysis, which include all the generated images and maps and the numerical data associated to DDMs and cDDMs. The images are saved in uncompressed “.tiff” format, while other analyses outputs are saved as portable csv and excel files. A detailed explanation of coDDMaker utilization can be found in the software documentation [299].

The software completes the colocalization analysis of a couple of images under standard setting (*i.e.*, global image segmentation and $WS=3$) in less than 30 sec on entry-level computers, although the total elapsed time strongly depend on different factors (*e.g.*, the size of the objects to be segmented), as exemplified in Table 5.7.

Table 5.7. *coDDMaker* time performance evaluation.

Image size	Background correction	WS (image segmentation) ¹	WS (density analysis)	Elapsed Time ²
1024×1024	No	Global	3	20''
512×512	No	Global	3	15''
512×512	Yes	Global	3	20''
512×512	Yes	3	3	50''
512×512	Yes	15	3	1'20''
512×512	Yes	15	9	1'25''

¹Otsu thresholding method. ²Local density and co-density analysis in a couple images on a PC endowed with Intel i3-4005U, 1.70 GHz processor, and 8 GB RAM.

As before, the software does not require any training or expertise before use. As much as *DDMaker*, or even more so, *coDDMaker* could serve as a checkpoint for long-lasting experiments, follow-up and large-scale studies, that can be monitored on-line and adjusted on the basis of the software feedbacks, therefore, optimizing time and costs. *coDDMaker* is available as a public open-source software written in MATLAB® and as a 64-bit stand-alone application [299].

5.6 Conclusions

Image colocalization is commonly assessed by a combination of co-occurrence and correlation. However, all current methods exploiting pixel intensities neglect information regarding pixel interconnections that, if considered, could permit the enforcement of colocalization information. In this perspective, we introduce the co-density distribution map as a novel tool for improving the actual colocalization analysis framework in biomedical images. Given two imaged markers and built their *DDMs*, the *cDDM* uniquely describes the distribution of the signal local densities, in terms of relative position and abundance of marked structures. When imaging objects above the pixel resolution, the *cDDM* also becomes a powerful indicator of colocalization, which can identify the image regions at which colocalization is stronger, adding reliability to the correlation coefficients normally employed. Conversely, regions where colocalization is weaker are disregarded by the *cDDM* method, method, that can therefore be used also as a density-based

denoising tool. The cDDM also provides information about the degree of colocalization, which can complement and validate quantitation by other methods. Most importantly, cDDM information is, altogether, qualitative, quantitative and local, making it a powerful tool for the fast and comprehensive inspection of imaged systems. Consequently, it can open the door to new biological considerations, both at the global and the regional level. Working locally, DDM (and cDDM consequently) can increase the confidence of colocalization when this is not achievable by increasing the acquisition resolution, thus enhancing the information regarding distributions. Notably, our maps can be applied to any resolution study. In addition, being easy to build, the cDDM can benefit routine, large-scale and follow-up experiments by providing a tool for near real-time monitoring to be used for the adjustment and optimization of experiments. In practice, the cDDM we propose represents a fundamental tool to be integrated into each colocalization analysis framework, whether it is based on intensity correlation or not, to be used synergically with correlation analysis by masking the original images before computing the different coefficients. Even though it provides only an indication and not a direct measure of the degree of colocalization and, at present, it only works for the colocalization of two signals, the cDDM can be used to answer a variety of biological questions involving protein–protein interactions or co-compartmentalization.

5.7 Content-aware contribution and future developments

Just as stated for DDM (Sect. 4.7), the interdisciplinary and content-aware nature of my approach permitted me to better estimate cDDM necessity in the framework of both our specific experimental goals and general scientific scenario, therefore sustaining the method and software conceiving and development. Additionally, thanks to my biological formation I could choose the best datasets in my hand to demonstrate the validity of the cDDM method, as I could indeed hypothesise a priori the expected colocalization features basing on the images biological content. Finally, my biological formation drove the elaboration of the concept of degree of colocalization and, remarkably, its separation from the

concept of molecular stoichiometry of interaction, with which I found it is often riskily and erroneously confused.

As far as the future development of cDDM method is concerned, the main issue to address, that has already emerged in this first method presentation, is the overlooking by the method of positional information in the co-density pattern. Indeed, colocalizing image signals by definition must appear with the same connecting pattern of pixels. Therefore, colocalization can be surely improved by cDDM introduction, as it moves from being estimated on the sole pixel intensity to also their connectivity. However, at the current state, the method considers only the *number* of pixels connection, but not their *position*. Therefore, the cDDM method could be improved by introducing a *pattern matching* constrain on the definition of the image sub-region within which quantify colocalization (Figure 5.15).

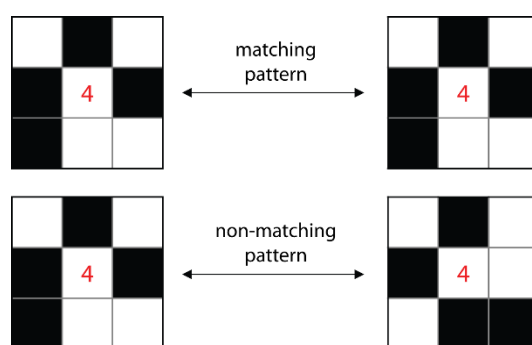


Figure 5.15. Pattern matching approach for colocalization quantification. The cDDM method can be improved by including in the equi-density region all pixels with $cLDI=0$, but only if they are also defined by a same neighbourhood configuration (*i.e.*, matching pattern).

The introduction of a pattern matching constrain also opens for the quantification of the probability of colocalization. Following a combinatory statistical approach, the probability to observe colocalization of two imaged markers m_1 and m_2 at the pixel $p(x, y)$ can be defined as the joint probability of marker signals co-occurrence, co-density and pattern matching:

$$\begin{aligned}
P_{\text{colocalization}} &= P_{\text{co-occurrence}} \cdot P_{\text{co-density}} \cdot P_{\text{pattern matching}} = \\
&= \frac{1}{\text{BW range width}} \cdot \frac{1}{\text{cDDM range width}} \cdot \frac{1}{\text{possible configurations}} = \quad (5.5) \\
&= \frac{1}{2} \cdot \frac{1}{n} \cdot \frac{1}{\binom{n}{k}} = \frac{1}{n} \cdot \frac{k!(n-k)!}{n!}
\end{aligned}$$

Where:

- BW range width is the number of possible pixel value in the binary masks (that is 0 or 1, *i.e.*, 2) identifying m1 and m2 occurrence region
- cDDM range width (*i.e.*, n) is the number of possible cLDI values
- k is the LDI value of the co-dense pixel $p_{(x,y)}$ (*i.e.*, $\text{cLDI}_p=0$).

In turn, the (key) value of n can be calculated as:

$$n = 2 \cdot \Delta x \cdot \Delta y - 1 - \text{BG}_{\text{cDDM}_p} \quad (5.6)$$

where Δx and Δy are the dimensions of the search window size and $\text{BG}_{\text{cDDM}_p}$ is the number of cDDM background pixels included by the search window in the neighborhood of pixel p. Therefore, $\text{BG}_{\text{cDDM}_p}$ acts as a correcting factor for the calculation of the probability of colocalization at the co-occurrence region edges, lowering the number of possible co-densities accordingly to local border indentation.

Though preliminary and very naïve in its formulation, the inclusion of the pattern matching constrain and the (local) estimation of the probability of colocalization is believed to be the ultimate contribution to the creation of a stand-alone comprehensive tool capable of providing a new indicator of colocalization, merging the information from pixel intensity and density.

Finally, among our future perspective there is also the biological validation of the method through nearfield biophysical techniques such as FRET, to confirm that the colocalization quantified by our maps does reflect a real interaction between molecules.

Chapter 6

Content-aware approach in oncology: RNA:DNA hybrids role in tumour stress response by automated quantitative imaging

After theoretically introducing preclinical models (Chapter 2) and imaging modalities (Chapter 3), and after presenting our main cross-topic methodological results (DDMs, Chapter 4, and cDDMs, Chapter 5), the next three Chapters present the interdisciplinary collaborative projects that have characterized this PhD, where we developed on-purpose imaging solutions to different biomedical problems. Importantly, it will be discussed how the automated quantitative imaging performed with a *content-aware* approach has led to significant methodological and biological improvements of our analyses.

In this Chapter, we present the application of our content-aware approach to the phenomization of tumour cell response to stress by confocal fluorescent imaging. The study was composed of two main investigation blocks. The first block identifies the role of onco-suppressor p53 and of the macromolecule group of RNA:DNA hybrids in tumour response to cell irradiation (IR). The second block expanded the investigation on RNA:DNA hybrids role in cell response to a p53-defective context and to a new source of stress, different from IR.

In Sect. 6.1, the collaboration framework is first introduced. Then, in Sect. 6.2, the biological and image processing theoretical background for our image analysis is discussed. Subsect. 6.2.1 summarises the controversial state of the art for RNA:DNA hybrids, while Subsect. 6.2.2 briefly discusses geodesic reconstruction

by dilation, a method that enabled the image segmentation of RNA:DNA hybrids structures in spite of their unfixed size. Sect. 6.3 introduces the state of the art, surveying the abscopal effect, tumour cell response to stress and current methods for RNA:DNA hybrids imaging. Besides presenting the developed methods for image analysis, the successive Material and Methods (Sect. 6.4) covers also the previous steps of sample preparation and image acquisition. However, for a comprehensive understanding of our work, Results and Discussion (Sect. 6.5) also includes the main molecular results of the study, besides all image analysis results. Finally, after drawing the main conclusions (Sect. 6.6), the contribution of the content-aware approach to the study is recalled, together with future perspectives (Sect. 6.7).

6.1 Study context

At the beginning of the first year, we started the two-year PHENOMICS Project in collaboration with the Radiobiomics and Drug Discovery Unit of the IRCCS-IRST (Meldola, FC). The main goal of PHENOMICS (cancer stress PHENomics: autOmatic Microscopic image analysis for *in vitro* phenotypization of heterogeneity of stressed tumor Cells) was the functional *in vitro* phenotypization of tumour cells stress response through automatic microscopic quantitative imaging. The Project stemmed from some important experimental *in vivo* observations related to the onset of radiation-induced *abscopal effect*, which is observed when localized radiation induces a systemic antitumor response, leading to the shrinking or disappearance of tumours in distant body districts not directly targeted by therapy. Such data firstly casted doubts on immune system sole involvement in abscopal effect mediation, opening for possible additional or alternative mechanisms, to be investigated at the cellular level.

The Project activities can be grouped in two main research blocks. First, we focused on the role of the onco-suppressor p53 in tumour response to irradiation, in the framework of abscopal effect. This first part of the study identified a class of molecules, generally recalled as RNA:DNA hybrids, as partly responsible for conveying a senescence message out of IR cells, capable of reaching the unirradiated (UnIR) tumour masses. Once defined the pivotal role of wtp53 and

RNA:DNA hybrids in tumour cell response to irradiation stress, the second research block expanded the investigation on RNA:DNA hybrids role to a p53-defective context and to a new source of stress, that is oxidative stress. For both research blocks, my activity consisted of characterizing the subcellular distribution of marked molecules of interest in confocal microscopy images, to gain insight into their function in stress response. The characterization concerned – mainly but not only – RNA:DNA hybrids, and required the development of a robust pipeline for structure segmentation, able to efficiently define the objects of interest independently of cell line, source of stress, and nature of marked molecules.

6.2 Theoretical background

6.2.1 RNA:DNA hybrids

During transcription, the nascent RNA very transiently anneals to the single-stranded (ss) DNA template within the active site of the RNA polymerase, giving rise to a short transient double-stranded (ds) RNA:DNA hybrid, which is resolved by release of the nascent RNA through a dedicated channel [300]. More stable RNA:DNA hybrids can form by very same mechanism behind the polymerase, and are feasible to level up to three-stranded R-loop structures by coiling with the displaced ss DNA. However, it is still hard to separate nuclear R-loops from RNA:DNA hybrids, to the point that the terms are mostly used interchangeably, to refer to a unique class of molecules. Despite their accidental origin, R-loops (and so RNA:DNA hybrids) are widespread in the genome and enriched at active genes, where they have been surprisingly found to play physiological roles. R-loops are indeed crucial for many cellular processes such as transcription activation and termination [301, 302], chromatin organization and chromosome segregation [301, 303-305], immunoglobulin class switching recombination of B cells in vertebrates [306], CRISPR-Cas9 gene editing [307] and telomere homeostasis [308]. However, R-loops persistence or mislocation inside cell nucleus has been reported to interfere with DNA replication, repair and transcription, therefore leading to double-stranded DNA breaks (DSBs), genomic instability and ultimately to many diseases onset, including cancer [309, 310]. To keep the genome stable, cells have

evolved a slew of mechanisms to prevent aberrant RNA:DNA hybrids accumulation. However, when these mechanisms fail to contain them, hybrids start to accumulate and to damage the genome. Many factors have been identified as involved in promoting, avoiding or resolving RNA:DNA hybrids formation. The Rad51 protein, for example, is a major player in homologous recombination during DNA repair of DSBs, and has been shown to promote the strand exchange necessary for hybrids formation. Surprisingly, hybrids have been found to accumulate more at Rad51 absence, especially inside cell cytosol [311, 312]. Here, the exonuclease TREX1 is the main responsible for the degradation of unwanted ss DNA, ds DNA and RNA:DNA hybrids. Defects in TREX1 have been indeed associated to hybrids cytoplasmic accumulation, too [313]. Today, it is well acknowledged that cytoplasmic RNA:DNA hybrids have a pro-inflammatory role as activators of the cGAS-STING pathway, a component of the innate immune system that helps tissues in contrasting tumorigenesis, viral infections, and invasion by some intracellular bacteria, by triggering the expression of inflammatory genes that can lead to cellular senescence or to the activation of defence mechanisms through the exportation of molecular messages in the tumour microenvironment [314]. However, despite more than four decades of investigation, we are still far from elucidating the complexity of RNA:DNA hybrids functioning inside and outside the cell.

6.2.2 Geodesic reconstruction

Image segmentation (Subsect. 4.2.2) is the process of partitioning a digital image into multiple image regions made of sets of pixels that share salient characteristics, such as colour, intensity, or texture. Here, we shall take the perspective that there are essentially two kinds of image segmentation, depending on the characteristics of the objects of interest. In the first case, the image contains textured objects and is partitioned into regions that share a characteristic set of features (in principle, an object can be composed of more sub-regions). In the second case we speak of “particles”, meant as usually small objects where the texture cannot be assessed nor used as a discriminating factor. In this case, objects are defined as coherent and connected sets of pixels (*i.e.*, each object is unitary), this meaning that the extraction

of object contour become fundamental. However, it may happen that particles touch one another, or even partially overlap, thus needing for a processing method able to separate them by introducing as little error as possible. One smart solution makes use of geodesic functions, exploiting the idea that each particle is centred around its marker, a smaller object that uniquely identifies the particle itself. In this Chapter, the marked structures in fluorescent images are always particles. The pipeline (Figure 6.1 (a)) is the following: first, the particles are collectively defined by conservative thresholding, resulting in a unique binary mask whose foreground includes all particles, with different degrees of overlap. Then, for each particle a marker is identified by ultimate erosion. Binary erosion (Subsect. 5.2.1) is a morphological operation that erodes the boundaries of foreground regions, thus shrinking them in size and enlarging object holes. By ultimate erosion (Figure 6.1. (b)), the foreground is iteratively eroded, and its components progressively shrunk and separated from the rest of the set, stopping right before they are completely removed from the image. Finally, using the pre-erosion binary mask as a marker, the shape of distinct particles is recovered by geodesic reconstruction by dilation. Oppositely to binary erosion, binary dilation enlarges the boundaries of foreground regions, making objects bigger and holes smaller. By geodesic dilation (Figure 6.1 (b)), the particle markers are iteratively dilated by a predefined circle-shaped structuring element (*geodesic ball*, here of 1-pixel radius), bounded by the pre-erosion binary mask. At each dilation, each marker can “conquer” the binary mask pixels that have not yet been subdued by another marker. This way, each pixel of the binary mask is associated to its closest marker, and particle boundaries indirectly defined by a minimum distance principle [315].

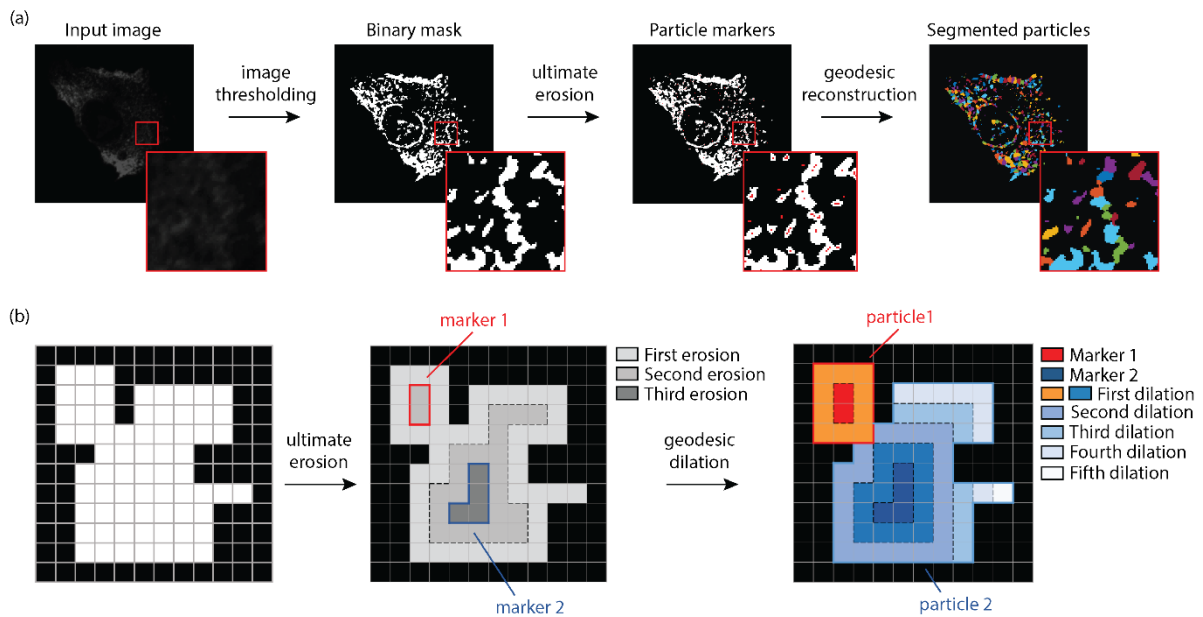


Figure 6.1. Particle segmentation by geodesic reconstruction. (a) Starting from an input grey level image, the particle signal is binarized by an appropriate method. Then, particle markers are extracted by ultimate erosion. Finally, markers are “grown” back into the initial binary mask by geodesic dilation, until full assignment of binary mask’s pixels to the closest marker. (b) Ultimate erosion consists of iterative object erosion carried out for $n-1$ steps, where n is the number of erosions necessary to make a marker disappear. Starting from identified markers, geodesic dilation consists of masked iterative dilations, in which each new pixel identified by dilation is assigned to the closest marker.

6.3 State of the art

One of the most adopted strategies for solid tumours treatment is local radiotherapy (RT), that exerts its clinical effects within the irradiated field for locoregional tumour control. However, regression in metastatic lesions distant from IR field, albeit uncommon, has been described in patients with different types of cancer including non-small cell lung cancer (NSCLC) [316–320]. This phenomenon, first described in 1953 and named “abscopal effect” (AE) [321], has been an enigma for the scientific community for many years. A growing body of evidence addresses the immune system activation as the dominant player in radiation-induced AE [322-325]. However, there is very few knowledge about the molecular mechanisms involved. Camphausen et al. in 2003 [325] firstly linked functional p53 to radiation-induced AE in mice. After his pioneering work, it has been confirmed that numerous cancer cell lines carrying wtp53 develop hallmarks

of therapy-induced senescence (TIS) in response to DNA-damaging stresses, such as radiation or oxidative stress [322, 326]. Recent literature has shed light on the importance of cytoplasmic nucleic acid sensors in DNA-damage response (DDR). Indeed, when DNA is damaged, the misplaced nucleic acids into the cytoplasm engage evolutionary-conserved sensors that trigger inflammation, IFN α / β pathways and, as recently hypothesized, the establishment of senescence-associated pro-inflammatory secretome [257]. Besides dsDNA and ssDNA, double-stranded RNA:DNA hybrids have been surprisingly found in the cytosol of a variety of cell lines acting as activators of the cGAS-STING pathway, triggering the expression of inflammatory genes that can lead to cellular senescence or to the activation of defence mechanisms through the exportation of molecular messages in the tumour microenvironment [327, 328]. Intriguingly, it was also reported that RNA:DNA hybrids may be largely constituted by transposable elements, in particular, long interspersed element-1 (LINE-1), the most ubiquitous transposable element in the mammalian genome, and proposed as hallmark of aging [327, 329].

Despite their rise in prominence, the rules that govern RNA:DNA hybrids formation and dynamics are still controversial, and technical improvements that permit the measurement of their turnover are hugely required to distinguish and quantify stable and transient hybrids. New technical advances in hybrids mapping, such as DNA–RNA immunoprecipitation sequencing and ribonuclease H1 (RNaseH1) chromatin immunoprecipitation [302], have allowed the assessment of RNA:DNA hybrids distribution and dynamics throughout the genome. However, these techniques do not apply to investigation outside of the nuclear compartment. Though concerns about its specificity have been raised more than once [330, 331], the S9.6 antibody still represents one of the main solutions for hybrids detection and, at present, the only available antibody for hybrids detection by fluorescence microscopy. However, when coupled with rigorous quantitative image analysis it can still provide insights about the radiomorphometry of hybrids distribution, necessary to collect information about their subcellular location and function in response to treatment. In this perspective, we have also developed a novel tool for the local density mapping of fluorescent marked molecules, including RNA:DNA hybrids immunostained with S9.6 antibody [130].

In this study, we demonstrated that single high dose irradiation significantly inhibits tumour growth in contralateral non-irradiated (NIR) xenografts mice, only subordinately to the presence of functional p53 in both IR and NIR tumours. Moreover, we showed that *in vitro* IR A549 cells adopt a senescence-associated secretory phenotype (SASP) secreting CD63 positive extracellular vesicles (CD63+ EVs) loaded with RNA:DNA hybrids and LINE-1 retrotransposon inducing senescence of distant NIR cells. Finally, we demonstrated that RNA:DNA hybrids intracellular levels and localization can still be affected in p53-defective cells, when a source of oxidative stress is provided.

6.4 Material and methods

Cells

A549 cells (adenocarcinomic human alveolar basal epithelial cells, ATCC, Rockville, MD) were cultured in F12K medium (ATCC) supplemented with 10% FBS (Euroclone, Milan, Italy). H1299 cells (human non-small lung adenocarcinoma cells, ATCC) were cultured in RPMI 1640 medium (ATCC) supplemented with 10% FBS (Euroclone) and glutamine 2 Mm (Euroclone). HeLa cells (human cervix adenocarcinoma, ATCC) were cultured in EMEM medium (ATCC) supplemented with 10% FBS (Euroclone), 1% penicillin/streptomycin (GE Healthcare, Milan, Italy) and 2% amphotericin B (Euroclone). 3.0×10^4 A549 cells/well were infected with either lentiviruses LV-THM-sh-scr (scrambled shRNA, control) or LV-THM-shp53 at MOI 10 TU/cell, as previously described [245] to generate A549sh/scr (control) and A549sh/p53 cell cultures. 3.0×10^4 H1299 cells/well were transfected with wtp53-expressing vector [332] (1 μ g/well) with TransIT®-LT1 Transfection Reagent (Thermo Fisher Scientific, Milan, Italy) and used after 72 h to create a H1299p53+ (control) culture. All cultures were checked periodically for mycoplasma contamination using the MycoAlert™ Mycoplasma Detection Kit (Lonza, Basel, Switzerland). Both cell lines were expanded and maintained as a monolayer at 37 °C and subcultured weekly.

***In vitro* cell treatment**

A549, A549sh/p53, H1299 and H1299p53+ cells were 1× γ -IR at 10 Gy or 20 Gy using the linear accelerator Elekta Synergy Platform system (Elekta Oncology Systems, Stockholm, Sweden) as detailed before [246]. HeLa cells were either subjected to irradiation (RAD) or oxidative (OX) treatment. RAD treatment consisted of 1× γ irradiation at 2 Gy, 7.5 Gy, 10 Gy or 20 Gy as in [246]. OX treatment consisted of: a) 72 h of hypoxic culturing conditions (37°C, 1% O₂); b) full cell growth under normoxic conditions (37°C, 21% O₂), followed by 1 h of cell exposure to hyperbaric oxygen (37°C, 1.9 ATA HBO) and then 24 h of normoxic culturing conditions; c) a sequential combination of hypoxic culturing conditions (48 h, 37°C, 1% O₂) and cell exposure to hyperbaric oxygen (1 h, 37°C, 1.9 ATA HBO). HBO treatment was performed in a hyperbaric chamber expressly designed for preclinical studies [333]. First, the air inside the chamber is replaced with 100% O₂ and the pressure increased for 15 min until 1.9 ATA are reached and maintained for 1 h. Finally, decompression from 1.9 ATA back to atmospheric pressure is gradually performed over 15 min.

Fluorescent microscopy

Cells were either fixed and permeabilized with ice-cold methanol or paraformaldehyde, stained with 1 μ g/mL 4',6-diamidino-2-phenylindole (DAPI), incubated (overnight at 4 °C) with primary anti-S9.6 antibody (1:100, Kerfast, Boston, MA, USA), anti-CD63 antibody (1:150, Abcam, Cambridge, UK) or anti-ORF1 antibody (1:1000, Sigma-Aldrich, St. Louis, MO), PBS washed, and incubated with secondary goat anti-mouse Alexa Fluor 546 (Life Technologies, Carlsbad, CA) overnight. Cells were imaged with an inverted confocal laser-scanning microscope Eclipse Ti2-e (Nikon Corporation, Tokyo, Japan) equipped with NIS-Elements software. 12-bit images were acquired with a Plan Apo 60×/1.4 oil objective with XY pixel size of 0.1 μ m and an optical sections number sufficient for the full scan of cell volumes. For each treatment conditions, at least 30 cells among at least 6 images are acquired.

Image segmentation

All following procedures were implemented in MATLAB® (R2019a v.9.6.0, The MathWorks, Natick, MA, USA). Acquired 3-D 2-channel confocal images were first summarised in 2-D single-channel images (MIPs) by maximum intensity projection, and further quantized to 8-bit for denoising purposes. For each image, single cell border, single nuclei, single cytoplasm and foci of marked structure were segmented by our own developed pipeline (Figure 6.2).

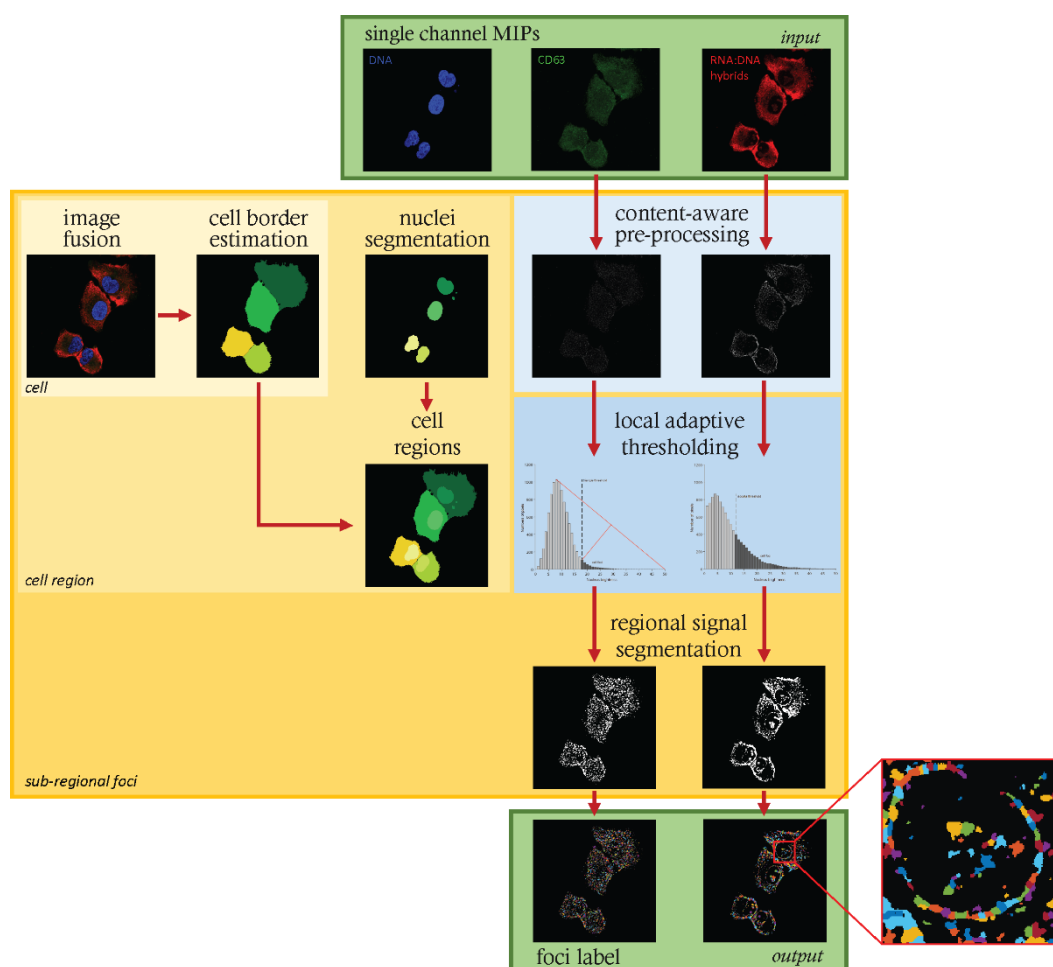


Figure 6.2. Method pipeline for RNA:DNA hybrids, CD63+ EVs and ORF1+ retrotransposons foci segmentation. 2-channel (DAPI+marker) confocal stacks are first summarised as single channel MIPs. From their combination (fusion), the cell border can be estimated as conservatively as possible. The nuclear envelope is outlined from DAPI signal and the cytoplasm region segmented by difference. Within each region, markers (S9.6, CD63 or ORF1) signal is pre-processed and adaptively segmented in coherent particles of different size, called foci, that constitute the analysis unit for following analyses.

Starting from DAPI staining, the nuclear region was segmented by global (A549, H1299) or local (Hela, OX) intensity thresholding by ISODATA method [334], followed by area-based object retainment (threshold setting by triangle method [335]). As an exception, IR HeLa cell nuclei were segmented by computing the image local median map [336] and thresholding it at the 50th percentile. Single cell borders were conservatively outlined by fusion of 8-bit single-channel MIPs, image binarization at histogram mode, and finally by separation of touching cells by watershed transform [337]. Single-cell nuclei and cytoplasms were then segmented from previously obtained binary masks using logical operators. Subregional cell foci segmentation was finally carried out in three steps. First, the 2-D single-channel MIP of CD63+ signal was pre-processed by top-hat transform [125] by an EVs-sized structuring element, to enhance most informative signal foci in cell cytoplasm. This step was not needed for RNA:DNA hybrids and ORF1 retrotransposons, which have no fixed size. Then, by mean of single-cell nuclei and cytoplasms masks, the signal was separately segmented inside each cell nucleus and cytoplasm by local median map computing and thresholding at the third quartile. Finally, single foci were segmented by ultimate erosion and geodesic reconstruction by dilation (Subsect. 6.2.2) [315]. Additionally, hybrids nuclear clusters were separated from nuclear foci on a size basis, set after preliminary experiment, and further distinguished in perinuclear and nucleolar clusters basing on their contiguity with the nuclear membrane.

Local density analysis

Local density analysis was performed by computing the density distribution map (DDM) of each cell, as described in [130] and Chapter 4, using a minimal 3×3 search window. Each pixel was thus assigned with a local density index (LDI) ranging from 0 for isolated pixels to 8 for full-connected ones, and the distribution was quantified and visualized in colormaps that associate each local density with a different colour.

Assessment of results

At the regional level (*i.e.*, whole nucleus and whole cytoplasm), abundance of markers foci (*i.e.*, RNA:DNA hybrids, CD63+ EVs and ORF1+ retrotransposons) and clusters (RNA:DNA hybrids) was quantified through measurements of their number (normalized by region area), size and brightness. Given the small dimension of imaged structures, possibly close to pixel size, we here introduced a new feature, the Foci Granulation Index (FGI, *i.e.*, the percentage of regional foci having 1-pixel area) to quantify those hybrids foci occurring at a size close to the resolution limit. By definition, FGI does not apply to nuclear cluster analysis. Finally, RNA:DNA hybrids distribution in HeLa cells was also investigated by local density analysis. When coupled with global measurements, DDMs permit to investigate whether regional phenomena are mirrored at the subregional local level, or if a subregional homogeneity is wrongly assumed and summarized in a regional measure.

Statistical analysis

Data deviation from normality is early verified by histogram inspection, followed by the Shapiro-Wilk test, based on which the discriminatory power of descriptors is assessed by either two-tail Student's t-test or Wilcoxon rank-sum test with Bonferroni correction for unequal sample size. p-values < 0.05 are considered for statistical significance.

6.5 Results and discussion

Radiation treatment induces SASP in A549 cells *in vitro*

Over the years, several hypotheses have been put forward to explain the molecular mechanisms behind the indirect anticancer effects of radiotherapy outside the radiation site. Choosing solid murine tumours in immunocompetent mice as a model, Camphausen et al. [325] firstly demonstrated that p53 is a key mediator of the IR-induced AE *in vivo*, suggesting its action as a transcription factor for the expression and a release in the tumour microenvironment (TME) of

cytokines or other factors, leading to a systemic antiangiogenic antitumor effect. Tesei et al. [18], using solid xenograft tumours in athymic immunocompromised mice, first confirmed the necessity of functional p53 in both IR and NIR tumour masses for AE observation, further proving AE independence from T cells and reporting the presence of IL6 and senescent cells in contralateral NIR mass. To investigate whether AE could be ascribed to the release of pro-senescence molecules from IR cells, senescence markers expression *in vitro* was quantified. We found that A549 (p53+) but not H1299 (p53-) exhibited a senescence profile after irradiation with a dose of at least 10 Gy, with increased levels of p53 and its target gene p21^{Waf1/Cip1}, and expression of IFN- β , IL-1 α , IL6 and NF- κ B. A549sh/p53 cells exhibited only a limited expression of these markers [18]. SASP onset in A549 cells was ultimately confirmed by the collection of increasing amounts of CD63+ EVs from culture medium, not observable for A549sh/p53 cells. However, the significant radiation dose-dependent increment of EVs production observed in H1299 cells led to the exclusion of p53 involvement in modulating EVs secretion upon irradiation.

Image analysis after CD63 signal revealed a significant increase in this exosome marker fluorescence intensity in A549 cells, proportional to radiation dose (Figure 6.3 (a, b), 3-fold increase after 10 Gy, $p < 0.001$). Conversely, the CD63 signal intensity was significantly decreased in irradiated H1299 (Figure 6.3 (c, d), -50% after 10 Gy, $p < 0.001$) and significantly attenuated in A549sh/p53 cells, consistently with previous results (Figure 6.3 (e, f), -29% after 10 Gy, $p < 0.01$).

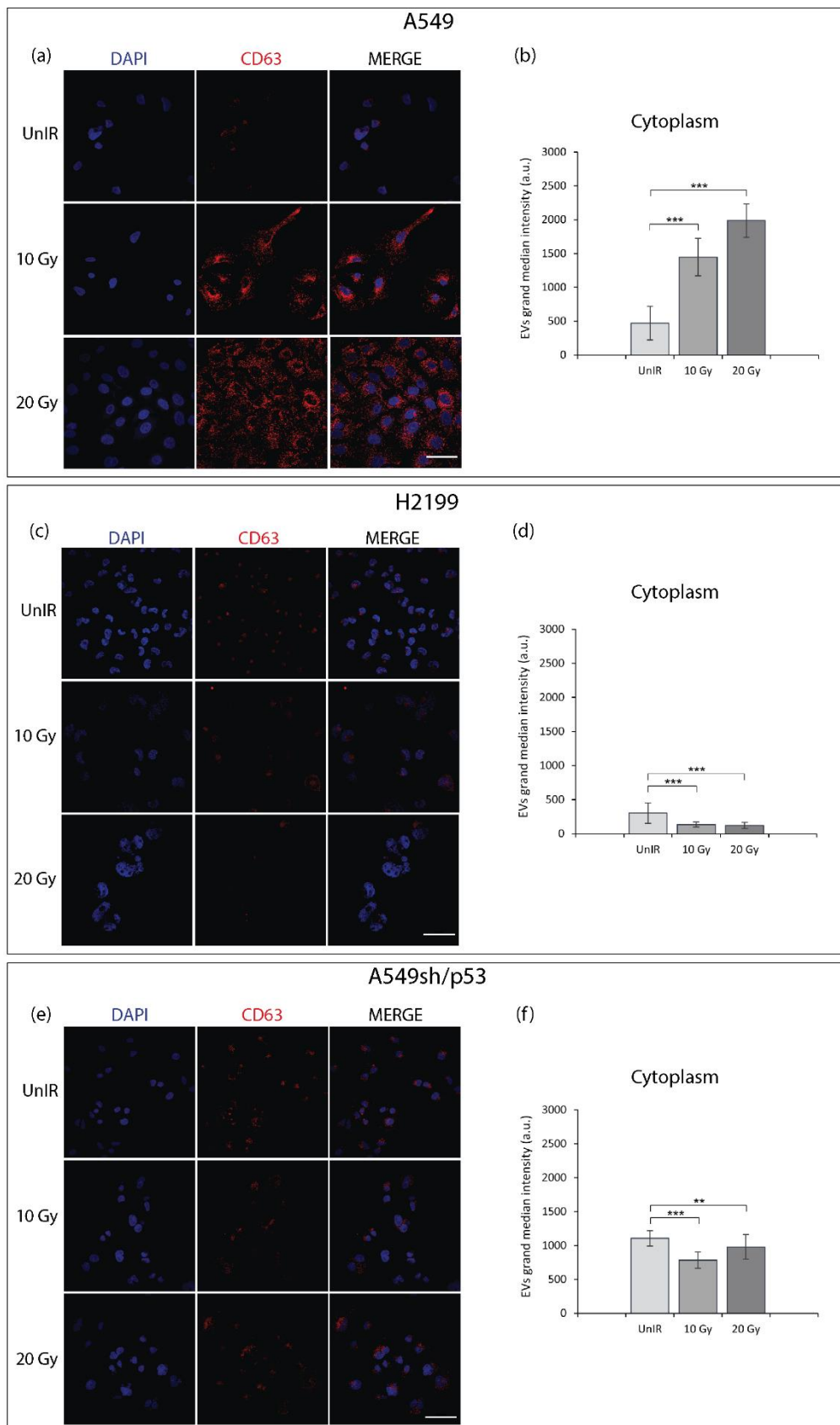


Figure 6.3. CD63+ EVs subcellular distribution in IR NSCLC cells. Representative images of A549 (a), H1299 (c) and A549sh/p53 (e) cells exposed to 10 Gy or 20 Gy IR. Scale bars: 50 μ m. Cytoplasm CD63+ foci intensity quantification in A549 (b), H1299 (d) and A549sh/p53 (f) cells, reported as grand median \pm MAD. * $p < 0.05$, ** $p < 0.01$, *** $p < 0.001$. Image reproduced from [18] under the CC-BY Creative Commons Attribution 4.0 International licence.

Radiation induces secretion of EVs carrying RNA:DNA hybrids in wtp53 NSCLC cells

Since the cytoplasmic misplacement of nucleic acids has recently been suggested in the establishment of the senescence-associated pro-inflammatory secretome [257], we investigated RNA:DNA hybrids subcellular distribution upon irradiation. Interestingly, RNA:DNA hybrids staining intensity was significantly reduced in the cytoplasm of IR H1299 (Figure 6.4 (c, d), -58% after 10 Gy, $p < 0.001$) and IR A549sh/p53 cells (Figure 6.4 (e, f), -46% after 10 Gy, $p < 0.001$) but not in IR A549 cells, where a not significant yet remarkable intensity increase was observed at a dose of 10 Gy (Figure 6.4 (a, b)). Furthermore, radiation exposure induced significant cluster accumulation of RNA:DNA hybrids in the nuclei of IR A549 cells (Figure 6.4 (a, b), +35% after 10 Gy, $p < 0.001$) but not in IR H1299 (Figure 6.4 (c, d), -38% after 10 Gy, $p < 0.05$) and IR A549sh/p53 (Figure 6.4 (e, f), -64% after 10 Gy, $p < 0.001$). To investigate whether the wtp53-dependent increase of RNA:DNA hybrids resulted in their secretion outside the cells, we investigated through dot blot analysis their presence in EVs isolated from conditioned media of A549, H1299, and A549sh/p53 cells after different radiation doses. The presence of RNA:DNA hybrids were detected in 10 Gy-IR A549 EVs but not in the microvesicle (MV) fraction. Conversely, neither EVs nor MVs secreted by H1299 and A549sh/p53 were positive for the presence of RNA:DNA hybrids. (Figure 6.4 (g)). Involvement of p53 in RNA:DNA hybrids secretion through EVs was further supported by transient ectopic expression of wtp53 in H1299 cells. Comparably to A549, IR H1299p53+ cells released EVs but not MVs loaded with RNA:DNA hybrids (Figure 6.4 (g)), with a senescent phenotype similar to that observed in IR A549 cells. Accordingly, the EVs secreted by H1299p53+ carrying RNA:DNA hybrids also significantly inhibited the colony growth, and induced senescent phenotype of H1299 p53+ [18]. As a further control, IR A549 3-D spheroid, bringing a better representation of TME, were assessed for senescence, confirming a strong positivity to β -Gal assay, a significant induction of the SASP driver molecules p21^{Waf1/Cip1}, INF- β and IL6, and a massive nuclear production of RNA:DNA hybrids after 10 Gy, but not after 20 Gy, according to confocal image analysis [18].

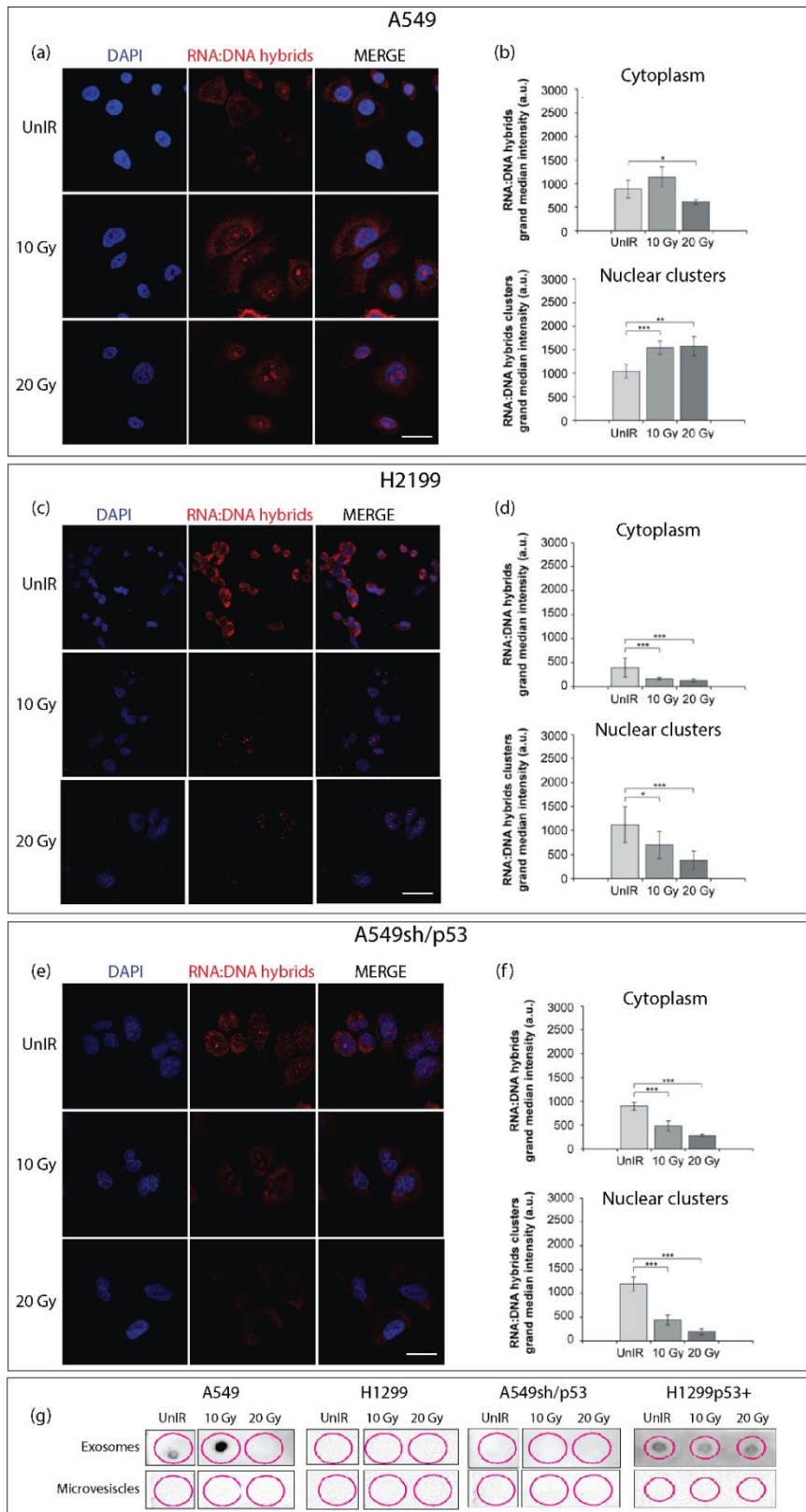


Figure 6.4. RNA:DNA hybrid subcellular distribution in IR NSCLC cells. Representative images of A549 (a), H1299 (c) and A549sh/p53 (e) cells exposed to 10 Gy or 20 Gy IR. Scale bars: 25 μ m. Quantification of cytoplasm RNA:DNA hybrids foci and nuclear RNA:DNA hybrids clusters intensity in A549 (b), H1299 (d) and A549sh/p53 (f) cells, reported as grand median \pm MAD. (g) Dot blot analysis of RNA:DNA hybrids EVs or MVs fraction 72 h post-irradiation and immunoblotted with S9.6 antibody. * $p < 0.05$, ** $p < 0.01$, *** $p < 0.001$. Image reproduced from [18]

IR A549 cells deliver abscopal signals through EVs loaded with RNA:DNA hybrids

Confocal analysis revealed that UnIR A549 cells exposure to EVs secreted by 10 Gy-IR A549 did not affect cytoplasmic hybrids (Figure 6.5, (a, b)) but significantly increased RNA:DNA hybrids intensity of nuclear foci and clusters (Figure 6.5 (c, d), +78% on average from unexposed cells, $p < 0.001$). Moreover, UnIR A549 cells exposed to EVs from IR A549 (10 Gy or 20 Gy) induced in recipient cells β -Gal positivity, increased expression of p21^{Waf1/Cip1} and IL6, significant inhibition of colony-forming ability and, according to *in vivo* results, polarization of both human and murine macrophage toward M1 pro-inflammatory phenotype [18].

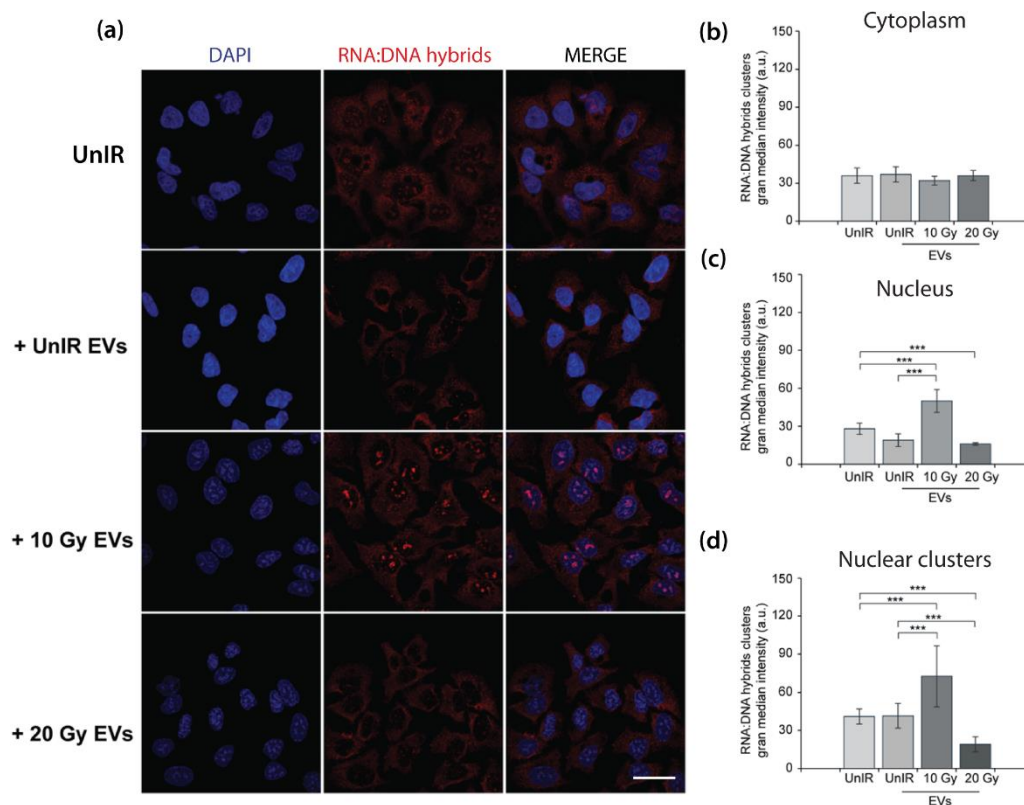


Figure 6.5. RNA:DNA hybrid subcellular distribution in UnIR A549 cells exposed to IR A549 EVs. (a) Representative images of unexposed UnIR A549 cells and UnIR A549 cells exposed to EVs isolated from culture medium of A549 cells non irradiated or irradiated at 10 Gy or 20 Gy. Scale bar: 25 μ m. Quantification of cytoplasmic (b) and nuclear (c) RNA:DNA hybrids foci and nuclear RNA:DNA hybrids clusters (d) intensity in UnIR A549 cells exposed to EVs from IR A549 cells, reported as grand median \pm MAD. * $p < 0.05$, ** $p < 0.01$ *** $p < 0.001$. Image reproduced from [18] under the CC-BY Creative Commons Attribution 4.0 International licence.

All considered, the data collected so far strongly support the hypothesis that -ether with cellular senescence, apoptosis and innate immunity may drive the abscopal effect in our *in vivo* and *in vitro* model. Of note, we observed that a minimum radiation dose of 10 Gy was needed for the establishment of a SASP phenotype characterized by a large cytoplasmic amount of tetraspanin CD63, an increase of RNA:DNA hybrids in p53+ cells nuclei and cytoplasm, and the secretion of hybrids-loaded EVs capable to induce SASP and reduce cell growth in recipient cells.

Irradiation induces the activation of LINE-1 retrotransposon in p53wt-bearing A549 cells.

To explore the possibility that RNA:DNA hybrids may be constituted by LINE-1 retrotransposon, previously proposed as hallmark cellular senescence [329], we analysed the expression level of both ORF-1 protein and ORF-1/ORF-2 mRNA in A549 and A549sh/p53 cells (Figure 6.6).

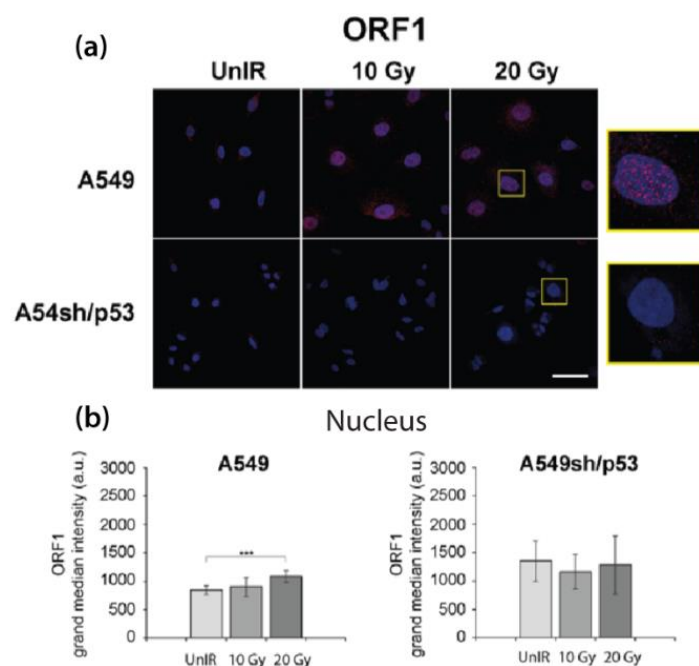


Figure 6.6. Retrotransposon ORF1 subcellular distribution in A549 and A549sh/p53 cells. (a) Representative images of A549 and A549sh/p53 cells exposed to 10 Gy or 20 Gy IR. Scale bar: 50 μ m. (b) Quantification of nuclear ORF1 retrotransposons foci intensity in A549 and A549sh/p53 cells, reported as grand median \pm MAD. * p <0.05, ** p <0.01 *** p <0.001. Image reproduced from [18] under the CC-BY Creative Commons Attribution 4.0 International licence.

Confocal analysis showed that both cell lines expressed LINE-1, but only in IR A549 a significant increase in ORF1 nuclear foci intensity was detected (Figure 6.6, +28% after 20 Gy, $p < 0.001$). Notably, co-labelling of ORF1 and RNA:DNA hybrids in A549 yielded a Mander's overlap coefficient (MOC) increasing with radiation dose and reaching statistical significance at 20 Gy (5-fold increase from UnIR, $p < 0.01$), whereas an opposite MOC trend was observed in IR A549sh/p53. Furthermore, a significant increase in ORF1 and ORF2 mRNA ($p < 0.05$) levels was observed in IR A549 cells, but not in IR A549sh/p53 cells, while RNA:DNA hybrids were reduced in both IR and UnIR A549 cells by the IR pre-treatment with Efavirenz, an antiretroviral agent that also abolished their inhibitory effects on colony-forming ability of UnIR A549 ($p < 0.001$).

It was previously reported that exposure to genotoxic stress, such as irradiation, often leads to the loss of global DNA methylation primarily from repetitive elements, in particular, LINE-1 [338]. The activation of LINE-1 elements may induce the synthesis of high amounts of RNA:DNA hybrids at the nuclear level, that therefore exit the nucleus in a process that mirrors the self-retrotranscription activity of retrotransposon elements, that also requires a cytoplasmic step before returning to the nucleus [339]. Furthermore, a large number of p53-responsive elements and p53 DNA binding sites were reported in LINE-1 elements, part of which were functional and served the increase of LINE-1 mRNA expression levels [340]. Therefore, it is not unreasonable to hypothesize that RNA:DNA hybrids conveyed by EVs secreted by IR p53+ cells are at least partly constituted by LINE-1 retrotransposons.

Irradiation decreases RNA:DNA hybrids production and affects their condensation in a dose-dependent fashion in p53-defective HeLa cells

Once established the pivotal role of p53 and RNA:DNA hybrids in tumour cell response to high-dose irradiation stress, we further investigated hybrids subcellular distribution in p53-defective HeLa cells including lower radiation doses of 2 Gy and 7.5 Gy and a different (*i.e.*, oxidative) stress [19]. According to the absence of functional p53, IR globally decreased RNA:DNA hybrids density (Figure 6.7 (a)) and intensity (Figure 6.7 (b)) in HeLa cells, showing similar trends for cell nucleus and cytoplasm.

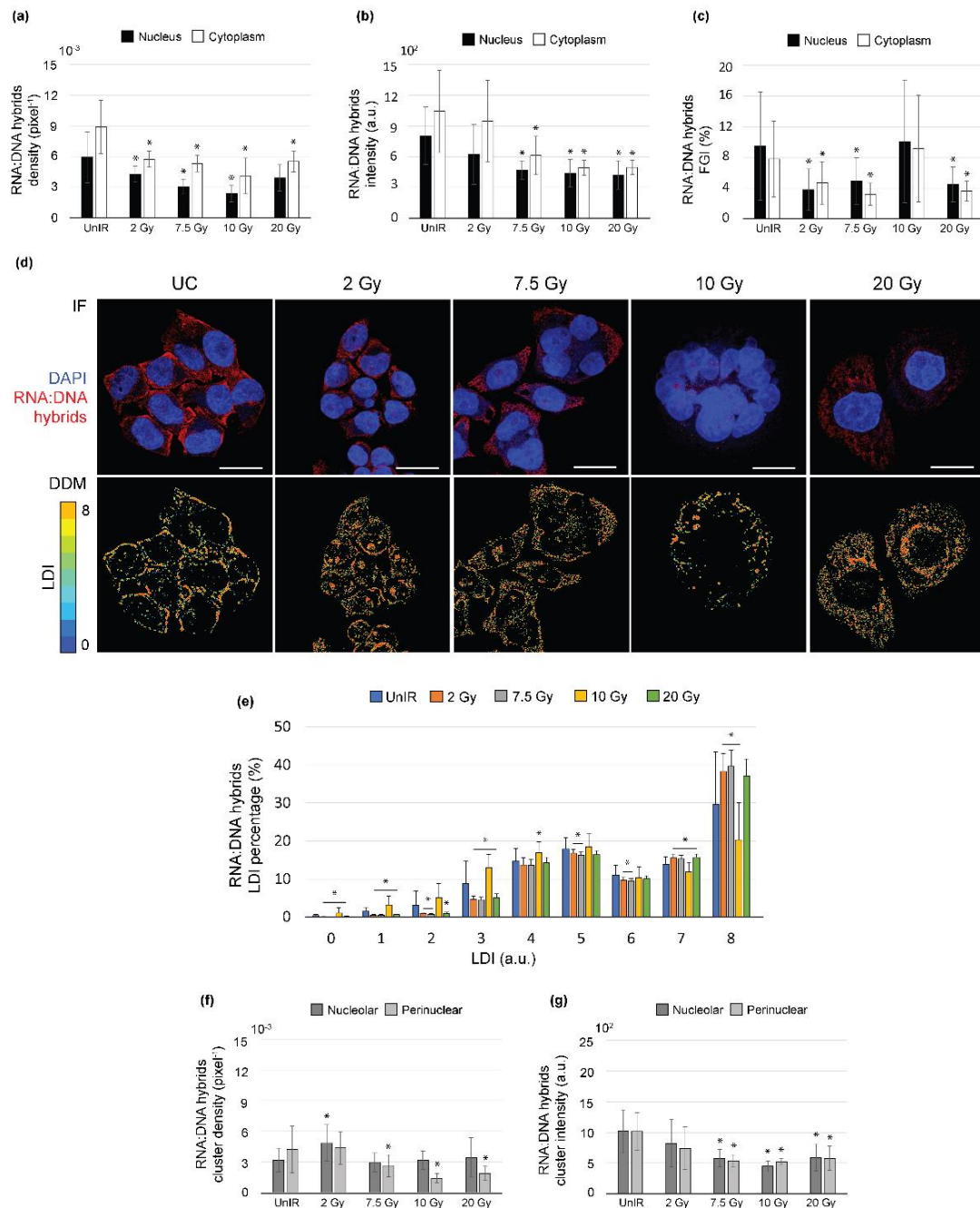


Figure 6.7. Effects of RAD treatments on RNA:DNA hybrids subcellular distribution in HeLa cells. Bar graphs of hybrids foci weighted number (density) (a), intensity (b) and FGI (c) in the main cell compartments, reported as median \pm MAD (a, b) and as mean \pm STD (c). (d) Representative RGB MIPs (IF, up) and DDMs (down) of HeLa cells unirradiator (UnIR) or irradiated at 2 Gy, 7.5 Gy, 10 Gy or 20 Gy, stained for DNA (blue) and immunolabeled against RNA:DNA hybrids (red). Scale bars: 25 μ m. (e) Bar graph of LDI percentages, reported as mean \pm STD. Bar graphs of hybrids perinuclear and nucleolar clusters density (f) and intensity (g) in the main cell compartments, reported as median \pm MAD. * p <0.001. Image reproduced from [19] under the CC-BY Creative Commons Attribution 4.0 International licence.

While a dose of 2 Gy moderately decreased hybrids foci number (Figure 6.7 (a), -32% on average, $p < 10^{-5}$), higher doses halved both hybrids number (Figure 6.7 (a), -48% on average, $p < 10^{-5}$) and intensity (Figure 6.7 (b), -47% on average, $p < 10^{-7}$). As cytoplasm hybrids are considered to derive from nuclear displacement [257], the parallel decrease in hybrids foci number and intensity in both nucleus and cytoplasm suggested an IR-induced declining in their production and a consequent exportation to cytoplasm. Also, the exception represented by the 2 Gy dose suggested it as a too mild stress for hybrids remarkable alteration, appreciable only from 7.5 Gy on. To investigate foci condensation, we introduced the Foci Granulation Index (FGI), that is a measure of the percentage of 1-pixel foci. Consistently with regional number, hybrids FGI was significantly decreased at all tested doses in both cell nucleus and cytoplasm (Figure 6.7 (c), -52% on average, $p < 10^{-4}$), except at 10 Gy. Accordingly, only 10 Gy-irradiated cells displayed a local hybrid distribution comparable to that of UC (Figure 6.7 (d), DDMs), with dense cytoplasmic hybrids crowding at the nuclear and cell membrane. Conversely, at 2 Gy, 7.5 Gy and 20 Gy hybrids appeared more and more scattered in the cell cytoplasm, with nuclear clusters appearing at 2 Gy and then gradually disappearing with dose from nuclei. Quantitatively, doses of 2 Gy, 7.5 Gy and 20 Gy induce a strong increase of high local densities (Figure 6.7 (e), LDI=7-8, +21% on average, $p < 10^{-6}$), at the expense of lower ones (Figure 6.7 (e), LDI=1-6, -41% on average, $p < 0.002$). Conversely, a dose of 10 Gy increased the presence of low and medium densities (Figure 6.7 (e), LDI=0-5, +69% on average, $p < 10^{-3}$), while decreasing the higher ones (Figure 6.7 (e), LDI=6-8, -17% on average, $p < 10^{-3}$). Therefore, DDMs and FGI indicated that IR induced hybrids condensation, except for the 10 Gy dose. The discordance between regional foci number, FGI and DDMs (Figure 6.7 (a)) revealed the heterogeneity of cell response, that produces subregional variations in foci number and intensity that cannot be summarized in a regional measure, at least after 10 Gy irradiation. Finally, an IR dose of at least 7.5 Gy decreased perinuclear cluster number (Figure 6.7 (f), -56% on dose average, $p < 0.002$) and both perinuclear and nucleolar clusters intensity (Figure 6.7 (g), -47% on average, $p < 10^{-3}$).

All considered, ionizing radiations can be speculated to reduce the RNA:DNA hybrids production in a dose-dependent manner, at least in HeLa cells. Dose

dependency of hybrids production had been only marginally investigated before [313], demonstrating the need for a functional p53 for IR-induced hybrids reduction. Accordingly, ionizing radiations decrease hybrids presence in HeLa cells, where p53 is essentially inactivated by HPV E6 protein. Interestingly, also the expression of the DNA exonuclease TREX1 has recently been proved to be dose-dependently induced by ionizing radiations [313]. Given TREX1 capability to remove cytosolic endogenous DNA and hybrids [256], dose-dependency of hybrids accumulation should be also examined in the perspective of being just a mirror of their degradation. Finally, according to our previous findings, hybrids crowding at the main cell membranes, especially evident at 10 Gy, could be read as a pro-exportation event, that could mirror EVs accumulation in multivesicular bodies (MVBs) before exiting the cell. Interestingly, given p53 absence in HeLa cells, this would mean that p53 is more necessary to hybrids production, rather than exportation. However, these hypotheses need solid confirmation by further experiments.

Perturbation of culture oxygenation increases RNA:DNA hybrids production and condensation in p53-defective HeLa cells.

Perturbation of oxygenic culture conditions globally increased the RNA:DNA hybrids foci number (Figure 6.8 (a)) and intensity (Figure 6.8 (b)), in both nucleus and cytoplasm of HeLa cells [19]. Specifically, the hybrid foci number was significantly increased under hypoxic conditions, especially inside cell nucleus (Figure 6.8 (a), +36%, $p=10^{-13}$), whereas hybrids intensity was increased after every perturbation of culture oxygenation, especially after HBO exposure and inside cell nucleus, where it is more than doubled (Figure 6.8 (b), +117%, $p=10^{-42}$). As cytoplasm hybrids are considered to derive from nuclear displacement [257], increase in foci number and intensity value in both compartments can reflect an increase in hybrids nuclear production and consequent exportation to cytoplasm, with no remarkable constrain [328].

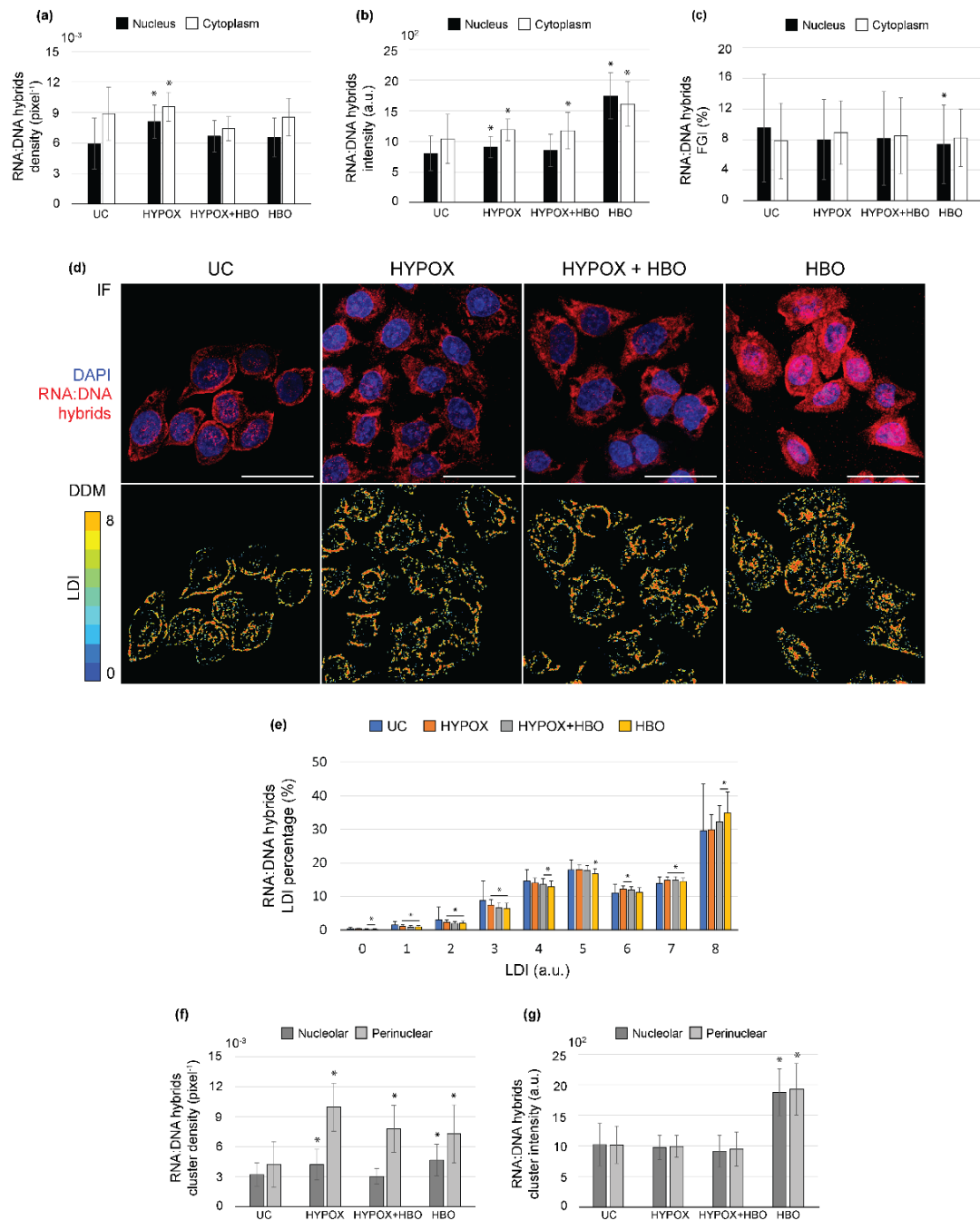


Figure 6.8. Effects of OX treatments on RNA:DNA hybrids subcellular distribution in HeLa cells. Bar graphs of hybrids foci weighted number (density) (a), intensity (b) and FGI (c) in the main cell compartments, reported as median \pm MAD (a, b) and as mean \pm STD (c). (d) Representative RGB MIPs (IF, top) and DDMs (bottom) of HeLa cells cultured under normoxic (UC), hypoxic (HYPOX), hyperoxic (HBO) or combined (HYPOX+HBO) conditions, stained for DNA (blue) and immunolabeled against RNA:DNA hybrids (red). Scale bars: 25 μm . (e) Bar graph of LDI percentages, reported as mean \pm STD. Bar graphs of hybrids perinuclear and nucleolar clusters density (f) and intensity (g) in the main cell compartments, reported as median \pm MAD. * $p < 0.001$. Image reproduced from [19] under the CC-BY Creative Commons Attribution 4.0 International licence.

The fact that hypoxic and hyperoxic conditions triggered a similar response could be ascribed to their common capability to promote intracellular oxidative stress through massive production of reactive oxygen species (ROS) [333, 341]. Different culture oxygenation levels are likely reflected in different intracellular concentration of ROS, that directly determines the extent of DNA breaks, from which hybrids are known to arise [342, 343]. Moreover, ROS and hybrids involvement in a common pathway is supported by the pro-inflammatory role of both [333, 344]. Accordingly, the cell culturing under sequential hypoxic and hyperoxic conditions almost never altered hybrids foci number or intensity, thus indicating that hyperoxic conditions can alleviate the stress caused on cells by hypoxia, as well acknowledged in HBO therapy [345]. In both cell nucleus and cytoplasm, under hypoxic conditions hybrid foci were more numerous (Figure 6.8 (a), +18% on average, $p < 10^{-8}$) but much less bright (Figure 6.8 (b), -92% inside nucleus, $p = 10^{-47}$, -36% inside cytoplasm, $p = 10^{-22}$) than under hyperoxia. This discrepancy pointed at different RNA:DNA hybrids foci condensation states under the two conditions, possibly dependent on oxygen level. To investigate the cause of such a difference, we analysed FGI and DDMs. Low and not significant differences between cytoplasmic hybrid FGI under hypoxic and hyperoxic conditions (Figure 6.8 (c), 8% average difference, $p \geq 0.06$) indicate that such imbalance between foci number and intensity was not due to a poor image resolution, insufficient to capture hybrids smaller than 1 pixel, but derived from a different foci distribution. To deepen the investigation, we performed a local density analysis by creating Density Distribution Maps (DDMs) [130], revealing different distribution of local densities under hyperoxic and hypoxic conditions (Figure 6.8 (d)). With respect to hypoxia, hyperoxia was significantly enriched in maximum local density (Figure 6.8 (e), LDI=8, +17%, $p = 10^{-24}$) at the expense of the lowest ones (Figure 6.8 (e), LDI=0-7, -11% on average, $p < 10^{-4}$), indicating more densely packed hybrids under hypoxia. A similar though milder response than hyperoxia was reported for the combinatory treatment. Qualitatively, DDMs depicted more similarities between signal distributions under hypoxic and hyperoxic conditions. In particular, the hybrids gathering at the cell membrane in UC cells was coupled to a scattered hybrids signal in cell cytoplasm after every treatment of the OX group, especially the hyperoxic one. Moreover, DDMs

highlighted dense hybrid clusters inside hyperoxic nuclei, as foreseen by FGI decrease. Accordingly, the analysis of nuclear clusters revealed an increase in perinuclear clusters number after every perturbation of culture oxygenation (Figure 6.8 (f), +97% on average, $p < 10^{-13}$) and an increase in perinuclear clusters intensity under hyperoxic conditions (Figure 6.8 (g), +89%, $p = 10^{-33}$). Similarly, hyperoxia also increased the hybrids nucleolar clusters intensity (Figure 7.8 (g), +84%, $p = 10^{-22}$) and number (Figure 6.8 (f), +45%, $p = 10^{-5}$), this latter variation also being induced by hypoxia (Figure 6.8 (f), +31%, $p = 10^{-5}$). Collectively, oxidative stress seemed to promote nuclear hybrids production and condensation in clusters, especially in consequence of hyperoxic culture conditions. Nucleolar clusters can be properly thought as to identify with cell nucleoli, in which hybrids have been often reported to accumulate, especially in stressed cancer cells [18, 346, 345]. On the other hand, increased perinuclear cluster may hint at over-produced hybrids that accumulate at the inner surface of nuclear membrane, before being exported to cytoplasm [328].

Despite being “only” imaging based, additional data on HeLa cell, investigating also low IR doses and a new source of stress, brings manyfold implications. First, being differently affected by different type of stress, RNA:DNA hybrids presence can be said to be stress-related but not stress-specific. Secondly, our data confirm that ionizing radiation capability to boost hybrids production requires the presence of a functional p53. On one hand, this implies that exists at least a p53-independent pathway for hybrids production stimulation, activatable by oxidative stress stimuli, alternative to radiation exposure. In particular, our results suggest that RNA:DNA hybrids could be strongly induced in the absence of a functional p53 by hyperbaric oxygen, a well-established treatment used as an adjunctive therapy in many disease settings. On the other hand, it indicates that stress could promote hybrids production independently of its nature, consistently with their capability to activate the pro-inflammatory cGAS-STING pathway [310]. Finally, even if in absence of EVs collection data, our DDMs quantification of hybrids accumulation at the main cell membranes suggest RNA:DNA hybrids exportation from cell nucleus to cytoplasm [257] and to TME, where they have

been found to convey a message of senescence stimulating innate immune response [18].

6.6 Conclusions

With the PHENOMICS Project we investigated the involvement of the onco-suppressor p53 and RNA:DNA hybrids in tumour response to stress *in vivo* and *in vitro*. We demonstrated that a single high-dose irradiation of 20 Gy and the presence of functional p53 in both IR and contralateral NIR tumour masses are necessary to observe the abscopal effect in an *in vivo* immunocompromised murine model. We further demonstrated that this threshold dose must be lowered to 10 Gy to reproduce the phenomenon *in vitro* at the cellular level, namely by triggering the expression of pro-inflammatory genes, inducing M1 macrophage polarization and setting a SASP through the production and exportation of a senescence message composed of RNA:DNA hybrids and retrotransposons. Finally, we collected evidence for RNA:DNA hybrids to work as SASP and inflammation mediators also when the stress source is different from ionizing radiation, and when p53 is non-functional or absent. All considered, a model for p53-mediated abscopal effect induced by radiotherapy can be produced (Figure 6.9). Our data suggest that p53 selectively regulates the secretion of CD63+ EVs carrying a senescence message composed of RNA:DNA hybrids and LINE-1 retrotransposons that can be perceived by cells outside the field of irradiation. This, in turn, may activate auto-destruction mechanisms such as cellular senescence, apoptosis and innate immunity. However, since EVs are exquisite carriers that can target specific cells [348], it is likely that the systemic delivery of the message may reach specifically cancer cells that belong to the same lineage as the primary tumour. While much remain to be investigated of hybrids roles and functions, this work suggests hybrids subcellular distribution and the automated quantitative imaging approach as a starting point for a comprehensive phenomization of cell response to stress.

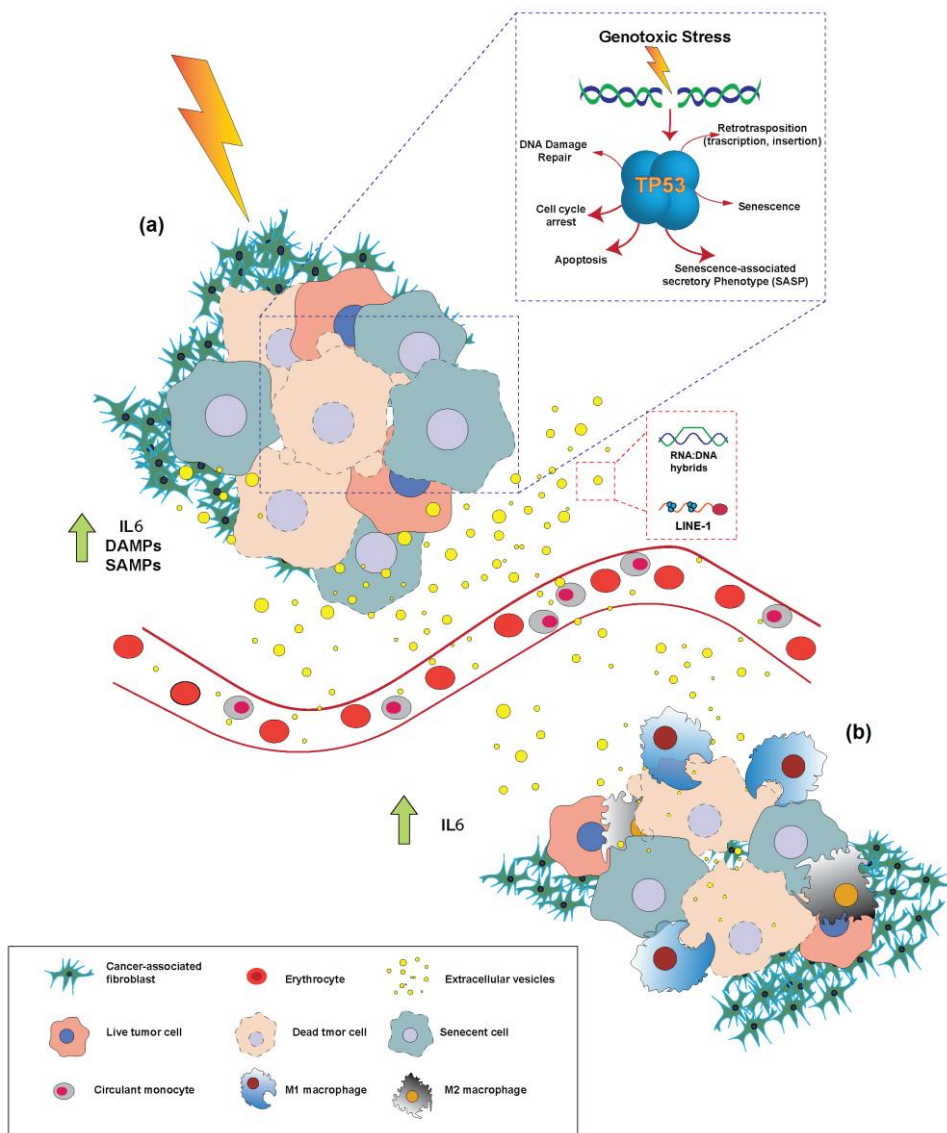


Figure 6.9. Diagram illustrating the p53-mediated abscopal effect induced by radiotherapy. (a) Radiotherapy induces cell damage that leads to cell cycle arrest, necrosis, programmed cell death and cellular senescence. In particular, the cells bearing functional p53 may acquire SASP and release cytokines, inflammatory- (DAMPs) or senescence- (SAMPs) associated molecules. In addition, at the presence of wtp53 radiotherapy activates retrotransposon elements which, in turn, increase the level of genotoxic stress. SASP cells also release EVs conveying RNA:DNA hybrids and/or retrotransposons which, outside the field of irradiation (b), activate autodestruction mechanisms such as cellular senescence, apoptosis and innate immunity in p53-competent tumour cells. Image reproduced from [18] under the CC-BY Creative Commons Attribution 4.0 International licence.

6.7 Content-aware contribution and future developments

Since its very beginning, the whole PHENOMICS Project was intended to benefit from a content-aware and interdisciplinary approach, that would merge biological and computer vision knowledge to exhaustively characterize the phenomenon of cell response to stress. My biological formation allowed me to better comprehend tumour cell dysfunctioning, irradiation and oxidative stress, and RNA:DNA hybrids dynamics. Crucially, I had the necessary biological and technical knowledge 1) to recognize and give due weight to the fact that the actual image resolution, allowed by the imaging modality, was insufficient to accurately locate hybrids, 2) to feel the necessity for a method to improve hybrids mapping, and 3) to finally conceive and develop such method, the DDM, to quantify and visualize molecule local density. By similar reasoning, I could address the problem of the measurement of RNA:DNA hybrid foci condensation state, by coupling a regional measure of foci abundance (*i.e.*, FGI) with a subregional investigation of foci local density (*i.e.*, DDM).

As regards future methodological developments, a first step would necessarily be the completion of the experimental panel with secondary yet important information (Table 6.1).

Table 6.1. Experimental panel for the PHENOMICS Project.

	A549	A549sh/p53	H1299	H1299 p53+	HeLa
p53 expression	✓	✓	✓	✓	
Senescence markers expression	✓	✓	✓		
β-gal and colony forming assays	✓	✓	✓	✓	
EVs quantification	✓	✓	✓		
EVs and MVs					
RNA:DNA hybrids content	✓	✓	✓	✓	
CD63+ EVs imaging	✓	✓	✓		
RNA:DNA hybrids imaging	✓	✓	✓	✓	✓
ORF1 imaging	✓	✓			

First of all, Table 6.1 highlights the necessity for confirmatory molecular experiments in HeLa cells, where RNA:DNA hybrids distribution has been

analysed by image analysis only. Secondly, given the results of such image analysis and all the results from the PHENOMICS Project, it is of primary interest to extend to all cell lines the study of IR-mediated AE at low IR doses, to investigate whether and how EVs, RNA:DNA hybrids and retrotransposons contribute to cell response in cell irradiated at 2 Gy and 7.5 Gy. In doing so, it is of capital importance to collect and quantify CD63+ EVs and their content in all cell lines and after each type of tested stress, to define once and for all the condition for a senescence message conveyance and confirm p53 role in the process. Further confirmation could derive from image analysis after co-staining of CD63+ EVs and RNA:DNA hybrids, irreplaceable for understanding hybrids entering and moving in the exocytosis pathway. In such analysis, DDMs and cDDM would allow the investigation and semi-quantification of EVs and hybrids colocalization. When focusing on hybrids production, I would also quantify the expression level and activity of p53, RNAseH and TREX1, to respectively confirm p53 influence, the hybrid nature of S9.6-marked molecules [349] and gain insights on their degradation [313]. Finally, I would verify whether and how non-cancer cells differently respond to tested stressing conditions, if they could contribute to AE and SASP onset, and if they are sensitive to hybrids loaded EVs.

From a methodological point of view, a first future development could be the identification of a better, *salient*, feature for hybrid distribution characterization, presumably multidimensional and arising from merging the features defined in this work. However, this feature validation would require to exponentially increase the sample size. Also, discussed relations between foci intensity, dimension and number, that we used to speculate on hybrid condensation state, are valid in a close system, in which hybrids total amount do not vary. Rather, in our open cellular system, hybrids presence is affected by continuous change in their production, degradation, and movement across cell boundaries. Secondly, it would be interesting to investigate the heterogeneity of cell response. As also shown in Sect. 4.5, hybrids seem to distribute differently in similarly stressed cells, even when close to each other. Moreover, more than once DDMs reported hybrids gathering at the interfaces between neighbouring cells. Considering the results collected in this study, such distribution can be definitely hypothesized to be functional.

Chapter 7

Content-aware approach in neuro-motor science: morphometric analysis and trabecular classification of murine tibial bone in micro-CT scans

In this Chapter, we present the application of our content-aware approach to a bone histomorphometry analysis, carried out within an interdisciplinary study on the role of the protein sclerostin in muscle-to-bone crosstalk [118]. The study composed of three sequential steps. First, despite being reportedly expressed by bone and cartilage only, sclerostin was identified as one of the myokines inhibiting bone cell differentiation *in vitro*. Then, sclerostin expression in muscle cells was extensively characterized in *in vitro* and *in vivo* murine model. Finally, after *in vivo* sclerostin over-expression in the tibialis anterior muscle of mice, we performed an *ex vivo* characterization of adjacent tibial bone microstructure from μ CT scans (Subsect. 3.3.1).

In the next Sections, the collaboration framework is first introduced, as well as the necessity for image analysis inclusion in the study (Sect. 7.1). Then, in Sect. 7.2, the biological and image processing theoretical background for our image analysis is discussed. Subsect. 7.2.1 summarises bone architecture and remodelling focusing on long bone, while Subsect. 7.2.2 approaches image filtering for texture analysis, serving the introduction of a method we have here developed to investigate the micro-architecture of bone samples. Sect. 7.3 introduces the state of the art for the whole study, surveying the main muscle-bone crosstalk factors,

including sclerostin (Subsect. 7.3.1), and revising current methods for quantitative bone imaging (Subsect. 7.3.2). Besides presenting the developed methods for image analysis, the successive Material and Methods (Sect. 7.4) covers also the previous steps of sample preparation and image acquisition. However, the Results and Discussion (Sect. 7.5) opens with a brief account of the molecular results that led to image analysis, before moving to discuss the methods applied to image analysis and their results. Finally, after drawing the main conclusions (Sect. 7.6), the contribution of the content-aware approach to the study is recalled, together with future perspectives (Sect. 7.7).

7.1 Study context

During the first year of the PhD and out of a specific research project, we entered a collaboration with Prof. Carla Palumbo and her research group at the Department of Biomedical, Metabolic and Neural Sciences of the University of Modena and Reggio Emilia, joining a preclinical study on muscle-to-bone crosstalk. First, the group investigated *in vitro* the effects of muscle cell-produced factors on the maturation process of osteoblasts, finding that the glycoprotein sclerostin was one of the myokines exerting an inhibitory effect on bone cell differentiation. Given the acknowledged role of bone/cartilage-derived sclerostin as a negative regulator of bone growth, the investigation moved to the *in vitro* and *in vivo* characterization of sclerostin production, and finally to the investigation of its effects on bone morphology at the macro- and micro-scale. My contribution to the collaboration regarded this last analysis. First, dried tibial bone samples were μ CT-scanned by Prof. Maria Pia Morigi and her team at the Department of Physics and Astronomy "Augusto Righi" of the University of Bologna. Then, we carried out an automatic image analysis of the scanned bone morphometry, that involved the development of an automated method for segmenting imaged metaphyseal trabeculae based on their thickness and orientation pattern.

7.2 Theoretical background

7.2.1 Bone architecture and remodelling

Bone is a living, highly vascularized and highly mineralized connective tissue. It largely consists of a very firm extracellular matrix, enriched in arranged collagen fibres stiffened by massive deposition of calcium phosphate nanocrystals. Matrix mineralization confers to bone the property of mechanical rigidity, necessary to protect vital organs from damage and enable movement, by providing mechanical support for joints, tendons and ligaments. Moreover, bone provides the medium (*i.e.*, the marrow) for the development and storage of blood cells, and act as a reservoir for calcium and phosphate, thus preserving normal mineral homeostasis [350, 351]. However, rigid bone is not steady, but a living tissue finely reshaped throughout life to maintain intact and responsive to new stress or demands. Bones constantly undergoes renewal and repair through the process of bone remodelling: osteoblasts, involved in bone deposition, and osteoclasts, specialized for bone resorption, coordinate this process, which in turn is subjected to systemic and local regulation by external cues [352].

Two main structural types of bone with different material properties can be distinguished: the trabecular (cancellous) bone, which is highly porous in structure, and the cortical (compact) bone, composed of a dense and highly calcified matrix (Figure 7.1).

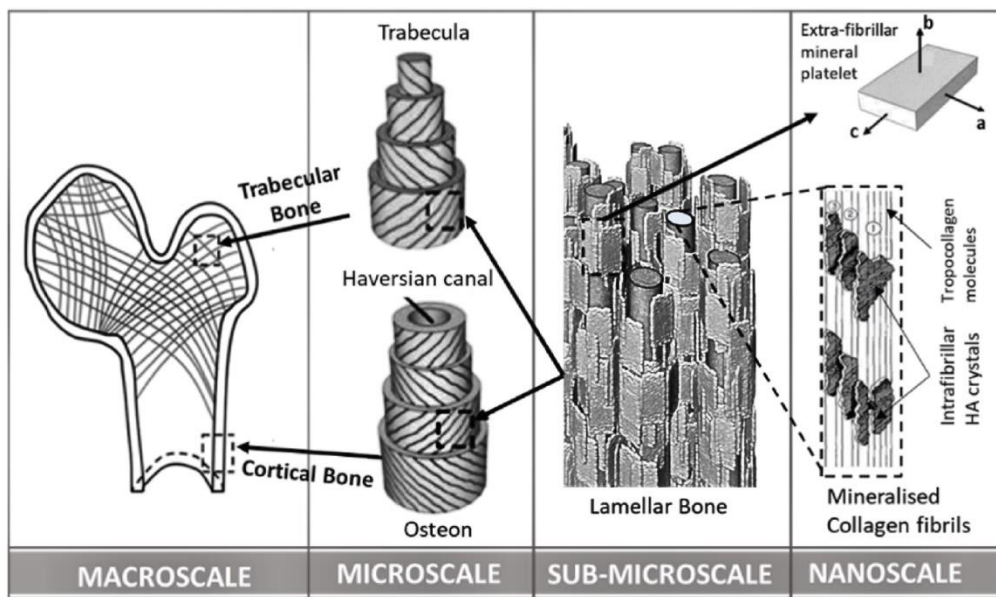


Figure 7.1. Hierarchical ultrastructure of bone, showing the macroscale (organ-level), microscale (tissue-level), sub-microscale (sub tissue-level) and nanoscale (constituent-level). Image reproduced from [353] under the CC-BY Creative Commons Attribution 4.0 International license.

Trabecular bone is organized into a network of interconnected rods and plates called trabeculae, which surround pores that are filled with bone marrow. Trabecular bone is less mineralized than cortical bone and has a larger surface exposed to the bone marrow and blood flow. On one side, this makes trabecular bone turnover and remodelling faster than in cortical bone. On the other side, it gives to the tissue more elasticity and ability to absorb mechanical shocks. Conversely, cortical bone is dense and forms an envelope around the marrow cavity. It is formed from Haversian systems, which consist of concentric lamellae of bone tissue surrounding a central canal that contains blood vessels. Because of its dense composition and architecture, cortical bone constitutes a rigid envelope for the bone tissue, especially resistant to longitudinal compression. Trabecular bone fills the centre of the long bones, flat bones and vertebrae, and is principally found in the epiphyses and metaphyses of the long bones. In contrast, cortical bone forms primarily the rigid shaft of long bones (Figure 7.2).

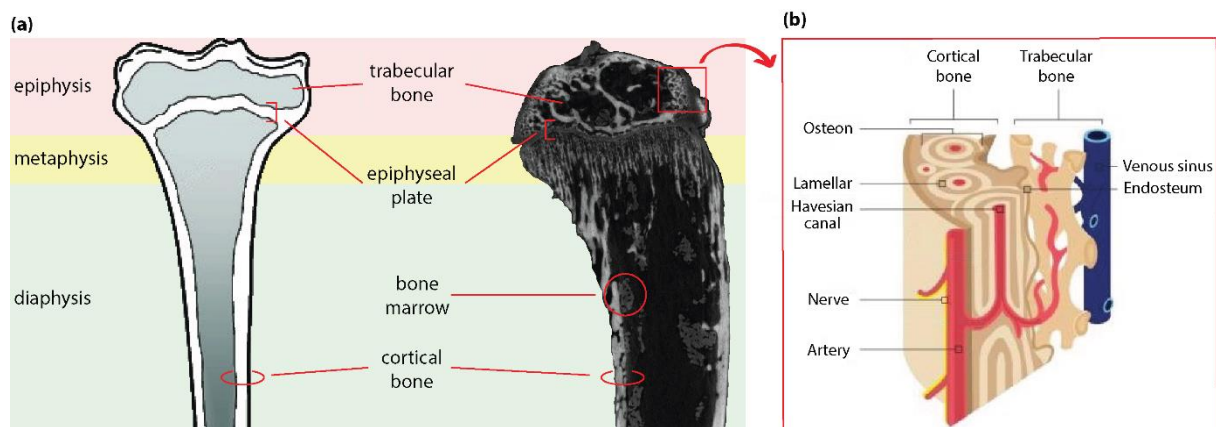


Figure 7.2. Schematic and μ CT of long bone anatomy and microstructure. (a) The macrostructure of long bones, such as tibia, femur and humerus, is divided into epiphysis, metaphysis and diaphysis. Epiphysis and metaphysis (separated by the epiphyseal plate in elongating bones) are mainly composed of trabecular (cancellous) bone interspaced by red bone marrow, while diaphysis is made of cortical (dense) bone, enclosing yellow bone marrow. (b) Detail of cortical and trabecular bone, adapted from [354] under the CC-BY Creative Commons Attribution 4.0 International license.

Long bones, especially the femur and tibia, are subjected to most of the load during daily activities and they are crucial for skeletal mobility. Accordingly, it is well established that trabecular structures within long bones are aligned in an organized manner associated with the direction of load distribution [355]. Long bones are structurally distinguishable in three regions: epiphysis, metaphysis and diaphysis. The proximal and distal epiphyses are the rounded ends which form joints with adjacent bones. Here, the trabecular bone transfers mechanical loads from the articular surface to the cortical bone. The diaphysis is the middle tubular part of a long bone, composed of compact bone which surrounds a central cavity which contains marrow and adipose tissue. The metaphysis is the intermediate region between the diaphysis and the epiphysis where bone growth occurs by endochondral ossification. During endochondral ossification, chondrocytes proliferate, undergo hypertrophy and die; the cartilage extracellular matrix they produce is then invaded by blood vessels, osteoclasts, bone marrow cells and osteoblasts, the last of which deposit bone on remnants of cartilage matrix. Ossification starts from primary (mid diaphysis) and secondary (epiphysis) centres of ossification, during prenatal and postnatal-to-adolescence development, respectively. The remnant cartilage between the primary and secondary

ossification centres is called the epiphyseal (or growth) plate, and it continues to form new cartilage up to late adolescence, undergoing ossification, and resulting in bone lengthening [356].

7.2.2 Texture analysis and Gabor filtering

Texture analysis refers to the characterization of regions in an image that present a specific pattern of distribution and dispersion of pixel intensity, repeated sequentially throughout the image. Mimicking characteristics of the human visual system (HVS), texture analysis attempts to quantify visual properties of images, such as smoothness, coarseness and regularity, as a function of the spatial variation of pixel intensities. Texture analysis is widely applied in biomedical image analysis, when objects in an image are characterized by their texture, besides “simple” pixel intensities. Research has demonstrated that the HVS analyses scenes generating a multi-resolution decomposition that can be modelled by 2-D wavelets, capable to reproduce HVS space–frequency localization properties. Among the wavelets, the Gabor wavelet stands out for its simplicity and robustness against local distortions, allowing object detection robustly to pose and imaging conditions. Moreover, frequency and orientation representations of the Gabor wavelet have been reported to represent those of human visual cortical cells. [355, 357, 358].

Introduced by Dennis Gabor in 1946 [359], the Gabor wavelet was firstly implemented as a multi-channel 2-D filter and applied to image textures by Daugman in the 80’s [360]. In this process, the Gabor filter act as the kernel in the neighbourhood operation of image filtering (Subsect. 4.2.1). Mathematically, spatial image filtering is carried out by *linear convolution*, that is the process of computing a linear combination of neighbouring image pixels using a predefined set of weights (*i.e.*, the kernel). When performed over discrete variables, as images are, the convolution can be defined as a ‘shift and multiply’ operation, performed by sliding the kernel over the image and sequentially recomputing each pixel value as follows:

$$O(x,y) = I(x,y) \otimes K(x,y) = \sum_{a=-n}^n \sum_{b=-m}^m I(x+a, y+b) K(a,b) \quad (7.1)$$

where O is the output image, I is the input image of dimension $X \times Y$, K is the kernel of dimension $m \times n$, x and y are the pixel coordinates, x goes from 1 to X and y goes from 1 to Y .

In the 2-D spatial domain, a Gabor filter can be formed by modulating a sinusoidal plane wave by a 2-D Gaussian kernel function (Figure 7.3 (a)).

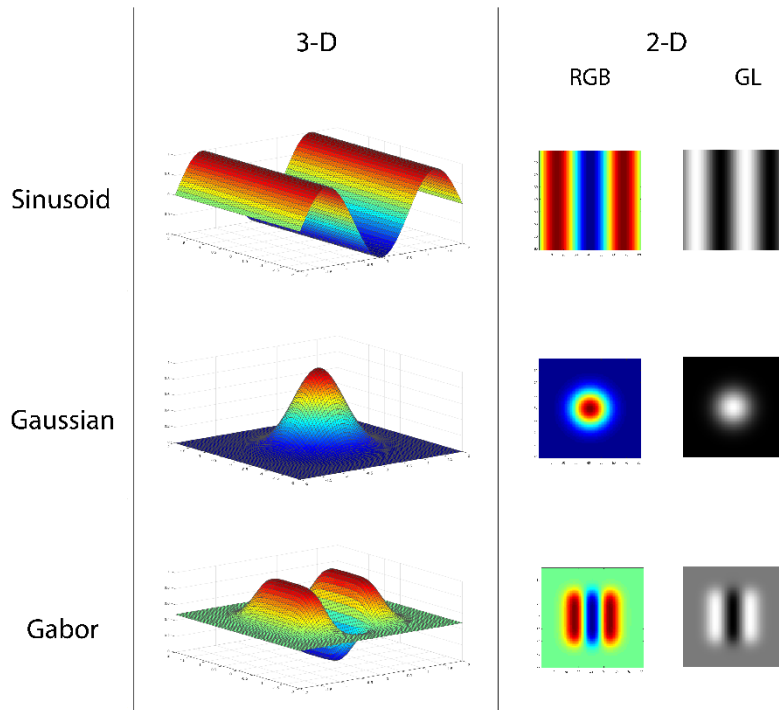


Figure 7.3. A Gabor filter is the product of a Gaussian kernel and a sinusoidal wave. From left to right and from top to bottom: 3-dimensional (3-D) and corresponding colour (RGB) and grey-level (GL) bi-dimensional (2-D) example of a sinusoid plane, a 2-D Gaussian and the Gabor filter.

In (x, y) coordinate space a simplified form of the Gabor function can be written as:

$$g(x, y, \lambda, \theta, \psi, \sigma, \gamma) = \exp\left(-\frac{x'^2 + \gamma^2 y'^2}{2\sigma^2}\right) \cos\left(2\pi \frac{x'}{\lambda} + \psi\right) \quad (7.2)$$

where $x' = x \cdot \cos\theta + y \cdot \sin\theta$, $y' = x \cdot \sin\theta + y \cdot \cos\theta$, λ is the wavelength of the sinusoidal factor, θ is the Gaussian orientation to the parallel stripes of the sinusoid, ψ is the phase offset, σ is the standard deviation of the Gaussian envelope, γ is the spatial aspect ratio that specifies the ellipticity of the support of the Gabor function.

Consequently, by varying the values of these parameters it is possible to modulate the appearance of the filter and therefore the type of pattern that can be detected. For this reason, a Gabor texture analysis is typically carried out with a multi-resolution approach, namely by parallelly convolving an image with a family (or bank) of Gabor filters, differing in parameters value (Figure 7.4). This way, the image is decomposed into a number of filtered images, each containing intensity variation over a narrow band of frequency and orientation.

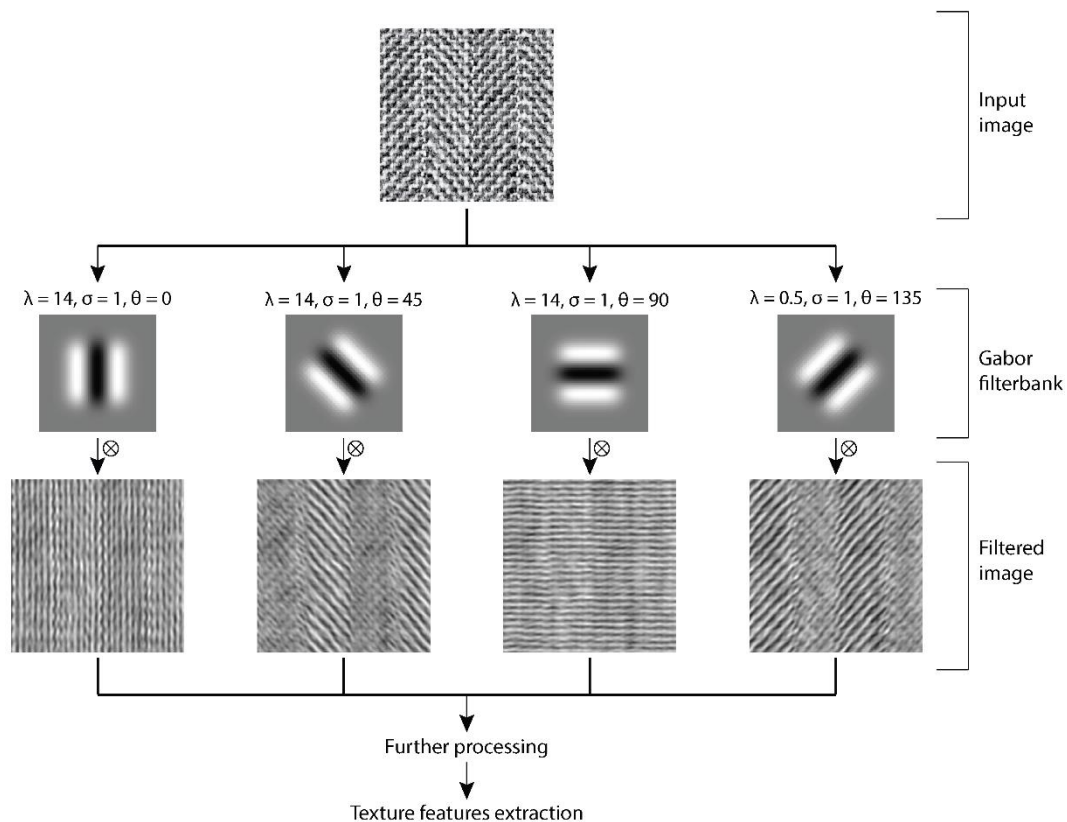


Figure 7.4. Workflow of Gabor-based texture analysis. A single input image is filtered (through convolution, \otimes) with a bank of n even-symmetric Gabor filters that uniformly covers the spatial-frequency domain. The operation, working as a high-pass filter, decomposes the image into n filtered images, enhancing the structures matching the shape of the corresponding filter. The filtered images usually undergo further processing, that serves the extraction and quantification of the texture features.

For each convolution, a new image in a transformed space is created, whose pixels intensity can be read as the degree of local similarity between the image and the filter. Finally, the filtered images usually undergo further processing before the extraction of texture features, namely quantifiable descriptors of the local

geometrical properties of the image. Common texture features include entropy, contrast and energy, the latter commonly used to measure the amount of variation (*i.e.*, texture uniformity) within a filtered image window [361].

In this Chapter, we apply a multi-resolution Gabor filtering method to the investigation of bone trabecular microstructure, aiming at classifying tibial metaphyseal trabeculae basing on their thickness and orientation.

7.3 State of the art

7.3.1 Muscle-bone crosstalk

The musculoskeletal system (MKS) is a complex organ which includes the skeletal bones, skeletal muscles, tendons, ligaments, cartilage, joints, and other connective tissue. The coupling of skeletal muscles and bones has long been considered primarily to be a mechanical one, in which bone provides an attachment site for muscles and muscles apply load to bone [362]. However, during the last decade, bone and muscle have been increasingly recognized as endocrine target tissues and endocrine organ themselves. In fact, the two tissues interact with each other by paracrine and endocrine signals and modulate their mutual development and function since intrauterine life to oldness, in a continuous crosstalk process of main regulatory importance on tissue function. Accordingly, dysregulation of biochemical MKS interaction has been associated to the onset of several diseases and disorders, system fractures, lifelong pathologies, genetic and metabolic diseases [363], and ageing in general [118]. Therefore, a better understanding of the molecular mechanisms responsible for the crosstalk among these tissues is needed.

The muscle–bone crosstalk is supported by preclinical and clinical data, showing the presence of many tissue-specific factors released by osteoblasts and osteocytes, including prostaglandin E2, osteocalcin, and IGF-1, which have a potential impact on skeletal muscle cells. Moreover, a growing number of muscle-released factors with bone modulating properties have been identified. These include insulin-like growth factor-1 (IGF-1), fibroblast growth factor-2,

Interleukines IL-6 and IL-15, myostatin, osteoglycin, irisin, and osteoactivin [364-370].

Among others, sclerostin is an established key molecular coordinator of both bone formation and bone resorption. Encoded in humans by the SOST gene and primarily produced by osteocytes, sclerostin is a secreted glycoprotein capable of binding to LRP4 chaperone and LRP5/6 co-receptors and inhibiting the Wnt/ β catenin signalling, ultimately leading to reduced bone deposition [371].

In this study, for the first time, sclerostin is also identified as a new putative myokine, demonstrating its expression in *in vitro* human myocytes and *in vivo* mice muscles of various age and metabolic and load-bearing features. Moreover, through a functional approach, muscle-originated sclerostin is demonstrated to have an anti-anabolic effect on adjacent bone, and thus hypothesised to act in combination with bone sclerostin, for example in severe conditions of increased bone fragility.

7.3.2 Bone quantitative imaging

Trabecular bone is a hierarchical, malleable and anisotropic tissue whose fine architecture conditions, and is conditioned and adaptively remodelled by, the mechanical loads that it is subject to. As bone strength directly depends on bone shape, imaging technologies rapidly became pillar to the field, allowing non-invasive quantification of bone morphology at different scales. In particular, given the high mineral content of the tissue, X-ray computed tomography (CT) and micro-computed tomography (μ CT) emerged as methods of choice. X-ray μ CT is a miniaturized form of CT scanning, used to create 3-D X-ray attenuation maps of specimens up to a few millimetres in size, with a resolution typically of the order of several microns (Subsect. 3.3.1). High sensitivity to bone and lung, short scan time and cost-effectiveness finally make these techniques optimal for trabecular bone analysis, both in *in vivo* and *ex vivo* applications [372, 373].

Trabecular architecture is commonly investigated in μ CT scans through standardized measurements of bone volume fraction and trabecular number, thickness and separation, among others [372]. More sophisticated approaches involve self-implemented methods for texture analysis based on image

decomposition by wavelets (Subsect, 7.2.2). Among them, the Gabor filter offers the possibility to simply yet robustly extract information about the oriented structures in an image pattern, mainly through the quantification of texture energy and derived anisotropy in filtered images [374, 375]. Since its first application to trabecular characterization in 1997 [376], Gabor-based image filtering has been extensively used for bone segmentation [377], fracture [378, 379] and osteoporotic patients [379, 380] classification and pure texture analysis [355, 381, 382]. Most of these studies provides a statistical global sampling of trabecular mass and orientation, disregarding the local heterogeneity information. Rather, many biomechanical studies highlight the importance of discriminating at least between the main trabecular orientations, which align with - and thus mostly bear - the major mechanical loads locally acting [357, 383]. Others have recognized the importance of discriminating between plate- and rod- like structures in trabecular microarchitecture, as different determinants of bone strength [384-386]. However, to the best of our knowledge, so far no study has classification single bone trabeculae on the basis of their primary attributes of orientation and thickness. To this purpose, we have developed a method for trabeculae categorization based on Gabor filtering of μ CT images, that can however be virtually extended to any other imaging solution. This method permits to produce a *trabecular map* explicative of the trabeculae partitioning in different classes of local texture energy, which can benefit biomechanical and more generally bone studies by providing a visual support for the trabecular pattern.

7.4 Materials and methods

In vivo gene transfer and electroporation procedures

Eight male C57BL/6 mice (Charles River) all belonging to the same progeny were housed in the institutional animal facility (Department of Cellular, Computational and Integrative Biology (CIBIO), University of Trento, Trento, Italy) and maintained on standard chow ad libitum. The pCMV6 expression plasmid (MR222588, Origene, Rockville, MD, USA) containing the SOST gene tagged with Myc-DDK was amplified in *Escherichia coli* for two rounds of mice electroporation. Eleven and seventeen days after birth, mice were anesthetized by

inhaled isoflurane and three animals were electroporated with the pCMV6-Myc-DDK-hSOST vector (SOST-ET, $n=3$), three were electroporated with the pCMV6-Myc-DDK (empty) vector (EV-ET, $n=3$), and two were non-electroporated (UC, $n=2$). Mice were injected into the tibialis anterior (TA), gastrocnemius (GA), and quadriceps femoris (QF) muscles of both hind limbs with a 0.3 mL insulin syringe through a 31-gauge needle in a constant volume of ~40 μ L, receiving ~240 μ g of plasmid DNA (80/site) each. Stainless-steel plates electrodes at 4–4.5 mm from each other were then placed over the muscle to encompass the injection area. 5 min after DNA injection, a constant-current (200 V/cm, 20 ms amplitude, 1 Hz) was delivered in eight consecutive square-wave pulses with a Digital Stimulator (Panlab 3100, Biological Instruments, Harvard Apparatus, Holliston, MA, USA). Animals were sacrificed twenty-five days after birth. Animal studies were approved by the institutional Animal Use and Welfare Committee and the National Ministry of Health (protocol No. 62/2020-PR, granted on the 29 January 2020). After sacrifice, both left and right tibiae of C57BL/6 mice were harvested, paraffin-fixed, and preserved at 4 °C by immersion in paraffine-PBS solution.

μ CT scanning

Tibiae samples were dried out and axially-scanned at room temperature from distal epiphysis to middle diaphysis using a KEVEX PXS10 130 kV–0.5 mA X-ray tube (70 kV) and a Photonic Science VHR1 CCD (charge-coupled device) camera with a fiber optic plate with a scintillator (FOS) 4000 2600 (9 μ m pixel) and with an isometric voxel size of 4.5 μ m³ and a 2X magnification. Scanning parameters were set as follows in Table 7.1:

Table 7.1. Set parameters for μ CT scanning of C57BL/6 mice tibiae.

Parameters	Setting
Voltage (kV)	70
Beam current (μ A)	35
N° projections	962-1231
Total rotation angle (°)	720/180
Exposure Time (s)	4.5

Images from single (sample) scans were grouped into single DICOM (Digital Imaging and Communications in Medicine) files. All following procedures are implemented in MATLAB® (R2019a v.9.6.0, The MathWorks, Natick, MA, USA).

Regional segmentation of tibial bone

Single axial scan sections are extracted from DICOM, the acquisition volume reconstructed, and single coronal sections drawn for following analyses. The most informative (*i.e.*, with less background and more signal, that is, imaged bone) coronal section is selected and analysed together with the previous five and the subsequent five, for a total of 11 analysed coronal sections per sample. For each section, the epiphysis, metaphysis and metaphyseal plate are segmented separately and automatically. The epiphysis is segmented by 1) maximum entropy thresholding [387], which identifies all the X ray-adsorbing regions of the samples, and 2) DDMs-based refinement of segmented regions [130] (Chapter 4), that permits to isolate thick epiphyseal trabeculae by performing a local density analysis with a search window size bigger than metaphyseal trabeculae dimension and spacing (Figure 7.5 (a)). The metaphysis is segmented by 1) adaptive histogram equalization [248], necessary to enhance the metaphyseal trabeculae contrast, 2) grey-level image top-hat by small structuring element (Subsect. 5.2.1), to selectively enhance bright and small objects (*i.e.*, metaphyseal trabeculae), 3) segmentation by maximum entropy thresholding, and 4) refinement by DDM, using a region-sized search window to isolate the left small objects that are also densely arranged (*i.e.*, metaphyseal trabeculae) (Figure 7.5 (b)). Finally, the epiphyseal plate is segmented by 1) logical ANDing (Subsect. 5.2.1) of dilated binary masks of previously segmented epiphyseal and metaphyseal region, to define the area of interest for further processing, 2) edge detection by Sobel operator [388], and ISODATA thresholding [334], to isolate the plate as the region of lower contrast, and 3) refinement by DDM, using a small search window size, heuristically determined after preliminary experiments, that permits to isolate the main body of the plate object (Figure 7.5 (c)). For methodological comparison, the epiphyseal plate is also manually segmented by an expert biologist in Fiji [202].

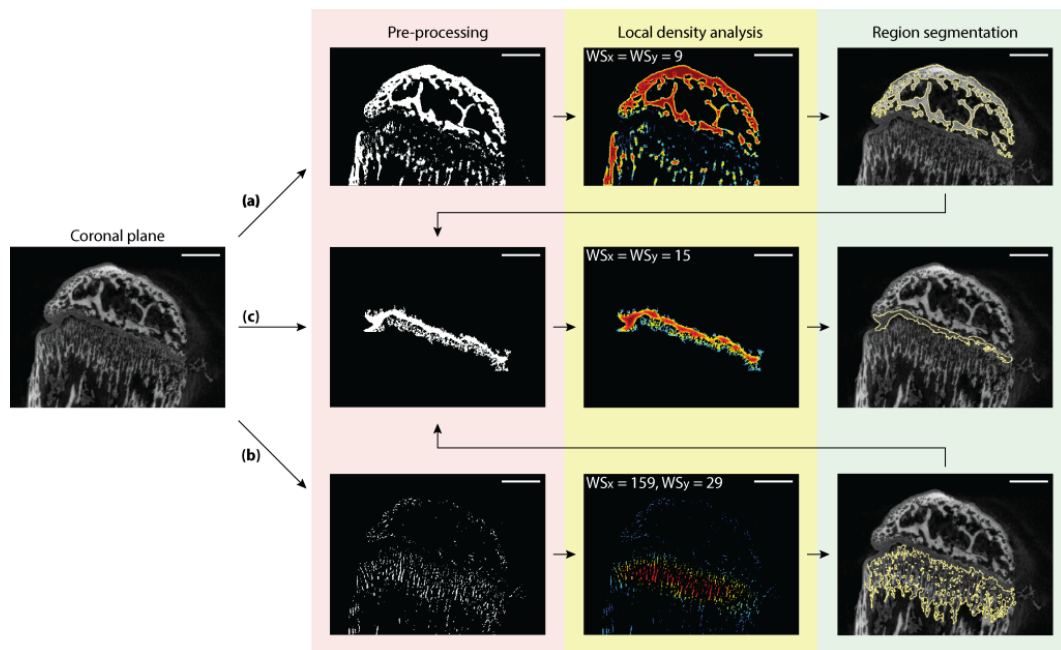


Figure 7.5. Epiphysis, metaphysis and epiphyseal plate segmentation by global thresholding and local density analysis in coronal section of μ CT scans. (a) Epiphysis is segmented by maximum entropy thresholding, DDM computation ($WS_x=WS_y=9$) and DDM ISODATA thresholding. (b) After enhancement by adaptive histogram equalization and top-hat filtering (SE =disk of 2 pixels-radius), metaphyseal trabeculae are segmented by maximum entropy thresholding, DDM computation ($WS_x=159, WS_y=29$) and DDM ISODATA thresholding. (c) After region of interest definition by logical ANDing of dilated epiphyseal and metaphyseal regions, the epiphyseal plate is segmented by ISODATA thresholding, DDM computation ($WS_x=WS_y=15$) and DDM ISODATA thresholding. Search window sizes are after preliminary experiments. Scale bars: 200 μ m.

Subregional segmentation of metaphyseal trabeculae

Due to its matrix composition and trabecular micro-architecture, the long bone metaphysis is expectedly one of the most sensitive regions to external remodelling stimuli. Accordingly, we developed a method for metaphyseal trabeculae segmentation and classification based on Gabor filtering of μ CT images, schematized in Figure 7.6 using a synthetic pattern, to highlight peculiarities.

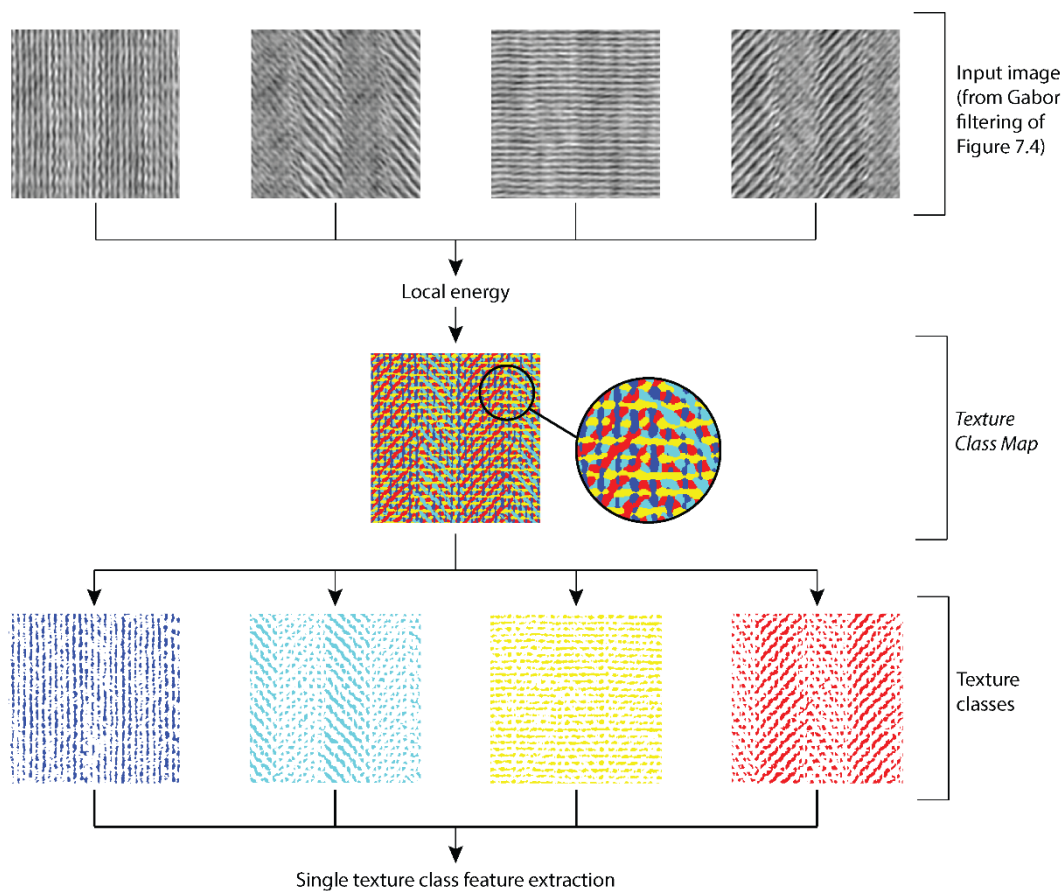


Figure 7.6. Developed method for automated trabecular classification by thickness and orientation. After normalizing pixel values for the isolation of the geometrical content, the input image is convolved with a family of Gabor filters distinguished by wavelength and orientation and set to uniformly cover an angle of 180° degrees. For each filtered images, the texture local energy is computed according to the corresponding filter wavelength. The image is finally recomposed by maximum intensity (*i.e.*, energy) projection, and color-coded for creating the texture colormap.

Starting from any 2-D grey-level image, the method application firstly requires a denoising and the input image normalization, to exclude the radiometric contribution from the analysis of the pattern geometry and reduce associated sensor noise. Then, the normalized image is convolved with a bank of 16 Gabor filters, whose members are specified by a unique combination of wavelength (λ) and orientation (θ) (Table 7.2).

Table 7.2. Wavelength and orientation values for applied Gabor filters.

Filter ID	λ (pixel/circle)	θ^1 (degrees)
1	2	0.0
2	3	0.0
3	2	22.5
4	3	22.5
5	2	45.0
6	3	45.0
7	2	67.5
8	3	67.5
9	2	90.0
10	3	90.0
11	2	112.5
12	3	112.5
13	2	135.0
14	3	135.0
15	2	157.5
16	3	157.5

¹ With respect to the epiphyseal plate major axis (clockwise direction).

The filter wavelengths have been empirically set to approximately match the imaged trabeculae width (*i.e.*, 2-3 pixels, roughly corresponding to 10-15 μm). The filter orientations have been heuristically set to uniformly covers all the orientations of spatial domain without overlapping. Aware that in the literature more than four different orientations are dubiously biologically informative [382], we still decided to further partition the space domain to explore possible sub-patterns. This procedure increases the computational time of the analysis, but does not reduce the data significance, as the results for single filterings can be subsequently cumulated to reduce the resolution of the analysis, and gain a more general perspective on the trabecular pattern. Accordingly, besides partitioning the trabeculae in 16 classes, we also pool the results (Sect. 7.5), to reduce the partitioning to two main classes of orientation.

The separate convolution of the normalized image with each filter of the bank resulted in 16 images whose intensity values represent the magnitude of local

similarity between the input image intensity and the shape of the corresponding filter. Then, for each resulting image, the local texture energy is computed by replacing each pixel value with the sum of pixel values in its specific neighbourhood (*i.e.*, $WS=\lambda$ of the filter that generated the image). Finally, a *trabecular map* is obtained by replacing each pixel of the input image with the “serial number” (*i.e.*, filter ID) of the energy image where the value of that pixel was maximum. This way, each pixel can be univocally assigned to the filter that best matched its geometry and thus led to its maximum energy value. The resulting trabecular map can be visualized by pseudo color-coding, to get a simplified and comprehensive view of the different trabecular pattern distribution in the image. Moreover, the trabecular map constitutes a segmentation of trabeculae by thickness and orientation, and can thus serve further quantitative texture analysis.

Assessment of results

For regional-level analysis of epiphysis and metaphysis, the mean trabecular thickness (Tb. Th), spacing (Tb. Sp), number (Tb. Nr) and intensity (Tb. Int) are quantified. Tb. Nr is computed as the inverse of Tb. Sp [372], which is derived via the distance-transform method [389], as well as Tb. Th. Tb. Int is analysed as a proxy measure of bone mineral density (BMD), aware that no BMD calibration has been performed prior to this study [390], as its primary goal is to perform a morphological – non radiometrical – bone analysis. Additionally, the epiphyseal plate thickness after manual or automated segmentation is expressed as Hausdorff Distance [391] between the superior and inferior border of the plate. For subregional-level analysis of metaphysis, the thickness (Tb. Th_m), number (Tb. Nr_m), eccentricity (Tb. Ec_m) and extension (Tb. A_m) are quantified for each class of segmented trabeculae.

Statistical analysis

Statistical analysis is performed by pooling the left and right tibiae within each experimental group (UC, EV-ET, SOST-EV) and testing two-sample hypotheses for each group pair and their samples. As an example, after comparing the EV-ET

group against the SOST-ET group for a specific feature, we also compared in a two-sample fashion all the tibiae of the EV-ET group with all the tibiae of the SOST-ET group, to see whether and how the trend observed at the group level is distinguished among its components. Two left tibiae samples (one from UC and one from SOST-ET group) are discarded as outliers, being more than three median absolute deviation (MAD) away from the median. One right tibia from the SOST-ET group is discarded from the analysis of epiphysis and epiphyseal plate, as the sample is broken and the regions missing.

Data deviation from normality is early verified by histogram inspection, followed by the Shapiro-Wilk test, based on which the discriminatory power of features is assessed by either two-tail Student's t-test or Wilcoxon rank-sum test with Bonferroni correction for multiple comparison procedures. p-values < 0.05 were considered for statistical significance.

7.5 Results and discussion

Plasmid electroporation increases muscle local but not circulating sclerostin levels

Sclerostin is a major secreted inhibitor of bone formation and stands out as an important actor upstream of the Wnt signalling pathway. Sclerostin is generally considered an osteocyte-specific protein, whose expression is restricted to bone tissue, despite circumstantial documentation of its presence in other organs. However, in this study sclerostin potential synthesis and secretion by muscle cells is investigated for the first time. First *in vitro* experiments confirmed sclerostin expression and release from both myoblast line and primary myocytes, with extracellular medium strongly inhibiting osteoblasts mineralization and differentiation in two weeks [118]. Further *in vivo* Western Blot analysis and ELISA assay confirmed remarkable, heterogeneous, and dynamically modulated sclerostin expression in muscles from different body districts and of different metabolic profile. Finally, to investigate a possible role for the muscle form of sclerostin, a gain-of-function experiment is performed by transiently overexpressing via electroporation a plasmid containing the SOST gene in muscles of young mice, as detailed in Figure 7.7 (a).

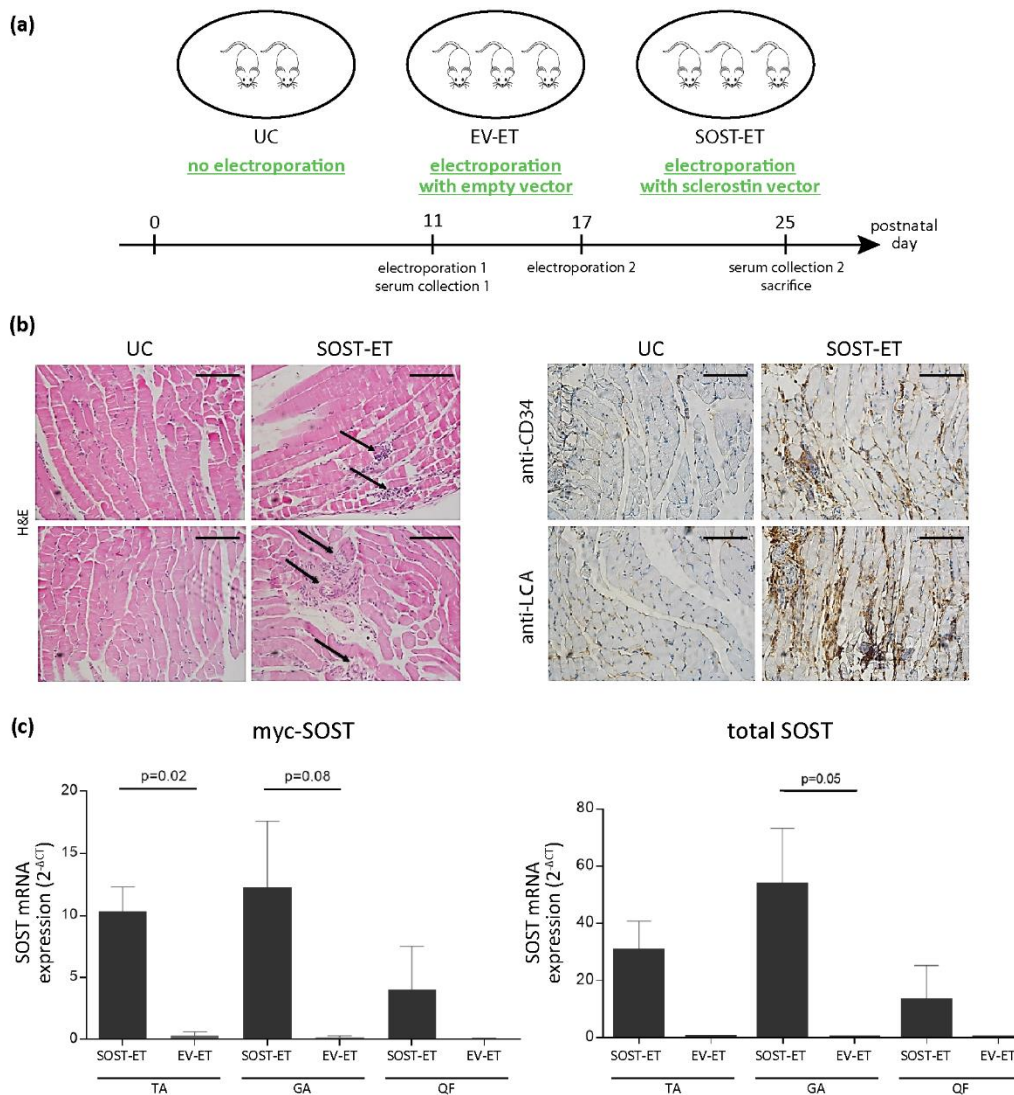


Figure 7.7. (a) Graphical scheme of the sclerostin overexpression experiment. Eight male C57BL/6 mice from the same progeny are randomly assigned to three different experimental groups: non-electroporated control (UC) or electroporated with an empty vector (EV-ET) or with the sclerostin vector (SOST-ET). At day 11 (before electroporation, set baseline) and day 25 (before sacrifice) blood serum is collected from each animal. **(b).** Representative histological sections of C57BL/6 TA muscles from UC and SOST-ET mice stained with H&E (left) or stained with anti-CD34 and anti-LCA antibodies (right). Black arrows indicate inflammatory infiltrate. Scale bar: 100 μ m. **(c)** Exogenous myc-tagged (left) and total (right) sclerostin expression by qRT-PCR in TA, GA, and QF muscles of SOST-ET and EV-ET mice, expressed as mean \pm STD. * $p < 0.05$ by two-tailed unpaired t-test. Image adapted from [118] under the CC-BY Creative Commons Attribution 4.0 International license.

To assess the potential injury induced by electroporation, histological analysis of electroporated muscles is performed at sacrifice. Hematoxylin and eosin (H&E)

staining (Figure 7.7 (b)) reveals limited presence of inflammatory infiltrates and newly formed blood vessels, suggesting that the electroporation procedure may induce mild inflammatory reactions yet counterbalanced by the onset of regenerative processes. Electroporation efficiency is assessed by quantitative reverse transcription-PCR (qRT-PCR, Figure 7.7 (c)), showing a significant increase of the myc-tagged sclerostin transcripts in electroporated TA muscle for the SOST-ET group. However, the level of circulating sclerostin appeared to be not significantly altered by the electroporation of the SOST-expressing plasmid (data not shown). Taken together, these data confirmed that plasmid electroporation was successful in yielding a strong local increase in sclerostin in the targeted muscles but highlight a limited influence on the circulating levels of sclerostin.

Sclerostin overexpression in muscle reduces metaphyseal bone trabeculae more parallel to the epiphyseal plate in adjacent long bone

In order to evaluate the microscopic events induced by muscle electroporation on adjacent skeletal segments, quantitative image analysis is performed on μ CT scans of mice tibiae, that lies between the TA and GA muscles targeted by the electroporation. For each analysed coronal sections, epiphysis and metaphysis morphology, beside the epiphyseal plate thickness, is compared between the UC, the EV-ET and the SOST-ET group. At the regional level, no significant changes in the epiphyseal and metaphyseal trabecular organization are detected in response to electroporation with either the empty or the SOST-bearing vector. When segmented manually, the epiphyseal plate thickness is reported to gradually increase following electroporation with empty vector (+6% from UC, $p=0.8094$, $p<0.0021$) and with SOST-expressing vector (+14% from UC, $p=10^{-4}$, $p<0.0025$), however with no significance between the two electroporations (SOST-ET: +8% from EV-ET, $p=0.0037$, $p<0.0017$). The total absence of significance for automatically segmented plate hints at the necessity to improve our method for its segmentation, made difficult by the total absence of mineralization (and therefore local image contrast) for this structure in μ CT scans. On the other side, the absence of a ground truth for manual plate segmentation cannot exclude some inaccuracies in (some steps of) this commonly employed approach [392-394].

At the subregional level, variations in the extension (Table 7.3) and number (Table 7.4) of metaphyseal trabeculae were found in response to electroporation with the SOST vector.

Table 7.3. Statistical analysis of metaphyseal trabecular classes extension expressed as percentage of metaphysis in UC, EV-ET and SOST-ET C57BL/6 mice.

Tb. class (Filter ID)	Tb. A _m Median ± MAD (pixel)			EV-ET – SOST-ET p-value (α=0.0014)
	UC	EV-ET	SOST-ET	
1	0.06 ± 0.02	0.10 ± 0.06	0.09 ± 0.01	0,8609
2	3.90 ± 0.11	1.64 ± 0.35	1.79 ± 0.14	0,0028
3	0.08 ± 0.04	0.07 ± 0.02	0.04 ± 0.04	0,0130
4	3.06 ± 0.29	1.58 ± 0.33	2.38 ± 0.83	0,0002
5	0.05 ± 0.02	0.07 ± 0.04	0.15 ± 0.05	0,0037
6	2.74 ± 0.52	2.71 ± 0.65	4.26 ± 1.18	2,92·10⁻⁶
7	0.03 ± 0.03	0.15 ± 0.09	0.04 ± 0.04	0,9433
8	3.02 ± 0.21	8.21 ± 1.75	23.71 ± 11.82	7,57·10⁻⁸
9	0.24 ± 0.03	0.11 ± 0.11	0.64 ± 0.55	0,1235
10	7.23 ± 3.64	39.06 ± 8.53	30.66 ± 11.00	0,0002
11	0.00 ± 0.00*	0.52 ± 0.10	0.04 ± 0.04	2,96·10⁻⁸
12	14.27 ± 4.14	31.53 ± 7.80	10.37 ± 4.67	1,37·10⁻¹⁸
13	0.65 ± 0.40	0.09 ± 0.02	0.10 ± 0.06	0,0356
14	37.71 ± 9.20	6.34 ± 0.68	5.12 ± 1.26	0,0006
15	0.08 ± 0.03	0.11 ± 0.02	0.09 ± 0.03	0,1678
16	12.54 ± 2.60	2.60± 0.89	2.01 ± 0.10	0,9040

*Trabecular class undetected in more than half of the samples.

Table 7.4. Statistical analysis of metaphyseal class trabecular number in UC, EV-ET and SOST-ET C57BL/6 mice.

Tb. class (Filter ID)	Tb. Nr _m Median ± MAD (pixel)			EV-ET – SOST-ET p-value (α=0.0014)
	UC	EV-ET	SOST-ET	
1	9,0 ± 2,0	11,0 ± 5.5	10,0 ± 4.0	0,2371
2	115,5 ± 14,5	74,5 ± 20.5	75,0 ± 11.0	0,0663
3	8,0 ± 3.5	9,5 ± 4.5	5,0 ± 4.0	0,0102
4	91,0 ± 10.0	61,0 ± 17.5	79,0 ± 20.0	0,0215
5	7,0 ± 3.0	8,0 ± 3.0	19,0 ± 3.0	0,0365
6	84,5 ± 11.5	77,5 ± 10.0	92,0 ± 10.0	0,0390
7	4,5 ± 3.5	12,5 ± 7.5	6,0 ± 6.0	0,7360
8	101,0 ± 22.5	144,0 ± 16.0	102,0 ± 9.0	0,0028
9	24,0 ± 3.0	9,5 ± 9.5	47,0 ± 35.5	0,0387
10	124,5 ± 14.0	130,0 ± 33.0	122,0 ± 10.0	0,0431
11	0,0 ± 0.0*	47,0 ± 15.5	6,0 ± 6.0	1,30·10⁻⁹
12	152,5 ± 13.0	135,5 ± 30.5	152,0 ± 11.0	0,0797
13	60,5 ± 25.2	12,0 ± 3.0	14,0 ± 9.0	0,2623
14	117,5 ± 15.5	139,5 ± 20.5	86,0 ± 15.0	1,56·10⁻¹⁰
15	11,0 ± 4.5	10,0 ± 3.0	11,0 ± 5.0	0,1118
16	152,5 ± 35.5	82,0 ± 17.0	83,0 ± 10.0	0,7517

*Trabecular class undetected in more than half of the samples.

A qualitative inspection of created trabecular maps highlights a shift in predominant colour from UC to SOST-ET, that reflects a change in the metaphyseal pattern (Figure 7.8 (a)). Then, to increase the biological translatability of the results, we grouped the trabeculae into two classes only, namely those “parallel” and “perpendicular” to the plate, according to the scheme of Figure 7.8 (b). We found that in SOST-electroporated mice parallel trabecular are strongly reduced (-60% Tb A_m from UC, p=10⁻⁷, p<0.0025) while perpendicular ones increase in occupancy (+9% Tb A_m from UC, p=10⁻⁷, p<0.0025) (Figure 7.8 (c)).

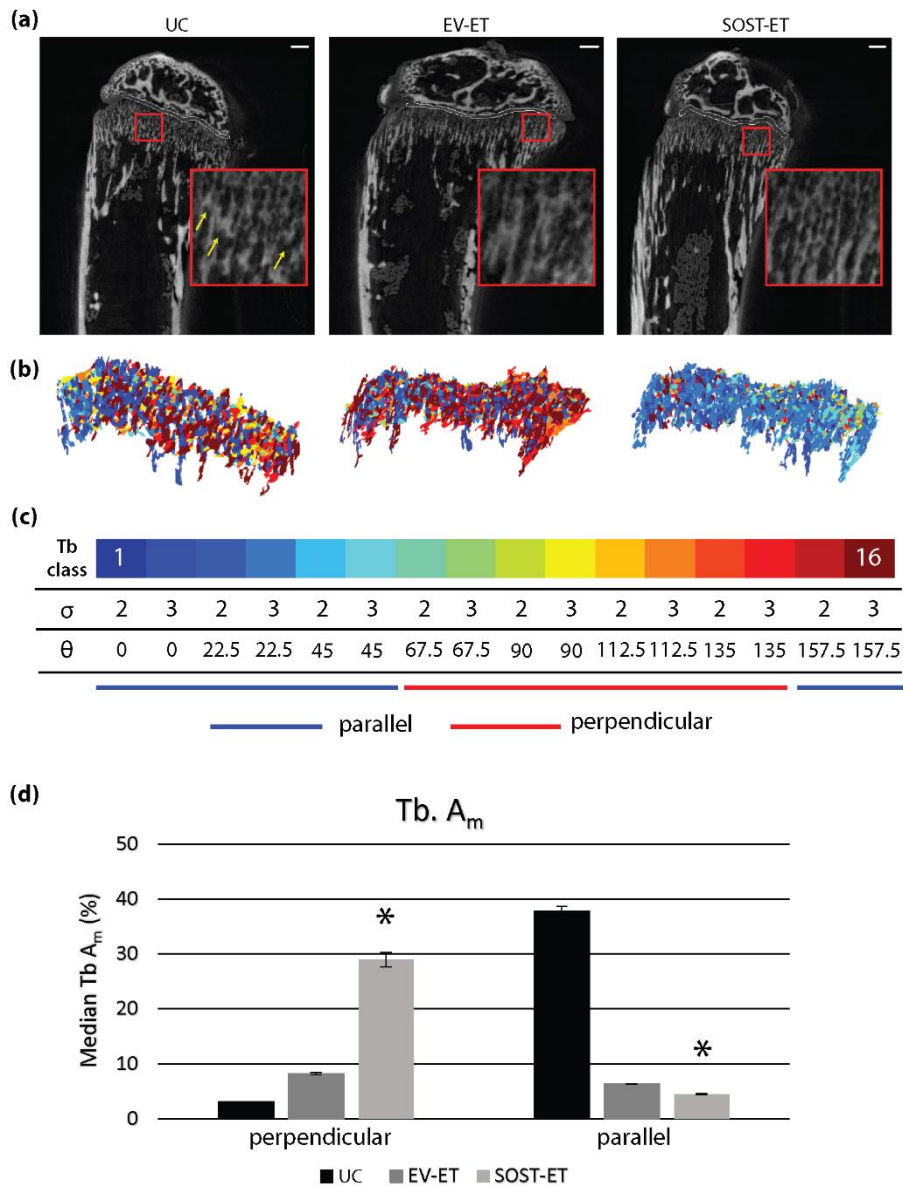


Figure 7.8. Sclerostin muscle overexpression effect on metaphyseal trabeculae in adjacent bone. (a) Exemplificative μ CT scans of distal tibial bone for UC, EV-ET and SOST-ET mice. Yellow arrows highlight trabeculae parallel to the epiphyseal plate, that reduce when SOST is overexpressed in adjacent muscle. Scale bars: 200 μ m. (b) Texture Class Map highlight by color-coding the variation in metaphysis trabecular composition from UC to SOST-ET. (c) Trabecular classes colour code and specification by thickness (σ) and orientation (θ). Classes 7 to 14 are pooled as perpendicular (to the epiphyseal plate), while remaining classes are pooled as parallel. (d) Trabecular class extension (Tb A_m , percentage of metaphysis) of pooled trabecular classes indicates a significant enrichment in perpendicular trabeculae at the expense of parallels. Data reported as median \pm MAD. Asterisk (*) indicates statistical significance in comparison with UC according to the Multiple Comparison test with the Bonferroni correction ($\alpha=0.0025$). Image reproduced from [118] under the CC-BY Creative Commons Attribution 4.0 International license.

These findings are in line with the expected anti-anabolic role of sclerostin, and with the acknowledged relation between load and trabecular microstructure [355, 396]. Accordingly, at the presence of overexpressed sclerostin we observe a selective enrichment in the trabeculae that are more perpendicular to the epiphyseal plate, as they are involved in most of the mechanical load bearing. Since oblique and more parallel trabeculae are physiologically expected to reduce with ageing [397], a muscle sclerostin contribution to this process should not be excluded. Thus, we argue that, particularly in dynamic situations (such as in the growing skeleton) and despite sophisticated analyses (such as μ CT), the effect of downregulation on osteogenesis exerted by sclerostin of muscular origin can be masked by the effect exerted on the skeleton by the increase in body mass during somatic growth.

7.6 Conclusions

Accumulating evidence indicates that myokines may affect adjacent bones through paracrine mechanisms, relying on different factors diffusion across muscle and bone tissues. In this study, the role of the sclerostin protein in muscle-to-bone crosstalk was investigated, identifying it as a new putative myokine involved in osteogenesis inhibition by paracrine signalling. *In vitro* analysis demonstrated sclerostin dynamic expression and secretion in myocyte cell line and primary culture during myogenic lineage progression. *In vivo* analysis revealed that the muscle metabolic and mechanical loading characteristics constitutes a further factor for sclerostin modulation. Finally, *in vivo* transient sclerostin overexpression followed by on-purpose μ CT image analysis disclosed a selective paracrine inhibitory role of the muscular sclerostin on adjacent bones, that reduced the metaphyseal trabeculae less subjected to increasing load during growth.

Taken together, these observations suggest that sclerostin released by skeletal muscle might synergistically interact with osseous sclerostin and potentiate negative regulation of osteogenesis possibly by acting in a paracrine/local fashion. Our data point out a role for muscle as a new source of sclerostin, that however need to be further investigated before proposing the validation of this protein as a therapeutic target. From a molecular point of view, the next steps will expectedly

involve the detailed analyses of the biochemical structure of muscular sclerostin, in comparison with the osseous one, beside the investigation of potential anti-sclerostin compounds, to also inhibit the muscular form. From an image analysis perspective, improvement of the developed trabecular classification method should firstly address the possibility to separate single trabeculae within a class, to open for new meaningful characterization (*e.g.*, trabeculae morphology) and improve statistical robustness. However, this will necessarily require imaging samples at a much higher resolution. The second limitation concerns reproducibility. As we directly experienced, the acquisition parameter values and the specimen position inside the μ CT scanner is of major importance and can strongly affect the outcome. Therefore, further analyses must prioritize the optimization and standardization of scanning procedures, under penalty of reduced or even masked out data significance.

7.7 Content-aware contribution and future developments

The entire activity I carried out within this collaboration benefitted the interdisciplinarity and the content-aware approach. Crucially, my biological formation allowed me to better comprehend bone dynamics and its architecture role. Additionally, the study of the Gabor filter opened for the selection and development of a more effective and biologically significant method for bone remodelling investigation. In particular, I could identify the metaphysis as the more responsive and malleable bone region, therefore more worthy of investigation. Secondly, I could better understand the importance of metaphyseal trabecular orientation and thickness, and how bone strength is a function of the formed trabecular pattern, rather than of individual trabeculae. Therefore, I decided to quantify muscle sclerostin effect on bone by searching for variation in the metaphyseal trabecular pattern, relying on 2-D Gabor filter for a texture analysis that resemble the biology of visual cortex [356], and focusing on those filter parameters (*i.e.*, σ and θ) that model the main trabecular characteristics.

As regarding future perspective, much can be done at the methodological level. With respect to this specific work, increasing the sample size would be the first necessity to improve significance, at present masked by limited number of samples

(especially in the control group) and a coarse division between perpendicular and parallel trabeculae. Increasing the sample size would also enable correlation analysis between molecular and imaging results, and possibly to an unsupervised classification analysis, to be separately conducted on right and left tibiae, searching for correspondence between paired samples.

To the best of our knowledge, this is the first example of application of Gabor filtering to metaphyseal trabecular pattern *classification*. Therefore, another pillar step would be to find further datasets to demonstrate the validity and generalizability of the trabecular classification method. Subordinately to an increase in μ CT scan resolution, a further step could be the segmentation of individual trabeculae and their division in plates and rods [398], for morphological investigation. Ideally, we could pair our imaging analysis with finite elements (FE) models to determine the strength and stiffness of the bone samples basing on the trabecular architecture information [399]. Nonetheless, despite the lack of experimental data about the mechanical validity of our trabecular classification, our method remains a valid tool for supporting molecular and biomechanics studies of bone architectures, not least to provide a visual overview of bone trabecular remodelling.

Chapter 8

Content-aware approach in developmental and regenerative dental biology: characterization of hDPSCs spheroids and molar innervation by automated quantitative imaging

In this Chapter, we present the application of our content-aware approach to dental biology carried out during my research period abroad, spent at the Orofacial Development and Regeneration Unit at the Institute of Oral Biology of the University of Zürich (UZH), in Switzerland, under the direct supervision of Professor Thimios A. Mitsiadis. The collaboration involved two main activities: the characterization of three-dimensional (3-D) organotypic spheroids of human dental pulp stem cells (hDPSCs), and the investigation of the role of the Nogo-A protein in the 3-D architecture of tooth innervation.

In the next Sections, the collaboration framework is first introduced (Sect. 8.1). Then, in Sect. 8.2, the theoretical background for the two activities is discussed. Subsect. 8.2.1 summarises the mammal tooth anatomy and cellular composition, focusing on the stem cell pools and DPSCs. Subsect. 8.2.2 instead recapitulates mammal dental innervation during development. Sect. 8.3 introduces the state of the art for the two activities. With respect to the 3-D hDPSCs spheroids characterization study, Subsect. 8.3.1 surveys difficulties and spheroid solutions of modelling mesenchymal stem cells (MSCs) and especially MSCs niche. Concerning the study of the role of Nogo-A in tooth innervation, Subsect. 8.3.2 summarises the

current knowledge on the neurite outgrowth inhibitor Nogo-A, and its functions in the nervous system. Then, Material and Methods (Sect. 8.4) and Results and Discussion (Sect. 8.5) for the two activities is explicitly separated in two Subsections, namely *hDPSC spheroids characterization* (Subsects. 8.4.1 and 8.5.1) and *Nogo-A role in tooth innervation* (Subsects. 8.4.2 and 8.5.2). Finally, after drawing the main conclusions for the two activities (Sect. 8.6), the contribution of the content-aware approach to the presented studies is recalled, together with future perspectives (Sect. 8.7).

8.1 Study context

At the beginning of the third year of the PhD, I carried out a three-month period as a visiting researcher at the Orofacial Development and Regeneration Unit at the Institute of Oral Biology of the UZH, in Switzerland, under the supervision of Prof. Thimios A. Mitsiadis. The laboratory is strategically located inside the Center of Dental Medicine in Zürich, enabling the direct and fast access to surgical specimens for research purposes. Furthermore, the laboratory can easily dispose of UZH key infrastructures and their expertise, such as the Center for Microscopy and Image Analysis and the Laboratory Animal Services Center (LASC).

Because of the interdisciplinarity of my PhD, I have been involved from the very first day in several lab projects, ending up on two activities. The first activity involved the characterization of 3-D organotypic hDPSC spheroids as a new reliable *in vitro* model of dental stem cells niche. My contribution to the activity was not limited to image analysis, but extended to image acquisition, carrying out of molecular experiments and to experimental planning, with a view to the needs of the following image analysis stage. Specifically, I was in charge of characterizing spheroids morphology and assessing their viability by image analysis, respectively after Bright Field and fluorescence microscopy imaging and developing of on-purpose analysis pipelines. The second activity involved the investigation of the role of the neurite outgrowth inhibitor Nogo-A in tooth innervation during development, using both *in vivo* (*i.e.*, extracted murine first molars) and *in vitro* (*i.e.*, *in vitro* cultures of explanted sensory ganglia such as Trigeminal Ganglia (TG) and Dorsal Root Ganglia (DRG)) models. For both models, I was involved in the

analysis of the neuronal network morphology, carried out by developing on-purpose methods for networks segmentation and quantification after fluorescent microscopy imaging (molar model) or by differential interference contrast (DIC) microscopy (TG/DRG model).

8.2 Theoretical background

8.2.1 Tooth anatomy and DPSCs

Teeth are hard, calcified structures occurring on the jaws and in or around the mouth and the pharynx areas of vertebrates. The general structure of a mammalian tooth consists of three layers that uniquely combine hard and soft tissues (Figure 8.1 (a)). An outer layer of inorganic enamel, the hardest tissue of the human body, covers the crown of the tooth. The enamel is supported by a middle layer of dentine, a highly mineralized tissue more similar to bone in composition. The dentine forms the main bulk of the tooth and is covered by enamel on the crown portion and by cementum on the roots. The innermost portion of the tooth is the dental pulp, a connective tissue that conveys innervation and vascularisation which guarantees trophic support and tooth survival and regeneration. Nerve fibres from the trigeminal ganglion enter the dental pulp from the apical foramen, an opening at the bottom of the roots, and extend right into the dentine, conducting pain and sensitivity. The gumline sets the separation between tooth crown and roots. The tooth is anchored to the surrounding alveolar bone through the periodontium, which absorbs the various shocks associated with mastication and provides the tooth with stability by continuously remodelling its extracellular matrix (ECM), the periodontal ligament. Another calcified tissue of the periodontium, the cementum, covers the roots and anchors the teeth to the alveolar bone through the periodontal ligament, that similarly to the dental pulp is supported by a rich vascular plexus and a rich neuronal network [400].

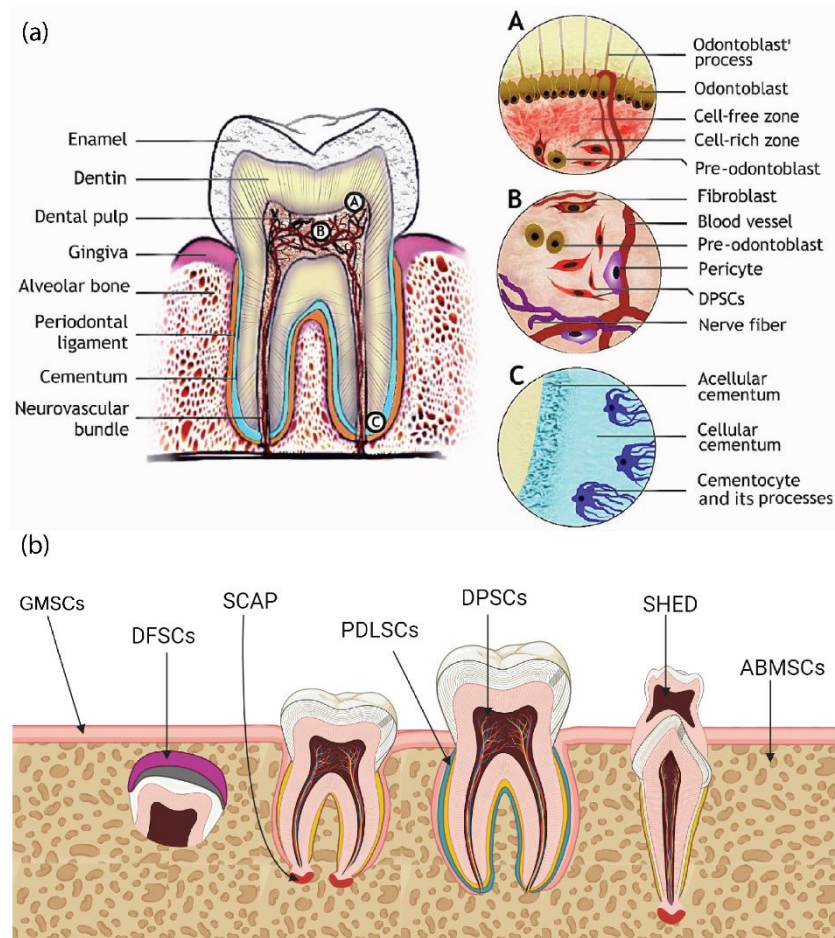


Figure 8.1. Mature tooth anatomy and stem cells. (a) Tooth structure and dental tissues, with details of odontoblast niche (A), pulp niche (B) and cementum. Image reproduced from [401] under the CC-BY Creative Commons Attribution 4.0 International license (<https://creativecommons.org/licenses/by/4.0/>). (b) Oral and dental stem cells. GMSCs, gingiva-derived mesenchymal stem cells; DFPCs, dental follicle precursor cells; SCAP, stem cells from apical papilla; PDLSCs, periodontal ligament stem cells; DPSCs, dental pulp stem cells; SHED, stem cells from human exfoliated deciduous teeth, ABMSCs, alveolar bone-derived mesenchymal stem cell. Image reproduced from [402] under the CC-BY Creative Commons Attribution 4.0 International license.

The development of the tooth results from sequential and reciprocal interactions between cells of the oral epithelium and the cranial neural crest-derived mesenchyme [403] (Subsect. 8.2.2). Oral epithelial cells generate ameloblasts (ABs) that produce the enamel and then drive the development of the dental roots. Dental mesenchymal cells generate odontoblasts (OBs), the cells responsible for dentine production, as well as the dental pulp and the periodontium [404-406]. Both ABs and OBs start matrix secretion in the

developmental stage, but while OBs survive the first deposition, ABs either undergo apoptosis or are shredded out during tooth eruption, meaning that damaged dentin, but not enamel, can be repaired throughout life. Recently, a single-cell profiling from the dental pulp and the periodontal tissues in human teeth has identified a variety of cell populations, including mesenchymal stem cells (MSCs), fibroblasts, odontoblasts, endothelial cells (ECs), Schwann cells (ScCs), immune cells, epithelial-like cells, and erythrocytes [407]. MSCs represented on average 12% of the adult dental pulp tissue and 19% of periodontium, remarking stem cell importance in regenerative processes of dental tissue upon injury.

Like other organs, tooth compartments harbour a niche of heterogeneous stem/progenitor cell populations of embryonic derivation. Three populations of stem cells can be found in the periodontium and the dental pulp: the periodontal stem cells (PDSCs), the dental pulp stem cells (DPSCs) and the stem cells from the apical papilla (SCAPs) (Figure 8.1 (b) [402]. Like bone marrow-derived mesenchymal stem cells (BM-MSCs), dental stem/progenitor cells exhibit self-renewal capacity and multilineage differentiation potential [409], besides expressing numerous MSCs stemness markers [408]. The decision between self-renewal and differentiation is driven by a specialized and highly regulated microenvironment called *stem cell niche*. While SCAPs can be found only in the apical root of immature teeth, DPSCs and PDSCs also characterize the adult tooth, where they respond to cellular, chemical and physical stimuli to ensure homeostasis and regeneration of dental tissues and associated immune system [400].

Despite expressing different MSC markers, DPSCs have an ectodermic origin from neural crests, explaining their high differentiation ability towards odontoblasts and neural cells. DPSCs, also called postnatal DPSCs, are mainly located in perivascular areas of the pulp chamber in adult teeth, where they play a central role in tooth regeneration upon injury. By establishing a continuous, bidirectional and bifunctional Notch-mediated signalling with ECs, DPSCs proliferate and migrate into the damaged tissue to differentiate into odontoblasts and form reparative dentin, which has been proposed to be the main mechanism leading to reparative dentinogenesis. Notch signalling is indeed fundamental in the interactions between stem cells and their microenvironment, mediating stem

cells responses to injury or stress and influencing cellular differentiation, proliferation and apoptotic events [407, 409, 410].

8.2.2 Odontogenesis and tooth innervation

Odontogenesis, or teeth generation, is a sequential process of several complex stages that go from embryonic cells aggregation to tooth eruption into the mouth. Remarkably, the tooth tissues originate from different cell lineages. The enamel develops from cells derived from the ectoderm of the oral cavity, whereas the cementum, dentin, and pulp tissues are derived from neural crest-mesenchyme cells of ectodermal and mesodermal origin [411, 412]. In mice, developing teeth go through distinct morphological phases that are tightly controlled by epithelial signalling centres. Mouse tooth development initiates around embryonic day 11 (E11, induction phase), when localized epithelial thickenings in the oral ectoderm form and establish the molar and incisor dental placodes at E11.5 (Figure 8.2). Subsequently, the dental epithelium proliferates and invaginates into the underlying mesenchyme, which condenses around the epithelium to form the tooth bud (E12.5–E13.5). The initial knot (IK), first described in incisors [413] and only recently in molars [414], is the earliest signalling centre thought to drive the placode-to-bud progression. Over the successive days, the epithelium continues to differentiate and extends around the dental mesenchyme, thereby forming a cap (visible at E13.5–E14.5) and later a bell shape (E15.5–E18.5). During the bud-to-cap transition, the primary enamel knot (pEK), a transient signalling centre located in the dental epithelium, sends key morphogenic signals to the developing molar and incisor tooth germs. The Notch/delta signalling has been found crucial for this stage. [415, 416]. In response to signals from the pEK, the dental epithelial tissue elongates transversely (molars) or longitudinally (incisors), thus extending into and around the underlying mesenchyme and forming the cervical loops (CLs) on both sides of the condensed mesenchyme, now referred to as the dental papilla. At the end of the cap stage, the pEK undergoes apoptosis and, in multicuspid teeth such as molars, is replaced by secondary EKs (sEKs). Invagination and elongation of the CLs into the dental mesenchyme define the inner and outer enamel epithelia (IEE and OEE, respectively), separated by the uniquely vascularized stellate

reticulum (SR). Following further invagination and elongation of the CLs into the dental mesenchyme, the crown and root are established, and the dental epithelial and mesenchymal cells further differentiate. By the bell stage, ABs precursors coordinate enamel deposition, and OBs, future dentine producers, are formed. In the final steps, the tooth erupts in the mouth. This involves the coordination of bone resorption and root development, and occurs postnatally. Tooth development is tightly controlled by multiple evolutionarily conserved signalling pathways. In particular, canonical Wnt and Shh signalling appears crucial for odontogenesis, as extensively recently reviewed [416].

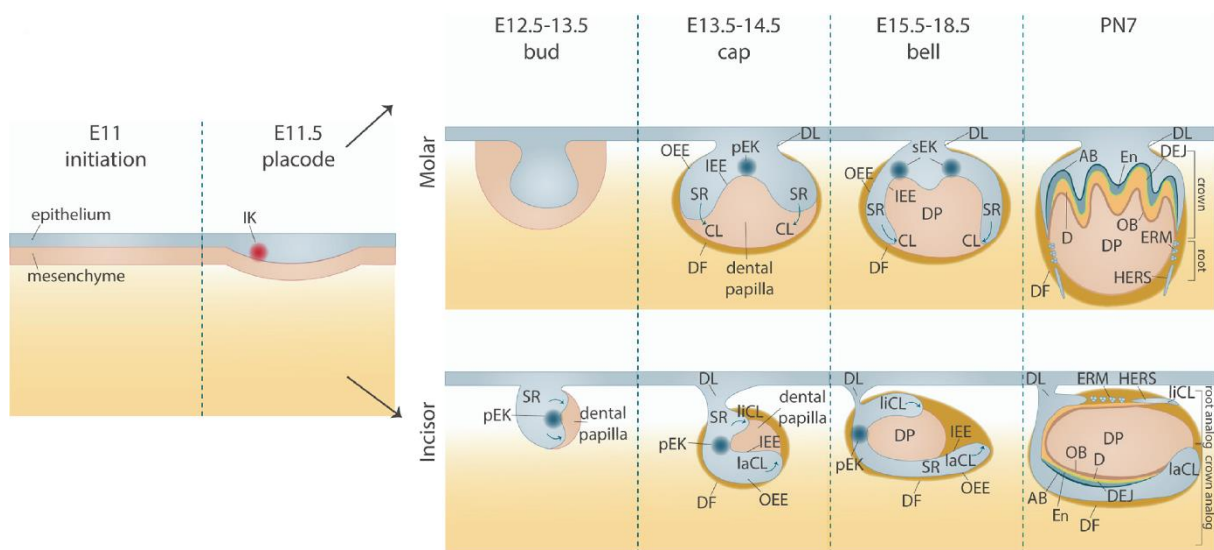


Figure 8.2. Overview of mouse tooth development. Embryonic stages of mouse tooth development, with divergent morphology of molar and incisor tooth germs. AB, ameloblasts; CL, cervical loop; D, dentin; DEJ, dentin-enamel junction; DF, dental follicle; DL, dental lamina; DP, dental pulp; En, enamel; E11, embryonic day 11; ERM, epithelial cells rests of Malassez; HERS, Hertwig's epithelial root sheath; IEE, inner enamel epithelium; IK, initiation knot; laCL, labial cervical loop; liCL, lingual cervical loop; pEK, primary enamel knot; PN7, postnatal day 7; sEK, secondary enamel knot; OB, odontoblasts; OEE, outer enamel epithelium; SR, stellate reticulum. Image adapted from [416] under the CC-BY Creative Commons Attribution 4.0 International license.

The tooth represents a unique exception to canonical tissue innervation, both in terms of development and nerve composition. Accordingly, tooth innervation plays unique and fundamental roles in pulp homeostasis, repair, and regeneration. First, being composed of highly dense and pain conducting fibres, the tooth neuronal network represents a primary surveillance system alerting the central

nervous system (CNS) for potential or actual injury. Second, pulp nervous fibres are key players in reparative processes as mediators of inflammation and modulators of the re-mineralization response. Finally, tooth nerve fibres contribute to tooth homeostasis, by taking part in the definition of stem cell niche and modulating enamel and dentin mineralization [417-421].

During development, teeth acquire a sensory innervation from the trigeminal ganglion (TG). Axons reach the jaws before tooth formation and surround the dental mesenchyme in basket-like formations already at embryonic day 13.5 (E13.5). However, it is only after the crown shape is set and the mineralization of both enamel and dentin has commenced, around postnatal (PN) day 3–4 in the mouse, that pioneer nerve fibres can enter the apical region of the tooth germ. Before that, the nerve ingrowth towards the dental epithelium and inside the papilla is actively inhibited and regulated by semaphorins [422, 423]. While the expression of these neurite inhibitory/repulsive factors decreases in a temporal pattern, the expression of different neurotrophins and axon guidance molecules takes over, allowing tooth innervation. However, it is only after complete tooth eruption, around PN20 in mice [424], that pulp neuronal fibres become functional and responsive to external stimuli. [425, 426].

With respect to other tissues, dental pulp innervation is highly dense, enriched in nociceptors and characterized by a progressive thinning and demyelination of fibres from roots to crown. Both unmyelinated and myelinated sensory nerves, as well as unmyelinated sympathetic neurons, innervate the mature tooth. Within the root pulp of permanent teeth, around 70–90% of large and medium axons are of unmyelinated sensory fibres, mostly A δ - and C- nociceptors, while the remainder axons of the sympathetic autonomous system, projecting from the superior cervical ganglion, serve the pulpal vasculature [427]. Accordingly, heat and cold pain is the predominant experience, if not the only, that can be evoked when pulpal nerves are excited; pressure and temperature sensations are indeed almost exclusive of periodontium nerves. Among the few A β -fibres present, some might be nociceptive, but most are thought to be low-threshold mechanoreceptors (LTMs) that subservise 'pre-pain' sensations. In the short intradental course from the radicular to the coronal pulp, the network undergoes extensive axonal arborization, while up to 90% of the myelinated axons lose their myelin below or

in the odontoblast layer region, entering a close association with these cells and their niche in what seems to be analogous to a blood-barrier system [428]. Some axon terminals proceed beyond this site and continue along the odontoblast processes into the dentinal tubules to innervate the inner segment of the dentin.

8.3 State of the art

8.3.1 MSCs niche modelling

Soon after their first description [429], MSCs have represented a unique and compelling opportunity for tissue engineering and regenerative medicine applications, ultimately aiming at repairing and renewing damaged tissue by MSCs transplant [430, 431]. In particular, dental stem cells (DSCs) are excellent candidates for such applications, as they are abundant, harvested with minimally invasive procedures, raise no ethical concerns and, importantly, apply to the regeneration of both dental and non-dental tissues [432, 433]. However, the behaviour of these and other stem cell populations is regulated by molecular cues produced in their microenvironment by stromal cells, neurons, vascular-related cells, and immune cells, as well as by physical factors such as stiffness, topography, and shear stress [434]. As a main example, the divergent migration and differentiation behaviour observed for DPSCs and PDSCs has been ascribed to their interaction with different niches, rather than to intrinsic differences [407]. Most of microenvironment cues are obviously missing in traditional 2-D *in vitro* culture models, as they are related to the three-dimensionality of real tissues. Consequently, traditional culture systems do not allow proper investigation of MSCs behaviour, nor the culturing of a representative MSCs population to be used in further preclinical and clinical applications. Indeed, a thorough understanding of the interactions between DSCs and their microenvironment niche is still lacking.

3-D multicellular spheroids constitute a simple yet effective solution to strongly improve the representativeness of MSCs models and of human dental tissues complexity. Accordingly, 3-D structures such as spheroids and organoids allow complex cell-cell interactions, the creation of more physiological gradients of oxygen, nutrients and catabolites, and the *in vivo*-like circulation of soluble

signals [435]. Moreover, self-assembly and self-ECM formation make spheroids particularly suitable for inexpensively modelling and exploring MSCs specific niche, including physiological hypoxic gradients [436]. Indeed, MSCs cultured in spheroids have been demonstrated to possess enhanced stemness features, anti-inflammatory, angiogenic, antifibrotic and anti-inflammatory properties, enhanced secretory profile and anti-oxidative capacity [75, 76]. Finally, both *in vitro* and *in vivo* studies have demonstrated that DSCs differentiation and osteogenic potential is improved when cultured as spheroids [436]. However, a major and recurrent drawback of spheroid models is the impact of their cell heterogeneity on data reproducibility [89] and, specifically to MSCs spheroids, the reduction of cell proliferation [436, 437].

In this context, we developed 3-D organotypic DPSC spheroids to be assessed as reliable models to recapitulate the dental pulp niche and investigate DPSCs regenerative potential and suitability for personalized regenerative medicine strategies. In this first step of the study, where I was directly involved, we chose an approach based on spheroid morphological pre-selection to reduce results variability, as previously introduced [89]. The main goal was to characterize our novel model in terms of DPSCs stemness, viability and proliferation, further defining the moment of culture at which spheroid properties are more stable, maximising model reproducibility.

8.3.2 Nogo-A role in the central nervous system

First discovered in the CNS [439, 440], Nogo-A is a myelin-associated oligodendrocyte membrane protein that interacts with neuronal receptors and inhibits neurite growth, overall reducing the length and ramification of the neuronal network [441, 442]. In the adult CNS, Nogo-A is expressed primarily by oligodendrocytes and is mainly known for its inhibitory effects on axon regeneration and compensatory sprouting after injury [443, 444]. Accordingly, there is a strong interest around Nogo-A potential for clinical applications in the treatment of CNS injuries [445-447]. Nogo-A plays further roles during CNS development. Depending on the moment and location of expression, Nogo-A can

contribute to the regulation of neural growth and branching, myelin formation, and neuronal plasticity [448].

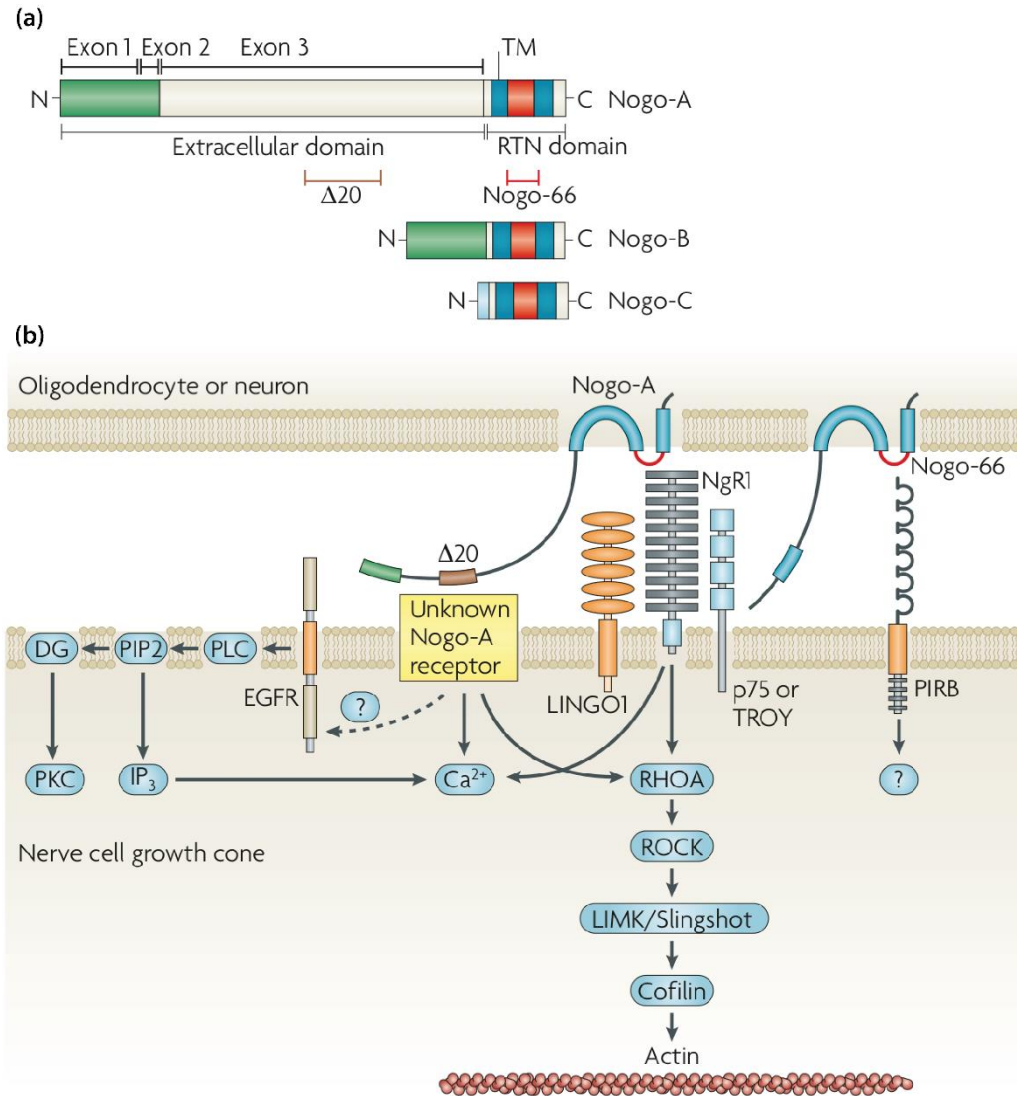


Figure 8.3. Domains, binding partners and signalling of cell membrane Nogo proteins.

(a) Structure of the three major Nogo isoforms (Nogo-A, Nogo-B and Nogo-C) and their functional domains. (b) Nogo-A inhibits neurite outgrowth through Nogo-66 domain to the complex NgR1-LINGO1-p75/TROY, leading to an increase in intracellular Ca^{2+} and activation of the Rho-Rho-associated coiled-coil containing protein kinase (ROCK) pathway, by which the actin cytoskeleton is destabilized, and the growth cone collapsed. The Nogo-A-specific $\Delta 20$ domain, interacting with a yet uncharacterized receptor, also activates the RHOA protein and increases intracellular Ca^{2+} levels. Transactivation of the epidermal growth factor receptor (EGFR) and of protein kinase C (PKC) has been shown, but the detailed pathways involved remain unknown. In addition to NgR1, Nogo-66 can interact with paired immunoglobulin-like receptor B (PIRB), an additional potential Nogo receptor subunit. Image reproduced from [449] under the CC-BY Creative Commons Attribution 4.0 International license.

Nogo-A is the largest member of the Nogo protein family encoded by the reticulon 4 (RTN4, also known as NOGO) gene (Figure 8.3 (a)). The three main Nogo isoforms (Nogo-A, Nogo-B and Nogo-C) only share the last 188 amino acids (AA) in the carboxyl terminus (C-t), the so-called Reticulon homology (RTN) domain, that contains two long hydrophobic stretches, each of which is long enough to span the cell membrane twice. They are linked together by a 66-AA segment called Nogo-66. The amino-terminal (N-t) segments of Nogo proteins have differing lengths and there is no homology between them. The N-t of Nogo-A and Nogo-B are identical, consisting of a 172-AA sequence that is encoded by RTN4 exons 1 and 2. In Nogo-A only, the N-t is followed by an 800-AA region (encoded by axon 3) containing the Nogo-A-specific Δ 20 active domain (AA 544–725). The shortest isoform, Nogo-C, is composed of an N-t of just a few amino acids directly followed by the RTN domain. Nogo-A and Nogo-B are derived from alternative splicing of the same primary transcript, while the N-t of Nogo-C is expressed after a different promoter. In all three Nogo isoforms, the N-t lacks a signal sequence for endoplasmic reticulum (ER) translocation. However, Nogo proteins are present at ER and cell surface, where the N-ts, Δ 20 and Nogo-66 domains face the cytoplasm and the extracellular space respectively (Figure 8.3 (b)) [449, 450].

Expressed in both glia and neurons, surface Nogo-A interacts via two separate extracellular domains (Δ 20 and Nogo-66) with several different receptors [449, 451, 452], such as Nogo receptor 1 (NgR1) [453], Sphingosine-1-phosphate receptor 2 (S1PR2) [454, 455] and Paired immunoglobulin-like receptor B (PIRB) [456]. In the course of axotomy or die-back upon CNS injury, signalling through these receptors typically activates actin-modifying pathways involving the actin-modulating small GTPase Rho and Rho-associated protein kinase [457, 458], which generally resulted in growth cone collapse and inhibition of axonal regeneration. Few studies also involve Nogo-A in the activation of intracellular pathways for gene expression modification and protein synthesis regulation through inhibition and deactivation of CREB [459] and mTOR [460, 461].

Despite being well characterized in the CNS, little is known about its functions in other body districts innervation. Nogo-A has been found to be strongly expressed in cranial nerves and in different organs of the orofacial complex [450,

462], suggesting its importance for the establishment of correct craniofacial innervation [426]. In this context, we first aimed at uncovering the roles of Nogo-A in the establishment of tooth innervation. Since this process is known to be driven by target-derived factors, and that their proper uptake depends on the three-dimensional structure of the network itself, we investigated Nogo-A effect on the morphology of the neuronal network under development both *in vitro* DRG cultures and *in vivo* mouse molars.

8.4 Materials and methods

8.4.1 hDPSC spheroids characterization

hDPSC spheroids production

Dental pulp tissues were collected at the Center of Dental Medicine (ZZM, UZH) from extracted human teeth of three anonymous healthy patients. For cell isolation, dental pulp was minced and then enzymatically digested for 1 h at 37 °C in 3 mg/mL collagenase I (Thermo Fisher Scientific, Waltham, MA) and 4 mg/mL dispase II (Sigma-Aldrich, St. Louis, MO). The filtered single-cell suspension was plated in a T25 flask with standard complete medium, composed of Dulbecco's Modified Eagle Medium/Nutrient Mixture F-12 (DMEM/F12, Thermo Fisher Scientific) supplemented with 20% of fetal Bovine Serum (FBS, Sigma-Aldrich), 100 µg/mL penicillin/streptomycin (P/S, 100 U/mL, Sigma-Aldrich), 1% L-glutamine (Gibco, Thermo Fisher Scientific), and 0.5 µg/ml Amphotericin B (Thermo Fisher Scientific). Cells were cultured in incubator at 37 °C and 5% of CO₂. DPSCs are selected by plastic adherence and self-renewal potential in culture [463]. At about 80% of confluence, isolated hDPSCs were expanded in standard complete medium and then cryopreserved at passage III. One week prior to each experiment, hDPSCs were thawed and 2-D cultured at 5x10⁵ cell/cm² in Mesencult medium (STEMCELL Technologies, Vancouver, CA), 10% FBS and 1% P/S. At the first day of the experiment, cells at passage IV were used for spheroid production by hanging drop technique [87]. For each spheroid, 20'000 cells or additionally at 10'000 cells were seeded in 25 µl drops of Mesencult medium previously placed on the inner side of a Petri dish lid, then flipped.

Phosphatase buffer saline (PBS, Thermo Fisher Scientific) was added at the bottom of the Petri dish to reduce medium evaporation. After 24 h, formed 3-D spheroids were transferred to 96 ultra-low attachment plates (ULA plates, Corning, Glendale, AZ) and cultured in 100 μ l of Mesencult medium for 7 days at 37 °C and 5% CO₂, with medium change every 72 h. Spheroids morphology and viability were assessed at days 1, 2, 3, 4 and 7 after transferring to ULA plates.

hDPSC spheroids treatment

24 h after spheroid seeding, a γ -secretase inhibitor (DAPT (GSI-IX), N-[N-(3,5-Difluorophenacetyl)-L-alanyl]-S-phenylglycine t-butyl ester, Sigma-Aldrich) was used to block Notch signalling. hDPSCs spheroids were treated at day 1 with 2.5 μ M, 5 μ M, 10 μ M or 15 μ M of DAPT (DMSO solution). Morphology and viability of treated and untreated spheroids were assessed at days 1, 2, 3 and 6 after treatment.

Bright Field imaging and morphological analysis

Spheroids were imaged with a Leica DM IL Inverted Microscope (Leica Microsystems, Wetzlar, Germany) equipped with a N PLAN 10x/0.25 air objective, a DFC 7000T camera (Leica Microsystems) and the Leica Application Suite X (LAS X, Leica Microsystems) software. 2-D 32-bit RGB images were obtained with an XY resolution of 1920 \times 1440 pixels and an isometric pixel size of 0.664 \times 0.664 μ m², then exported in “.tiff” format. Image analysis of spheroids morphology was implemented in MATLAB® (R2021b v.9.11.0, The MathWorks, Natick, MA). After image conversion from RGB to 8-bit greyscale, spheroids were segmented by ISODATA thresholding [334] and their binary masks hole-filled [464]. Spheroids morphology was then described through the quantification of descriptors of dimension, shape, and compactness, as detailed in Assessment of Results.

Alamar Blue assay

For each experiment, 5 spheroids were incubated with Alamar Blue (AIB, Thermo Fisher Scientific, 1:10 dilution in DMEM) at 37 °C in the dark. 4 h later, supernatants were transferred in a new 96-multiwell plate, and their absorbance read at 570 nm and 600 nm with a Synergy HT microplate reader (BIO-TEK instruments, Winooski, VT). The percentage of AIB reduction (resazurin, OX, to resorufin, RED) was calculated following the manufacture instruction as:

$$\% \text{ Reduced} = \frac{(\varepsilon_{OX})\lambda_2 A\lambda_1 - (\varepsilon_{OX})\lambda_1 A\lambda_2}{(\varepsilon_{RED})\lambda_1 A'\lambda_2 - (\varepsilon_{RED})\lambda_2 A'\lambda_1} \cdot 100 \quad (8.1)$$

where, the molar extinction coefficients of AIB are $\varepsilon_{OX} (570)=155.677 \text{ M}^{-1} \text{ cm}^{-1}$, $\varepsilon_{RED} (570)=80.586 \text{ M}^{-1} \text{ cm}^{-1}$, $\varepsilon_{OX} (600)=14.652 \text{ M}^{-1} \text{ cm}^{-1}$, $\varepsilon_{RED} (600)=117.216 \text{ M}^{-1} \text{ cm}^{-1}$.

FDA/PI staining and viability analysis

For each experimental condition, 5 spheroids were collected in a 1.5 ml sterile tube with 1 ml of DMEM, washed twice with PBS 1X, and incubated with 1.6 μl of fluorescein diacetate (FDA, 5 mg/mL acetone solution, Sigma-Aldrich) and 10 μl of propidium iodide (PI, 1.6 mg/mL PBS solution, Sigma-Aldrich) for 5 min at room temperature (rt) in the dark. After resuspension in PBS 1X, spheroids were transferred into a μ -Slide 8-well chamber (ibidi, Gräfelfing, Germany) and imaged with a Zeiss Leica DM6000 Microscope (Leica Microsystems) equipped with a HC PL FLUOTAR 5x/0.15 air objective (Leica Microsystems), a DFC 350FX camera (Leica Microsystems) and the Leica Application Suite X software (LAS X, Leica Microsystems) for discrimination between viable (FDA, $\lambda_{em}=525 \text{ nm}$) and dead (PI, $\lambda_{em}=590 \text{ nm}$) cells. Acquired 2-D 32-bit RGB images with XY resolution of 1392×1040 pixels and isometric pixel size of $1.84 \times 1.84 \mu\text{m}^2$ were then exported in ".tiff" format. Image analysis of spheroids viability after FDA/PI staining was implemented in MATLAB® (R2021b v.9.11.0, The MathWorks). After image conversion from RGB to 8-bit greyscale, spheroids were segmented by ISODATA thresholding [334], and their binary masks hole-filled [464] after intermediate cleaning by morphological opening and closing by minimal SE (Subsect. 5.2.1) [125]. Spheroids viability was then described through the quantification of

spheroids median FDA and PI pixel intensity, and by computation of local maps of median pixel intensity [336].

Assessment of results

The aim of this study was to characterize 3-D hDPSC spheroids in terms of cell viability and morphology during culture. Spheroid viability was assessed by quantification of FDA/PI staining intensity and by AlB assay. Spheroid morphology was described in terms of dimension, shape, and compactness through the quantification of spheroids equivalent diameter (ED), sphericity index (SI) [87], and border indentation (BI), respectively. The ED is defined as the diameter of the circle that has the same area as the 2-D major section of the spheroid (Equation (8.2) and Figure 8.4 (a)), and can be used as an indicator of spheroid volume in the presence of a non-perfect sphericity [89]. The SI quantifies spheroid roundness according to the Equation 8.3 (Figure 8.4(b)), returning a value ranging from 0 (very flat) to 1 (perfect circle). The BI, calculated as in Equation 8.4, describes the level of irregularity at the spheroid surface, since it arises from the comparison between the spheroids binary mask and convex mask (hull), so between its detected shape and convex one (Figure 8.4 (c)). BI varies between 0 (highly angular) to 1 (perfectly convex), and works as an indicator of spheroid compactness, since it is sensitive to the presence of buds and concavities.

$$ED = \sqrt{4 \frac{A_m}{\pi}} \quad (8.2)$$

$$SI = \frac{\pi \sqrt{\frac{4A_m}{\pi}}}{P_m} \quad (8.3)$$

$$BI = \frac{A_m P_h}{P_m A_h} \quad (8.4)$$

where A_m and P_m are respectively the area and perimeter of the spheroid cross-section binary mask (Figure 8.4 (b), m), and A_h and P_h are respectively the area and perimeter of the spheroid cross-section convex mask (Figure 8.4 (b), h).

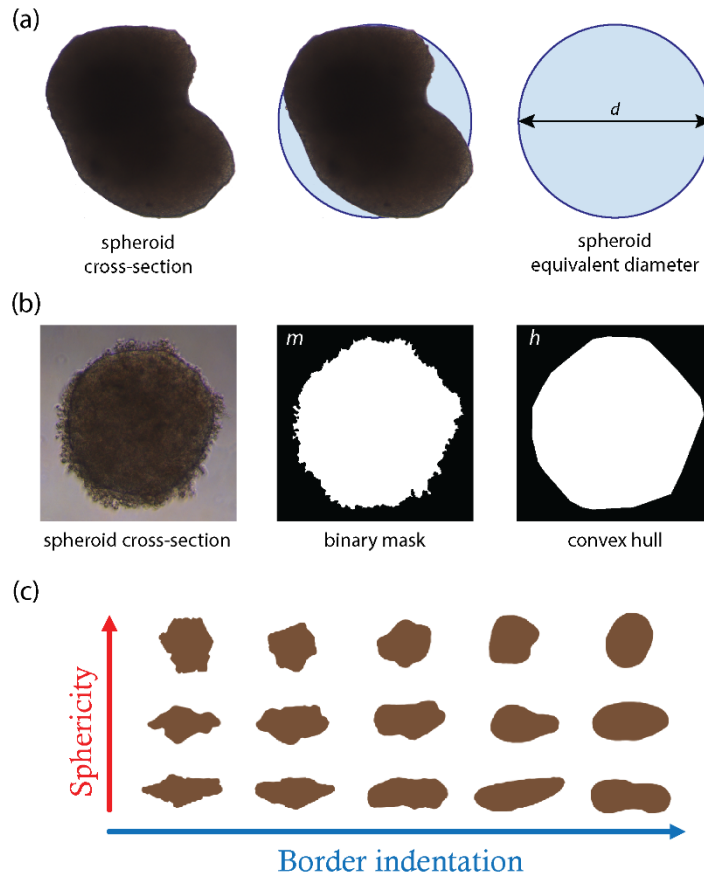


Figure 8.4. Spheroids morphology descriptors. (a) The ED is defined as the diameter of the circle that have the same area of the 2-D major section of the spheroid. (b) The convex hull (or mask) is the smallest convex polygon that can contain the object of interest. (c) Regular spheroids are characterized by both high SI and high BI, indicating global and local (surface) symmetry.

Statistical analysis

Data deviation from normality was early verified by histogram inspection, followed by the Shapiro-Wilk test, based on which the discriminatory power of descriptors is assessed by either two-tail Student's t-test or Wilcoxon rank-sum test. p-values < 0.05 were considered for statistical significance.

8.4.2 Nogo-A role in tooth innervation

Ethics statement

Animal housing and all animal experiments were performed according to the guidelines of the Swiss Animal Welfare Law and in compliance with the regulations of the Cantonal Veterinary Office of Zürich.

Generation of Nogo-A knockout mice / murine model

Nogo-A KO (-/-) mice were previously generated and kindly provided by the group of Prof. Martin Schwab (Institute for Brain Research, UZH and ETH Zürich). [121]. Mouse genotyping was performed via PCR using the following primers: Fw: 5' TGC TTT GAA TTA TTC CAA GTA GTC C 3', Rv1: 5' CCT ACC CGG TAG AAT ATC GAT AAG C 3', Rv2: 5' AGT GAG TAC CCA GCT GCA C 3'.

Dental pulp isolation

Dental pulp was isolated from wild-type (WT) and Nogo-A KO (-/-) C57/BL6J mice after birth (P0) at postnatal stages PN4, PN7, PN9, PN20, PN25 and PN27. Mice were sacrificed by decapitation, following (PN20, PN25, PN27) or not (PN4, PN7, PN9) anaesthetic injection (PN20: Ketamine 65mg/kg, PN25: Xylazine 13mg/kg, PN27: Acepromazine 2mg/kg). Left and right lower first molars were manually dissected from the lower jaw in cold 1X PBS (Gibco) and under a stereomicroscope. For the PN4, PN7 and PN9 stages, dental pulp was directly isolated from the forming hard tissues by hand-dissection, fixed in 4% paraformaldehyde (PFA, Sigma-Aldrich) pH 7.4 for 15 min rt, washed 3 times in 1X PBS and then stored in PBS 0.02% Sodium Azide (Sigma-Aldrich) at 4°C. For the PN20, PN25 and PN27 stages, dissected molars were fixed in 4% PFA pH 7.4 for 30 min rt. After 3 washes in 1X PBS, molars were decalcified in 0.5M EDTA (Fluka, Sigma-Aldrich) rt for at least a week. Once softened, the dental pulp was hand-dissected from the hard tissues and stored in PBS 0.02% Sodium Azide at 4°C.

Whole-mount immunostaining and Fluorescence confocal microscopy

Isolated dental pulps were incubated in blocking buffer solution (1X PBS, 0.02% Sodium Azide, 10% FBS (Sigma-Aldrich), 2% BSA (Carl Roth GmbH, Karlsruhe, Germany), 0.05% Saponin (Fluka)) overnight at 4°C on a shaker. Then, dental pulps were incubated with the primary antibodies (anti-Neurofilament Light antibody (Cell Signaling Technology, Denver, MA) for PN7 and PN9 stages, and anti-Peripherin antibody (Merck Millipore, Burlington, MA) for PN4, PN20, PN25 and PN27 stages, 1:100 dilution in blocking buffer) for 72 h at 4°C on a shaker. After 3 washes (1 h each, rt) on a shaker with blocking buffer, the dental pulps were incubated with the secondary antibodies (anti-Rabbit 488 (Invitrogen, Waltham, MA) for anti-Neurofilament Light, and anti-Rabbit 568 (Invitrogen) for anti-Peripherin, 1:100 dilution in blocking buffer) for 24 h at 4°C on a shaker, additioned with 1 µg/mL of 4',6-diamidino-2-phenylindole (DAPI, Tocris Bioscience, Bristol, UK) and incubated for another 24 h. After 3 washes (1 h each, rt) on a shaker with blocking buffer, dental pulps were finally incubated overnight at 4°C in HistoDenz™ (Sigma-Aldrich) for tissue clearing. Once cleared, the dental pulps were mounted on a cover slide moulded with silicone paste KORASILON™ (Sigma-Aldrich) and filled with HistoDenz™ to house the sample, finally covered with a glass coverslip. Samples were imaged with either a Leica SP8 Falcon or a Leica Stellaris confocal microscope (Leica Microsystems), each equipped with the Leica Application Suite X (LAS X, Leica Microsystems) software as mosaics of 2, 4 or 6 images, as needed to cover all dental pulp regions. 12-bit images were acquired with a HC PL Fluotar 10×/0.3 air objective with an isometric xyz pixel size of 0.89×0.89×4.28 µm³ and stitched by LAS X in images of different final resolution, before exporting in the proprietary “.lif” file format.

Molar neuronal network segmentation

Single-channel 12-bit grey-level images of Neurofilament Light or Peripherin signal were visualized and exported to uncompressed “.tiff” format by LAS X software. All subsequent image processing procedures were implemented in MATLAB® (R2021b v.9.11.0, The MathWorks). Molar neuronal network was first segmented in each 2-D optical section by histogram thresholding with Triangle

method [335]. Then, the 3-D network binary mask is created by simple juxtaposition of single section binary masks. The 3-D network mask is firstly cleaned of small objects, setting the threshold for elimination by Triangle method on the histogram of all object dimensions. Then, the maximum intensity projection (MIP) of the mask is created, to visually check and eventually manually eliminate the artifacts introduced at network periphery by dental pulp dissection. To investigate its morphology in terms of branching and extension, the segmented network was finally skeletonized (*i.e.*, reduced to 1-pixel wide curved lines, [465, 466]) to topologically separate nodes from branches without changing the essential structure of the image. Network, nodes, and branches properties have been then quantified as detailed in Assessment of Results.

***In vitro* DRG cultures**

WT and Nogo-A KO C57/BL6J mice were used at embryonic stages. After first detection of the mother vaginal plug (embryonic day (E)0) and following more accurate staging of the embryos according to morphological criteria, the pregnant mother was anaesthetized by injection with Ketamine 65mg/kg at day E13.5 (WT) or with Xylazine 13mg/kg at day E14 (KO), and death confirmed by decapitation. Collected embryos were kept in cold PBS, and DRG from all vertebral levels were manually dissected in cold PBS under a stereomicroscope. DRGs explanted from a same embryo were then plated on a same glass coverslip coated with 20 μ g/ml of Poly-D-Lysine (PDL) and 10 μ g/ml of Laminin (Sigma-Aldrich) and placed in a 12-well culture plate. Cultures were incubated at 37 °C and 5% CO₂ in Neurobasal medium (Gibco) supplemented with 20mM Glutamine (Gibco), 1X B-27 (Gibco), 100 ng/ml NGF (PeproTech, Thermo Fisher Scientific), and 1:100 of Pen/Strep (Sigma-Aldrich). 0.25pM cytosine arabinoside (Ara C, Sigma-Aldrich) was added to inhibit mitosis of non-neuronal cells. Prior to incubation, WT cultures were treated as following: 10 μ g/ml of anti-Nogo 11C7 antibody [467], or 10 μ g/ml of Mouse IgG antibody (Thermo Fisher Scientific), or 1 μ M of purified Nogo-A Δ 20 fragment [467], or no treatment. The culture was stopped after 2 days, after visible differences in DRG network extension following the different treatments. Cultures were then washed with warm (37°C) 1X PBS, incubated in warm 4% PFA pH 7.4

for 15 min, washed 3 times in 1X PBS and finally stored in 1X PBS at 4°C until imaging.

DIC imaging

DRG cultures were imaged by DIC microscopy with an inverted Leica DMI8 microscope (Leica Microsystem) equipped with a HC PL Fluotar 10×/0.32 air objective and the Leica Application Suite X (LAS X, Leica Microsystems) software. Mosaics of multiple images, needed to fully image DRG neuronal networks, were created by LAS X acquisition software prior to exportation in proprietary “.lif” file format, by stitching single 2-D 12-bit images with an XY resolution of 2048×2048 pixels and an isometric XY pixel size of 0.645×0.645 μm^2 .

DRG neuronal network segmentation

Mosaic images were visualized and exported to uncompressed “.tiff” format by LAS X software. Then, the region of interest (ROI) within segment the network fibres was defined by an ImageJ (NIH, Bethesda, MD) macro, written on-purpose. In brief, the Sobel operator was applied to detect image edges [468], and the histogram-based Triangle method [335] used to binarized the result. All following procedures were then implemented in MATLAB® (R2021b v.9.11.0, The MathWorks). First, the DRG was segmented by intensity thresholding of the original image values underlying the ROI with the ISODATA method [334]. Then, the network region (NR) was segmented by difference from the ROI. Within the NR, the network fibres were segmented by enhancing first the local image contrast [469] and then the elongated or tubular structures in the image using Hessian-based multiscale filtering [470], finally simply binarizing the result setting the intensity threshold to zero. Obtained network mask was finally cleaned from air bubble artifacts using a Circular Hough Transform-based algorithm [471-473].

Assessment of results

Two main descriptors of neuronal network morphology are branching (*i.e.*, single axon splitting) and defasciculation (*i.e.*, separation of single fibres/axons from a bundle) level. Accordingly, the morphology of the molar neuronal network both from WT and Nogo-A KO C57/BL6J mice was characterized at PN4, PN7, PN9, PN20, PN25 and PN27 by measurements of: a) network volume, surface, and surface-to-volume ratio (SVR), estimated from the non-skeletonized network mask, b) network length, nodes and branches number, estimated from the skeletonized network mask. Given the actual analysis resolution, unsuited to capture single axons, nodes and branches number were used as indicators of network ramification (without distinction between branching and (de)fasciculation), while network length was used as an indicator of network extension. Similarly, DRG neuronal network morphology was quantified through measurements of network surface, length, and maximum width, as well as network nodes and branches density (*i.e.*, nodes/branches number over network surface).

Statistical analysis

Data deviation from normality was early verified by histogram inspection, followed by the Shapiro-Wilk test, based on which the discriminatory power of descriptors is assessed by either two-tail Student's t-test or Wilcoxon rank-sum test. p-values<0.05 are considered for statistical significance.

8.5 Results and discussion

8.5.1 hDPSC spheroids characterization

With respect to traditional 2-D cultures, 3-D multicellular spheroids have been demonstrated to model the MSCs cellular microenvironment more accurately and, consequently, to better preserve stemness through culture [75, 76]. Preservation of DPSCs stemness was assessed through expression of MSC and ECM markers, besides visual inspection of spheroid surface by SEM imaging, which confirmed an abundant ECM secretion (data not shown).

Spheroids morphology and viability have been demonstrated to be a primary source of variability in spheroid-based preclinical research, potentially undermining the reproducibility of data [89]. Following previous evidence in this regard [89], we firstly assessed the capability of spheroid sphericity and dimension to affect other morphological parameters and spheroid viability over a culture period of 7 days (Figure 8.5 (a)).

Morphological analysis indicated that spherical (S, $SI \geq 0.9$) and non-spherical (NS, $0.8 \leq SI < 0.9$) spheroids do not differ in dimension (*i.e.*, ED), but differ in shape ($BI_S + 12\%$ than BI_{NS} on 7 days-average, $p < 10^{-5}$, data not shown). Expectedly, SI and BI positively correlate, as both negatively depend on spheroid cross-section perimeter (Equations 8.3 and 8.4), affected by irregularities at the spheroids border. S spheroids regularize in 24 h after creation, specifically reducing in dimension, increasing in sphericity, and stabilizing their morphology for 72 h. NS spheroids display a bit more irregular evolution through time, fully stabilizing their morphology only for 24 h, from day 3 to day 4 (data not shown). Both S and NS spheroids show comparable and strong viability, with FDA signal intensity 7 times higher than PI's on average ($p < 0.03$). Collectively, these data indicate that a pre-selection between S and NS spheroids is not necessary, though this last consideration may not hold for SI values lower than 0.8.

As far as spheroids dimension is concern, two different seeding densities (20'000 cells/drop and 10'000 cells/drop) were tested. Morphological analysis on Bright Field microscopy images indicates that 20'000 cell-spheroids (2CS) and 10'000 cell-spheroids (1CS) expectedly differ in dimension (ED_{2CS} 0.6 times bigger

than 1CS's on average, $p < 10^{-10}$), but not much in shape. As for morphology, 2CS and 1CS viability similarly evolved through time, with FDA signal intensity always doubling PI's (+91% on average of days for both 2CS and 1CS, $p < 0.03$). Despite their similarities, spheroids visual observation and manipulation suggested 2CS as being more resistant to external stress (*e.g.*, transferring, chemical dissolution), while 1CS, being much smaller, were lost or disrupted during manipulation. However, with due care, small 1CS can be ideal for specific applications, such as Organ-on-Chips cultures.

Without distinction of sphericity or dimension, 3-D hDPSC spheroids created by hanging drop technique have a median ED of $565 \pm 65 \mu\text{m}$ at day 1, progressively decreasing to $429 \pm 35 \mu\text{m}$ at day 7 of culture (Figure 8.6 (b), -24%, $p = 10^{-36}$). Spheroids are quite spherical already from day 1 (median SI = 0.81 ± 0.1), moderately increasing in sphericity after 24 h (+10%, $p = 10^{-6}$) and slightly dropping again at day 4 (-1.5%, $p = 0.034$). BI evolve similarly, remarking the necessity of a smooth surface for spherical spheroid definition (Figure 8.5 (b)). More generally, the collected results indicate that spheroids created by hanging-drop technique require 24 h for suitable morphological settlement (*i.e.*, all features strongly vary from day 1 to day 2, with p -values no higher than 10^{-6}), becoming more stable between day 2 and 3, when they stabilize their shape but not their dimension. Spheroids were highly viable during the culture period, reaching a maximum of FDA intensity at day 3, when it tripled its initial value ($p = 0.001$, vs dead cells). Moreover, cellular death (*i.e.*, PI intensity) was constitutively low (one order of degree lower than FDA's at each time point), showing no significant variation through time. Both FDA and PI signals decrease, although not significantly, after day 4 of culture (Figure 8.5 (c)). Finally, the metabolic activity of spheroids was stable throughout culture but constitutively lower than standard monolayer culture, though these differences are never statistically significant (Figure 8.5 (c), -35% on average, $p > 0.05$).

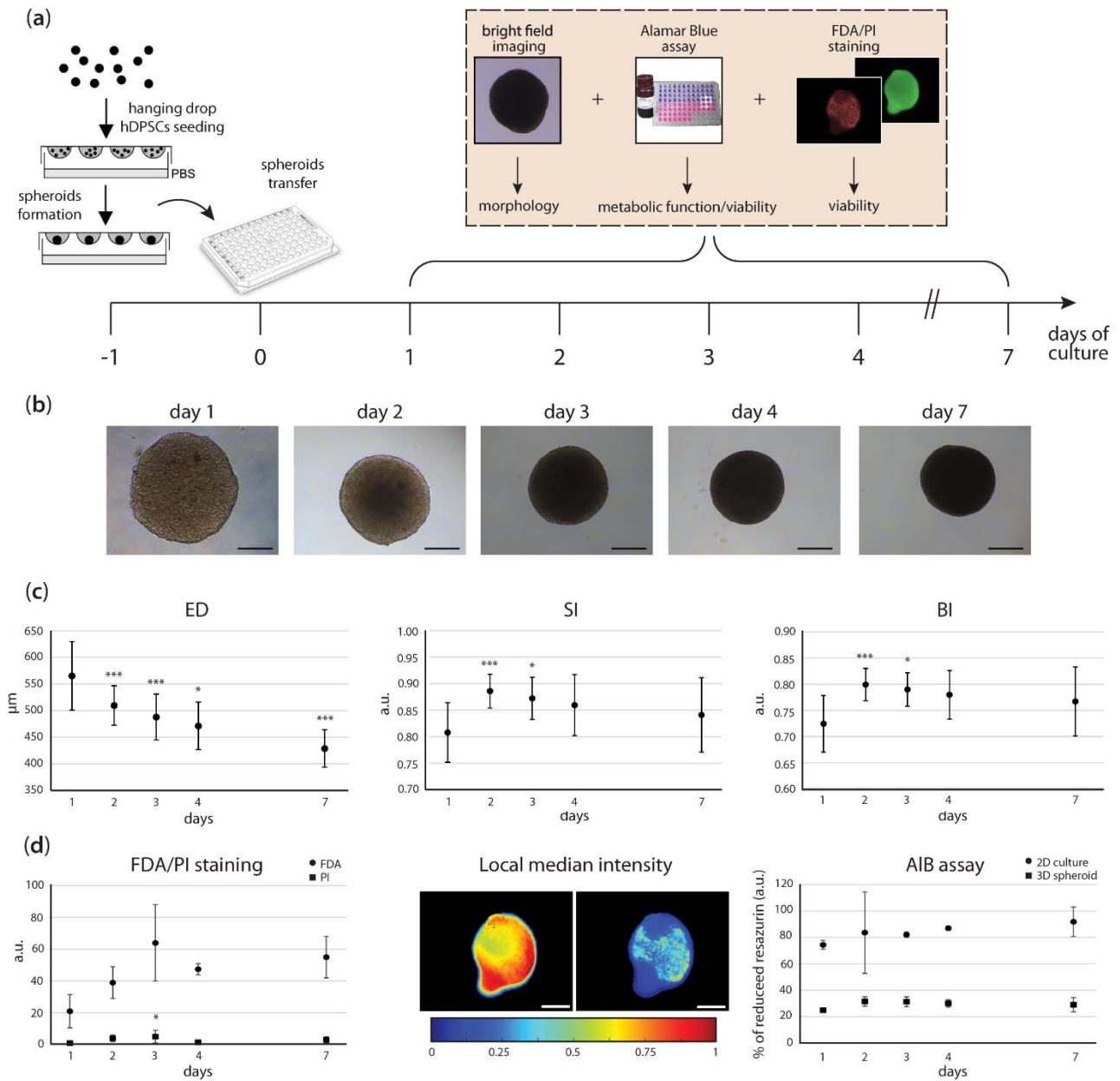
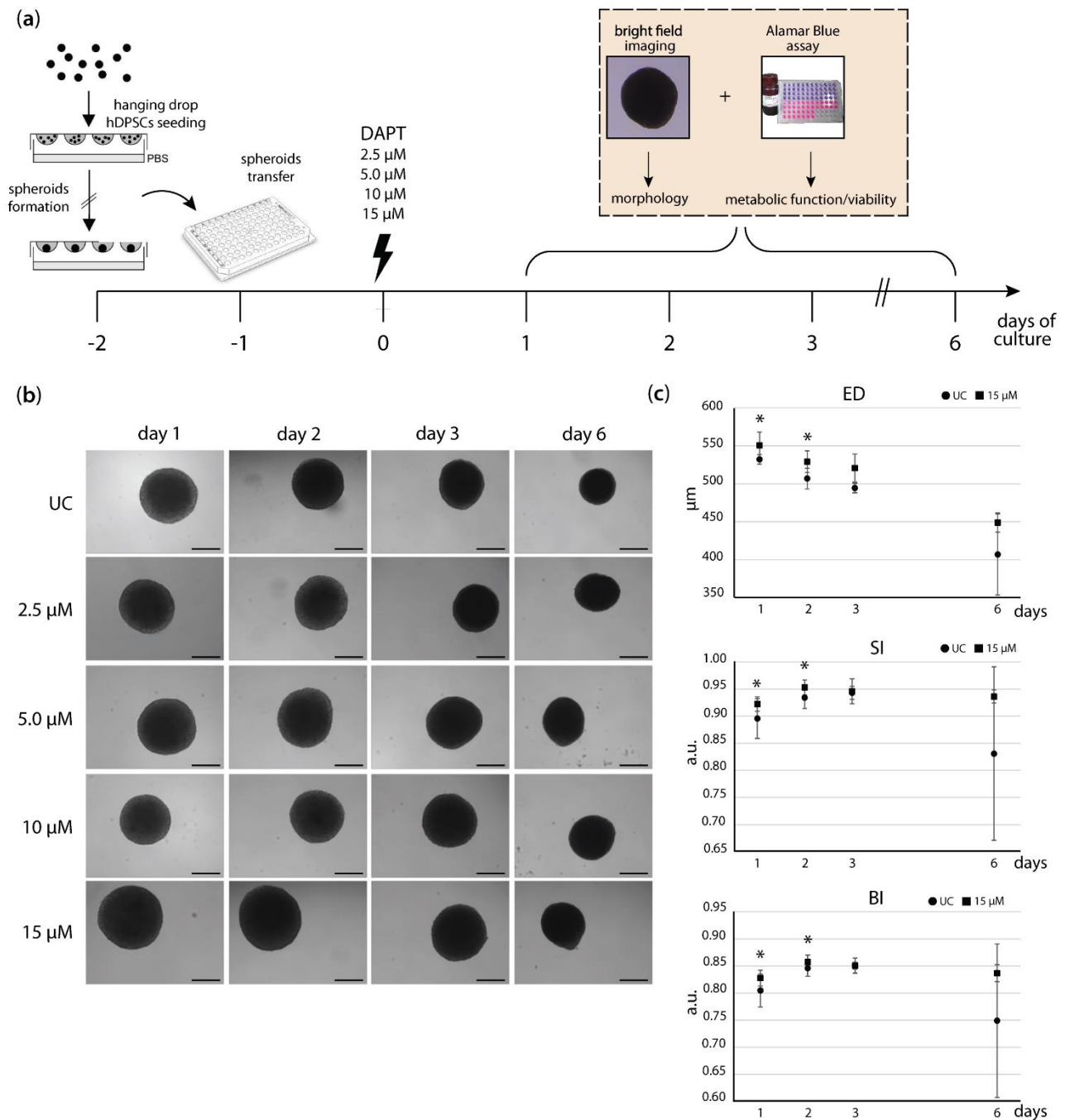


Figure 8.5. hDPSCs spheroids morphological characterization. (a) Experimental scheme. hDPSCs spheroids were created by hanging drop technique in 24 h and transferred to 96-well ULA plates for individual characterization of their morphology and viability. (b) Representative Bright Field images of spheroids evolution in time. Scale bars: 100 μm . (c) Time evolution of hDPSC spheroids dimension (ED), shape (SI), compactness (BI). (d) Time evolution of hDPSC spheroids viability, assessed through FDA/PI staining, local maps of median FDA/PI intensity (3 \times 3 pixels locality, scale bars: 200 μm) and metabolic activity over time expressed as percentage of reduced resazurin (AIB assay). Data reported as grand median \pm MAD (n=3). *p<0.05, **p<0.01 ***p<0.001 for comparison to day 1.

All considered, the hanging drop technique has a mean efficiency of spheroid creation of 82% at day 1 that rises to 87% after 24 h. The increase is due to the re-organization into proper spheroids within the first 24 h of those spheroids that fell back to loose cell aggregates during transfer from drop to plate well. As day 3 is the day at which viability (by FDA/PI staining) is the highest and morphology is more stable, it is here suggested as the best day for spheroids selection for further applications. Since no remarkable difference has been detected between 2CS and 1CS, seeding density may be varied (at least within this tested range) to custom spheroids dimension, for example after the needs of following spheroids application. Since no remarkable differences have been detected between spherical ($SI \geq 0.9$) and non-spherical ($0.8 \leq SI < 0.9$) spheroids, sphericity threshold can be lowered to $SI = 0.8$ for spherical spheroids selection. Accordingly, hanging drop technique has an efficiency of creation of spherical spheroids of 33% at day 1, increasing at 55% at day 3.

Finally, such established hDPSC 3-D *in vitro* model was used to investigate the influence of Notch signalling pathway. In details, hDPSC spheroids were treated with increasing doses of the Notch inhibitor DAPT prior to morphology and cell viability assessment. No significant difference from untreated control (UC) was ever detected below a DAPT dose of 15 μM . Over 15 μM DAPT, treated spheroids dimension and morphology differ from UC on day 1 and day 2 of culture, when spheroids are slightly bigger (Figure 8.6 (c), +5% ED on average of days 1-2, $p < 0.02$), more spherical (Figure 8.6 (c), +7% SI on average of days 1-2, $p < 0.04$) and more compact (Figure 8.6 (c), +3% BI, $p < 0.02$) than UC. ALB assay reported only a remarkable but not significant decrease in spheroids viability from day 1 to day 2 of culture, independently of treatment (data not shown). Together, these preliminary findings indicate that DAPT does not remarkably affect hDPSC spheroids morphology and viability. Addition data ($n=1$, data not shown) reported a DAPT dose of 50 μM as still being not effective on hDPSCs spheroids morphology. Rather, as seen for lower DAPT doses, spheroids appear a bit affected (disaggregated) right after treatment (*i.e.*, first 24 h), quickly recovering their original UC-like appearance in a 24-48 h (Figure 8.6 (b)). However, given the established Notch role in hDPSCs biology [474], Notch receptors expression and the effect of higher DAPT doses need to be tested before drawing any conclusion.



8.5.2 Nogo-A role in tooth innervation

Nogo-A impacts size and branching of *in vivo* molar and *in vitro* DRG innervation

From a morphological point of view, neuronal Nogo-A has been shown to regulate neurites fasciculation, branching and extension in the developing nervous system. In particular, while neuronal network physiological growth is characterized by both branching (*i.e.*, single axon splitting) and (de)fasciculation (*i.e.*, separation of single fibres/axons from a bundle), in conditions of Nogo-A genetic depletion the network is expected to be less branched and more fasciculated [475]. We therefore investigated how the presence of Nogo-A and the developmental moment affect the morphology of molar innervation in mice. At PN4, no significative differences were found between WT and Nogo-A KO network morphology. However, this could be due to the fact that at PN4 the innervation has just begun, and the network has not been properly structured and shaped by external cues yet. At PN7, the genetic ablation of Nogo-A more than halves the number of nodes and branches (-57% on average, $p < 0.03$), confirming the expected reduction in network ramification. However, our data indicates that this is not coupled with an increase in network extension in terms of length, volume or surface. No significative alteration of network morphology after Nogo-A depletion is detected in the adult stages (PN20, PN25, PN27). As a sporadic exception, at PN25 Nogo-A depletion reduces the network surface by one third (-31%, $p = 0.03$). When considering the network evolution in time, most significant changes were detected during the early development, between PN4 and PN7, when the WT network greatly expands in terms of volume ($\times 4.9$ -fold, $p = 0.003$), surface ($\times 4.1$ -fold, $p = 0.003$) and length ($\times 2.4$ -fold, $p = 0.045$). At Nogo-A absence these increments are doubled, accordingly to expectations for a more extended network. Furthermore, moving from PN4 to PN7 also the number of nodes ($\times 10$ -fold avg, $p < 0.02$) and branches ($\times 7$ -fold avg, $p < 0.03$) increases in both WT and Nogo-A KO mice. Nogo-A KO number of nodes and branches further (but more moderately) increases from PN7 to PN9 ($\times 2$ -fold avg, $p = 0.034$). Little to no significative changes occur after PN9. Collectively, Nogo-A seems to not

particularly influence the neuronal network morphology, more affected by the developmental stage. To assess whether more marked results could be masked by low sample sizes, we repeated the analysis after pooling the data by developmental stage. PN4 (*early stage*) was kept aside, as it is an initial phase of development very different from the others. Since tooth eruption represents a turning point for tooth innervation, at which the network becomes functional and responsive, PN7 and PN9 were pooled in a young (*pre-eruption*) stage, while PN20, PN25 and PN27 were pooled in an adult (*post-eruption*) stage. However, after data pooling no significant difference in neuronal network morphology between WT and Nogo-A KO is detected anymore, at any developmental stage. Accordingly, data pooling increases the variance associated to any quantified morphological descriptor, suggesting that, even if temporally close to each other, the pooled stages are too different to be effectively pooled (*i.e.*, to produce a reduction in variance by sample size increasing). On the other side, data pooling effectiveness is higher for what concern the time evolution of network morphology. Apart from network SVR in Nogo-A KO mice, all the other morphological descriptors increase from early to pre-eruption stage, according to the important network growth occurring in this time frame (data not shown). Following the pre-pooling evidence, except for branches number, all increases are doubled at Nogo-A absence. All descriptors further increase from pre- to post-eruption stage, with significance strengthened by data pooling. Again, the increase in network extension and ramification is more moderate in this second step, lowering the average increase for network descriptors from 6.8 folds (early to pre-eruption stage) to 2.6 folds (pre-eruption to post-eruption).

All considered, Nogo-A seems to affect the tooth neuronal network morphology, however poorly. These results are surely linked to the low number of samples, besides to the high variability of phenotypes that characterized the WT and especially the Nogo-A KO samples. Accordingly, the few significant differences detected between WT and Nogo-A KO network occurred at PN7, the stage with the higher sample size. However, our data can be considered as preliminary evidence of Nogo-A involvement in tooth innervation during development, as highlighted by data plotting over time (Figure 8.7).

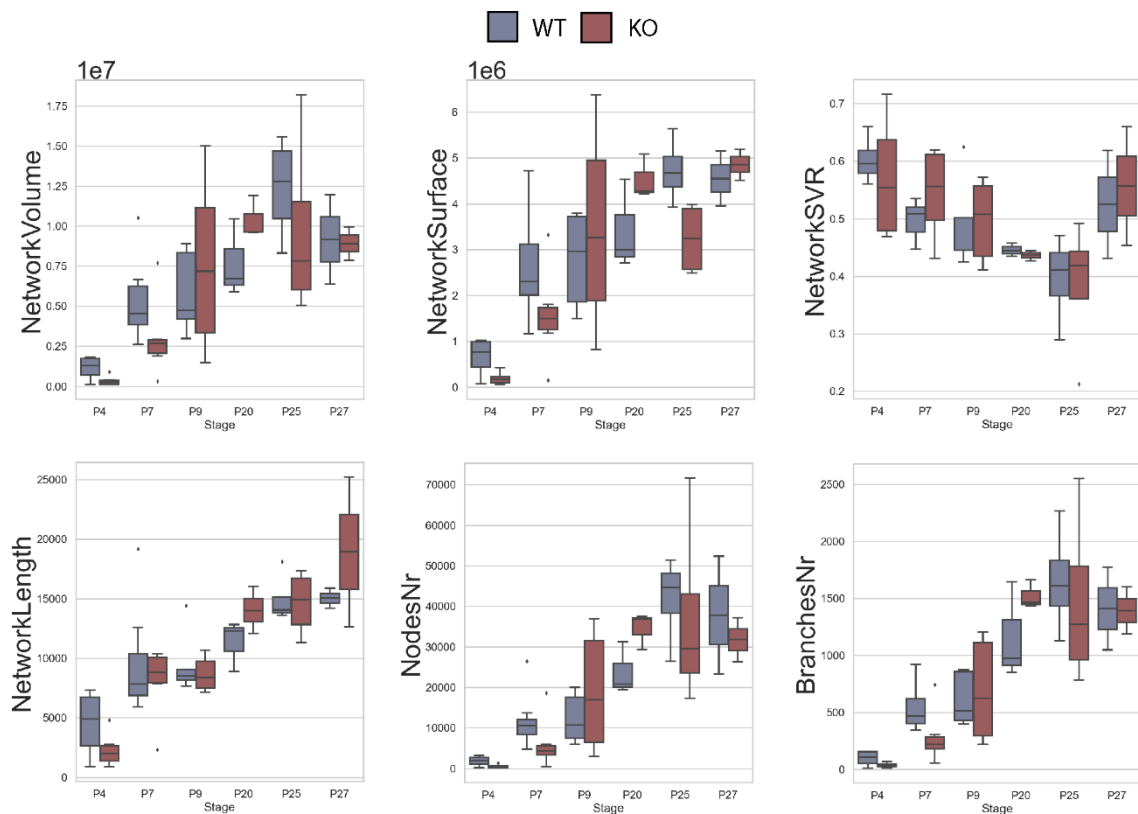


Figure 8.7. Development of neuronal network morphology in WT and Nogo-A KO mice molar. Tooth innervation during development is characterized by a progressive increase in network extension and ramification. Before tooth eruption (~PN20 in mice), the WT network is more extended and ramified than in Nogo-A KO, while such relationship is reversed at later stages, suggesting that Nogo-A may play different roles in early and late tooth developmental stages. Image courtesy of Laurence Pirene, PhD student, Orofacial Development and Regeneration Unit, IOB, UZH.

To further investigate the role of Nogo-A in tooth innervation, we also considered the neuronal network morphology in trigeminal ganglia *in vitro* cultures. However, due to technical issues, it was necessary to first move the investigation to dorsal root ganglia. First, more than 30 DRGs can be harvested from each embryo, while the TGs are just two. Second, the much bigger size of TGs, with respect to DRGs, makes ganglia attachment to the plate surface much harder, therefore strongly hampering the growth of the network. Finally, previous preliminary tests on TG (data not shown) seemed to not correlate to DRG results [475], suggesting that the TG and DRG may behave differently, when it comes to Nogo-A. For these reasons, we first focused on DRG cultures, to optimise the culturing, imaging and image processing protocols, so as to be able to move back

to TG. Besides assessing the extension and ramification of the neuronal network of DRG explanted from WT and Nogo-A KO mice, we also tested, as additional controls, the effect of the addition to the WT DRG culture medium of the 11C7 antibody, the IgG antibody, and the purified Nogo-A specific $\Delta 20$ fragment. The 11C7 antibody is expected to neutralize the Nogo-A protein, leading to its acute inhibition, and therefore to increase the length and reduce the ramification of the WT DRG network [467]. Oppositely, the IgG antibody is used as a negative control to the 11C7 antibody, as it mimics 11C7 structure, but does not specifically target the Nogo-A protein. This treatment is therefore not expected to affect the network morphology. Finally, the $\Delta 20$ fragment is expected to increase the length and reduce the ramification of the network, accordingly to its capability to activate Nogo-A receptors even in the absence of the whole protein [467] (Figure 8.8 (b)). Visually, the only appreciable change in DRG network morphology is its shortening and “condensation” after $\Delta 20$ addition to WT cultures (Figure 8.8 (a)). Quantitatively, $\Delta 20$ addition to WT culture medium expectedly decreases both network surface and length (Figure 8.8 (b), -55% avg, $p=0.037$), while increasing nodes and branches density (Figure 8.8 (b), +37% avg, $p<0.003$), presumably reflecting an increase in axon fasciculation. According to previous evidence [475] and with respect to WT DRG cultures, the density of nodes and branches was higher in the Nogo-A KO DRG culture (Figure 8.8 (b), +30% avg, $p<10^{-5}$), while the maximum width (*i.e.*, extension) of the network was higher after 11C7 addition (Figure 8.8 (b), +13%, $p=0.04$) and lower after $\Delta 20$ addition (Figure 8.8 (b), -37%, $p<10^{-3}$). With respect to Nogo-A KO DRG network, the addition of anti-Nogo-A 11C7 antibody decreases ramification (*i.e.*, nodes and branches density, Figure 8.8 (b), -15% avg, $p<0.03$) and increases extension (Figure 8.8 (b), +29% network max width, $p=0.016$), suggesting an affective acute inhibition of Nogo-A by 11C7 antibody.

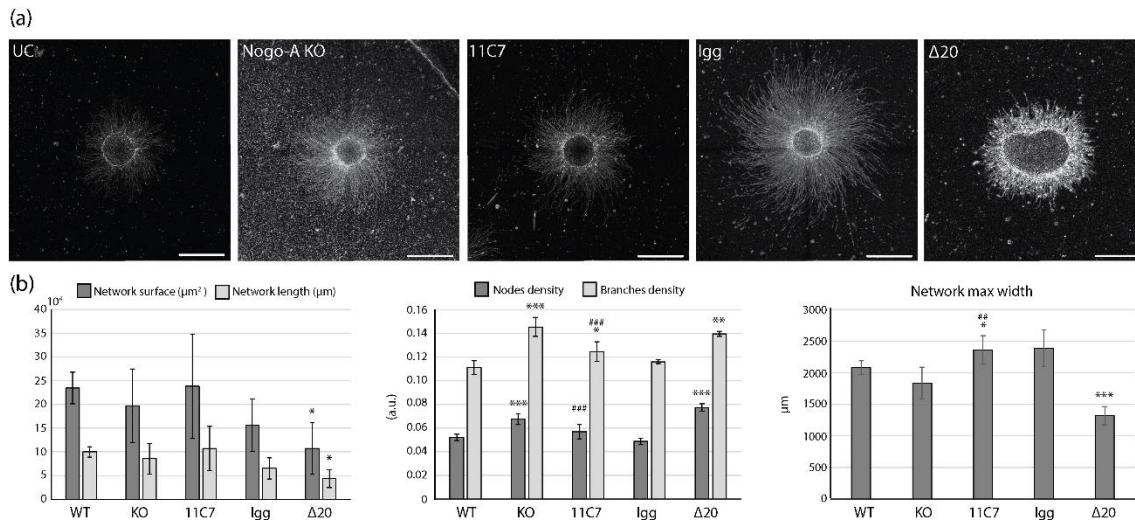


Figure 8.8. Nogo-A affects DRG network size and morphology. (a) Representative images of DRG explanted cultures. Scale bar: 500 μm . (b) Bar graphs for quantified morphology descriptors. Data reported as median \pm MAD. * significance to WT, # significance to Nogo-A KO. */# $p < 0.05$, **/# $p < 0.01$ ***/### $p < 0.001$.

All considered, similarly to what was observed in the *in vivo* molar model, our data indicate Nogo-A involvement in the neuronal network structuring, however with some controversial results for the Nogo-A KO condition. This could be due to fact that in the absence of Nogo-A different compensatory pathways are known to be activated. Therefore, the effect of Nogo-A absence on the network morphology could be masked by overexpression of other proteins with Nogo-A-like functions. Indeed, beside confirming Nogo-A mRNA expression in the WT mice only, RNA sequencing experiments reported an increased expression levels of other Nogo isoforms in Nogo-A KO mice (data not shown), as already demonstrated in the CNS [476], presumably triggering alternative compensative pathways. Moreover, in our KO mutant only the Nogo-A specific exon 3 is deleted, this meaning that compensatory mechanisms can be triggered by other Nogo-A domains (*e.g.*, C-t), other Nogo isoforms, or even other proteins, not encoded by RTN4.

8.6 Conclusions

In this Chapter, we applied our content-aware approach to two different studies of dental biology. The first aimed at characterizing 3-D hDPSC spheroids, in the perspective of their future utilization as organotypic models for

developmental and regenerative medicine studies. To this purpose, we followed the evolution in culture of hDPSC spheroids created by hanging drop technique, in terms of stemness, proliferation, morphology and viability. Although preliminary, collected data provide a solid characterization of 3-D hDPSC spheroids *in vitro*, that enhances stemness and ECM secretion with respect to 2-D cultures, without losing cell viability. Our results represent a first solid step towards the creation of a 3-D *in vitro* model of tooth, by which collectively investigate innervation, vascularization and immune response and establish the basis for future regenerative personalised treatments.

The second study concerned the investigation of the Nogo-A protein role in the 3-D architecture of tooth innervation. Our results showed that Nogo-A is expressed in DRG, TG and dental tissues from the earliest developmental stages, and that this expression persisted until adulthood. Genetic ablation of Nogo-A affected the branching and compactness of the dental pulp neuronal network, while in the DRG it affected the neuronal projections pattern. Taken together, our findings indicate that Nogo-A is a regulator of tooth innervation, whose importance in development, homeostasis and regeneration processes will be further unravelled by ongoing transcriptomic analyses.

8.7 Content-aware contribution and future developments

My presence in the laboratory during the collaboration period has remarkably increased the content-aware contribution I could give to the studies. Especially for the hDPSC spheroids characterization, for which a dataset of images had not yet been created by my arrival, my direct and entire involvement from the very beginning of the study allowed to define the best microscopy modality for spheroids imaging, to analyse its results in real time, and consequently to redefine the experimental pipeline on-line. This way, we could save time while increasing the robustness of the analysis, defining from the outset the necessary sample size and the importance and necessity of each experiment basing on previous results, thus coming to collect a large amount of imaging and molecular data in just three months, sufficient for a first high-level publication (on writing).

For what concern the study of *in vivo* molar innervation during development, my biological formation was fundamental for a fast and comprehensive understanding of the evolution of neuronal network in the developing tooth, and of the role of Nogo-A, that together allowed me to define the importance of network branching and extension, finally segmenting the 3-D network with an acceptable level of approximation, consistent with our timeline and aim.

For what concern 3-D hDPSC spheroids characterization, conceived as forerunner study for a multitude of applications based on this model, possible future developments are many and promising. First, we intend to increase the analysis robustness and completeness by testing the effect of higher doses of the Notch inhibitor DAPT on spheroids properties, with further negative and positive controls, also verifying the expression of Notch and its target genes (*e.g.*, DII4, Hes1, Hes2, Hey1, Hey2) in both hDPSC 3-D spheroids and 2-D cultures. Then, the following steps of the studies will involve: 1) the assessment of spheroids regenerative potential by gene and protein expression analysis on spheroid-released exosomes content, 2) the assessment of spheroids angiogenesis potential by creation and characterization of heterotypic spheroids of DPSCs and ECs (HUVECs or primary hECs). In this phase, image analysis will be fundamental to reconstruct the vascular network and assess its geometrical properties. Once validated, this heterotypic model could be a key elucidator of perivascular niche mechanisms [474]. A further step would be to add trigeminal ganglia neuronal cells to such heterotypic spheroid, to further study tooth innervation and the extracellular cues driving its formation. Finally, the transition to Organ-On-Chip cultures will ideally enable the creation of a 3-D model of tooth that emulate the physiology of human dental tissues, allowing the study of their response to environmental and pharmacological stimuli, as well as the generation of fully functional dental tissues for regenerative medicine and more meaningful drug testing applications. From a methodological point of view, a first necessary improvement would be the validation of equivalent diameter measurements by confocal microscopy, to demonstrate that, at least up to a certain convenient dimension, spheroid volume and ED can be said to linearly correlate (so far, we are just assuming a strong local symmetry). Similarly, it would be interesting to verify that also in our model, where spheroids are smaller than 650 μm in

diameter, spheroids viability is linear to volume, as in [89]. Secondly, spheroid heterogeneity could be investigated through the creation of a library of local feature maps [336], to look for recurrent patterns and analyse buds presence and characteristics. Further development may include the investigation of properties of highly irregular spheroids (*e.g.*, $SI < 0.7$, or very different dimension), the refinement of viability results by sample size increasing, and the investigation of local spheroid properties, for example after imaging by light sheet microscopy.

For what concern the investigation of the role of Nogo-A in molar innervation, additional samples are currently being collected, to investigate the variability of Nogo-A KO phenotypes and reduce its impact on the significance of the analysis. Then, a first future step will be the comparison of image analysis results with the RNA sequencing data checking the expression of Nogo-A, other Nogo isoforms and the activation of compensatory pathways in WT and Nogo-A KO mice. Methodologically, the next step of image analysis would be the separate investigation of tooth crown and roots in adult tooth, to assess a potential different role for Nogo-A in the two regions. Interestingly, no method for the automated roots-crown separation in microscopy images is currently available in the literature. Therefore, one could think of searching for one (or more) neuronal network morphological properties on which automatedly basing the distinction. In such work, local density analysis by DDMs (Chapter 4, [130]) could provide an interesting starting point. Further structural information (*e.g.*, volumetric crown-to-roots ratio) could be finally drawn from μ CT imaging.

Relatively to DRG analysis, “future” developments are currently focusing on the optimization and standardization of DRG culturing and imaging (possibly by fluorescence microscopy, to increase the precision of thin fibres segmentation) and the setting of methods and pipelines for network image analysis, in order to be able to translate the investigation to trigeminal ganglia cultures, in the end. Finally, real time monitoring and multimodal imaging of cultures could provide further insight into Nogo-A role during development.

Chapter 9

Conclusions

The last decades have witnessed a new era of biomedical imaging science. From microscopy and X-ray imaging to modern computer aided CT, MRI, and PET, mankind's naked vision is no longer restricted by the conventional notions of space, time, scales, and visibility. Imaging has become a basic investigational tool in the field, capable to provide unique advantages to the experimental design, from the visual assessment of spatial distributions to the collection of quantitative and otherwise unattainable data. Over the last several decades, biomedical imaging has been undergoing rapid technological advancements, seeing the development of many new imaging technologies and methods for quantitative image analysis. Biomedical imaging is indeed a highly interdisciplinary field, that requires collaboration among biologists, chemists, medical physicists, pharmacologists, computer scientists, and biomedical engineers. However, to benefit multidisciplinary work at most, the knowledge transfer between researchers of the single disciplines is mandatory. This is especially important in biomedical image processing and analysis, since it requires that the experiments are designed also considering the needs of automated image analysis to extract reliable quantitative information.

The goal of this Thesis was to demonstrate the superiority of an interdisciplinary approach to biomedical investigation based on quantitative image analysis. In particular, the activities of this Thesis have been carried out with a *content-aware* approach, that merges biological and computer science knowledges to improve the relevance of results, by providing new methodological solutions for image analysis that increase the statistical significance of the data, meanwhile enforcing the biological outcomes. The effectiveness of such content-aware approach has here been proved through its application to different studies

of biomedical character, where it helped the experimental design and planning, the development of new methods for image analysis, and the extraction of biologically meaningful data, with rigorousness and precision. To this purpose, the studies of this Thesis collectively demonstrated that:

1. It is important to know and understand the biological problem under investigation, in order to be able to choose the best model for reproducing the phenomenon of interest, and accordingly the most suitable imaging modality, to capture the most salient features for its description (Figure 11.1, red arrows)
2. It is also equally important to know the pitfalls of image acquisition, the properties of an image and the methods for its processing. Following the backward path in Figure 11.1 (blue arrows), the posed biological question defines the salient features for its description, whose measurability depends on the chosen imaging modality, which in turn affects the choice of the biomedical model to be imaged.

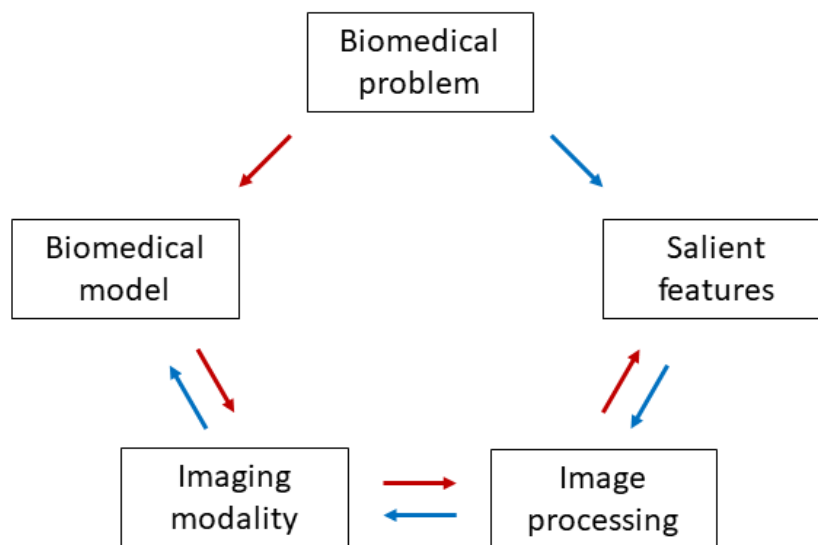


Figure 9.1. Content-aware experimental planning of biomedical imaging investigations. The nature of the biomedical problem poses constraints on the choice of both the study model and the phenomenon descriptors, that influence each other through the choice of the imaging modality and of the methods for salient features extraction. Therefore, an optimal biomedical investigation takes into account these interdependencies, building on both biomedical and image processing expertise.

Three arguments are often made in favour of interdisciplinary research. First, complex modern problems are not amenable to single-discipline investigation, but they often require many types of expertise across very different disciplines. Second, discoveries are said to be more likely on the boundaries between fields, where the latest techniques, perspectives and insights can reorient or increase knowledge. Third, these encounters with others benefit single disciplines, extending their horizons [477]. The future of health sciences is inevitably linked to the use of technologies, and imaging, a central part of present biomedical research, is expected to increasingly establish itself as one of the leading fields in the next future. In this scenario, biomedical researchers are encouraged to fearfully nurture dialogue across traditional disciplines boundaries, to draw the most of old and new technologies potential, and synergically advance current sciences.

List of abbreviations

β -Gal	β -Galactosidase
μ CT	Micro Computed Tomography
1CS	10'000 Cell-Spheroid
2CS	20'000 Cell-Spheroid
2-D	Two-Dimensional
3-D	Three-Dimensional
Ab	Antibody
AB	Ameloblast
ABMSC	Alveolar Bone-Derived Mesenchymal Stem Cell
ADC	Analog to Digital Converter
AE	Abscopal Effect
AIDS	Acquired Immune Deficiency Syndrome
AlB	Alamar Blue (<i>assay</i>)
ATA	ATmosphere Absolute
ATP	Adenosine Triphosphate
BF	Emission (Blocking) Filter
BFM	Bright Field Microscopy
BG	Background
BI	Border Indentation
BM	Bone Marrow
BMD	Bone Mineral Density
BSA	Bovine Serum Albumin
BW	Black & White Image (<i>binary mask</i>)
CCD	Charge-Coupled Device
cDDM	Co-Density Distribution Map
cGAS	cyclic GMP-AMP Synthase
CL	Cervical Loop
cLDI	Local Co-Density Index
CLSM	Confocal Laser Scanning Microscopy
CMOS	Complementary Metal Oxide Semiconductor
CNS	Central Nervous System
cOM	co-Occurrence Map
CREB	Camp Response Element-Binding (<i>protein</i>)

CT	Computed Tomography
C-t	Carboxyl-terminus (<i>of protein</i>)
CV	Coefficient of Variation
D	Dentin
DAMP	Damage-Associated Molecular Pattern
DAPI	40,6-diamidino-2-phenylindole
DAPT	(2S)-N-[(3,5-Difluorophenyl)acetyl]-L-alanyl-2-phenylglycine 1,1-dimethylethyl ester
DDM	Density Distribution Map
DDMm	Density Distribution Map mask
DDR	DNA-Damage Response
DFPC	Dental Follicle Precursor Cell
DG	Diacylglycerol
DIC	Differential Interference Contrast
DICOM	Digital Imaging and COmmunications in Medicine
DM	Dichromatic (Dichroic) Mirror
DMEM	Dulbecco's Modified Eagle Medium
DMS	Dorsal Median Sulcus
DMSO	Dimethyl Sulfoxide
DNA	Deoxyribonucleic Acid
DPSC	Dental Pulp Stem Cell
DRG	Dorsal Root Ganglia
ds	double strand (<i>nucleic acid</i>)
DSB	Double Strand Break
DSC	Dental Stem Cell
E	Embryonic (<i>day</i>)
EC	Endothelial Cell
ECM	Extracellular Matrix
ED	Equivalent Diameter
EDTA	Ethylenediaminetetraacetic Acid
EF	Emission Filter
EGFR	Epidermal Growth Factor Receptor
ELISA	Enzyme-Linked Immunosorbent Assay
EM	Electromagnetic
EMEM	Eagle's Minimum Essential Medium
En	Enamel
ER	Endoplasmic Reticulum
ERM	Epithelial Cells Rests of Malassez
EV	Extracellular Vesicle

EV-ET	(<i>sample</i>) Electroporated with Empty Vector
FBS	Fetal Bovine Serum
FDA	Fluorescein Diacetate
FE	Finite Elements (<i>model</i>)
FFC	Flat-Field Correction
FGI	Foci Granulation Index
FITC	Fluorescein Isothiocyanate
FLIP	Fluorescence Loss In Photobleaching
FM	Fluoromyelin
FN	False Negative
FNR	False Negative Rate
FP	False Positive
FRAP	Fluorescence Recovery After Photobleaching
FRET	Fluorescence Resonance Energy Transfer
GA	Gastrocnemius (<i>muscle</i>)
GFP	Green Fluorescent Protein
GL	Grey Level
GMSC	Gingiva-Derived Mesenchymal Stem Cell
GT	Ground Truth
GTP	Guanosine Triphosphate
GUI	Graphical User Interface
h	Hours
H&E	Hematoxylin and Eosin (<i>staining</i>)
HBO	Hyperbaric Oxygen
HBOT	Hyperbaric Oxygen Therapy
hDPSC	Human Dental Pulp Stem Cell
hEC	Human Endothelial Cell
HeLa	Henrietta Lacks (<i>cell line</i>)
HERS	Hertwig's Epithelial Root Sheath
HPV	Human Papilloma Virus
HT	Heterozygous
HU	Hounsfield Unit
HUVEC	Human Umbilical Vein Endothelial Cells
HVS	Human Visual System
HYPOX	Hypoxia (<i>treatment</i>)
IEE	Inner Enamel Epithelium
IF	Immunofluorescence
IFN	Interferon
IGF-1	Insulin-Like Growth Factor-1

IgG	Immunoglobulin G
IK	Initial Knot
IL	Interleukin
Im	Image mask
Im1	Area-Based Denoised Im
Im2	4-Connectivity-Based Denoised Im
Im3	Diagonal Connectivity-Based Denoised Im
Im4	Full Connectivity-Based Denoised Im
IP ₃	Inositol Triphosphate
IR	(<i>Ionizing</i>) Irradiation
KO	Knockout
LaCL	Labial Cervical Loop
Lamp-1	Lysosomal-associated membrane protein 1
LDI	Local Density Index
LED	Light-Emitting Diode
LiCL	Lingual Cervical Loop
.lif	Leica Image File Format
LINE-1	Long Interspersed Element-1
LINGO1	Leucine Rich Repeat And Ig Domain Containing 1
LRP	LDL Receptor-Related Protein
LSFM	Light Sheet Fluorescence Microscopy
LSM	Laser Scanning Microscope
LTM	Low-Threshold Mechanoreceptors
M1	Mander's coefficient 1
M2	Mander's coefficient 2
MAD	Median Absolute Deviation
min	Minutes
MIP	Maximum Intensity Projection
MKS	Musculoskeletal System
MOC	Manders' Overlap Coefficient
MOI	Multiplicity Of Infection
MRI	Magnetic Resonance Imaging
mRNA	Messenger Ribonucleic Acid
MRS	Magnetic Resonance Spectroscopy
MSC	Mesenchymal Stem Cell
MT	Microtubule
mTOR	mechanistic Target Of Rapamycin
MV	Microvesicle
MVB	Multivesicular Bodies

NA	Numerical Aperture
NCC	Normalized Cross Correlation
nCT	Nano Computed Tomography
NF	Neurofilament
NF-kB	Nuclear Factor Kappa-Light-Chain-Enhancer of Activated B Cells
NGF	Nerve Growth Factor
NgR1	Nogo Receptor 1
NIR	Non-Irradiated
NP	Nanoparticle
NR	Network Region
NS	Non-Spherical (<i>spheroid</i>)
NSCLC	Non-Small-Cell Lung Carcinoma
N-t	Amino-terminus (<i>of protein</i>)
OB	Odontoblast
OEE	Outer Enamel Epithelium
OOC	Organ-On-a-Chip
ORF1	Open Reading Frame 1 (<i>protein</i>)
ORF2	Open Reading Frame 2 (<i>protein</i>)
OX	Oxidative (<i>treatment</i>)
p53	Tumour Protein p53 (<i>protein</i>)
PALM	Photo-Activated Localization Microscopy
PBS	Phosphate Buffered Saline
PCC	Pearson's Correlation Coefficient (ρ)
PCR	Polymerase Chain Reaction
PDL	Poly-D-Lysine
PDLSC	Periodontal Ligament Stem Cell
pEK	primary Enamel Knot
PET	Positron Emission Tomography
PFA	Paraformaldehyde
PI	Propidium Iodide
PIP2	Phosphatidylinositol 4,5-Biphosphate
PIRB	Paired Immunoglobulin-Like Receptor B
PKC	Protein Kinase C
PLC	Phospholipase C
PLM	Polarized Light Microscopy
PN	Post-Natal (<i>day</i>)
PSF	Point Spread Function
PTX	Paclitaxel
QF	Quadriceps Femoris (<i>muscle</i>)

qRT-PCR	quantitative Real Time - Polymerase Chain Reaction
RAD	Irradiation (<i>treatment</i>)
RAM	Random Access Memory
Rb	Retinoblastoma
RGB	Red Green Blue (<i>image</i>)
RNA	Ribonucleic Acid
ROCK	Rho-Associated Protein Kinase
ROI	Region Of Interest
ROS	Reactive Oxygen Species
RT	Radiotherapy
rt	Room Temperature
RTN	Reticulon Homology (<i>domain</i>)
RTN4	Reticulon 4 (<i>gene</i>)
S	Spherical (<i>spheroid</i>)
S1PR2	Sphingosine-1-Phosphate Receptor 2
SAMP	Senescence-Associated Morphological Profile
SASP	Senescence-Associated Secretory Phenotype
SCAP	Stem Cell From Apical Papilla
ScC	Schwann Cell
SCI	Spinal Cord Injury
SCLC	Small Cell Lung Carcinoma
SDCM	Spinning-Disk Confocal Microscopy
SDR	Stoichiometric Detection Rate
SE	Structuring Element
sec	Seconds
sEK	secondary Enamel Knot
SEM	Scanning Electron Microscopy
sh	short hairpin (<i>RNA</i>)
SHED	Stem Cell From Human Exfoliated Deciduous Teeth
Shh	Sonic Hedgehog (<i>protein</i>)
SI	Sphericity Index
SIM	Structured Illumination Microscopy
SMLM	Single-Molecule Localization Microscopy
SOST	Sclerostin (<i>gene</i>)
SOST-ET	(<i>sample</i>) Electroporated with SOST-bearing Vector
SPECT	Single-Photon Emission Computed Tomography
SR	Stellate Reticulum
SRCC	Spearman Rank Correlation Coefficient (ρ_s)
ss	single strand (<i>nucleic acid</i>)

STING	Stimulator Of Interferon Genes
STORM	STochastic Optical Reconstruction Microscopy
STP	Standard Temperature and Pressure
SVR	Surface-to-Volume Ratio
SYP	Synaptophysin (<i>protein</i>)
TA	Tibialis Anterioris (<i>muscle</i>)
Tb. A _m	Metaphyseal Trabecular Area (Trabecular Class Extension)
Tb. Nr	Trabecular Number
Tb. Nr _m	Metaphyseal Trabecular Number
Tb. Sp	Trabecular Spacing
Tb. Sp _m	Metaphyseal Trabecular Spacing
Tb. Th	Trabecular Thickness
Tb. Th _m	Metaphyseal Trabecular Thickness
TbM	Trabecular Map
TG	Trigeminal Ganglia
.tiff	Tagged Image File Format
TIRF	Total Internal Reflection Fluorescence Microscopy
TIS	Therapy-Induced Senescence
TME	Tumour Microenvironment
TN	True Negative
TP	True Positive
TP53	Tumour Protein p53 (<i>gene</i>)
TPR	True Positive Rate
TREX1	Three Prime Repair Exonuclease 1
TU	Transduction Unit
UC	Untreated Control
UnIR	Unirradiated
UV	Ultraviolet
V2R	Vasopressin 2 Receptor
VGLUT1	Vesicular Glutamate Transporter 1
WFM	Widefield Microscopy
WS	Window Size
WT	Wild-Type

List of figures

1.1	Pyramid of the benefits from a content-aware approach.....	4
1.2	Thesis content flowchart.....	6
2.1	2-D <i>in vitro</i> cell models.....	14
2.2	Scheme of diverse 3-D cell culture strategies.....	20
2.3	Methods for spheroids creation.....	23
2.4	Spheroid pathophysiological gradients and viability differentiation.....	24
2.5	Deletion scheme for the RTN4 gene exons 2 and 3, from Simonen et al.....	30
3.1	Digital images quantization and point spread function.....	36
3.2	Microscopy classification.....	39
3.3	Modern bright-field compound microscope configuration.....	40
3.4	Polarized light and DIC microscope configuration.....	42
3.5	Widefield epifluorescence microscope.....	46
3.6	Laser scanning and spinning-disk confocal microscopy.....	48
3.7	CT and μ CT.....	53
3.8	Biomedical quantitative imaging steps.....	57
4.1	Local analysis and pixel connectivity.....	62
4.2	Flowchart of a DDM creation pipeline.....	70
4.3	DDM mask creation.....	71
4.4	DDMs are effective and robust to quantify spatial distributions.....	76
4.5	DDMs disclose hidden distribution properties.....	79
4.6	DDMs can capture relevant spatial distributions.....	82
4.7	DDMs can detect and quantify sample heterogeneity.....	83
4.8	DDMs application to image segmentation.....	87
4.9	Main GUI and logo of <i>DDMaker</i>	88
5.1	Structuring elements.....	96
5.2	Binary erosion.....	97
5.3	Pearson's coefficient quantifies linear correlation only.....	99
5.4	Monotonic functions.....	101
5.5	Definition of the image domains for Manders' coefficients computation.....	102

5.6	Flowchart of cDDM creation pipeline for a couple of markers (m1, m2).....	107
5.7	The equi-density region is strictly contained in the co-occurrence region.....	108
5.8	Functional implications of coDDM.....	112
5.9	Scatterplot of m1 and m2 markers intensity for the SYP-VGLUT1 dataset of Figure 5.8, within (red) and outside (blue) the equi-density region identified by the cDDM.....	116
5.10	Scatterplot of m1 and m2 markers intensity for the SYP-VGLUT1 dataset of Figure 5.8, partitioned by cLDI sign.....	117
5.11	Scatterplot of m1 and m2 markers intensity for the SYP-VGLUT1 dataset of Figure 5.8, partitioned by cLDI value.....	118
5.12	cDDM discloses information about the degree of colocalization.....	119
5.13	cDDM opens to the formulation of new biological considerations.....	122
5.14	Main GUI and logo of <i>coDDMaker</i>	125
5.15	Pattern matching approach for colocalization quantification.....	129
6.1	Particle segmentation by geodesic reconstruction.....	136
6.2	Method pipeline for RNA:DNA hybrids, CD63+ EVs and ORF1+ retrotransposons foci segmentation.....	140
6.3	CD63+ EVs subcellular distribution in IR NSCLC cells.....	144
6.4	RNA:DNA hybrid subcellular distribution in IR NSCLC cells.....	146
6.5	RNA:DNA hybrid subcellular distribution in UnIR A549 cells exposed to IR A549 EVs.....	147
6.6	Retrotransposon ORF1 subcellular distribution in A549 and A549sh/p53 cells.....	148
6.7	Effects of RAD treatments on RNA:DNA hybrids subcellular distribution in HeLa cells.....	150
6.8	Effects of OX treatments on RNA:DNA hybrids subcellular distribution in HeLa cells.....	153
6.9	Diagram illustrating the p53-mediated abscopal effect induced by radiotherapy.....	157
7.1	Hierarchical ultrastructure of bone.....	164
7.2	Schematic and μ CT of long bone anatomy and microstructure.....	165
7.3	A Gabor filter is the product of a Gaussian kernel and a sinusoidal wave.....	167
7.4	Workflow of Gabor-based texture analysis.....	168
7.5	Epiphysis, metaphysis and epiphyseal plate segmentation by global thresholding and local density analysis in coronal section of μ CT scans.....	174
7.6	Developed method for automated trabecular classification by thickness and orientation.....	175

7.7	Graphical scheme of the sclerostin overexpression experiment.....	179
7.8	Sclerostin muscle overexpression effect on metaphyseal trabeculae in adjacent bone.....	183
8.1	Mature tooth anatomy and stem cells.....	190
8.2	Overview of mouse tooth development.....	193
8.3	Domains, binding partners and signalling of cell membrane Nogo proteins...	197
8.4	Spheroids morphology descriptors.....	203
8.5	hDPSCs spheroids morphological characterization.....	211
8.6	γ -secretase inhibitor DAPT does not affect hDPSCs spheroids properties.....	213
8.7	Development of neuronal network morphology in WT and Nogo-A KO mice molar.....	216
8.8	Nogo-A affects DRG network size and morphology.....	218
9.1	Content-aware experimental planning of biomedical imaging investigations..	224

List of tables

4.1	Contingency table for object counting with density-, area- and connectivity-based approach.....	76
4.2	Stoichiometric detection rate for object counting with density-, area- and connectivity-based approach.....	77
4.3	Comparison of density-, area- and connectivity-based approach effects on objects erosion during detection.....	77
4.4	Comparison between COL7 and COL7-h.....	78
4.5	Median MTs intensity in MG-63 cells.....	80
4.6	Statistical analysis of MTs LDI percentage in MG-63 cells.....	81
4.7	Statistical analysis of hybrids LDI percentage in A549sh/p53 cells.....	82
4.8	Median hybrids LDI percentage and blobs number in HeLa cells.....	84
4.9	Statistical analysis of hybrids LDI percentage and blob number in HeLa cells.....	85
4.10	Variance of hybrids LDI percentage and blob number in HeLa cells.....	85
5.1	Binary NOT, ANDing and ORing.....	96
5.2	Data ranking.....	100
5.3	Comparison between binary erosion and co-density analysis in refining the correlation computation domain.....	114
5.4	Comparison between SYP and VGLUT1 intensity and local density colocalization analysis, before and after refinement for local co-density.....	116
5.5	Comparison between Lamp-1 and PTX-Ce6@kerag intensity and local density colocalization analysis, before and after refinement for local co-density.....	120
5.6	Comparison between NF200 and FM intensity and local density colocalization analysis, before and after refinement for local co-density.....	123
5.7	<i>coDDMaker</i> time performance evaluation.....	127
6.1	Experimental panel for the PHENOMICS Project.....	158
7.1	Set parameters for μ CT scanning of C57BL/6 mice tibiae.....	172
7.2	Wavelength and orientation values for applied Gabor filters.....	176
7.3	Statistical analysis of metaphyseal trabecular classes extension expressed as percentage of metaphysis in UC, EV-ET and SOST-ET C57BL/6 mice.....	181
7.4	Statistical analysis of metaphyseal class trabecular number in UC, EV-ET and SOST-ET C57BL/6 mice.....	182

Bibliography

- [1] National Research Council. (1998). Biomedical models and resources: current needs and future opportunities. National Academies Press.
- [2] National Research Council. (1930). Models for biomedical research. National Academies Press.
- [3] Dietrich, M. R., Ankeny, R. A., Crowe, N., Green, S., & Leonelli, S. (2020). How to choose your research organism. *Studies in History and Philosophy of Science Part C: Studies in History and Philosophy of Biological and Biomedical Sciences*, 80, 101227.
- [4] Russell, W. M. S., & Burch, R. L. (1959). The principles of humane experimental technique. *Methuen*.
- [5] Colquitt, R. B., Colquhoun, D. A., & Thiele, R. H. (2011). In silico modelling of physiologic systems. *Best practice & research Clinical anaesthesiology*, 25(4), 499-510.
- [6] Ud-Din, S., & Bayat, A. (2017). Non-animal models of wound healing in cutaneous repair: in silico, in vitro, ex vivo, and in vivo models of wounds and scars in human skin. *Wound Repair and Regeneration*, 25(2), 164-176.
- [7] Moore, G. E., & Ulrich, K. (1965). Suspension cultures of mammalian cells: A review. *Journal of Surgical Research*, 5(6), 270-282.
- [8] Kapałczyńska, M., Kolenda, T., Przybyła, et al. (2018). 2-D and 3-D cell cultures—a comparison of different types of cancer cell cultures. *Archives of Medical Science*, 14(4), 910-919.
- [9] Marino, S., Bishop, R. T., Ridder, D. D., Delgado-Calle, J., & Reagan, M. R. (2019). 2-D and 3-D in vitro co-culture for cancer and bone cell interaction studies. In *Bone Research Protocols* (pp. 71-98). Humana Press, New York, NY.
- [10] Sanyal S. Culture and assay systems used for 3-D cell culture. Corning 2014; 9: 1-18.
- [11] <https://handling-solutions.eppendorf.com/>
- [12] Zhu, S., Ehnert, S., Rouß, M., et al. (2018). From the clinical problem to the basic research—co-culture models of osteoblasts and osteoclasts. *International journal of molecular sciences*, 19(8), 2284.
- [13] Harrison, R. (1907). Biology and medicine. Observations on the living developing nerve fiber. In *Science Proceedings* (Vol. 98).

- [14] Jacoby, W., & Pasten, I. (1979). *Methods in Enzymology: Cell Culture*. Vol. 58.
- [15] Bakhtiar, S. M., Butt, H. A., Zeb, S., et al. (2018). 3-D printing technologies and their applications in biomedical science. In *Omics Technologies and Bio-Engineering* (pp. 167-189). Academic Press.
- [16] Mirabelli, P., Coppola, L., & Salvatore, M. (2019). Cancer cell lines are useful model systems for medical research. *Cancers*, 11(8), 1098.
- [17] De Santis, I., Bevilacqua, A., Mitsiadis, T. A., Stanco, D. Characterization of human dental pulp stem cells multicellular spheroids as organotypic three-dimensional in vitro model. *GISM Annual Meeting 2022, Torino, Italia, 20-21 October 2022*.
- [18] Tesei, A., Arienti, C., Bossi, G., et al. (2021). TP53 drives abscopal effect by secretion of senescence-associated molecular signals in non-small cell lung cancer. *Journal of Experimental & Clinical Cancer Research*, 40(1), 1-15.
- [19] De Santis, I., Zanoni, M., Pignatta, S., et al. (2022). Pro-inflammatory RNA: DNA Hybrids Are p53 Independently Boosted by Hyperbaric Oxygen: a Subcellular Distribution Analysis by Automated Quantitative Imaging. *Molecular Imaging and Biology*, 1-9.
- [20] Giard, D. J., Aaronson, S. A., Todaro, G. J., et al. (1973). In vitro cultivation of human tumors: establishment of cell lines derived from a series of solid tumors. *Journal of the National Cancer Institute*, 51(5), 1417-1423.
- [21] Ye, M., Yu, M., Yang, D., et al. (2020). Exogenous hydrogen sulfide donor NaHS alleviates nickel-induced epithelial-mesenchymal transition and the migration of A549 cells by regulating TGF- β 1/Smad2/Smad3 signaling. *Ecotoxicology and Environmental Safety*, 195, 110464.
- [22] Lieber, M., B. Smith, A. Szakal, W. Nelson-Rees, and G. Todaro. (1976). A Continuous Tumor-Cell Line from a Human Lung Carcinoma with Properties of Type II Alveolar Epithelial Cells. *International Journal of Cancer* 17: 62–70.
- [23] a549.com
- [24] Martin, A., & Sarkar, A. (2017). Overview on biological implications of metal oxide nanoparticle exposure to human alveolar A549 cell line. *Nanotoxicology*, 11(6), 713-724.
- [25] atcc.org
- [26] Mulshine, J. L., Ujhazy, P., Antman, M., et al. (2020). From clinical specimens to human cancer preclinical models—a journey the NCI-cell line database—25 years later. *Journal of cellular biochemistry*, 121(8-9), 3986-3999.
- [27] Lin, D. L., & Chang, C. (1996). p53 is a mediator for radiation-repressed human TR2 orphan receptor expression in MCF-7 cells, a new pathway from

- tumor suppressor to member of the steroid receptor superfamily. *Journal of Biological Chemistry*, 271(25), 14649-14652.
- [28] Giaccone, G., Battey, J., Gazdar, A. F., et al. (1992). Neuromedin B is present in lung cancer cell lines. *Cancer research*, 52(9_Supplement), 2732s-2736s.
- [29] bionumbers.hms.harvard.edu
- [30] Gey, G. (1952). Tissue culture studies of the proliferative capacity of cervical carcinoma and normal epithelium. *Cancer Research*, 12, 264-265.
- [31] Smith, V. (2002). Wonder woman: The life, death, and life after death of Henrietta Lacks, unwitting heroine of modern medical science. Baltimore City Paper, 17.
- [32] Salmina, K., Gerashchenko, B. I., Hausmann, et al. (2019). When three isn't a crowd: A digyny concept for treatment-resistant, near-triploid human cancers. *Genes*, 10(7), 551.
- [33] Percell Biolytica. Growth of HeLa cells, Application note 116. <https://www.percell.se>
- [34] Meck, R. A., Carsten, A. L., & Kelsch, J. J. (1976). Growth of HeLa cells in diffusion chamber cultures in vivo. *Cancer Research*, 36(7_Part_1), 2317-2320.
- [35] Sato, S., Rancourt, A., Sato, Y., & Satoh, M. S. (2016). Single-cell lineage tracking analysis reveals that an established cell line comprises putative cancer stem cells and their heterogeneous progeny. *Scientific Reports*, 6(1), 1-11.
- [36] Johnson, B. W., Takahashi, K., & Cheng, Y. Y. (2021). Preclinical Models and Resources to Facilitate Basic Science Research on Malignant Mesothelioma—A Review. *Frontiers in Oncology*, 4734.
- [37] Von Der Mark, K., Gauss, V., Von Der Mark, H., & Müller, P. (1977). Relationship between cell shape and type of collagen synthesised as chondrocytes lose their cartilage phenotype in culture. *Nature*, 267(5611), 531-532.
- [38] Petersen, O. W., Rønnov-Jessen, L., Howlett, A. R., & Bissell, M. J. (1992). Interaction with basement membrane serves to rapidly distinguish growth and differentiation pattern of normal and malignant human breast epithelial cells. *Proceedings of the National Academy of Sciences*, 89(19), 9064-9068.
- [39] Mahmud, G., Campbell, C. J., Bishop, et al. (2009). Directing cell motions on micropatterned ratchets. *Nature physics*, 5(8), 606-612.
- [40] Kilian, K. A., Bugarija, B., Lahn, B. T., & Mrksich, M. (2010). Geometric cues for directing the differentiation of mesenchymal stem cells. *Proceedings of the National Academy of Sciences*, 107(11), 4872-4877.
- [41] Weaver, V. M., Lelièvre, S., Lakins, J. N., et al. (2002). β 4 integrin-dependent formation of polarized three-dimensional architecture confers resistance to

- apoptosis in normal and malignant mammary epithelium. *Cancer cell*, 2(3), 205-216.
- [42] Meyers, J., Craig, J., & Odde, D. J. (2006). Potential for control of signaling pathways via cell size and shape. *Current biology*, 16(17), 1685-1693.
- [43] Ferreira, L. P., Gaspar, V. M., & Mano, J. F. (2018). Design of spherically structured 3-D in vitro tumor models-Advances and prospects. *Acta Biomaterialia*, 75, 11-34.
- [44] Pampaloni, F., Reynaud, E. G., & Stelzer, E. H. (2007). The third dimension bridges the gap between cell culture and live tissue. *Nature reviews Molecular cell biology*, 8(10), 839-845.
- [45] Baker, B. M., & Chen, C. S. (2012). Deconstructing the third dimension—how 3-D culture microenvironments alter cellular cues. *Journal of cell science*, 125(13), 3015-3024.
- [46] Hickman, J. A., Graeser, R., de Hoogt, R., et al. (2014). Three-dimensional models of cancer for pharmacology and cancer cell biology: capturing tumor complexity in vitro/ex vivo. *Biotechnology journal*, 9(9), 1115-1128.
- [47] Bissell, M. J., Rizki, A., & Mian, I. S. (2003). Tissue architecture: the ultimate regulator of breast epithelial function. *Current opinion in cell biology*, 15(6), 753.
- [48] Stock, K., Estrada, M. F., Vidic, S, et al. (2016). Capturing tumor complexity in vitro: Comparative analysis of 2-D and 3-D tumor models for drug discovery. *Scientific reports*, 6(1), 1-15.
- [49] Ferrari, E., & Rasponi, M. (2021). Liver–Heart on chip models for drug safety. *APL bioengineering*, 5(3), 031505.
- [50] Martinez-Pacheco, S., & O'Driscoll, L. (2021). Pre-Clinical In Vitro Models Used in Cancer Research: Results of a Worldwide Survey. *Cancers*, 13(23), 6033.
- [51] Ghosh, S., Spagnoli, G. C., Martin, I., et al. (2005). Three-dimensional culture of melanoma cells profoundly affects gene expression profile: A high density oligonucleotide array study. *Journal of cellular physiology*, 204(2), 522-531.
- [52] Powers, M. J., Janigian, D. M., Wack, K. E., et al. (2002). Functional behavior of primary rat liver cells in a three-dimensional perfused microarray bioreactor. *Tissue engineering*, 8(3), 499-513.
- [53] Frieboes, H. B., Zheng, X., Sun, C. H., et al. (2006). An integrated computational/experimental model of tumor invasion. *Cancer research*, 66(3), 1597-1604.
- [54] Semino, C. E., Merok, J. R., Crane, G. G., Panagiotakos, G., & Zhang, S. (2003). Functional differentiation of hepatocyte-like spheroid structures from

- putative liver progenitor cells in three-dimensional peptide scaffolds. *Differentiation*, 71(4-5), 262-270.
- [55] Marushima, H., Shibata, S. I., Asakura, T., et al. (2011). Three-dimensional culture promotes reconstitution of the tumor-specific hypoxic microenvironment under TGF β stimulation. *International journal of oncology*, 39(5), 1327-1336.
- [56] Berthiaume, F., Moghe, P. V., Toner, M., & Yarmush, M. L. (1996). Effect of extracellular matrix topology on cell structure, function, and physiological responsiveness: hepatocytes cultured in a sandwich configuration. *The FASEB journal*, 10(13), 1471-1484.
- [57] Benien, P., & Swami, A. (2014). 3-D tumor models: history, advances and future perspectives. *Future oncology*, 10(7), 1311-1327.
- [58] Carrel, A. (1912). On the permanent life of tissues outside of the organism. *The Journal of experimental medicine*, 15(5), 516.
- [59] Leighton, J. (1951). A sponge matrix method for tissue culture. Formation of organized aggregates of cells in vitro. *Journal of the National Cancer Institute*, 12(3), 545-561.
- [60] Hamburger, A. W., & Salmon, S. E. (1977). Primary bioassay of human tumor stem cells. *Science*, 197(4302), 461-463.
- [61] Hoffman, R. M. (1993). To do tissue culture in two or three dimensions? That is the question. *Stem Cells*, 11(2), 105-111.
- [62] Jedrzejczak-Silicka, M. (2017). History of cell culture. *New insights into cell culture technology*, 1-41.
- [63] de Dios-Figueroa, G. T., Aguilera-Marquez, J. D. R., Camacho-Villegas, T. A., & Lugo-Fabres, P. H. (2021). 3-D cell culture models in covid-19 times: A review of 3-D technologies to understand and accelerate therapeutic drug discovery. *Biomedicines*, 9(6), 602.
- [64] Ma, C., Peng, Y., Li, H., & Chen, W. (2021). Organ-on-a-chip: a new paradigm for drug development. *Trends in pharmacological sciences*, 42(2), 119-133.
- [65] Datta, P., Dey, M., Ataie, Z., Unutmaz, D., & Ozbolat, I. T. (2020). 3-D bioprinting for reconstituting the cancer microenvironment. *NPJ precision oncology*, 4(1), 1-13.
- [66] Mozafari, M., Mehraien, M., Vashae, D., & Tayebi, L. (2012). Electroconductive nanocomposite scaffolds: a new strategy into tissue engineering and regenerative medicine. INTECH Open Access Publisher, 369-392.
- [67] cubibox.it

- [68] Burdett, E., Kasper, F. K., Mikos, A. G., & Ludwig, J. A. (2010). Engineering tumors: a tissue engineering perspective in cancer biology. *Tissue Engineering Part B: Reviews*, 16(3), 351-359.
- [69] Kim, J. B. (2005). Three-dimensional tissue culture models in cancer biology. In *Seminars in cancer biology* (Vol. 15, No. 5, pp. 365-377). Academic Press.
- [70] Lin, R. Z., & Chang, H. Y. (2008). Recent advances in three-dimensional multicellular spheroid culture for biomedical research. *Biotechnology Journal: Healthcare Nutrition Technology*, 3(9-10), 1172-1184.
- [71] Smalley, K. S., Lioni, M., & Herlyn, M. (2006). Life ins't flat: Taking cancer biology to the next dimension. *In Vitro Cellular & Developmental Biology-Animal*, 42(8), 242-247.
- [72] wikipedia.org/wiki/Organoid
- [73] de Souza, N. (2018). Organoids. *Nature Methods*, 15(1), 23-23.
- [74] Bhatia, S. N., & Ingber, D. E. (2014). Microfluidic organs-on-chips. *Nature biotechnology*, 32(8), 760-772.
- [75] Tamama, K., McFadden, K., & Guan, J. (2016). Improving stem and progenitor cell therapeutics. *Stem Cells International*, 2016.
- [76] Ferreira, J. R., Teixeira, G. Q., Santos, S. G., et al. (2018). Mesenchymal stromal cell secretome: influencing therapeutic potential by cellular preconditioning. *Frontiers in immunology*, 9, 2837.
- [77] Pinto, B., Henriques, A. C., Silva, P. M., & Bousbaa, H. (2020). Three-dimensional spheroids as in vitro preclinical models for cancer research. *Pharmaceutics*, 12(12), 1186.
- [78] Jubelin, C., Muñoz-Garcia, J., Griscom, L., et al. (2022). Three-dimensional in vitro culture models in oncology research. *Cell & Bioscience*, 12(1), 1-28.
- [79] Holtfreter, J. (1944). A study of the mechanics of gastrulation. *Journal of Experimental Zoology*, 95(2), 171-212.
- [80] Moscona, A., & Moscona, H. (1952). The dissociation and aggregation of cells from organ rudiments of the early chick embryo. *Journal of anatomy*, 86(Pt 3), 287.
- [81] Sutherland, R. M., Inch, W. R., McCredie, J. A., & Kruuv, J. (1970). A multi-component radiation survival curve using an in vitro tumour model. *International Journal of Radiation Biology and Related Studies in Physics, Chemistry and Medicine*, 18(5), 491-495.
- [82] Hirschhaeuser, F., Menne, H., Dittfeld, C., et al. (2010). Multicellular tumor spheroids: an underestimated tool is catching up again. *Journal of biotechnology*, 148(1), 3-15.

- [83] Achilli, T. M., Meyer, J., & Morgan, J. R. (2012). Advances in the formation, use and understanding of multi-cellular spheroids. *Expert opinion on biological therapy*, 12(10), 1347-1360.
- [84] Page, H., Flood, P., & Reynaud, E. G. (2013). Three-dimensional tissue cultures: current trends and beyond. *Cell and tissue research*, 352(1), 123-131.
- [85] Souza, G. R., Molina, J. R., Raphael, et al. (2010). Three-dimensional tissue culture based on magnetic cell levitation. *Nature nanotechnology*, 5(4), 291-296.
- [86] Liu, D., Chen, S., & Win Naing, M. (2021). A review of manufacturing capabilities of cell spheroid generation technologies and future development. *Biotechnology and Bioengineering*, 118(2), 542-554.
- [87] Kelm, J. M., Timmins, N. E., Brown, C. J., Fussenegger, M., & Nielsen, L. K. (2003). Method for generation of homogeneous multicellular tumor spheroids applicable to a wide variety of cell types. *Biotechnology and bioengineering*, 83(2), 173-180.
- [88] Hofmann, S., Cohen-Harazi, R., Maizels, Y., & Koman, I. (2022). Patient-derived tumor spheroid cultures as a promising tool to assist personalized therapeutic decisions in breast cancer. *Translational Cancer Research*, 11(1), 134.
- [89] Zaroni, M., Piccinini, F., Arienti, et al. (2016). 3-D tumor spheroid models for in vitro therapeutic screening: a systematic approach to enhance the biological relevance of data obtained. *Scientific reports*, 6(1), 1-11.
- [90] Melo, F. D. S. E., Vermeulen, L., Fessler, E., & Medema, J. P. (2013). Cancer heterogeneity—a multifaceted view. *EMBO reports*, 14(8), 686-695.
- [91] Myungjin Lee, J., Mhawech-Fauceglia, P., Lee, N., Cristina Parsanian, L., et al. (2013). A three-dimensional microenvironment alters protein expression and chemosensitivity of epithelial ovarian cancer cells in vitro. *Laboratory investigation*, 93(5), 528-542.
- [92] Hirsch, C., & Schildknecht, S. (2019). In vitro research reproducibility: Keeping up high standards. *Frontiers in pharmacology*, 10, 1484.
- [93] Belma, P., Dina, F., Emina, A., Nermina, Ž., & Fahir, B. (2019). Animal models in modern biomedical research. *European Journal of Pharmaceutical and Medical Research*, 6, 35-38.
- [94] Khan, A., Waqar, K., Shafique, A., Irfan, R., & Gul, A. (2018). In vitro and in vivo animal models: The engineering towards understanding human diseases and therapeutic interventions. In *Omics Technologies and Bio-Engineering* (pp. 431-448). Academic Press.
- [95] Boyd, B. J., Bergström, C. A., Vinarov, Z., et al. (2019). Successful oral delivery of poorly water-soluble drugs both depends on the intraluminal

- behavior of drugs and of appropriate advanced drug delivery systems. *European Journal of Pharmaceutical Sciences*, 137, 104967.
- [96] Nunes, R., Silva, C., & Chaves, L. (2016). Tissue-based in vitro and ex vivo models for intestinal permeability studies. *Concepts and Models for Drug Permeability Studies*, 203-236.
- [97] Pearce, S. C., Coia, H. G., Karl, J. P., et al. (2018). Intestinal in vitro and ex vivo models to study host-microbiome interactions and acute stressors. *Frontiers in physiology*, 9, 1584.
- [98] Xu, Y., Shrestha, N., Pr at, V., & Beloqui, A. (2021). An overview of in vitro, ex vivo and in vivo models for studying the transport of drugs across intestinal barriers. *Advanced Drug Delivery Reviews*, 175, 113795.
- [99] Barthe, L., Woodley, J., & Houin, G. (1999). Gastrointestinal absorption of drugs: methods and studies. *Fundamental & clinical pharmacology*, 13(2), 154-168.
- [100] Xu, Y., Shrestha, N., Pr at, V., & Beloqui, A. (2021). An overview of in vitro, ex vivo and in vivo models for studying the transport of drugs across intestinal barriers. *Advanced Drug Delivery Reviews*, 175, 113795.
- [101] Kaletta, T., & Hengartner, M. O. (2006). Finding function in novel targets: *C. elegans* as a model organism. *Nature reviews Drug discovery*, 5(5), 387-399.
- [102] Yamaguchi, M., & Yoshida, H. (2018). *Drosophila* as a model organism. *Drosophila Models for Human Diseases*, 1-10.
- [103] Chakraborty, C., Hsu, C. H., Wen, Z. H., Lin, C. S., & Agoramoorthy, G. (2009). Zebrafish: a complete animal model for in vivo drug discovery and development. *Current drug metabolism*, 10(2), 116-124.
- [104] Gama Sosa, M. A., De Gasperi, R., & Elder, G. A. (2012). Modeling human neurodegenerative diseases in transgenic systems. *Human genetics*, 131(4), 535-563.
- [105] Puschnik, A. S., Majzoub, K., Ooi, Y. S., & Carette, J. E. (2017). A CRISPR toolbox to study virus–host interactions. *Nature Reviews Microbiology*, 15(6), 351-364.
- [106] Krishnakumar, V., Durairajan, S. S. K., Alagarasu, K., Li, M., & Dash, A. P. (2019). Recent updates on mouse models for human immunodeficiency, influenza, and dengue viral infections. *Viruses*, 11(3), 252.
- [107] Kumari, M., Singla, M., & Sobti, R. C. (2022). Animal models and their substitutes in biomedical research. In *Advances in Animal Experimentation and Modeling* (pp. 87-101). Academic Press.
- [108] National Research Council. (1988). Use of laboratory animals in biomedical and behavioral research. National Academic Press.

- [109] Hickman, D. L., Johnson, J., Vemulapalli, T. H., Crisler, J. R., & Shepherd, R. (2017). Commonly used animal models. *Principles of animal research for graduate and undergraduate students*, 117.
- [110] Bockamp, E., Maringer, M., Spangenberg, C., et al. (2002). Of mice and models: improved animal models for biomedical research. *Physiological genomics*, 11(3), 115-132.
- [111] Baumans, V. (2005). Science-based assessment of animal welfare: laboratory animals. *Revue Scientifique Et Technique-Office International Des Epizooties*, 24(2), 503.
- [112] Turner, P. V., Pang, D. S., & Lofgren, J. L. (2019). A review of pain assessment methods in laboratory rodents. *Comparative medicine*, 69(6), 451-467.
- [113] Neely, C. L., Pedemonte, K. A., Boggs, K. N., & Flinn, J. M. (2019). Nest building behavior as an early indicator of behavioral deficits in mice. *Journal of Visualized Experiments*, 152, e60139.
- [114] Lieggi, C., Kalueff, A. V., Lawrence, C., & Collymore, C. (2019). The influence of behavioral, social, and environmental factors on reproducibility and replicability in aquatic animal models. *ILAR journal*, 60(2), 270-288.
- [115] Loss, C. M., Melleu, F. F., Domingues, K., Lino-de-Oliveira, C., & Viola, G. G. (2021). Combining Animal Welfare With Experimental Rigor to Improve Reproducibility in Behavioral Neuroscience. *Frontiers in Behavioral Neuroscience*, 15.
- [116] Hylander, B. L., Repasky, E. A., & Sexton, S. (2022). Using Mice to Model Human Disease: Understanding the Roles of Baseline Housing-Induced and Experimentally Imposed Stresses in Animal Welfare and Experimental Reproducibility. *Animals*, 12(3), 371.
- [117] criver.com
- [118] Magarò, M. S., Bertacchini, J., Florio, F., et al. (2021). Identification of sclerostin as a putative new myokine involved in the muscle-to-bone crosstalk. *Biomedicines*, 9(1), 71.
- [119] Pirenne, L., Lai, C.F., Pagella, P., et al. Functional roles of Nogo-A in tooth innervation. *Tooth Morphogenesis and Differentiation (TMD) conference*, Prague, Czech Republic, 26 June -1 July 2022.
- [120] European Bioinformatics Institute (2002). Initial sequencing and comparative analysis of the mouse genome. *Nature*, 420(6915), 520-562.
- [121] Simonen, M., Pedersen, V., Weinmann, O., et al. (2003). Systemic deletion of the myelin-associated outgrowth inhibitor Nogo-A improves regenerative and plastic responses after spinal cord injury. *Neuron*, 38(2), 201-211.
- [122] Robinson, N. B., Krieger, K., Khan, F. M., et al. (2019). The current state of animal models in research: A review. *International Journal of Surgery*, 72, 9-13.

- [123] Pound, P., Ebrahim, S., Sandercock, P., Bracken, M. B., & Roberts, I. (2004). Where is the evidence that animal research benefits humans? *Bmj*, 328(7438), 514-517.
- [124] Richter, S. H. (2017). Systematic heterogenization for better reproducibility in animal experimentation. *Lab animal*, 46(9), 343-349.
- [125] Gonzalez, R. C. (2009). Digital image processing. Pearson education India.
- [126] olympus-lifescience.com
- [127] Ye, Y., Jiang, H., Zhang, H., et al. (2013). Resolution of slit-lamp microscopy photography using various cameras. *Eye & contact lens*, 39(3), 205-213.
- [128] Abbe, E. (1873). Beiträge zur Theorie des Mikroskops und der mikroskopischen Wahrnehmung. *Archiv für mikroskopische Anatomie*, 9(1), 413-468.
- [129] Bayguinov, P. O., Oakley, D. M., Shih, C. C., et al. (2018). Modern laser scanning confocal microscopy. *Current protocols in cytometry*, 85(1), e39.
- [130] De Santis, I., Zanoni, M., Arienti, C., Bevilacqua, A., & Tesei, A. (2021). Density Distribution Maps: A Novel Tool for Subcellular Distribution Analysis and Quantitative Biomedical Imaging. *Sensors*, 21(3), 1009.
- [131] Croft, W. J. (2006). Under the microscope: a brief history of microscopy (Vol. 5). World Scientific.
- [132] Trinh, L. A., & Fraser, S. E. (2015). Imaging the cell and molecular dynamics of craniofacial development: challenges and new opportunities in imaging developmental tissue patterning. *Current topics in developmental biology*, 115, 599-629.
- [133] Von Ardenne, M., & Hawkes, P. (2021). On the history of scanning electron microscopy, of the electron microprobe, and of early contributions electron microscopy to transmission. *The Beginnings of Electron Microscopy-Part 1*, 36, 25.
- [134] Piston, D. W. (1998). Choosing objective lenses: the importance of numerical aperture and magnification in digital optical microscopy. *The Biological Bulletin*, 195(1), 1-4.
- [135] Alberts, B., Johnson, A., Lewis, J., et al. (2002). *Molecular Biology of the Cell*; New York and London: Garland Science.
- [136] Conn, P. M. (2012). *Imaging and spectroscopic analysis of living cells: optical and spectroscopic techniques*. Academic Press.
- [137] Inoué, S. (2002). Polarization microscopy. *Current protocols in cell biology*, 13(1), 4-9.
- [138] Gao, P. F., Lei, G., & Huang, C. Z. (2021). Dark-field microscopy: recent advances in accurate analysis and emerging applications. *Analytical Chemistry*, 93(11), 4707-4726.

- [139] Burrows, G. E., & Connor, C. (2020). Chloroplast Distribution in the Stems of 23 Eucalypt Species. *Plants*, 9(12), 1814.
- [140] Gray, N. (2009). Knowing the limit. *Nature Cell Biology*, 11(1), S8-S8.
- [141] Nomarski, G. (1955). Microinterféromètre différentiel à ondes polarisées. *Journal of Physical Radiology*, 16, 9S-13S.
- [142] Trĩnh, H. X., Lin, S. T., Chen, L. C., Yeh, S. L., & Chen, C. S. (2017). Differential interference contrast microscopy using Savart plates. *Journal of Optics*, 19(4), 045601.
- [143] Bercher, M., Wahl, J., Vogel, B. E., et al. (2001). mua-3, a gene required for mechanical tissue integrity in *Caenorhabditis elegans*, encodes a novel transmembrane protein of epithelial attachment complexes. *The Journal of cell biology*, 154(2), 415-426.

- [144] Rosenthal, C. K. (2009). Contrast by interference. *Nature Cell Biology*, 11(1), S11-S12.
- [145] Kandel, M. E., Fanous, M., Best-Popescu, C., & Popescu, G. (2018). Real-time halo correction in phase contrast imaging. *Biomedical optics express*, 9(2), 623-635.
- [146] Jonkman, J., Brown, C. M., Wright, G. D., Anderson, K. I., & North, A. J. (2020). Tutorial: guidance for quantitative confocal microscopy. *Nature protocols*, 15(5), 1585-1611.
- [147] Wiederschain, G. Y. (2011). The Molecular Probes handbook. A guide to fluorescent probes and labeling technologies. *Biochemistry (Moscow)*, 76(11), 1276-1277.
- [148] Lichtman, J. W., & Conchello, J. A. (2005). Fluorescence microscopy. *Nature methods*, 2(12), 910-919.
- [149] Ren, T. B., Xu, W., Zhang, W., et al. (2018). A general method to increase stokes shift by introducing alternating vibronic structures. *Journal of the American Chemical Society*, 140(24), 7716-7722.
- [150] Lleres, D., Swift, S., & Lamond, A. I. (2007). Detecting protein-protein interactions in vivo with FRET using multiphoton fluorescence lifetime imaging microscopy (FLIM). *Current protocols in cytometry*, 42(1), 12-10.
- [151] Lutz, M. I., Schwaiger, C., Hochreiter, B., Kovacs, G. G., & Schmid, J. A. (2017). Novel approach for accurate tissue-based protein colocalization and proximity microscopy. *Scientific reports*, 7(1), 1-10.
- [152] Ranjit, S., Lanzanò, L., Libby, A. E., Gratton, E., & Levi, M. (2021). Advances in fluorescence microscopy techniques to study kidney function. *Nature Reviews Nephrology*, 17(2), 128-144.
- [153] Ford, P. C. (2018). Metal complex strategies for photo-uncaging the small molecule bioregulators nitric oxide and carbon monoxide. *Coordination Chemistry Reviews*, 376, 548-564.
- [154] Lippincott-Schwartz, J., Altan-Bonnet, N. & Patterson, G. H. Photobleaching and photoactivation: following protein dynamics in living cells. *Nature Cell Biology*, Suppl, S7-S14 (2003).
- [155] Steinegger, A., Wolfbeis, O. S., & Borisov, S. M. (2020). Optical sensing and imaging of pH values: spectroscopies, materials, and applications. *Chemical reviews*, 120(22), 12357-12489.
- [156] Stelzer, E. H., Strobl, F., Chang, B. J., et al. (2021). Light sheet fluorescence microscopy. *Nature Reviews Methods Primers*, 1(1), 1-25.
- [157] Borile, G., Sandrin, D., Filippi, A., Anderson, K. I., & Romanato, F. (2021). Label-free multiphoton microscopy: much more than fancy images. *International Journal of Molecular Sciences*, 22(5), 2657.

- [158] Valli, J., Garcia-Burgos, A., Rooney, L. M., et al. (2021). Seeing beyond the limit: A guide to choosing the right super-resolution microscopy technique. *Journal of Biological Chemistry*, 297(1).
- [159] micro.magnet.fsu.edu
- [160] Swedlow, J. R., & Platani, M. (2002). Live cell imaging using wide-field microscopy and deconvolution. *Cell structure and function*, 27(5), 335-341.
- [161] Conchello, J. A., & Lichtman, J. W. (2005). Optical sectioning microscopy. *Nature methods*, 2(12), 920-931.
- [162] Bolte, S., & Cordelières, F. P. (2006). A guided tour into subcellular colocalization analysis in light microscopy. *Journal of microscopy*, 224(3), 213-232.
- [163] Dunn, K. W., Kamocka, M. M., & McDonald, J. H. (2011). A practical guide to evaluating colocalization in biological microscopy. *American Journal of Physiology-Cell Physiology*, 300(4), C723-C742.
- [164] Elliott, A. D. (2020). Confocal microscopy: principles and modern practices. *Current protocols in cytometry*, 92(1), e68.
- [165] Benninger, R. K., & Piston, D. W. (2013). Two-photon excitation microscopy for the study of living cells and tissues. *Current protocols in cell biology*, 59(1), 4-11.
- [166] Schermelleh, L., Ferrand, A., Huser, T., et al. (2019). Super-resolution microscopy demystified. *Nature cell biology*, 21(1), 72-84.
- [167] Piccinini, F., Lucarelli, E., Gherardi, A., & Bevilacqua, A. (2012). Multi-image based method to correct vignetting effect in light microscopy images. *Journal of microscopy*, 248(1), 6-22.
- [168] Pei, W., Zhu, Y., Liu, C., & Xia, Z. (2009). Non-uniformity correction for SLM microscopic images. *Image and Vision Computing*, 27(6), 782-789.
- [169] Sun, C., Beare, R., Hilsenstein, V. & Jackway, P. (2006) Mosaicing of microscope images with global geometric and radiometric corrections. *Journal of Microscopy*, 224, 158–165.
- [170] Chae, Y. S., Hong, J. K., & Kim, M. Y. (2014). Circle Fitting to Overcome Vignetting Effect of Afocal Tracking System. In *2014 International Symposium on Optomechatronic Technologies* (pp. 66-68). IEEE.
- [171] Piccinini, F., & Bevilacqua, A. (2018). Colour vignetting correction for microscopy image mosaics used for quantitative analyses. *BioMed research international*, 2018.
- [172] Lee, S. S., Pelet, S., Peter, M., & Dechant, R. (2014). A rapid and effective vignetting correction for quantitative microscopy. *Rsc Advances*, 4(95), 52727-52733.

- [173] Tan, Y., Qiu, F., Yang-Luowa, Q., et al. (2011) Amniotic membrane inhibits squamous metaplasia of human conjunctival epithelium. *American Journal of Physiology Cell Physiology*, 70, C115–C125.
- [174] Cavalcanti, P.G. & Scharcanski, J. (2011) Automated prescreening of pigmented skin lesions using standard cameras. *Computerized Medical Imaging and Graphics*, 35, 481–491.
- [175] Filippini, M., Gasparoni, F., Grasso, T., et al. (2021). A Success Story of Digitalisation for Asset Integrity Management: 3-D Reconstruction of Subsea Wellheads with Clean Sea Hybrid AUV/ROV. In *OMC Med Energy Conference and Exhibition*. OnePetro.
- [176] Bevilacqua, A., & Piccinini, F. (2012). Is an empty field the best reference to correct vignetting in microscopy. In *7th IEEE International Workshop on Bio-signal Interpretation (BSI 2012)* Como, Italy.
- [177] Smith, K., Li, Y., Piccinini, F., et al. (2015). CIDRE: an illumination-correction method for optical microscopy. *Nature methods*, 12(5), 404-406.
- [178] Diaspro, A., Chirico, G., Usai, C., Ramoino, P., & Dobrucki, J. (2006). Photobleaching. In *Handbook of biological confocal microscopy* (pp. 690-702). Springer, Boston, MA.
- [179] Demchenko, A. P. (2020). Photobleaching of organic fluorophores: quantitative characterization, mechanisms, protection. *Methods and Applications in Fluorescence*, 8(2), 022001.
- [180] Cortesi, M., Bandiera, L., Pasini, A., et al. (2017). Reliable measurement of E. coli single cell fluorescence distribution using a standard microscope set-up. *Journal of biological engineering*, 11(1), 1-9.
- [181] Peng, T., Thorn, K., Schroeder, T., et al. (2017). A BaSiC tool for background and shading correction of optical microscopy images. *Nature communications*, 8(1), 1-7.
- [182] Miura, K. (2020). Bleach correction ImageJ plugin for compensating the photobleaching of time-lapse sequences. *F1000Research*, 9.
- [183] Klonis, N., Rug, M., Harper, I., et al. (2002). Fluorescence photobleaching analysis for the study of cellular dynamics. *European Biophysics Journal*, 31(1), 36-51.
- [184] Withers, P. J., Bouman, C., Carmignato, S., et al. (2021). X-ray computed tomography. *Nature Reviews Methods Primers*, 1(1), 1-21.
- [185] Kruth, J. P., Bartscher, M., Carmignato, S., et al. (2011). Computed tomography for dimensional metrology. *CIRP annals*, 60(2), 821-842.
- [186] Hughes, S. (2011). CT scanning in archaeology. *Computed Tomography-Special Applications*/Ed. L. Saba. In *Tech Europe*, 57-70.

- [187] De Chiffre, L., Carmignato, S., Kruth, J. P., Schmitt, R., & Weckenmann, A. (2014). Industrial applications of computed tomography. *CIRP annals*, 63(2), 655-677.
- [188] Mottola, M. (2021). New methodologies in CT perfusion and MRI analysis to develop cancer imaging biomarkers.
- [189] Liguori, C., Frauenfelder, G., Massaroni, C., et al. (2015). Emerging clinical applications of computed tomography. *Medical Devices*, 8, 265.
- [190] Elliott, J. C., Dowker, S. E. P., & Knight, R. D. (1981). Scanning X-ray microradiography of a section of a carious lesion in dental enamel. *Journal of Microscopy*, 123(1), 89-92.
- [191] Flohr, T. (2013). CT systems. *Current Radiology Reports*, 1(1), 52-63.
- [192] Hupfer, M., Nowak, T., Brauweiler, R., Eisa, F., & Kalender, W. A. (2012). Spectral optimization for micro-CT. *Medical physics*, 39(6Part1), 3229-3239.
- [193] Clark, D. P., & Badea, C. T. (2014). Micro-CT of rodents: state-of-the-art and future perspectives. *Physica medica*, 30(6), 619-634.
- [194] Ashton, J. R., West, J. L., & Badea, C. T. (2015). In vivo small animal micro-CT using nanoparticle contrast agent. *Frontiers in pharmacology*, 6, 256.
- [195] Cong, W., Xi, Y., Fitzgerald, P., De Man, B., & Wang, G. (2020). Virtual monoenergetic CT imaging via deep learning. *Patterns*, 1(8), 100128.
- [196] Li, H., Zhang, H., Tang, Z., & Hu, G. (2008). Micro-computed tomography for small animal imaging: Technological details. *Progress in natural science*, 18(5), 513-521.
- [197] Keklikoglou, K., Arvanitidis, C., Chatzigeorgiou, G., et al. (2021). Micro-CT for biological and biomedical studies: a comparison of imaging techniques. *Journal of Imaging*, 7(9), 172.
- [198] Lin, A. S., Barrows, T. H., Cartmell, S. H., & Guldberg, R. E. (2003). Microarchitectural and mechanical characterization of oriented porous polymer scaffolds. *Biomaterials*, 24(3), 481-489.
- [199] Orhan, K., Faria Vasconcelos, K. D., & Gaêta-Araujo, H. (2020). Artifacts in micro-CT. In *Micro-computed Tomography (micro-CT) in Medicine and Engineering* (pp. 35-48). Springer, Cham.
- [200] Clark, D. P., & Badea, C. T. (2021). Advances in micro-CT imaging of small animals. *Physica Medica*, 88, 175-192.
- [201] Boas, F. E., & Fleischmann, D. (2012). CT artifacts: causes and reduction techniques. *Imaging Med*, 4(2), 229-240.
- [202] Ferreira, T., & Rasband, W. (2012). ImageJ user guide. *ImageJ/Fiji*, 1, 155-161.
- [203] imaris.oxinst.com

- [204] Carpenter, A. E., Jones, T. R., Lamprecht, et al. (2006). CellProfiler: image analysis software for identifying and quantifying cell phenotypes. *Genome biology*, 7(10), 1-11.
- [205] De Santis, I., Lorenzini, L., Moretti, M., et al. (2021). Co-density distribution maps for advanced molecule colocalization and co-distribution analysis. *Sensors*, 21(19), 6385.
- [206] Zhang, L., Khattar, N., Kemenes, I., et al. (2018). Subcellular peptide localization in single identified neurons by capillary microsampling mass spectrometry. *Scientific reports*, 8(1), 1-10.
- [207] Xu, Y. Y., Yao, L. X., & Shen, H. B. (2018). Bioimage-based protein subcellular location prediction: a comprehensive review. *Frontiers of Computer Science*, 12(1), 26-39.
- [208] Hung, M. C., & Link, W. (2011). Protein localization in disease and therapy. *Journal of cell science*, 124(20), 3381-3392.
- [209] Wapinski, O., & Chang, H. Y. (2011). Long noncoding RNAs and human disease. *Trends in cell biology*, 21(6), 354-361.
- [210] Muslimov, I. A., Eom, T., Iacoangeli, A., et al. (2018). BC RNA mislocalization in the fragile X premutation. *Eneuro*, 5(2).
- [211] Zheng, F., Xiong, W., Sun, S., Zhang, P., & Zhu, J. J. (2019). Recent advances in drug release monitoring. *Nanophotonics*, 8(3), 391-413.
- [212] Mondal, A., Ashiq, K. A., Phulpagar, P., Singh, D. K., & Shiras, A. (2019). Effective visualization and easy tracking of extracellular vesicles in glioma cells. *Biological procedures online*, 21(1), 1-12.
- [213] Qiao, D., Li, L., Shen, T., Yang, J., Chang, H., Liang, X., ... & Shang, L. (2020). Establishment of a customizable fluorescent probe platform for the organelle-targeted bioactive species detection. *ACS sensors*, 5(7), 2247-2254.
- [214] Li, X., Cheng, Z., & Jin, H. (2012). Dynamics of Ras complexes observed in living cells. *Sensors*, 12(7), 9411-9422.
- [215] Buckley, A. G., Looi, K., Iosifidis, T., et al. (2018). Visualisation of multiple tight junctional complexes in human airway epithelial cells. *Biological Procedures Online*, 20(1), 1-9.
- [216] Cai, M., Liao, Z., Chen, T., et al. (2017). Characterization of the subcellular localization of Epstein-Barr virus encoded proteins in live cells. *Oncotarget*, 8(41), 70006.
- [217] Wilk, R., Hu, J., Blotsky, D., & Krause, H. M. (2016). Diverse and pervasive subcellular distributions for both coding and long noncoding RNAs. *Genes & development*, 30(5), 594-609.

- [218] Stadler, C., Rexhepaj, E., Singan, V. R., et al. (2013). Immunofluorescence and fluorescent-protein tagging show high correlation for protein localization in mammalian cells. *Nature methods*, 10(4), 315-323.
- [219] Samacoits, A., Chouaib, R., Safieddine, A., et al. (2018). A computational framework to study sub-cellular RNA localization. *Nature Communications*, 9(1), 1-10.
- [220] Hedde, P. N., & Nienhaus, G. U. (2010). Optical imaging of nanoscale cellular structures. *Biophysical reviews*, 2(4), 147-158.
- [221] Lee, S., Batjikh, I., & Kang, S. H. (2020). Toward sub-diffraction imaging of single-DNA molecule sensors based on stochastic switching localization microscopy. *Sensors*, 20(22), 6667.
- [222] Baddeley, D., & Bewersdorf, J. (2018). Biological insight from super-resolution microscopy: what we can learn from localization-based images. *Annual review of biochemistry*, 87, 965-989.
- [223] Floderer, C., Masson, J. B., Boilley, E., et al. (2018). Single molecule localisation microscopy reveals how HIV-1 Gag proteins sense membrane virus assembly sites in living host CD4 T cells. *Scientific reports*, 8(1), 1-15.
- [224] Xia, Y., & Fu, B. M. (2018). Investigation of Endothelial Surface Glycocalyx Components and Ultrastructure by Single Molecule Localization Microscopy: Stochastic Optical Reconstruction Microscopy (STORM). *The Yale Journal of Biology and Medicine*, 91(3), 257-266.
- [225] Laplante, C. (2018). Building the contractile ring from the ground up: A lesson in perseverance and scientific creativity. *Biophysical Reviews*, 10(6), 1491-1497.
- [226] Peters, R., Griffié, J., Burn, G. L., Williamson, D. J., & Owen, D. M. (2018). Quantitative fibre analysis of single-molecule localization microscopy data. *Scientific reports*, 8(1), 1-8.
- [227] Bänfer, S., Schneider, D., Dewes, J., et al. (2018). Molecular mechanism to recruit galectin-3 into multivesicular bodies for polarized exosomal secretion. *Proceedings of the National Academy of Sciences*, 115(19), E4396-E4405.
- [228] Hennen, J., Hur, K. H., Kohler, J., Luxton, G. G., & Mueller, J. D. (2019). Challenges and Opportunities for Characterizing the Assembly of Nuclear Envelope Proteins by Fluorescence Fluctuation Spectroscopy. *Biophysical Journal*, 116(3), 279a.
- [229] Lambert, T. J., & Waters, J. C. (2017). Navigating challenges in the application of superresolution microscopy. *Journal of Cell Biology*, 216(1), 53-63.
- [230] Wegel, E., Göhler, A., Lagerholm, B. C., et al. (2016). Imaging cellular structures in super-resolution with SIM, STED and Localisation Microscopy: A practical comparison. *Scientific reports*, 6(1), 1-13.

- [231] Tinguely, J. C., Helle, Ø. I., Coucheron, D. A., et al. (2018). Photonic integrated circuits for nanoscopy. In *Integrated Photonics Research, Silicon and Nanophotonics* (pp. IW2B-5). Optica Publishing Group.
- [232] González, G., & Evans, C. L. (2019). Biomedical Image Processing with Containers and Deep Learning: An Automated Analysis Pipeline: Data architecture, artificial intelligence, automated processing, containerization, and clusters orchestration ease the transition from data acquisition to insights in medium-to-large datasets. *BioEssays*, 41(6), 1900004.
- [233] Conway, J. R., Carragher, N. O., & Timpson, P. (2014). Developments in preclinical cancer imaging: innovating the discovery of therapeutics. *Nature Reviews Cancer*, 14(5), 314-328.
- [234] Cunha, L., Horvath, I., Ferreira, S., et al. (2014). Preclinical imaging: an essential ally in modern biosciences. *Molecular diagnosis & therapy*, 18(2), 153-173.
- [235] Li, W., Field, K. G., & Morgan, D. (2018). Automated defect analysis in electron microscopic images. *npj Computational Materials*, 4(1), 1-9.
- [236] Uroy, L., Mony, C., & Ernoult, A. (2019). Additive effects of connectivity provided by different habitat types drive plant assembly. *Scientific reports*, 9(1), 1-13.
- [237] Lyashenko, V. V., Babker, A. M. A. A., & Kobylin, O. A. (2016). The methodology of wavelet analysis as a tool for cytology preparations image processing. *Cukurova Medical Journal*, 41(3), 453-463.
- [238] Smith, K., Piccinini, F., Balassa, T., Koos, K., Danka, T., Azizpour, H., & Horvath, P. (2018). Phenotypic image analysis software tools for exploring and understanding big image data from cell-based assays. *Cell systems*, 6(6), 636-653.
- [239] O'Donoghue, S. I., Baldi, B. F., Clark, S. J. et al. (2018). Visualization of biomedical data. *Annual Review of Biomedical Data Science*, 1(1), 275-304.
- [240] Zuckerkandl, E., & Pauling, L. (1965). Evolutionary divergence and convergence in proteins. In *Evolving genes and proteins* (pp. 97-166). Academic Press.
- [241] Gut, G., Herrmann, M. D., & Pelkmans, L. (2018). Multiplexed protein maps link subcellular organization to cellular states. *Science*, 361(6401).
- [242] cellimagelibrary.org
- [243] Apaja, P. M., Xu, H., & Lukacs, G. L. (2010). Quality control for unfolded proteins at the plasma membrane. *Journal of Cell Biology*, 191(3), 553-570.
- [244] Martella, E., Ferroni, C., Guerrini, A., et al. (2018). Functionalized keratin as nanotechnology-based drug delivery system for the pharmacological

- treatment of osteosarcoma. *International journal of molecular sciences*, 19(11), 3670.
- [245] Bossi, G., Marampon, F., Maor-Aloni, R., et al. (2008). Conditional RNA interference in vivo to study mutant p53 oncogenic gain of function on tumor malignancy. *Cell Cycle*, 7(12), 1870-1879.
- [246] Tesei, A., Sarnelli, A., Arienti, C., et al. (2013). In vitro irradiation system for radiobiological experiments. *Radiation Oncology*, 8(1), 1-12.
- [247] Ridler, T. W., & Calvard, S. (1978). Picture thresholding using an iterative selection method. *Transactions on Systems, Man, and Cybernetics*, 8(8), 630-632.
- [248] Kapur, J. N., Sahoo, P. K., & Wong, A. K. (1985). A new method for gray-level picture thresholding using the entropy of the histogram. *Computer vision, graphics, and image processing*, 29(3), 273-285.
- [249] Pizer, S. M., Amburn, E. P., Austin, J. D., et al. (1987). Adaptive histogram equalization and its variations. *Computer vision, graphics, and image processing*, 39(3), 355-368.
- [250] Treuting, P. M., Dintzis, S., & Montine, K. S. (Eds.). (2017). Comparative anatomy and histology: a mouse, rat, and human atlas. Academic Press.
- [251] Alves, R. C., Fernandes, R. P., Eloy, J. O., Salgado, H. R. N., & Chorilli, M. (2018). Characteristics, properties and analytical methods of paclitaxel: a review. *Critical reviews in analytical chemistry*, 48(2), 110-118.
- [252] Barnes, E., Guan, X., Alberts, E. M., et al. (2020). Interplay between convective and viscoelastic forces controls the morphology of in vitro paclitaxel-stabilized microtubules. *Crystals*, 10(1), 43.
- [253] Zar, J. H. (1999). Biostatistical analysis. Pearson Education India.
- [254] Sandberg, K. (2007). Introduction to image processing in Matlab. Dept. of Applied Mathematics, Colorado. BIODATA.
- [255] sourceforge.net/projects/DDMaker
- [256] Mankan, A. K., Schmidt, T., Chauhan, D., et al. (2014). Cytosolic RNA: DNA hybrids activate the cGAS-STING axis. *The EMBO journal*, 33(24), 2937-2946.
- [257] Storci, G., De Carolis, S., Papi, A., et al. (2019). Genomic stability, anti-inflammatory phenotype, and up-regulation of the RNaseH2 in cells from centenarians. *Cell Death & Differentiation*, 26(9), 1845-1858.
- [258] Piccinini, F., Bevilacqua, A., Smith, K., & Horvath, P. (2013, April). Vignetting and photo-bleaching correction in automated fluorescence microscopy from an array of overlapping images. In *2013 IEEE 10th International Symposium on Biomedical Imaging* (pp. 464-467). IEEE.
- [259] Varga, Z., Fehér, B., Kitka, D., et al. (2020). Size measurement of extracellular vesicles and synthetic liposomes: the impact of the hydration shell and the protein corona. *Colloids and Surfaces B: Biointerfaces*, 192, 111053.

- [260] wikipedia.org/wiki/Pearson_correlation_coefficient
- [261] Pearson, K. (1896). VII. Mathematical contributions to the theory of evolution. III. Regression, heredity, and panmixia. *Philosophical Transactions of the Royal Society of London. Series A, containing papers of a mathematical or physical character*, (187), 253-318.
- [262] Lee Rodgers, J., & Nicewander, W. A. (1988). Thirteen ways to look at the correlation coefficient. *The American Statistician*, 42(1), 59-66.
- [263] Taylor, R. (1990). Interpretation of the correlation coefficient: a basic review. *Journal of diagnostic medical sonography*, 6(1), 35-39.
- [264] Aaron, J. S., Taylor, A. B., & Chew, T. L. (2018). Image co-localization-co-occurrence versus correlation. *Journal of cell science*, 131(3), jcs211847.
- [265] Lagache, T., Sauvonnet, N., Danglot, L., & Olivo-Marin, J. C. (2015). Statistical analysis of molecule colocalization in bioimaging. *Cytometry Part A*, 87(6), 568-579.
- [266] Adler, J., & Parmryd, I. (2010). Quantifying colocalization by correlation: the Pearson correlation coefficient is superior to the Mander's overlap coefficient. *Cytometry Part A*, 77(8), 733-742.
- [267] Artusi, R., Verderio, P., & Marubini, E. (2002). Bravais-Pearson and Spearman correlation coefficients: meaning, test of hypothesis and confidence interval. *The International journal of biological markers*, 17(2), 148-151.
- [268] Gry, M., Rimini, R., Strömberg, S., et al. (2009). Correlations between RNA and protein expression profiles in 23 human cell lines. *BMC genomics*, 10(1), 1-14.
- [269] Zhao, L., Kong, H., Sun, H., et al. (2018). LncRNA-PVT1 promotes pancreatic cancer cells proliferation and migration through acting as a molecular sponge to regulate miR-448. *Journal of cellular physiology*, 233(5), 4044-4055.
- [270] Boere, J., van de Lest, C. H. A., de Grauw, J. C., et al. (2019). Extracellular vesicles in synovial fluid from juvenile horses: No age-related changes in the quantitative profile. *The Veterinary Journal*, 244, 91-93.
- [271] Molnár, G., Rózsa, M., Baka, J., et al. (2016). Human pyramidal to interneuron synapses are mediated by multi-vesicular release and multiple docked vesicles. *Elife*, 5, e18167.
- [272] Rappez, L., Stadler, M., Triana, S., et al. (2019). Spatial single-cell profiling of intracellular metabolomes in situ. *BioRxiv*, 510222.
- [273] Yip, G. G., Lo, M. C., Yan, W., Lee, K. C., Lai, Q. T., Wong, K. K., & Tsia, K. K. (2021). Multimodal FACED imaging for large-scale single-cell morphological profiling. *APL Photonics*, 6(7), 070801.

- [274] Manders, E. M. M., Verbeek, F. J., & Aten, J. A. (1993). Measurement of colocalization of objects in dual-colour confocal images. *Journal of microscopy*, 169(3), 375-382.
- [275] Adler, J., & Parmryd, I. (2019). Quantifying colocalization: The MOC is a hybrid coefficient—an uninformative mix of co-occurrence and correlation. *Journal of Cell Science*, 132(1).
- [276] Aaron, J. S., Taylor, A. B., & Chew, T. L. (2019). The Pearson's correlation coefficient is not a universally superior colocalization metric. Response to 'Quantifying colocalization: the MOC is a hybrid coefficient—an uninformative mix of co-occurrence and correlation'. *Journal of Cell Science*, 132(1).
- [277] Adler, J., & Parmryd, I. (2021). Quantifying colocalization: The case for discarding the Manders overlap coefficient. *Cytometry Part A*, 99(9), 910-920.
- Landmann, L., & Marbet, P. (2004). Colocalization analysis yields superior results after image restoration. *Microscopy research and technique*, 64(2), 103-112.
- [278] Zhou, L., Cai, M., Tong, T., & Wang, H. (2017). Progress in the correlative atomic force microscopy and optical microscopy. *Sensors*, 17(4), 938.
- [279] Landmann, L., & Marbet, P. (2004). Colocalization analysis yields superior results after image restoration. *Microscopy research and technique*, 64(2), 103-112.
- [280] Wells, K. S., Sandison, D. R., Strickler, J., & Webb, W. W. (1990). Quantitative fluorescence imaging with laser scanning confocal microscopy. In *Handbook of biological confocal microscopy* (pp. 27-39). Springer, Boston, MA.
- [281] Akner, G., Mossberg, K., Wikström, A. C., Sundqvist, K. G., & Gustafsson, J. Å. (1991). Evidence for colocalization of glucocorticoid receptor with cytoplasmic microtubules in human gingival fibroblasts, using two different monoclonal anti-GR antibodies, confocal laser scanning microscopy and image analysis. *The Journal of Steroid Biochemistry and Molecular Biology*, 39(4), 419-432.
- [282] Pike, J. A., Styles, I. B., Rappoport, J. Z., & Heath, J. K. (2017). Quantifying receptor trafficking and colocalization with confocal microscopy. *Methods*, 115, 42-54.
- [283] Silver, M. A., & Stryker, M. P. (2000). A method for measuring colocalization of presynaptic markers with anatomically labeled axons using double label immunofluorescence and confocal microscopy. *Journal of neuroscience methods*, 94(2), 205-215.
- [284] Oheim, M., & Li, D. (2007). Quantitative colocalisation imaging: concepts, measurements, and pitfalls. In *Imaging cellular and molecular biological functions* (pp. 117-155). Springer, Berlin, Heidelberg.

- [285] Lachmanovich, E., Shvartsman, D. E., Malka, Y., et al. (2003). Co-localization analysis of complex formation among membrane proteins by computerized fluorescence microscopy: application to immunofluorescence co-patching studies. *Journal of microscopy*, 212(2), 122-131.
- [286] Adler, J., Pagakis, S. N., & Parmryd, I. (2008). Replicate-based noise corrected correlation for accurate measurements of colocalization. *Journal of microscopy*, 230(1), 121-133.
- [287] Singan, V. R., Jones, T. R., Curran, K. M., & Simpson, J. C. (2011). Dual channel rank-based intensity weighting for quantitative co-localization of microscopy images. *BMC bioinformatics*, 12(1), 1-15.
- [288] Herce, H. D., Casas-Delucchi, C. S., & Cardoso, M. C. (2013). New image colocalization coefficient for fluorescence microscopy to quantify (bio-) molecular interactions. *Journal of microscopy*, 249(3), 184-194.
- [289] Sheng, H., Stauffer, W., & Lim, H. N. (2016). Systematic and general method for quantifying localization in microscopy images. *Biology Open*, 5(12), 1882-1893.
- [290] Li, Q., Lau, A., Morris, T. J., et al. (2004). A syntaxin 1, Gα_o, and N-type calcium channel complex at a presynaptic nerve terminal: analysis by quantitative immunocolocalization. *Journal of Neuroscience*, 24(16), 4070-4081.
- [291] Wang, S., Arena, E. T., Becker, J. T., et al. (2019). Spatially adaptive colocalization analysis in dual-color fluorescence microscopy. *IEEE Transactions on Image Processing*, 28(9), 4471-4485.
- [292] Gilles, J. F., Dos Santos, M., Boudier, T., Bolte, S., & Heck, N. (2017). DiAna, an ImageJ tool for object-based 3-D co-localization and distance analysis. *Methods*, 115, 55-64.
- [293] Costes, S. V., Daelemans, D., Cho, E. H., Dobbin, Z., Pavlakis, G., & Lockett, S. (2004). Automatic and quantitative measurement of protein-protein colocalization in live cells. *Biophysical journal*, 86(6), 3993-4003.
- [294] Cordelieres, F. P., & Bolte, S. (2014). Experimenters' guide to colocalization studies: finding a way through indicators and quantifiers, in practice. *Methods in cell biology*, 123, 395-408.
- [295] Giuliani, A., Sivilia, S., Baldassarro, V. A., et al. (2019). Age-related changes of the neurovascular unit in the cerebral cortex of Alzheimer disease mouse models: a neuroanatomical and molecular study. *Journal of Neuropathology & Experimental Neurology*, 78(2), 101-112.
- [296] Spearman, C. (1904). The proof and measurement of association between two things, *American Journal*.
- [297] Saliani, A., Perraud, B., Duval, T., et al. (2017). Axon and myelin morphology in animal and human spinal cord. *Frontiers in neuroanatomy*, 11, 129.

- [298] Gherardi, A., Bevilacqua, A., & Piccinini, F. (2011, April). Illumination field estimation through background detection in optical microscopy. In 2011 IEEE Symposium on Computational Intelligence in Bioinformatics and Computational Biology (CIBCB) (pp. 1-6). IEEE.
- [299] sourceforge.net/projects/coDDMaker
- [300] Újvári, A., & Luse, D. S. (2006). RNA emerging from the active site of RNA polymerase II interacts with the Rpb7 subunit. *Nature structural & molecular biology*, 13(1), 49-54.
- [301] García-Muse, T., & Aguilera, A. (2019). R loops: from physiological to pathological roles. *Cell*, 179(3), 604-618.
- [302] Petermann, E., Lan, L., & Zou, L. (2022). Sources, resolution and physiological relevance of R-loops and RNA–DNA hybrids. *Nature Reviews Molecular Cell Biology*, 1-20.
- [303] Crossley, M. P., Bocek, M., & Cimprich, K. A. (2019). R-loops as cellular regulators and genomic threats. *Molecular cell*, 73(3), 398-411.
- [304] Niehrs, C., & Luke, B. (2020). Regulatory R-loops as facilitators of gene expression and genome stability. *Nature Reviews Molecular Cell Biology*, 21(3), 167-178.
- [305] Marnef, A., & Legube, G. (2021). R-loops as Janus-faced modulators of DNA repair. *Nature cell biology*, 23(4), 305-313.
- [306] Yu, K., Chedin, F., Hsieh, C. L., Wilson, T. E., & Lieber, M. R. (2003). R-loops at immunoglobulin class switch regions in the chromosomes of stimulated B cells. *Nature immunology*, 4(5), 442-451.
- [307] Ivančić-Baće, I., Howard, J. A., & Bolt, E. L. (2012). Tuning in to interference: R-loops and cascade complexes in CRISPR immunity. *Journal of molecular biology*, 422(5), 607-616.
- [308] Fernandes, R. V., Feretzaki, M., & Lingner, J. (2021). The makings of TERRA R-loops at chromosome ends. *Cell Cycle*, 20(18), 1745-1759.
- [309] Kim J, Yoon J, Ju M, et al. (2013). Identification of two HIV inhibitors that also inhibit human RNaseH2. *Molecules and Cells* 36:212-218.
- [310] Brambati A, Zardoni L, Nardini E, Pellicoli A, Liberi G (2020). The dark side of RNA: DNA hybrids. *Mutation Research/Reviews in Mutation Research* 784:108300.
- [311] Skourti-Stathaki, K., & Proudfoot, N. J. (2014). A double-edged sword: R loops as threats to genome integrity and powerful regulators of gene expression. *Genes & development*, 28(13), 1384-1396.
- [312] Bhattacharya, S., Srinivasan, K., Abdisalaam, S., et al. (2017). RAD51 interconnects between DNA replication, DNA repair and immunity. *Nucleic acids research*, 45(8), 4590-4605.

- [313] Vanpouille-Box, C., Demaria, S., Formenti, S. C., & Galluzzi, L. (2018). Cytosolic DNA sensing in organismal tumor control. *Cancer Cell*, 34(3), 361-378.
- [314] Govindaraj, S., Paruchuru, L. B., Razin, E. (2021). The pLysRS-Ap4A Pathway in Mast Cells Regulates the Switch from Host Defense to a Pathological State. *International Journal of Molecular Science*, 22:5620.
- [315] Vincent, L. (1993). Morphological grayscale reconstruction in image analysis: Applications and efficient algorithms. *IEEE Transaction in Image Processing* 2:176-201.
- [316] Poleszczuk, J. T., Luddy, K. A., Prokopiou, S., et al. (2016). Abscopal Benefits of Localized Radiotherapy Depend on Activated T-cell Trafficking and Distribution between Metastatic Lesions T-cell Trafficking in Abscopal Response. *Cancer research*, 76(5), 1009-1018.
- [317] Abuodeh, Y., Venkat, P., & Kim, S. (2016). Systematic review of case reports on the abscopal effect. *Current problems in cancer*, 40(1), 25-37.
- [318] Reynders, K., Illidge, T., Siva, S., Chang, J. Y., & De Ruyscher, D. (2015). The abscopal effect of local radiotherapy: using immunotherapy to make a rare event clinically relevant. *Cancer treatment reviews*, 41(6), 503-510.
- [319] Siva, S., Lobachevsky, P., MacManus, M. P., et al. (2016). Radiotherapy for Non-Small Cell Lung Cancer Induces DNA Damage Response in Both Irradiated and Out-of-field Normal Tissues DNA Damage in Normal Tissues during Lung Radiotherapy. *Clinical Cancer Research*, 22(19), 4817-4826.
- [320] Cong, Y., Shen, G., Wu, S., & Hao, R. (2017). Abscopal regression following SABR for non-small-cell-lung cancer: a case report. *Cancer biology & therapy*, 18(1), 1-3.
- [321] Mole, R. H. (1953). Whole body irradiation—radiobiology or medicine? *The British journal of radiology*, 26(305), 234-241.
- [322] Ewald, J. A., Desotelle, J. A., Wilding, G., & Jarrard, D. F. (2010). Therapy-induced senescence in cancer. *JNCI: Journal of the National Cancer Institute*, 102(20), 1536-1546.
- [323] Li, X., Shao, C., Shi, Y., & Han, W. (2018). Lessons learned from the blockade of immune checkpoints in cancer immunotherapy. *Journal of hematology & oncology*, 11(1), 1-26.
- [324] Schrand, B., Verma, B., Levay, A., et al. (2017). Radiation-Induced Enhancement of Antitumor T-cell Immunity by VEGF-Targeted 4-1BB Costimulation. *Cancer research*, 77(6), 1310-1321.
- [325] Camphausen, K., Moses, M. A., Ménard, C., et al. (2003). Radiation abscopal antitumor effect is mediated through p53. *Cancer research*, 63(8), 1990-1993.

- [326] Pole, A., Dimri, M., & Dimri, G. P. (2016). Oxidative stress, cellular senescence and ageing. *AIMS molecular science*, 3(3).
- [327] Shen, Y. J., Le Bert, N., Chitre, A. A., et al. (2015). Genome-derived cytosolic DNA mediates type I interferon-dependent rejection of B cell lymphoma cells. *Cell reports*, 11(3), 460-473.
- [328] Koo, C. X. E., Kobiyama, K., Shen, Y. J., et al. (2015). RNA polymerase III regulates cytosolic RNA: DNA hybrids and intracellular microRNA expression. *Journal of Biological Chemistry*, 290(12), 7463-7473.
- [329] De Cecco, M., Ito, T., Petrashen, A. P., et al. (2019). L1 drives IFN in senescent cells and promotes age-associated inflammation. *Nature*, 566(7742), 73-78.
- [330] Vanoosthuyse, V. (2018). Strengths and weaknesses of the current strategies to map and characterize R-loops. *Non-coding RNA*, 4(2), 9.
- [331] Smolka, J. A., Sanz, L. A., Hartono, S. R., & Chédin, F. (2021). Recognition of RNA by the S9. 6 antibody creates pervasive artifacts when imaging RNA: DNA hybrids. *Journal of Cell Biology*, 220(6), e202004079.
- [332] Ubertini, V., Norelli, G., d'Arcangelo, D., et al. (2015). Mutant p53 gains new function in promoting inflammatory signals by repression of the secreted interleukin-1 receptor antagonist. *Oncogene*, 34(19), 2493-2504.
- [333] Arienti, C., Pignatta, S., Zanoni, M., et al. (2021). High-pressure oxygen rewires glucose metabolism of patient-derived glioblastoma cells and fuels inflammasome response. *Cancer Letters*, 506:152-166.
- [334] Velasco, F. R. (1979). Thresholding using the ISODATA clustering algorithm. Maryland University College Park Computer Science Center.
- [335] Zack, G. W., Rogers, W. E., & Latt, S. A. (1977). Automatic measurement of sister chromatid exchange frequency. *Journal of Histochemistry & Cytochemistry*, 25(7), 741-753.
- [336] Bevilacqua, A., Barone, D., Baiocco, S., Gavelli, G. (2017). A novel approach for semi-quantitative assessment of reliability of blood flow values in DCE-CT perfusion. *Biomedical Signal Processing and Control*, 31:257-264.
- [337] Meyer, F. (1994). Topographic distance and watershed lines. *Signal Processing*, 38:113-125.
- [338] Miousse, I. R., Kutanzi, K. R., & Koturbash, I. (2017). Effects of ionizing radiation on DNA methylation: from experimental biology to clinical applications. *International journal of radiation biology*, 93(5), 457-469.
- [339] Burns, K. H. (2017). Transposable elements in cancer. *Nature Reviews Cancer*, 17(7), 415-424.
- [340] Harris, C. R., Dewan, A., Zupnick, A., et al. (2009). p53 responsive elements in human retrotransposons. *Oncogene*, 28(44), 3857-3865.

- [341] Yen, C. C., Chang, W. H., Tung, M. C., et al. (2020). Lactoferrin protects hyperoxia-induced lung and kidney systemic inflammation in an in vivo imaging model of NF- κ B/luciferase transgenic mice. *Molecular imaging and biology*, 22(3), 526-538.
- [342] Nishida, K., Kuwano, Y., Nishikawa, T., Masuda, K., & Rokutan, K. (2017). RNA binding proteins and genome integrity. *International journal of molecular sciences*, 18(7), 1341.
- [343] Rondón, A. G., & Aguilera, A. (2019). What causes an RNA-DNA hybrid to compromise genome integrity? *DNA repair*, 81, 102660.
- [344] Schwenck, J., Mehling, R., Thaiss, W. M., et al. (2020). Temporal dynamics of reactive oxygen and nitrogen species and NF- κ B activation during acute and chronic T cell-driven inflammation. *Molecular imaging and biology*, 22(3), 504-514.
- [345] Kim, S. W., Kim, I. K., & Lee, S. H. (2020). Role of hyperoxic treatment in cancer. *Experimental Biology and Medicine*, 245(10), 851-860.
- [346] Tsekrekou, M., Stratigi, K., & Chatzinikolaou, G. (2017). The nucleolus: in genome maintenance and repair. *International journal of molecular sciences*, 18(7), 1411.
- [347] Lindström, M. S., Jurada, D., Bursac, S., Orsolich, I., Bartek, J., & Volarevic, S. (2018). Nucleolus as an emerging hub in maintenance of genome stability and cancer pathogenesis. *Oncogene*, 37(18), 2351-2366.
- [348] Peinado, H., Alečković, M., Lavotshkin, S., et al. (2012). Melanoma exosomes educate bone marrow progenitor cells toward a pro-metastatic phenotype through MET. *Nature medicine*, 18(6), 883-891.
- [349] Santos-Pereira, J. M., & Aguilera, A. (2015). R loops: new modulators of genome dynamics and function. *Nature Reviews Genetics*, 16(10), 583-597.
- [350] Ralston, S. H. (2013). Bone structure and metabolism. *Medicine*, 41(10), 581-585.
- [351] Blumer, M. J. (2021). Bone tissue and histological and molecular events during development of the long bones. *Annals of Anatomy-Anatomischer Anzeiger*, 235, 151704.
- [352] Hadjidakis, D. J., & Androulakis, I. I. (2006). Bone remodeling. *Annals of the New York academy of sciences*, 1092(1), 385-396.
- [353] Alijani, H., & Vaughan, T. J. (2022). A multiscale finite element investigation on the role of intra-and extra-fibrillar mineralisation on the elastic properties of bone tissue. *Journal of the Mechanical Behavior of Biomedical Materials*, 129, 105139.
- [354] osteoporosis.foundation/health-professionals/about-osteoporosis

- [355] Gdyczynski, C. M., Manbachi, A., Hashemi, S., Lashkari, B., & Cobbold, R. S. (2014). On estimating the directionality distribution in pedicle trabecular bone from micro-CT images. *Physiological measurement*, 35(12), 2415.
- [356] Mellon, S. J., & Tanner, K. E. (2012). Bone and its adaptation to mechanical loading: a review. *International Materials Reviews*, 57(5), 235-255.
- [357] Livens, S., Scheunders, P., Van de Wouwer, G., & Van Dyck, D. (1997). Wavelets for texture analysis, an overview.
- [358] Clausi, D. A., & Jernigan, M. E. (2000). Designing Gabor filters for optimal texture separability. *Pattern Recognition*, 33(11), 1835-1849.
- [359] Gabor, D. (1946). Theory of communication. Part 1: The analysis of information. *Journal of the Institution of Electrical Engineers-part III: radio and communication engineering*, 93(26), 429-441.
- [360] Daugman, J. G. (1988). Complete discrete 2-D Gabor transforms by neural networks for image analysis and compression. *IEEE Transactions on acoustics, speech, and signal processing*, 36(7), 1169-1179.
- [361] Chen, W., Liao, B., & Li, W. (2018). Use of image texture analysis to find DNA sequence similarities. *Journal of Theoretical Biology*, 455, 1-6.
- [362] Brotto, M., & Johnson, M. L. (2014). Endocrine crosstalk between muscle and bone. *Current osteoporosis reports*, 12(2), 135-141.
- [363] McCarthy, E. F. (2011, February). Genetic diseases of bones and joints. In *Seminars in diagnostic pathology* (Vol. 28, No. 1, pp. 26-36). WB Saunders.
- [364] Pedersen, B. K. (2011). Muscles and their myokines. *Journal of Experimental Biology*, 214(2), 337-346.
- [365] Kaji, H. (2016). Effects of myokines on bone. *BoneKEy reports*, 5.
- [366] Colaianni, G., Mongelli, T., Cuscito, C., et al. (2017). Irisin prevents and restores bone loss and muscle atrophy in hind-limb suspended mice. *Scientific reports*, 7(1), 1-16.
- [367] Gomasasca, M., Banfi, G., & Lombardi, G. (2020). Myokines: The endocrine coupling of skeletal muscle and bone. *Advances in clinical chemistry*, 94, 155-218.
- [368] Wood, C. L., Pajevic, P. D., & Gooi, J. H. (2017). Osteocyte secreted factors inhibit skeletal muscle differentiation. *Bone reports*, 6, 74-80.
- [369] Cianferotti, L., & Brandi, M. L. (2014). Muscle–bone interactions: basic and clinical aspects. *Endocrine*, 45(2), 165-177.
- [370] Han, Y., You, X., Xing, W., Zhang, Z., & Zou, W. (2018). Paracrine and endocrine actions of bone—the functions of secretory proteins from osteoblasts, osteocytes, and osteoclasts. *Bone research*, 6(1), 1-11.

- [371] Duan, P., & Bonewald, L. F. (2016). The role of the wnt/ β -catenin signaling pathway in formation and maintenance of bone and teeth. *The international journal of biochemistry & cell biology*, 77, 23-29.
- [372] Bouxsein, M. L., Boyd, S. K., Christiansen, B. A., Guldberg, R. E., Jepsen, K. J., & Müller, R. (2010). Guidelines for assessment of bone microstructure in rodents using micro-computed tomography. *Journal of bone and mineral research*, 25(7), 1468-1486.
- [373] Morigi, M. P., & Albertin, F. (2022). X-ray Digital Radiography and Computed Tomography. *Journal of Imaging*, 8(5), 119.
- [374] Zuñiga, A. G., Florindo, J. B., & Bruno, O. M. (2014). Gabor wavelets combined with volumetric fractal dimension applied to texture analysis. *Pattern Recognition Letters*, 36, 135-143.
- [375] Zehani, S., Ouahabi, A., Oussalah, M., Mimi, M., & Taleb-Ahmed, A. (2021). Bone microarchitecture characterization based on fractal analysis in spatial frequency domain imaging. *International Journal of Imaging Systems and Technology*, 31(1), 141-159.
- [376] Jarvi, A., Tammissalo, E., & Nevalainen, O. (1997). Characterization of radiographic trabecular bone structure with Gabor wavelets. In *Medical Imaging 1997: Image Processing* (Vol. 3034, pp. 671-680). SPIE.
- [377] Ruikar, D. D., Santosh, K. C., & Hegadi, R. S. (2019). Automated fractured bone segmentation and labeling from CT images. *Journal of medical systems*, 43(3), 60.
- [378] Yap, D. W. H., Chen, Y., Leow, W. K., Howe, T. S., & Png, M. A. (2004). Detecting femur fractures by texture analysis of trabeculae. In *Proceedings of the 17th International Conference on Pattern Recognition, 2004. ICPR 2004.* (Vol. 3, pp. 730-733). IEEE.
- [379] Pramudito, J. T., Soegijoko, S., Mengko, T. R., Muchtadi, F. I., & Wachjudi, R. G. (2007). Trabecular pattern analysis of proximal femur radiographs for osteoporosis detection. *Journal of Biomedical & Pharmaceutical Engineering*, 1(1), 45-51.
- [380] Oulhaj, H., Rziza, M., Amine, A., et al. (2017). Trabecular bone characterization using circular parametric models. *Biomedical Signal Processing and Control*, 33, 411-421.
- [381] Yingling, V. R., Xiang, Y., Raphan, T., et al. (2007). The effect of a short-term delay of puberty on trabecular bone mass and structure in female rats: a texture-based and histomorphometric analysis. *Bone*, 40(2), 419-424.
- [382] Xiang, Y., Yingling, V. R., Malique, R., et al. (2007). Comparative assessment of bone mass and structure using texture-based and histomorphometric analyses. *Bone*, 40(2), 544-552.

- [383] Shi, X., Liu, X. S., Wang, X., Guo, X. E., & Niebur, G. L. (2010). Type and orientation of yielded trabeculae during overloading of trabecular bone along orthogonal directions. *Journal of biomechanics*, 43(13), 2460-2466.
- [384] Chen, C., Jin, D., & Saha, P. K. (2015). Fuzzy skeletonization improves the performance of characterizing trabecular bone micro-architecture. In *International Symposium on Visual Computing* (pp. 14-24). Springer, Cham.
- [385] Stauber, M., Rapillard, L., van Lenthe, G. H., Zysset, P., and Müller, R. (2006). Importance of individual rods and plates in the assessment of bone quality and their contribution to bone stiffness, *Journal of Bone and Mineral Research*, 21(4), pp. 586–595.
- [386] Almhdie-Imjabber, A., Rozenbaum, O., Lespessailles, E., & Jennane, R. A. (2011). New local shape classification method for trabecular bone characterization, *International Conference on Signal, Image, Vision and their Applications*.
- [387] Wong, A. K., & Sahoo, P. K. (1989). A gray-level threshold selection method based on maximum entropy principle. *IEEE Transactions on Systems, Man, and Cybernetics*, 19(4), 866-871.
- [388] Kanopoulos, N., Vasanthavada, N., & Baker, R. L. (1988). Design of an image edge detection filter using the Sobel operator. *IEEE Journal of solid-state circuits*, 23(2), 358-367.
- [389] Danielsson, P. E. (1980). Euclidean distance mapping. *Computer Graphics and image processing*, 14(3), 227-248.
- [390] Eggermont, F., Verdonschot, N., van der Linden, Y., & Tanck, E. (2019). Calibration with or without phantom for fracture risk prediction in cancer patients with femoral bone metastases using CT-based finite element models. *PLoS One*, 14(7), e0220564.
- [391] Huttenlocher, D. P., Klanderman, G. A., & Rucklidge, W. J. (1993). Comparing images using the Hausdorff distance. *IEEE Transactions on pattern analysis and machine intelligence*, 15(9), 850-863. ISO 690
- [392] Yotsumoto, T., Morozumi, N., Nakamura, R., et al. (2019). Safety assessment of a novel C-type natriuretic peptide derivative and the mechanism of bone- and cartilage-specific toxicity. *PloS one*, 14(9).
- [393] Wang, D., Chen, Q., Cai, F., et al. (2017). Impacts of triamcinolone acetonide on femoral head chondrocytic structures in lumbosacral plexus block. *Saudi pharmaceutical journal*, 25(4), 492-497.
- [394] Bijelić, N., Belovari, T., Stolnik, D., Lovrić, I., & Lončar, M. B. (2017). Histomorphometric parameters of the growth plate and trabecular bone in wild-type and trefoil factor family 3 (Tff3)-deficient mice analyzed by free and open-source image processing software. *Microscopy and Microanalysis*, 23(4), 818-825.

- [395] Huang, D., Wu, S., Hou, X., et al. (2017). The skeletal developmental toxicity of chlormequat chloride and its underlying mechanisms. *Toxicology*, 381,1-9.
- [396] Spingarn, C., Wagner, D., Rémond, Y., & George, D. (2017). Multiphysics of bone remodeling: a 2-D mesoscale activation simulation. *Bio-medical materials and engineering*, 28(s1), S153-S158.
- [397] Chen, H., Zhou, X., Fujita, H., Onozuka, M., & Kubo, K. Y. (2013). Age-related changes in trabecular and cortical bone microstructure. *International journal of endocrinology*, 2013.
- [398] Liu, X. S., Sajda, P., Saha, P. K., et al. (2008). Complete volumetric decomposition of individual trabecular plates and rods and its morphological correlations with anisotropic elastic moduli in human trabecular bone. *Journal of Bone and Mineral Research*, 23(2), 223-235.
- [399] Parashar, S. K., & Sharma, J. K. (2016). A review on application of finite element modelling in bone biomechanics. *Perspectives in Science*, 8, 696-698.
- [400] Pagella, P., Cordiale, A., Marconi, G. D., et al. (2021). Bioengineered tooth emulation systems for regenerative and pharmacological purposes.
- [401] Baranova, J., Büchner, D., Götz, W., Schulze, M., & Tobiasch, E. (2020). Tooth formation: are the hardest tissues of human body hard to regenerate? *International journal of molecular sciences*, 21(11), 4031.
- [402] Al Madhoun, A., Sindhu, S., Haddad, D., et al. (2021). Dental pulp stem cells derived from adult human third molar tooth: a brief review. *Frontiers in Cell and Developmental Biology*, 2780.
- [403] Kollar, E. J. (1986). Tissue interactions in development of teeth and related ectodermal derivatives. *Manipulation of Mammalian Development*, 297-313.
- [404] Diekwisch, T. G. (2004). The developmental biology of cementum. *International Journal of Developmental Biology*, 45(5-6), 695-706.
- [405] Mitsiadis, T. A., & Graf, D. (2009). Cell fate determination during tooth development and regeneration. *Birth Defects Research Part C: Embryo Today: Reviews*, 87(3), 199-211.
- [406] Nanci, A. (2007). *Ten Cate's Oral Histology: Development, Structure, and Function*. St. Louis, Mo, USA: Mosby.
- [407] Pagella, P., de Vargas Roditi, L., Stadlinger, B., Moor, A. E., & Mitsiadis, T. A. (2021). A single-cell atlas of human teeth. *IScience*, 24(5), 102405.
- [408] Kobolak, J., Dinnyes, A., Memic, A., Khademhosseini, A., & Mobasher, A. (2016). Mesenchymal stem cells: Identification, phenotypic characterization, biological properties and potential for regenerative medicine through biomaterial micro-engineering of their niche. *Methods*, 99, 62-68.

- [409] Montagnani, S., Rueger, M. A., Hosoda, T., & Nurzynska, D. (2016). Adult stem cells in tissue maintenance and regeneration. *Stem cells international*, 2016.
- [410] Mitsiadis, T. A., & Rahiotis, C. (2004). Parallels between tooth development and repair: conserved molecular mechanisms following carious and dental injury. *Journal of dental research*, 83(12), 896-902.
- [411] Zheng, L., Ehardt, L., McAlpin, B., et al. (2014). The tick tock of odontogenesis. *Experimental Cell Research*, 325, 83–89.
- [412] Rathee, M., and Jain, P. (2021). *Embryology, Teeth*. Treasure Island, FL: StatPearls.
- [413] Ahtiainen, L., Uski, I., Thesleff, I., and Mikkola, M. L. (2016). Early epithelial signaling center governs tooth budding morphogenesis. *Journal of Cell Biology*, 214, 753–767.
- [414] Mogollón, I., Moustakas-Verho, J. E., Niittykoski, M., and Ahtiainen, L. (2021). The initiation knot is a signaling center required for molar tooth development. *Development*, 148:194597.
- [415] Jernvall, J., Kettunen, P., Karavanova, I., Martin, L. B., & Thesleff, I. (2002). Evidence for the role of the enamel knot as a control center in mammalian tooth cusp formation: non-dividing cells express growth stimulating Fgf-4 gene. *International Journal of Developmental Biology*, 38(3), 463-469.
- [416] Hermans, F., Hemeryck, L., Lambrichts, I., Bronckaers, A., & Vankelecom, H. (2021). Intertwined signaling pathways governing tooth development: A give-and-take between canonical Wnt and Shh. *Frontiers in Cell and Developmental Biology*, 3043.
- [417] Diogenes, A. (2020). Trigeminal sensory neurons and pulp regeneration. *Journal of endodontics*, 46(9), S71-S80.
- [418] Zhan, C., Huang, M., Yang, X., & Hou, J. (2021). Dental nerves: a neglected mediator of pulpitis. *International Endodontic Journal*, 54(1), 85-99.
- [419] Zhao, H., Feng, J., Seidel, K., et al. (2014). Secretion of shh by a neurovascular bundle niche supports mesenchymal stem cell homeostasis in the adult mouse incisor. *Cell stem cell*, 14(2), 160-173.
- [420] Galler, K. M., Weber, M., Korkmaz, Y., Widbiller, M., & Feuerer, M. (2021). Inflammatory response mechanisms of the dentine–pulp complex and the periapical tissues. *International journal of molecular sciences*, 22(3), 1480.
- [421] Liu, A. Q., Zhang, L. S., Fei, D. D., et al. (2020). Sensory nerve-deficient microenvironment impairs tooth homeostasis by inducing apoptosis of dental pulp stem cells. *Cell Proliferation*, 53(5), e12803.
- [422] Kettunen, P., Løes, S., Furmanek, T., et al. (2005). Coordination of trigeminal axon navigation and patterning with tooth organ formation: epithelial-

- mesenchymal interactions, and epithelial Wnt4 and Tgf β 1 regulate semaphorin 3a expression in the dental mesenchyme. *Development*, 132 (2), 323–334.
- [423] Luukko, K., Kvinnsland, I. H., & Kettunen, P. (2005). Tissue interactions in the regulation of axon pathfinding during tooth morphogenesis. *Developmental Dynamics*, 234(3), 482-488.
- [424] Huang, X. F., Zhao, Y. B., Zhang, F. M., & Han, P. Y. (2009). Comparative study of gene expression during tooth eruption and orthodontic tooth movement in mice. *Oral Diseases*, 15(8), 573-579.
- [425] Fried, K., & Gibbs, J. L. (2014). Dental pulp innervation. In *The dental pulp* (pp. 75-95). Springer, Berlin, Heidelberg.
- [426] Pagella, P., Jiménez-Rojo, L., & Mitsiadis, T. A. (2014). Roles of innervation in developing and regenerating orofacial tissues. *Cellular and molecular life sciences*, 71(12), 2241-2251.
- [427] Fried, K., Sessle, B. J., & Devor, M. (2011). The paradox of pain from the tooth-pulp: Low-threshold “algoneurons”? *Pain*, 152(12), 2685.
- [428] Farahani, R. M., Simonian, M., & Hunter, N. (2011). Blueprint of an ancestral neurosensory organ revealed in glial networks in human dental pulp. *Journal of Comparative Neurology*, 519(16), 3306-3326.
- [429] Friedenstein, A. J., Gorskaja, J. F., & Kulagina, N. (1976). Fibroblast precursors in normal and irradiated mouse hematopoietic organs. *Experimental haematology*, 4(5), 267-274.
- [430] Hilfiker, A., Kasper, C., Hass, R., & Haverich, A. (2011). Mesenchymal stem cells and progenitor cells in connective tissue engineering and regenerative medicine: is there a future for transplantation? *Langenbeck's Archives of Surgery*, 396(4), 489-497.
- [431] Rodríguez-Fuentes, D. E., Fernández-Garza, L. E., Samia-Meza, J. A., et al. (2021). Mesenchymal stem cells current clinical applications: a systematic review. *Archives of Medical Research*, 52(1), 93-101.
- [432] Volponi, A. A., Pang, Y., & Sharpe, P. T. (2010). Stem cell-based biological tooth repair and regeneration. *Trends in cell biology*, 20(12), 715-722.
- [433] Orsini, G., Pagella, P., & Mitsiadis, T. A. (2018). Modern trends in dental medicine: an update for internists. *The American journal of medicine*, 131(12), 1425-1430.
- [434] Lane, S. W., Williams, D. A., & Watt, F. M. (2014). Modulating the stem cell niche for tissue regeneration. *Nature biotechnology*, 32(8), 795-803.
- [435] Yin, X., Mead, B. E., Safaee, H., et al. (2016). Engineering stem cell organoids. *Cell stem cell*, 18(1), 25-38.

- [436] Kouroupis, D., & Correa, D. (2021). Increased mesenchymal stem cell functionalization in three-dimensional manufacturing settings for enhanced therapeutic applications. *Frontiers in bioengineering and biotechnology*, 9, 621748.
- [437] Marconi, G. D., Porcheri, C., Trubiani, O., & Mitsiadis, T. A. (2021). Three-dimensional culture systems for dissecting notch signalling in health and disease. *International journal of molecular sciences*, 22(22), 12473.
- [438] Jauković, A., Abadjieva, D., Trivanović, D., et al. (2020). Specificity of 3-D MSC spheroids microenvironment: impact on MSC behaviour and properties. *Stem cell reviews and reports*, 16(5), 853-875.
- [439] Caroni, P., & Schwab, M. E. (1988). Two membrane protein fractions from rat central myelin with inhibitory properties for neurite growth and fibroblast spreading. *The Journal of cell biology*, 106(4), 1281-1288.
- [440] Spillmann, A. A., Bandtlow, C. E., Lottspeich, F., Keller, F., & Schwab, M. E. (1998). Identification and characterization of a bovine neurite growth inhibitor (bNI-220). *Journal of Biological Chemistry*, 273(30), 19283-19293.
- [441] Brösamle, C., Huber, A. B., Fiedler, M., Skerra, A., & Schwab, M. E. (2000). Regeneration of lesioned corticospinal tract fibers in the adult rat induced by a recombinant, humanized IN-1 antibody fragment. *Journal of Neuroscience*, 20(21), 8061-8068.
- [442] Chen, M. S., Huber, A. B., van der Haar, M. E., et al. (2000) Nogo-A is a myelin-associated neurite outgrowth inhibitor and an antigen for monoclonal antibody IN-1. *Nature*, 403, 434-439.
- [443] Schwab, M. E. (2004). Nogo and axon regeneration. *Current Opinions in Neurobiology*, 14, 118-124.
- [444] Yiu, G. and He, Z. (2006). Glial inhibition of CNS axon regeneration. *Nature Reviews Neuroscience*, 7, 617-627.
- [445] Kucher, K., Johns, D., Maier, D., et al. (2018). First-in-man intrathecal application of neurite growth-promoting anti-Nogo-A antibodies in acute spinal cord injury. *Neurorehabilitation and Neural Repair*, 32(6-7), 578-589.
- [446] Pradhan, L. K., & Das, S. K. (2021). The regulatory role of reticulons in neurodegeneration: insights underpinning therapeutic potential for neurodegenerative diseases. *Cellular and Molecular Neurobiology*, 41(6), 1157-1174.
- [447] Zörner, B., & Schwab, M. E. (2010). Anti-Nogo on the go: From animal models to a clinical trial. *Annals of the New York Academy of Sciences*, 1198, E22-E34.
- [448] Kempf, A., & Schwab, M. E. (2013). Nogo-A represses anatomical and synaptic plasticity in the central nervous system. *Physiology*, 28(3), 151-163.
- [449] Schwab, M. E. (2010). Functions of Nogo proteins and their receptors in the nervous system. *Nature Reviews Neuroscience*, 11(12), 799-811.

- [450] Pagella, P. (2015). The role of Nogo-a in tooth development and regeneration (Doctoral dissertation, University of Zurich).
- [451] Wang, K. C., Kim, J. A., Sivasankaran, R., Segal, R., & He, Z. (2002). P75 interacts with the Nogo receptor as a co-receptor for Nogo, MAG and OMgp. *Nature*, 420(6911), 74-78.
- [452] Mi, S., Lee, X., Shao, Z., et al. (2004). LINGO-1 is a component of the Nogo-66 receptor/p75 signaling complex. *Nature neuroscience*, 7(3), 221-228.
- [453] Fournier, A. E., GrandPre, T., & Strittmatter, S. M. (2001). Identification of a receptor mediating Nogo-66 inhibition of axonal regeneration. *Nature*, 409(6818), 341-346.
- [454] Kempf, A., Tews, B., Arzt, M. E., et al. (2014). The sphingolipid receptor S1PR2 is a receptor for Nogo-a repressing synaptic plasticity. *PLoS biology*, 12(1), e1001763.
- [455] Schwab, M. E., & Strittmatter, S. M. (2014). Nogo limits neural plasticity and recovery from injury. *Current opinion in neurobiology*, 27, 53-60.
- [456] Atwal, J. K., Pinkston-Gosse, J., Syken, J., et al. (2008). PirB is a functional receptor for myelin inhibitors of axonal regeneration. *Science*, 322(5903), 967-970.
- [457] Niederöst, B., Oertle, T., Fritsche, J., McKinney, R. A., & Bandtlow, C. E. (2002). Nogo-A and myelin-associated glycoprotein mediate neurite growth inhibition by antagonistic regulation of RhoA and Rac1. *Journal of Neuroscience*, 22(23), 10368-10376.
- [458] Montani, L., Gerrits, B., Gehrig, P., et al. (2009). Neuronal Nogo-A modulates growth cone motility via Rho-GTP/LIMK1/cofilin in the unlesioned adult nervous system. *Journal of Biological Chemistry*, 284(16), 10793-10807.
- [459] Joset, A., Dodd, D. A., Halegoua, S., & Schwab, M. E. (2010). Pincher-generated Nogo-A endosomes mediate growth cone collapse and retrograde signaling. *Journal of Cell Biology*, 188(2), 271-285.
- [460] Wang, B., Xiao, Z., Chen, B., et al. (2008). Nogo-66 promotes the differentiation of neural progenitors into astroglial lineage cells through mTOR-STAT3 pathway. *PloS one*, 3(3), e1856.
- [461] Bi, Y. Y., & Quan, Y. (2018). PirB inhibits axonal outgrowth via the PI3K/Akt/mTOR signaling pathway. *Molecular Medicine Reports*, 17(1), 1093-1098.
- [462] Josephson, A., Trifunovski, A., Widmer, H. R., et al. (2002). Nogo-receptor gene activity: cellular localization and developmental regulation of mRNA in mice and humans. *Journal of Comparative Neurology*, 453(3), 292-304.
- [463] Galipeau, J., Krampera, M., Barrett, J., et al. (2016). International Society for Cellular Therapy perspective on immune functional assays for mesenchymal stromal cells as potency release criterion for advanced phase clinical trials. *Cytotherapy*, 18(2), 151-159.

- [464] Soille, P., *Morphological Image Analysis: Principles and Applications*, Springer-Verlag, 1999, pp. 173–174.
- [465] Lee, T. C., Kashyap, R. L., & Chu, C. N. (1994). Building skeleton models via 3-D medial surface axis thinning algorithms. *CVGIP: Graphical Models and Image Processing*, 56(6), 462-478.
- [466] Kerschnitzki, M., Kollmannsberger, P., Burghammer, M., et al. (2013). Architecture of the osteocyte network correlates with bone material quality. *Journal of bone and mineral research*, 28(8), 1837-1845.
- [467] Oertle, T., Van Der Haar, M. E., Bandtlow, C. E., et al. (2003). Nogo-A inhibits neurite outgrowth and cell spreading with three discrete regions. *Journal of Neuroscience*, 23(13), 5393-5406.
- [468] Pratt, W. K. (1978). *Digital image processing. a wiley-interscience publication*. New York: Wiley, 1(1978), 2.
- [469] Zuiderveld, K. (1994). Contrast limited adaptive histogram equalization. *Graphics gems*, 474-485.
- [470] Frangi, A. F., Niessen, W. J., Vincken, K. L., & Viergever, M. A. (1998, October). Multiscale vessel enhancement filtering. In *International conference on medical image computing and computer-assisted intervention* (pp. 130-137). Springer, Berlin, Heidelberg.
- [471] Atherton, T. J., & Kerbyson, D. J. (1999). Size invariant circle detection. *Image and Vision computing*, 17(11), 795-803.
- [472] Yuen, H. K., Princen, J., Illingworth, J., & Kittler, J. (1990). Comparative study of Hough transform methods for circle finding. *Image and vision computing*, 8(1), 71-77.
- [473] Davies, E. R. (2004). *Machine vision: theory, algorithms, practicalities*. Elsevier.
- [474] Pagella, P., Vargas Roditi, L., Stadlinger, B., Moor, A. E., & Mitsiadis, T. A. (2021). Notch signaling in the dynamics of perivascular stem cells and their niches. *Stem Cells Translational Medicine*, 10(10), 1433-1445.
- [475] Petrinovic, M. M., Duncan, C. S., Bourikas, D., et al. (2010). Neuronal Nogo-A regulates neurite fasciculation, branching and extension in the developing nervous system. *Development*, 137(15), 2539-2550.
- [476] Kempf, A., Montani, L., Petrinovic, M. M., et al. (2013). Upregulation of axon guidance molecules in the adult central nervous system of Nogo-A knockout mice restricts neuronal growth and regeneration. *European Journal of Neuroscience*, 38(11), 3567-3579.
- [477] Rylance, R. (2015). Global funders to focus on interdisciplinarity. *Nature*, 525(7569), 313-315.

Acknowledgements

Many people deserve to be acknowledged for having made possible this work. First, I need to thank both my PhD supervisor, Prof. Alessandro Bevilacqua, and my co-supervisor, Prof. Laura Calzà. To Prof. Alessandro Bevilacqua goes my most sincere gratitude, for have patiently walked me through my interdisciplinary transition, always believing in me and in the Project, even when I did not. A deep thanks also to Prof. Laura Calzà, that has given me the opportunity to confirm the power of our interdisciplinary approach, first collaborating in our methods development, and then fostering my collaborations abroad. In this regard, I would also like to thank Prof. Thimios A. Mitsiadis, leading the Orofacial Development and Regeneration Unit at the Institute of Oral Biology of the University of Zürich (CH), for having welcomed me in its laboratory and group, believing from the beginning in my contribution to the activities. Thank you also to all the other group members, that made me feel so welcome, and especially to Dr. Deborah Stanco and Laurence Pirenne, for involving me in their brilliant research projects.

My gratitude extends to Dr. Anna Tesei and the whole Radiobiomics and Drug Discovery Unit of the IRCCS-IRST (Meldola, IT), for the long cooperative relationship, and to all the other researchers that have contributed to the collaboration studies of this Thesis. Thanks to Dr. Enrico Lucarelli, Dr. Elisa Martella, and the Regeneration Therapy in Oncology Unit of the Rizzoli Hospital (Bologna, IT), as well as to the researchers of the IRET Foundation (Ozzano dell'Emilia, IT), for having provided important datasets for our image processing method development. Thanks to Prof. Carla Palumbo and her team at the Department of Biomedical, Metabolic and Neural Sciences of the University of Modena and Reggio Emilia (Modena, IT), together with Prof. Maria Pia Morigi and Dr. Matteo Bettuzzi of the Department of Physics and Astronomy of the University of Bologna, (Bologna, IT), for giving me the possibility to experience new imaging modalities and image processing methods. I sincerely look forward to maintaining and growing the contacts and collaborations established in this PhD.

Finally, on a personal note, I would like to thank all those people who helped me through the PhD years with their support and patience. In particular, a special thanks goes to Carla and Sabrina, because nobody will ever believe in me more than them. And lastly, my deepest appreciation to Manuel, that lets me pursue all my intensive interests, accepts me and the path I have chosen, and yet remains by my side, helping me being a more balanced person.

THESIS END

Ilaria De Santis

E-mail: i.desantis@unibo.it

Research group website: <https://cvg.deis.unibo.it/>

Personal website: <https://www.unibo.it/sitoweb/i.desantis>

(Curriculum Vitae available on the personal website)

Office address:

Via Toffano 2/2, 40125, Bologna, Italy

Home address:

Via Lasie 3, 40026 , Imola, Italy